Autonomous ocean carbon system observations from gliders

Luca Possenti

PhD candidate

University of East Anglia

Centre for Ocean and Atmospheric Sciences

School of Environmental Sciences

September 2020

Supervised by: Professor Jan Kaiser, Dr Matthew Humphreys, Dr Liam Fernand, Professor Matthew Mowlem, Dr Socratis Loucaides

Abstract

Climate change is altering the ocean carbonate system decreasing the seawater pH. To quantify these changes novel sampling and monitoring methods are necessary. One of these methods are gliders. The sensors to fit on a glider need to have a compact size, low-cost, stability, accuracy and fast response. For the first time, a CO_2 optode (Aanderaa), a potentiometric pH glass electrode (Fluidion) and a spectrophotometric lab-on-chip pH sensor (UK National Oceanography Centre) were tested on gliders.

The CO_2 optode was deployed for 8 months in the Norwegian Sea, with an O_2 optode. The CO_2 measurements required several corrections. The calibrated optode CO_2 concentrations and a regional parameterisation of total alkalinity (A_T) were used to calculate dissolved inorganic carbon concentrations (C_T) with a standard deviation of 11 µmol kg^{-1}. The O_2 and CO_2 data were used to calculate C_T- and O_2-based net community production (NCP) from inventory changes combined with estimates of air-sea exchange, diapycnal mixing and entrainment of deeper waters. Because of the summer period the NCP was largely positive.

The spectrophotometric pH sensor, the glass electrode and an O_2 optode were deployed on a Seaglider for 10 days in the North Sea. Before the deployment, laboratory tests showed that the main source of error for glass electrodes is drift when deployed in seawater. The spectrophotometric sensor was stable with an accuracy of 0.002 and was used as reference to calibrate the glass electrode. The potentiometric sensor failed after 2 days' deployment and was not affected by drift (<0.01), because it had been stored in seawater for 2 months. The spectrophotometric sensor had a mean bias of 0.006±0.008 (1σ) compared with pH derived from discrete A_T and C_T samples, higher than in the laboratory. The data were used to calculate O_2 and CO_2 air-sea fluxes and bottom respiration rates.

Table of Contents

Abstract **2**

Table of Contents **4**

List of Figures **8**

List of Tables **12**

List of Abbreviations **14**

List of Symbols used in equations **15**

Acknowledgements **17**

1 Introduction **19**

1.1 Ocean carbon system 19

1.2 Sensors to measure seawater pH 22

1.2.1 Potentiometric 22

1.2.2 Spectrophotometric 23

1.2.3 ISFET 24

1.2.4 Luminescence 25

1.3 Gliders: the high-resolution platform 25

1.4 Net Community Production 27

1.5 Study area 28

1.5.1 Norwegian Sea 28

1.5.2 North Sea 30

1.6 Thesis aim 33

1.7 Thesis outline 35

2 Norwegian Sea net community production estimated from O_2 and prototype CO_2 optode measurements on a Seaglider 37

2.1 Summary 37

2.2 Introduction 38

2.3 Material and methods 40

2.3.1 Glider sampling 40

2.3.2 Discrete sampling 42

2.3.3 Oxygen optode calibration 42

2.3.4 CO_2 optode measurement principle 45

2.3.5 CO_2 optode lag and drift correction 46

2.3.6 CO_2 optode calibration 48

2.3.7 Regional algorithm to estimate A_T 51

2.3.8 Quality control of other measurement variables 51

2.3.9 Calculation of oxygen-based net community production, $N(O_2)$ 53

2.3.10 Calculation of inorganic carbon-based net community production, $N(C_T)$ 55

2.4 Results 57

2.4.1 O_2 optode calibration 59

2.4.2 CO_2 optode calibration 61

2.4.3 Air-sea exchange 63

2.4.4 Oxygen-based net community production, $N(O_2)$ 66

2.4.5 Inorganic carbon-based net community production, $N(C_T)$ 67

2.5 Discussion 70

2.5.1 Sensor performance 70

2.5.2 Norwegian Sea net community production 71

2.6 Conclusions 73

3 An evaluation of potentiometric and spectrophotometric pH sensors 76

3.1 Summary 76

3.2 Introduction 77

3.3 Materials and methods 79

3.3.1 Sensor description 79

3.3.2 Temperature probe calibration 82

3.3.3 Tris buffer preparation and quality control 83

3.3.4 Temperature effect 85

3.3.5 Response time 87

3.3.6 Sensor performance in seawater 88

3.3.7 Calibration method 88

3.4 Results 89

3.4.1 Equimolar Tris buffer quality control 89

3.4.2 Temperature effect on pH 89

3.4.3 Sensor performance in seawater 93

3.4.4 Glass electrodes response times 94

3.4.5 Use of the spectrophotometric pH sensor as a reference to calibrate glass electrodes 96

3.4.6 Test in Southampton dock 97

3.5 Discussion 100

3.5.1 Performance of different pH sensors 100

3.5.2 Storage effect on different pH sensors 102

3.5.3 Temperature effect on different pH sensors 102

3.5.4 In situ calibration of glass electrodes 103

3.6 Conclusions 104

4 North Sea pH and O_2 variability using two experimental potentiometric and spectrophotometric pH sensors and an O_2 optode on a Seaglider 107

4.1 Summary 107

4.2 Introduction 108

4.3 Material and methods 110

4.3.1 Glider sampling 110

4.3.2 Discrete sampling 114

4.3.3 Spectrophotometric pH sensor corrections 115

4.3.4 Potentiometric pH sensor corrections 116

4.3.5 Regional algorithm to estimate A_T 116

4.3.6 Oxygen optode drift correction 117

4.3.7 Quality control of CTD measurements 119

4.3.8 Air-sea exchange calculation 120

4.3.9 Apparent Carbon Production 122

4.4 Results 123

4.4.1 Spectrophotometric pH sensor lag correction 123

4.4.2 O_2 optode calibration 125

4.4.3 Three different environmental regions 126

4.4.4 Air-sea exchange 132

4.4.5 Remineralisation in deep waters 136

4.4.6 O_2 and pH diel cycle 138

4.5 Discussion 138

4.5.1 pH sensor performance 138

4.5.2 North Sea subsurface oxygen maximum 139

4.5.3 North Sea air-sea exchange 143

4.6 Conclusions 145

5 Conclusions and Outlook 148

5.1 Best practices in the use of pH sensors 148

5.2 New carbonate sensors on a glider 150

5.3 Best practices to calculate net community production using gliders 153

5.4 Capture ocean inorganic carbon and oxygen changes using gliders 155

References 158

Appendices 180

A Supplementary Figures 180

List of Figures

Figure 1.1 Picture of a Kongsberg Seaglider……26

Figure 1.2 Map of the Nordic Seas and their main surface currents……29

Figure 1.3 Bathymetry of the North Sea……..31

Figure 1.4 Vertical sections of total inorganic carbon concentrations in the North Sea along 0.5° W, 2.5° E and 60° N……33

Figure 2.1 Map of the glider deployment area in the Norwegian Sea and the main water masses……41

Figure 2.2 Under a water density of 1028 kg m^{-3} glider oxygen concentration coloured by latitude……44

Figure 2.3 Correction of the oxygen optode drift ……45

Figure 2.4 CO_2 optode vertical profiles after each correction……..47

Figure 2.5 Histogram of the distribution of the r used to correct the CO_2 optode drift…..48

Figure 2.6 Calibration of the CO_2 optode against the $c(CO_2)$ discrete samples……50

Figure 2.7 Comparison between the satellite and the glider chlorophyll……52

Figure 2.8 Raw glider data of temperature, salinity, oxygen, uncorrected CO_2 optode output and chlorophyll *a* concentration……58

Figure 2.9 Comparison between the discrete samples and gliders oxygen before and after corrections……59

Figure 2.10 Contour plot of the drift corrected oxygen and oxygen saturation.……60

Figure 2.11 Contour plot of the dissolved inorganic carbon, C_T……..62

Figure 2.12 Comparison between SOCAT and glider surface $f(CO_2)$……63

Figure 2.13 Norwegian Sea CO_2 and oxygen air-sea flux……....65

Figure 2.14 Norwegian Sea oxygen-based net community production……..67

Figure 2.15 Norwegian Sea inorganic carbon-based net community production…….70

Figure 3.1 Calibration of the Pt100 raw Temperature using a mercury thermometer as a reference……..83

Figure 3.2 Schematic of the laboratory experiment set up……...…86

Figure 3.3 Example of the AMT glass electrode response time……..……87

Figure 3.4 Comparison between the Dickson's and homemade Tris buffer …….89

Figure 3.5 Series of 3 experiments performed in Tris to assess the two glass electrodes and the spectrophotometric sensor performance varying the solution temperature……91

Figure 3.6 Average offset from the Tris pH at different temperatures ……92

Figure 3.7 Series of 3 experiments performed in seawater varying the solution temperature……94

Figure 3.8 Glass electrodes response time (τ)……..……95

Figure 3.9 Calibration of the glass electrodes using the spectrophotometric pH as reference……96

Figure 3.10 Dock deployment of the AMT glass electrode and the lab-on-chip spectrophotometric pH sensor……...98

Figure 3.11 Temperature and salinity effect on the AMT and lab-on-chip spectrophotometric pH sensor during the dock deployment……99

Figure 3.12 Salinity effect on the AMT pH sensor during the dock deployment……...100

Figure 4.1 Map of the North Sea glider deployment area……..111

Figure 4.2 Seaglider equipped with the Aanderaa 4831F oxygen optode, a Sea-Bird CTD, Fluidion potentiometric pH sensor and the NOC lab-on-chip spectrophotometric pH sensor……...112

Figure 4.3 Raw glider data of temperature, salinity, oxygen, Fluidion pH and the spectrophotometric pH……113

Figure 4.4 Spectrophotometric pH sensor lag calculated as the time difference from the first CTD samples……..115

Figure 4.5 Comparison between total alkalinity (A_T) directly measured in discrete samples and and the glider based A_T derived from temperature and salinity……117

Figure 4.6 Surface glider $c(O_2)$ at 1 m during the ascent and descent……..118

Figure 4.7 Temperature and Oxygen comparison between a normal dive and a loiter dive……120

Figure 4.8 Spectrophotometric pH before and after the lag correction against temperature……...124

Figure 4.9 Vertical profiles of the spectrophotometric pH after each correction …….125

Figure 4.10 Oxygen optode calibration and drift correction using the discrete samples collected at the glider deployment and recovery ……126

Figure 4.11 North Sea surface temperature, salinity, total alkalinity, dissolved inorganic carbon, pH and partial pressure of CO_2……127

Figure 4.12 North Sea deep temperature, salinity, total alkalinity, dissolved inorganic carbon, pH and partial pressure of CO_2……128

Figure 4.13 North Sea difference between the surface and deep water density…….129

Figure 4.14 Contour plots of the calibrated and drift corrected oxygen, oxygen saturation and apparent oxygen utilisation (AOU) ……...130

Figure 4.15 North Sea spectrophotometric pH after all the corrections……132

Figure 4.16 North Sea potentiometric pH after all the corrections……132

Figure 4.17 North Sea oxygen air-sea flux.....134

Figure 4.18 North Sea CO_2 air-sea flux ……135

Figure 4.19 Under 60 m waters apparent oxygen utilisation (AOU) and apparent carbon utilisation (ACP)……...137

Figure 4.20 Surface 5 meters pH(NOC) normalised to 15 °C and $c(O_2)$…….....138

Figure 4.21 North Sea 5 days composite mean of the satellite chlorophyll before and during the glider deployment……..142

Figure 4.22 North Sea CO_2 air-sea gas exchange calculated from the discrete samples….....145

Figure 5.1 Ideal glider mission to calculate the net community production (NCP)……..154

List of tables

Table 1.1 Analytical precision and accuracy of measurements of pH, A_T, C_T and $f(CO_2)$ Millero (2007) analytical precision and accuracy of measurements of pH, A_T, C_T and $f(CO_2)$……...20

Table 1.2 Estimated errors in the calculation of the carbonate system……..20

Table 2.1 Average time needed by the different sensors to perform an in situ measurement…….41

Table 2.2 Uncertainty of the input variables used to calculate the oxygen and inorganic carbon-based net community production……57

Table 2.3 Estimates of Norwegian Sea net community production from previous studies…….69

Table 3.1 List of laboratory experiments ……85

Table 4.1 Uncertainty of the input variables used to calculate the oxygen and CO_2 air-sea flux…….....122

List of Abbreviations

ACP	Apparent Carbon Production
AOU	Apparent Oxygen Utilisation
AUV	Autonomous Underwater Vehicle
BML	Bottom of Mixed Layer
CDOM	Coloured Dissolved Organic Matter
Cefas	Centre for Environment, Fisheries and Aquaculture Science
CNSW	Central North Sea Water
CRM	Certified Reference Material
CTD	Conductivity-Temperature-Depth
DCM	Deep Chlorophyll Maximum
DIC	Dissolved Inorganic Carbon
DLR	Dual Lifetime Referencing
DOM	Dissolved Organic Matter
EMF	Electromotive Force
GEBCO	General Bathymetric Chart of the Oceans
GLODAP	Global Ocean Data Analysis Project
GOA-ON	Global Ocean Acidification Observing Network
ISFET	Ion-Sensitive Field Effect Transistor
LoC	Lab-on-a-chip
*m*CP	metacresol purple
MLR	Multiple Linear Regression
NAOI	North Atlantic Oscillation Index
NAW	North Atlantic Water
NBS	National Bureau of Standards
NCC	Norwegian Coastal Current

NOC National Oceanography Centre, Southampton, UK

NSDW Norwegian Sea Deep Water

NwAC Norwegian Atlantic Current

OA Ocean Acidification

OTE Ocean Technology and Engineering Group, National Oceanography Centre, Southampton, UK

OWSM Ocean Weather Station M

PML Plymouth Marine Laboratory, Plymouth, UK

PQ Photosynthetic Quotient

SML Surface of Mixed Layer

SOCAT Surface Ocean CO_2 Atlas

SOCCOM Southern Ocean Carbon and Climate Observations and Modelling

SOM Subsurface Oxygen Maximum

SOP Standard Operating Procedure

SW Skagerrak Water

TDI Thermal Developments International

UEA University of East Anglia, Norwich, UK

VINDTA Versatile INstrument for the Determination of Total inorganic carbon and titration Alkalinity

VOS Voluntary Observing Ships

List of Symbols used in equations

Φ	air-sea flux
Δ_{bub}	bubble injection
c	concentration
Chl *a*	chlorophyll a
φ	CO_2 optode raw data (“CalPhase”)
z_{DCM}	deep chlorophyll maximum depth
C_T	dissolved inorganic carbon concentration
x	dry mole fraction
E	electromotive force (EMF)
F_E	entrainment
F_v	diapycnal mixing$f(CO_2)$ fugacity of CO_2
R	gas constant
I	inventory
z_{lim}	integration depth
z_{mix}	mixed layer depth
N	net community production
pH_T(NOC)	NOC pH lag corrected
pH_C(NOC)	NOC pH lag and temperature corrected
$p(CO_2)$	partial pressure of CO_2
σ_0	potential density
τ	response time
S	salinity
Sc	Schmidt number
θ	temperature in Celsius
T	temperature in kelvin
t	time
A_T	total alkalinity
k_w	transfer velocity
U	wind speed

Acknowledgments

I want to thank for the support, patience and guidance from all my supervisors: Jan Kaiser, Matthew Humphreys, Liam Fernand, Socratis Loucaides and Matthew Mowlem. Also, I want to thank Bastien Queste for his initial guidance. During these 4 years, they helped me to appreciate and love a field completely new for me.

For providing me the funding for this work, I thank the University of East Anglia and Nexuss.

I also want to thank Ingunn Skjelvan and Anders Tengberg who allowed me to work on the Norwegian Sea deployment dataset and Dariia Atamanchuk for her insights on the CO_2 optode. The North Sea deployment would not have been possible without Marcos Cobas García and Gareth Lee who worked on land to prepare the cruise equipment and the glider. Marcos helped me to understand how a glider works and taught me the best practices to deploy and recover a glider. During the cruise, the work of all the crew and the help and support of Francesco Pallottino were fundamental for the success of the deployment. I want to thank Dorothee Bakker for the help and guidance on the analysis of the discrete samples and to provide me the Rothera seawater used in the laboratory experiments (section 3 of the thesis). The North Sea deployment data analysis would not have been possible without Tom Hull help and insights.

These 4 years were not just a moment to study, but I also had a great time with amazing friends: Giovanni, Nicholas, TK, Konstantina, Emma, Mantha, Keira, Jennifer, Idil, Ingrid, Olivia, Francesco, Clement, Stuart, et al. My work would not have been the same without my colleagues: Jack, Shenjie, Matt, Pierre, Tom, Yuanxin, Jan, and Richard. A special mention to Matt who was sitting next to me in the office and lost his life a couple of years ago.

Also, I want to thank all the Kaiser Lab gang for the cakes on Thursday, the nice trips and tasty BBQs.

I want to thank my friends in Milan for their support and relaxing nights when I was back in Italy. Last but not least, I want to thank my parents for their support, critical comments and love during all these years.

Chapter 1

Introduction

1.1 Ocean carbon system

In the ocean, dissolved inorganic carbon occurs in four different forms: aqueous carbon dioxide ($CO_2(aq)$), bicarbonate ions (HCO_3^-), carbonate ions (CO_3^{2-}) and carbonic acid (H_2CO_3). These chemical species are linked by equilibrium reactions between atmospheric CO_2 and seawater (Zeebe and Wolf-Gladrow, 2001):

$$CO_2(g) \rightleftharpoons CO_2(aq) + H_2O \rightleftharpoons HCO_3^- + H^+ \rightleftharpoons CO_3^{2-} + 2H^+ \qquad (1.1)$$

The concentration of H_2CO_3 is considered negligible ($<10^{-3}$ %). For that reason, it is summed together with the other uncharged dissolved form ($CO_2(aq)$) and is usually denoted by CO_2 or $H_2CO_3^*$.

The ocean carbonate system can be quantified using four quantities: dissolved inorganic carbon concentration (C_T), total alkalinity (A_T), pH, partial pressure of CO_2 ($p(CO_2)$) or fugacity of CO_2 ($f(CO_2)$) and CO_3^{2-} concentration. These concentrations are controlled by the equilibrium of equation 1.1. For example, an increase of atmospheric CO_2 ($CO_2(g)$) would shift the equilibrium to the left having a lower pH and a higher concentration of CO_3^{2-}. Instead, a decrease of atmospheric CO_2 ($CO_2(g)$) would shift the equilibrium to the right with a higher pH, lower $f(CO_2)$ and C_T. The measurement of two of the four quantities along with temperature, salinity and pressure allow the calculation of the two remaining quantities. Different pairs of combinations lead to different accuracies for the derived quantities (Dickson and Riley, 1979; Millero et al., 1993; Dickson, 2010). Using as input the uncertainties reported in Table 1.1, the uncertainties in the calculated quantities are reported in Table 1.2 (Millero, 2007).

Table 1.1: Analytical precision and accuracy in the laboratory of measurements of pH, A_T, C_T and $f(CO_2)$. From Millero (2007).

variable (analysis method)	precision	accuracy
pH (spectrophotometric)	±0.0004	±0.002
A_T (potentiometric)	±1 µmol kg^{-1}	±3 µmol kg^{-1}
C_T (coulometric)	±1 µmol kg^{-1}	±2 µmol kg^{-1}
$f(CO_2)$ (infrared)	± 0.5 µatm	±2 µatm

Table 1.2: Estimated errors due to experimental errors in carbonate system calculations. From Millero (2007).

input variables	pH	A_T / (µmol kg^{-1})	C_T / (µmol kg^{-1})	$f(CO_2)$ / µatm
pH & A_T			±3.8	±2.1
pH & C_T		±2.7		±1.8
pH & $f(CO_2)$		±21	±18	
$f(CO_2)$ & C_T	±0.0025	±3.4		
$f(CO_2)$ & A_T	±0.0026		±3.2	
A_T & C_T	±0.0062			±5.7

C_T is defined as the sum of the concentrations of the dissolved inorganic carbon species CO_2, HCO_3^- and CO_3^{2-}. In seawater at temperature θ = 25 °C, practical salinity S = 35 and pH = 8.1 the most common species is HCO_3^- accounting for 86.5 %, CO_2 accounts just for 0.5 % and CO_3^{2-} for 13 % (Zeebe and Wolf-Gladrow, 2001).

A_T is defined as the excess concentration of proton acceptors over proton donors. The concentration excess is defined as the sum of the charges of major cations Na^+, K^+, Mg^{2+}, and Ca^{2+} that are not exactly balanced by the major anions Cl^{2-} and SO_4^{2-}. The changes in A_T are related to processes connected to salinity (e.g. precipitation, evaporation, freshwater input and sea-ice melting and formation) and to processes that also affect temperature (e.g. convective mixing of cold deep waters with high A_T) (Lee et al., 2006). Another major change in A_T is caused by biogeochemical processes such as biogenic precipitation of calcium carbonate ($CaCO_3$), nitrogen assimilation by plants and release during remineralisation of dissolved inorganic nitrogen from organic compounds. Routinely, A_T can be regionally estimated from S and θ (Chu et al., 2020; Lee et al., 2006; Nondal et al., 2009; Saba et al., 2019).

The partial pressure of CO_2 for a gas-phase mole fraction $x(CO_2)$ in equilibrium with seawater at total pressure p_T is described by the following equation:

$$p(CO_2) = x(CO_2)\, p_T \qquad (1.2)$$

However, partial pressure is a concept strictly appropriate only for ideal gases and for that reason should be reported as fugacity of CO_2, $f(CO_2)$. However, $p(CO_2)$ and $f(CO_2)$ are almost the same numbers and can be assumed equal for studies that do not require accuracies better than 0.7 % (Weiss, 1974).

The fourth quantity is pH and is defined as the negative logarithm of the activity of H^+ (commonly replaced with the concentration $[H^+]$). Typically, ocean pH is measured using the Total scale (Hansson, 1973) that is based on artificial seawater. The scale includes the hydrogensulfate ion concentration:

$$pH_T = lg([H^+]_F + [HSO_4^-]) = -lg[H^+]_T \qquad (1.3)$$

where $[H^+]_F$ is the free hydrogen ion concentration.

After the creation of the Total pH scale, a series of new standard buffers based on artificial seawater were introduced. One of these is made using 2-amino-2-hydroxymethyl-1,3-propanediol (Tris) and it is available from the laboratory of Prof A. G. Dickson, Scripps Institution of Oceanography, San Diego (DelValls and Dickson, 1998; Nemzer and Dickson, 2005).

The ocean carbon system has been modified since the industrial revolution (starting around 1760) by the increase of atmospheric $x(CO_2)$ by more than 100 µmol mol^{-1} resulting in a decrease of the global ocean pH average from 8.21 to 8.10, corresponding to a 29 % increase in H^+ activity (Doney et al., 2009a; Fabry et al., 2008). The increase of $x(CO_2)$ is driven by human activities such as fossil fuel combustion and deforestation (Doney and Schimel, 2007). Future projections suggest that in the next decades the ocean CO_2 uptake will continue, decreasing the ocean pH in a process known as ocean acidification (OA). In fact, since the industrial revolution (year 1760), global surface ocean pH has fallen from 8.21 to 8.10 (corresponding to a 30 % increase in H^+ ion activity) (Doney et al., 2009a; Fabry et al., 2008). New high-resolution pH sensors can provide the accurate measurements needed to quantify the magnitude and variability of OA around the globe. OA is lowering the calcium carbonate saturation state ($\Omega_{carbonate}$) and carbonate ion concentration, which impacts shell-forming organisms from plankton to benthic molluscs, echinoderms and corals (e.g. Scleractinia) (Doney, Fabry, et al., 2009; Hofmann et al., 2011). $\Omega_{carbonate}$ is defined as a measure of the thermodynamic tendency for the mineral calcium carbonate to form ($\Omega > 1$) or to dissolve ($\Omega < 1$). The oceanic CO_2 uptake has resulted in a shoaling of the aragonite saturation ($\Omega_{aragonite}$)

horizon ($\Omega_{aragonite}$ = 1) by 40 m to 200 m (Feely et al., 2004) and the formation of potentially corrosive waters (Ω < 1) that would dissolve the marine organisms shells and skeleton, for example in the western continental shelf in North America (Feely et al., 2008).

1.2 Sensors to measure seawater pH

In the next sections are described the most common methods to measure ocean pH using in-situ sensors.

1.2.1 Potentiometric

The most widely used method to measure pH is potentiometry using a glass electrode and a silver/silver chloride reference electrode. The sample (X) pH is defined in terms of the electromotive force (EMF) by the Nernst equation:

$$\mathrm{pH(X)} = \mathrm{pH(S)} + \frac{E_S - E_X}{RT\ln 10/F} \quad (1.4)$$

where S is a standard buffer of known pH, *E* is the EMF, *R* is the gas constant, *T* is the temperature in Kelvin and *F* is the Faraday constant.

The residual liquid junction (all the implications are explained in section 3.2) is defined as the difference in junction potentials between measurements with the sample and the standard buffer. The single liquid junction potential is immeasurable, but differences in liquid junction potential can be estimated (Buck et al., 2001). Liquid junction potentials vary with the composition of the solutions forming the junction and the geometry of the junction. The Nernst equation (1.4) assumes an ideal condition measurement where this difference is zero. However, this error cannot be ignored when the ionic strengths of the standard buffer and the sample are different (Kadis and Leito, 2010). This error is minimised by matching the calibration standard buffer composition to the composition of seawater (Dickson, 1993). For example, by making a buffer in synthetic seawater or by calibrating the sensor directly in seawater. Along with the creation of new buffers that match the seawater composition new pH scales have been developed specifically for ocean studies such as the Total scale (Eq 1.3) (Hansson, 1973), Free scale (Dickson, 1984) and Seawater scale (Goyet and Poisson, 1989).

The advantages of the potentiometric method are the low cost, small size, lightweight and the potential to collect high-frequency measurements (> 1 Hz) (Hemmink et al.,

2009). The glass electrodes can achieve an accuracy < 0.01 (Seiter and DeGrandpre, 2001) and a precision in the laboratory of 0.003 (Bane et al., 1988). However, the measured pH is affected by a series of problems: uncertainties caused by temperature changes, glass and reference electrode drift (up to 0.02 d^{-1}), electromagnetic interferences, residual liquid-junction potential variation and ionic strength changes (Dickson, 1993; Seiter and DeGrandpre, 2001). Long deployments of glass electrodes are challenging because they require regular calibration. McLaughlin et al. (2017) used the pH measured by a benchtop spectrophotometer to regularly calibrate glass electrodes and achieved a mean difference between discrete samples and calibrated pH of 0.002. An alternative can be using as reference miniaturised spectrophotometric pH sensors (Liu et al., 2011; Martz et al., 2003; Rérolle et al., 2013; Seidel et al., 2008), reducing the labour cost and allowing prolonged unattended deployments. The glass electrodes are affected by drift when transferred from the 3 M KCl storage solution into seawater. The drift is driven by the ionic strength difference between seawater and the storage solution and the reaction between the AgCl reference electrode and bromide forming $AgCl_xBr_{1-x}$, which shifts the sensor reference potential by 2 to 5 mV (Takeshita et al., 2014).

1.2.2 Spectrophotometric

Byrne and Breland (1989) were the first to measure seawater pH using a spectrophotometer with an accuracy of 0.001. The method uses an acid-base sulfonephthalein indicator dye (e.g. *meta*-cresol purple and thymol blue) that changes colour according to pH with a second dissociation constant pK_A close to the seawater pH (Rérolle et al., 2012). The seawater pH is determined from the distinct absorbance at the wavelengths where the protonated and deprotonated dye forms absorb light. The spectrophotometric method does not require any calibration and is not affected by drift, making it the most precise and accurate method to measure seawater pH with an accuracy as good as 0.001 (Seidel et al., 2008; Wang et al., 2007). However, sensors using the spectrophotometric method can lose accuracy (< 0.004) (Bellerby et al., 2002) in case of variations in the background absorption, the optical cell, the strength and the spectrum of the light source and the sensitivity of the detector (Rérolle et al., 2012).

This method has been extensively used for shipboard measurement; however, the application to miniaturised sensors is challenging due to the complexity and high power requirement needed by the system that requires storing an indicator dye, frequently measuring blanks and valves and pumps to propel the sample and indicator dye through the system (Clarke et al., 2015; Martz et al., 2010). Other problems arise from bubbles

and particles in the system and the limited lifetime of the indicator dye (1 year) (DeGrandpre et al., 1995). In recent years new miniaturised spectrophotometric pH sensors (lab-on-a-chip) have been developed (Aßmann et al., 2011; Bellerby et al., 2002; Carter et al., 2013; Martz et al., 2003; Rérolle et al., 2013; Seidel et al., 2008). These new systems are smaller and simpler because they consist of a pump to collect and inject the sample and dye, a mixer where the sample and dye are mixed and an absorption cell where the absorbances are measured. An example is the SAMI-pH instrument (Seidel et al., 2008) that showed a precision between 0.0003 and 0.0016 with a measurement interval of 15 min (Seidel et al., 2008).

1.2.3 ISFET

One of the most recent technologies developed to measure seawater pH is the ion-sensitive field effect transistor (ISFET). The method determines the H^+ ion activity using the interference potential between a semiconducting ion sensing transistor coated with silicon dioxide (SiO_2) and silicon nitride (Si_3N_4) and a reference electrode. The final pH is obtained by the voltage between the reference electrode and the source electrode, which follows a Nernst equation form. The advantages of using ISFET sensors are the low power consumption (2 mW) (Martz et al., 2010), rapid response to pH changes (<15 s) (Bresnahan et al., 2016; Briggs et al., 2017), small size (Chou and Weng, 2001), low cost (Hemmink et al., 2009), limited drift and robustness with respect to sampling noise due to stray currents. Similarly to glass electrodes, to avoid any drift caused by the reconditioning of the AgCl electrode the ISFET sensors need to be stored in seawater for weeks before being deployed (Gonski et al., 2018; Johnson et al., 2017; Martz et al., 2010).

One of these sensors is the DuraFET sensor (Johnson et al., 2016) that is currently deployed on 86 biogeochemical profiling floats across the globe as part of the Southern Ocean Carbon and Climate Observations and Modelling (SOCCOM) program. The sensors showed an accuracy of 0.01, a multiyear precision of 0.005 (Johnson et al., 2016) and an annual drift < 0.01 a^{-1} (Johnson et al., 2017). Despite the potential of the technology, the 2000 m-rated version is only commercialised in the SeapHOx configuration. The application of this configuration is limited to moorings due to the high-power consumption and large size (55.88 cm x 28.25 cm x 12.90 cm) as the instrument compromises of a CTD, an oxygen sensor and an ISFET pH sensor. In recent years, two different ISFET sensors have been tested on a glider (Hemming et al., 2017; Saba et al., 2019) showing the potential of the technology to be applied on different sampling platforms.

1.2.4 Luminescence

The luminescence method measures seawater pH using the luminescent variation of a pH-dependent indicator dye immobilised in a gas impermeable membrane. In the past, this method has been successfully applied to oxygen (Bittig *et al*, 2018) and CO_2 optodes (Atamanchuk et al., 2014). pH optodes use a time-domain dual-lifetime referencing (t-DLR), which combines ratiometric and lifetime measurements (Liebsc*h* et al., 2001). The pH is calculated from the fluorescence intensity ratio of two luminescent indicators: one with a short luminescent lifetime sensitive to pH and another non-pH-sensitive with a longer lifetime. The sensor measurement time varies from 5 to 200 s and the response time depends on the seawater diffusion through the impermeable membrane (Clarke et al., 2015).

The main advantages of optodes are the low power consumption and small size. However, the luminescence method is not widely used because it is affected by a series of problems. In particular, the final pH needs to be corrected for the seawater temperature and ionic strength and the sensor performance is affected by foil bleaching and sensitive to ambient light (Rérolle et al., 2012). Long exposure to ambient light and excitation light causes the bleach of indicator molecules making the sensor less sensitive to pH changes. Commonly, foil bleaching leads to a continuous drift driven by the different bleaching rates of the pH-sensitive dye and the reference dye (Clarke et al., 2015). These series of limitations related to light sensitivity have restricted the application of this method to measurements of sediment pH (Schröder et al., 2005; Zhu et al., 2005; Hakonen and Hulth, 2010; Larsen et al. (2011). Larsen et al., (2011) tested a pH optode in a Tris buffer, and found an excellent precision of 0.00064. Clarke et al. (2015) deployed another pH optode for 5 weeks on an underway surface ocean system achieving a precision of 0.0074, but also observed a drift of 0.06 over this period.

1.3 Gliders as novel instrument platforms

The need for high-resolution and affordable data brought Stommel (1989) to suggest underwater gliders to the oceanographic community. Gliders are autonomous underwater vehicles (AUV). There are three widely used models: the Scripps Institution of Oceanography's and Woods Hole Oceanographic Institution's Spray glider (Sherman et al., 2001), Webb Research's Slocum glider (Webb et al., 2001) and the University of

Washington's Seaglider now distributed by Kongsberg (Figure 1.1) (Eriksen et al., 2001). In this thesis we used the Seaglider (called glider throughout the thesis).

Figure 1.1: example of a Kongsberg Seaglider developed by the University of Washington's Seaglider now distributed by Kongsberg.

Underwater gliders can perform a 1000 m dive in 6 hours (descent and ascent), moving vertically at 10 cm s^{-1} and horizontally 20-30 cm s^{-1} (4-6 km per dive). The use of lithium batteries and the energy-efficient system gives the potential for several months' deployments (Rudnick, 2016). The vehicle is buoyancy-driven and its vertical movements are controlled by varying the glider's volume, which influences its density. The glider has two wings attached to either side of its body that provides the lift for the horizontal movement. At the end of every dive, the glider sits at the surface for 5 to 15 minutes to communicate via satellite with a base station on land to send back the data collected and receive commands for the following dive. Gliders found rapid acceptance in the oceanography community after their introduction because they allow studies with long temporal (several months) and good spatial (up to 25 km d^{-1}) coverage (Queste et al., 2012). Also, gliders are cheaper to operate than research ships and are preferable to Argo floats because they allow control over the horizontal direction. The deployment cost can be significantly reduced using small rigid-hulled inflatable boats rather than research vessels to deploy and recover the glider.

The use of gliders is very versatile due to the large number of sensors that can be used. Every glider is equipped with a conductivity-temperature-depth (CTD) sensor and can be equipped with other sensors to measure oxygen (e.g. Aanderaa optodes), chlorophyll *a* and coloured dissolved organic matter (CDOM) fluorescence, optical backscatter at different wavelengths (e.g. WET Labs Eco Puck) and turbulence (e.g. Ocean Microstructure Gliders - OMGs). In the last few years, new sensors have emerged to measure nitrate concentrations, pH, $p(CO_2)$, acoustic backscatter, optical transmission, passive acoustics and microstructure temperature. Different sensors have different temporal resolution that can vary from a couple of seconds to several minutes. Even if the temporal resolution is several minutes the use of gliders is still preferable to ships because the number of samples is larger, the cost is lower and the length of the deployment is longer.

1.4 Net Community Production

The plankton community regulates biological activity in the open ocean. This activity can be autotrophic (phytoplankton) fixing inorganic carbon to organic carbon compounds by photosynthesis; and heterotrophic (zooplankton) consuming the organic compounds and release inorganic carbon in the system through remineralisation. The importance of remineralisation of organic carbon decreases exponentially with depth following the “Martin curve” (Martin et al., 1987). The process is widely known as the “biological carbon pump”, in particular the organic carbon not remineralised is stored for a long time in deep waters.

The amount of carbon that is fixed by the phytoplankton is defined as gross primary production (GPP) and the amount of carbon remineralised is defined as community respiration (CR). The difference between GPP and CR is defined as net community production (NCP) and represents the rate at which the whole community exports carbon to the mesopelagic and deep waters (Lockwood et al., 2012). A system is defined as autotrophic when GPP is larger than CR (i.e. NCP is positive) and as heterotrophic when CR is larger than GPP (i.e. NCP is negative) (Ducklow and Doney, 2013).

In the past the oceanographic community has used different methods to estimate NCP (Alkire et al., 2014; Binetti et al., 2020; Neuer et al., 2007; Plant et al., 2016; Quay et al., 2012; Seguro et al., 2019; Sharples et al., 2006). Across most of the globe the real value of NCP is still uncertain and there is still a debate if they can be defined as autotrophic or heterotrophic and the variability can be even seen in the same period of the year (Duarte et al., 2013; Ducklow and Doney, 2013; Williams et al., 2013). The uncertainty is linked to many factors such interannual variability of biological activity and the limitation of the equipment used to measure the changes.

In general NCP is derived by vertical integration to a specific depth, that is commonly defined relative to the mixed layer depth (z_{mix}) or the bottom of the euphotic zone (Plant et al., 2016). Several methods can be used to estimate NCP such as bottle incubations or in situ biogeochemical budgets (Sharples et al., 2006; Quay, et al, 2012; Seguro et al., 2019). Bottle incubations involve measuring production and respiration in vitro under dark and light conditions. Biogeochemical budgets combine O_2 and C_T inventory changes with estimates of air-sea gas exchange, entrainment, advection and vertical mixing (Neuer et al., 2007; Alkire et al., 2014; Binetti et al., 2020) (an estimate of NCP in the Norwegian Sea is described in chapter 2).

An important component of NCP changes is the air-sea gas exchange. It is an important process regulating the effect of anthropogenic greenhouse emission because it regulates the absorption of the excess of atmospheric CO_2. The flux of a soluble nonreactive gas (such as O_2 and CO_2) across the air-sea interface (ϕ), can be defined as the product of gas transfer velocity (k_w) and the concentration difference between the top and the bottom of the liquid boundary layer:

$$\phi = k_w (c_w - c_0) \qquad (1.5)$$

where c_o is the gas concentration at the water surface and c_w is the gas concentration in the well-mixed bulk fluid below (the air). The flux is defined positive when it is from the ocean to the atmosphere and it is negative when it from the atmosphere to the ocean.

1.5 Study area

1.5.1 Norwegian Sea

The Norwegian Sea is part of the Nordic Seas (Greenland, Iceland and the Norwegian Sea) and comprises the Norwegian Basin and the Lofoten Basin. The North Atlantic warm and saline waters (S varying between 35.1 and 35.3 and θ > 6° C) identified as Norwegian Atlantic Current (NwAC) flows north, accessing the Norwegian Sea as an extension of the Gulf Stream from the Iceland-Faeroe-Shetland ridge (Figure 1.2) (Swift, 1986). Next to the Norwegian coast, the less saline (S < 35) northward-flowing Norwegian Coastal Current (NCC) originates primarily from the Baltic and freshwater run-off from Norway (Sætre, 1999). When the NwAC is north of 70° N, it bifurcates into two branches, one entering in the Barents Sea and the other continuing north to the Arctic Ocean. NwAC in the northward route is cooled due to heat loss to the atmosphere and mixing with the surrounding waters. Typically, NwAC and NCC are distinguished by S = 35 (Hopkins, 1991) and the Atlantic Waters occupy the top 500-600 m in the Norwegian Basin and 800-900 m in the Lofoten Basin. Cold and less saline waters identified as Norwegian Sea Deep Water (NSDW) occupy the water column from 1000 m to the bottom. In between NwAC and NSDW, there is an intermediate layer of fluctuating thickness called Arctic Intermediate Water.

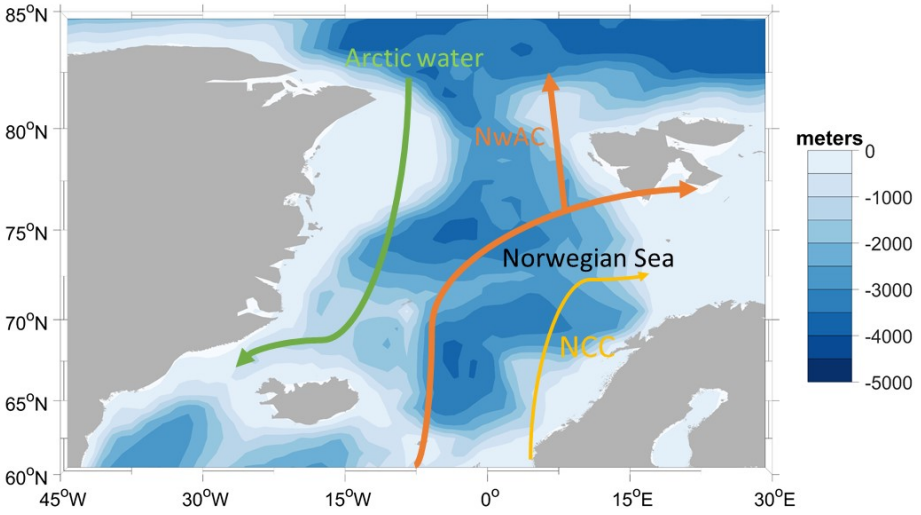

Figure 1.2: Norwegian Sea map and the main water masses. The three main currents (Skjelvan et al., 2008) are the Norwegian Coastal Current (NCC, yellow), the Norwegian Atlantic Current (NwAC, orange) and Arctic Water (green).

The Norwegian Sea biogeochemistry is largely controlled by the seasonality of the mixed layer depth (z_{mix}). During autumn and winter, z_{mix} can reach 300 m and the deepening is controlled by the cooling of surface waters. The deepening of z_{mix} introduces nutrients and low oxygen waters into the surface layer. During spring and summer, the warming of the surface waters controls the shallowing of z_{mix} to 20 m and primary production starts increasing the surface oxygen concentration and consuming nutrients (Nilsen and Falck, 2006). The organic matter produced during the summer is transformed into secondary products such as particulate debris and dissolved organic matter (DOM) that are remineralised at depth. The surface oxygen seasonality makes the Norwegian Sea an O_2 sink during autumn and winter and an O_2 source in spring and summer. Skjelvan et al. (2001) found that on an annual base the Norwegian Sea is an oxygen sink of (3.4±0.4) mol m^{-2} a^{-1} in transect 1 and (4.9±0.5) mol m^{-2} a^{-1} in transect 2 (Figure 1.3). The surface oxygen increases from south to north due to air-sea exchange and phytoplankton production (Skjelvan et al., 2001). Gislefoss et al. (1998) found the opposite seasonality for the central Norwegian Sea (66° N, 2° E) surface C_T that was 2140 µmol kg^{-1} in winter and decreased to 2040 µmol kg^{-1} during the summer. Instead, under z_{mix} C_T remained almost constant during all the year at (2170±10) µmol kg^{-1}. The surface layer is generally CO_2 undersaturated and has been identified as a CO_2 sink (Takahas*hi* et al., 2002;

Skjelvan et al., 2005). The northward cooling of NwAC increases the CO_2 sink and this water in the Greenland Sea is overturned in the deep water that flows south in the Atlantic (Figure 1.2) (Skjelvan et al., 2005). At lower latitudes, this CO_2 enriched water upwells reaching the surface.

1.5.2 North Sea

The North Sea is located in western Europe between Britain, France, Belgium, the Netherlands, Germany, Denmark and Norway, covering 575300 km^2 with an average depth of 74 m that increases from south to north (ICES, 1983) (Figure 1.3). The North Sea bathymetry creates two different biogeochemical regions. The southern North Sea has an average depth of 30 m and is fully mixed year-round (Otto et al., 1990). The northern North Sea is deeper and the depth gently increases northward to 250 m, leading to the formation of seasonal stratification (Otto et al., 1990; Sharples et al., 2006). The southern and northern North Sea are separated at 54° N by the shallow Dogger Bank (15 to 20 m deep) (Lenhart et al., 2004). Thomas et al. (2005) determined that North Sea inflows are dominated by Atlantic water (90 %) followed by English Channel input (8 %) and a combination of Baltic and riverine flow (2 %). The North Atlantic inflow enters at the north-west boundary and circulates southward next to the Scottish coast and turns north at Dogger Bank (Brown et al., 1999; Hill et al., 2008; Turrell et al., 1992). The strength and direction of this circulation is associated with the North Atlantic Oscillation Index (NAOI). When the NAOI is positive the circulation is anticlockwise; when it is negative the anticlockwise circulation is greatly reduced (Lenhart et al., 1995, 2004; Rodwell et al., 1999). The anticlockwise circulation has the consequence that very little inflow from the northern boundary reaches the southern North Sea (Thomas et al., 2005). This warm saline North Atlantic water (NAW) during the summer can be mixed with a combination of fresher coast and/or Skagerak Water (SW) forming the central North Sea water mass (CNSW) (Bozec et al., 2006; Kempe and Pegler, 1991; Omar et al., 2010; Salt et al., 2013). The second inflow in the northern North Sea is located in the north-east were less saline waters from the Baltic and the Norwegian Sea access the North Sea. In the southern North Sea waters enter through the Straits of Dover and eventually leaves the North Sea via the Norwegian Trench.

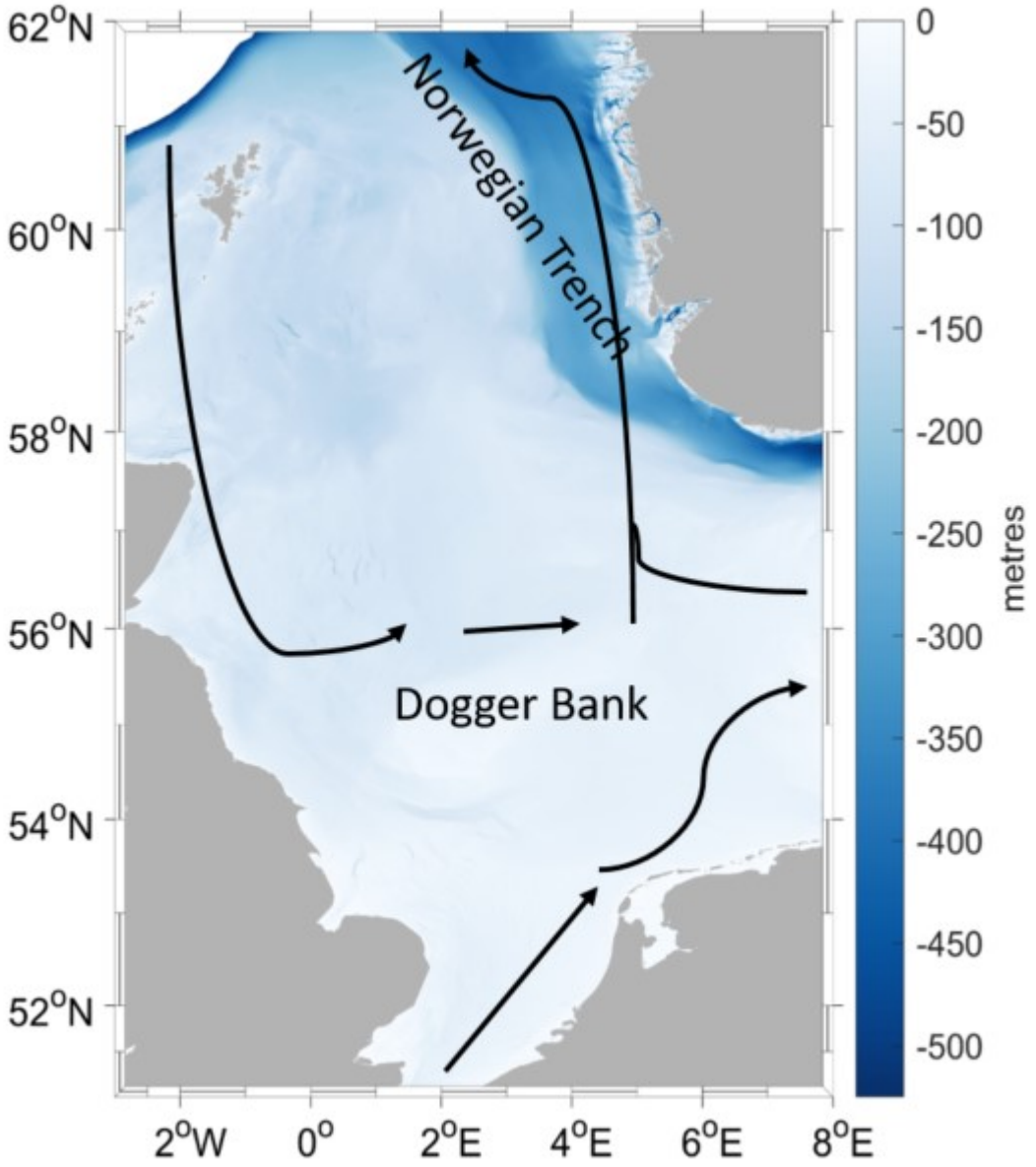

Figure 1.3: Bathymetry and general currents circulation of the North Sea.

Previous studies have studied the North Sea carbonate system started in the late 1980s (Hoppema, 1991; Kempe and Pegler, 1991; Pegler and Kempe, 1988). Recent studies allowed quantifying changes of surface $p(CO_2)$ in the entire North Sea (Omar et al., 2010; Thomas et al., 2005, 2007). Omar et al. (2010) found a decrease of $f(CO_2)$ from south to north of -12 µatm per degree latitude that disappeared during spring. Thomas et al., (2004) identified the North Sea as a continental shelf pump (Tsunogai et al., 1999) where 93 % of 1.4 mol m^{-2} a^{-1} CO_2 absorbed is transported to the North Atlantic Ocean. The high biological activity, driven by high inputs and efficient use of nutrients, mediates CO_2

drawdown from the atmosphere and subsequent export to the sub-surface layer via the biological pump. The outflow of this CO_2 enriched waters by remineralisation in the bottom layer of the phytoplankton material produced at the surface is the continental shelf pump (Figure 1.4) (Thomas et al., 2004). The continental shelf pump is defined as a mechanism transferring atmospheric CO_2 into the open ocean, which is thought to substantially contribute to the global ocean's uptake of atmospheric CO_2 (Tsunogai et al., 1999). The southern North Sea carbon system is driven by riverine input from Rhine, Scheldt, Thames and Elbe and during the year is a weak CO_2 sink, except for the summer when it is a CO_2 source (Schiettecatte et al., 2007).

Salt et al. (2013) found a correlation between pH and CO_2 with the North Atlantic Oscillation (NAO). Under positive NAO there is the highest rate of inflow from the North Atlantic Ocean and the Baltic which outflow strengthened the north-south biogeochemical divide. The limited mixing between the north and the south lead to a steeper gradient in pH and $p(CO_2)$ between the two regions in the productive period.

Blackford and Gilbert (2007) looked at ocean acidification in the North Sea having pH ranges <0.2 in areas with low biological activity to >1.0 in areas influenced by riverine signals. Their study show on average a decrease of the North Sea pH by 0.1 in the past 50 years and by 0.5 compared with pre-industrial levels.

Bozec et al. (2006) calculated the North Sea net community production (NCP) finding that during winter advection and air-sea gas exchange control the C_T content. Later, from February to July the inventory changes control the NCP changes with a net uptake from 0.5 to 1.4 mol m^{-2} $month^{-1}$. During August to December the inventory changes control NCP in the southern North Sea with a net release ranging from 0.5 to 5.5 mol m^{-2} $month^{-1}$.

All these studies mostly used sparse samples in time and space, focusing on changes happening in large spatial areas that in most cases included the entire North Sea.

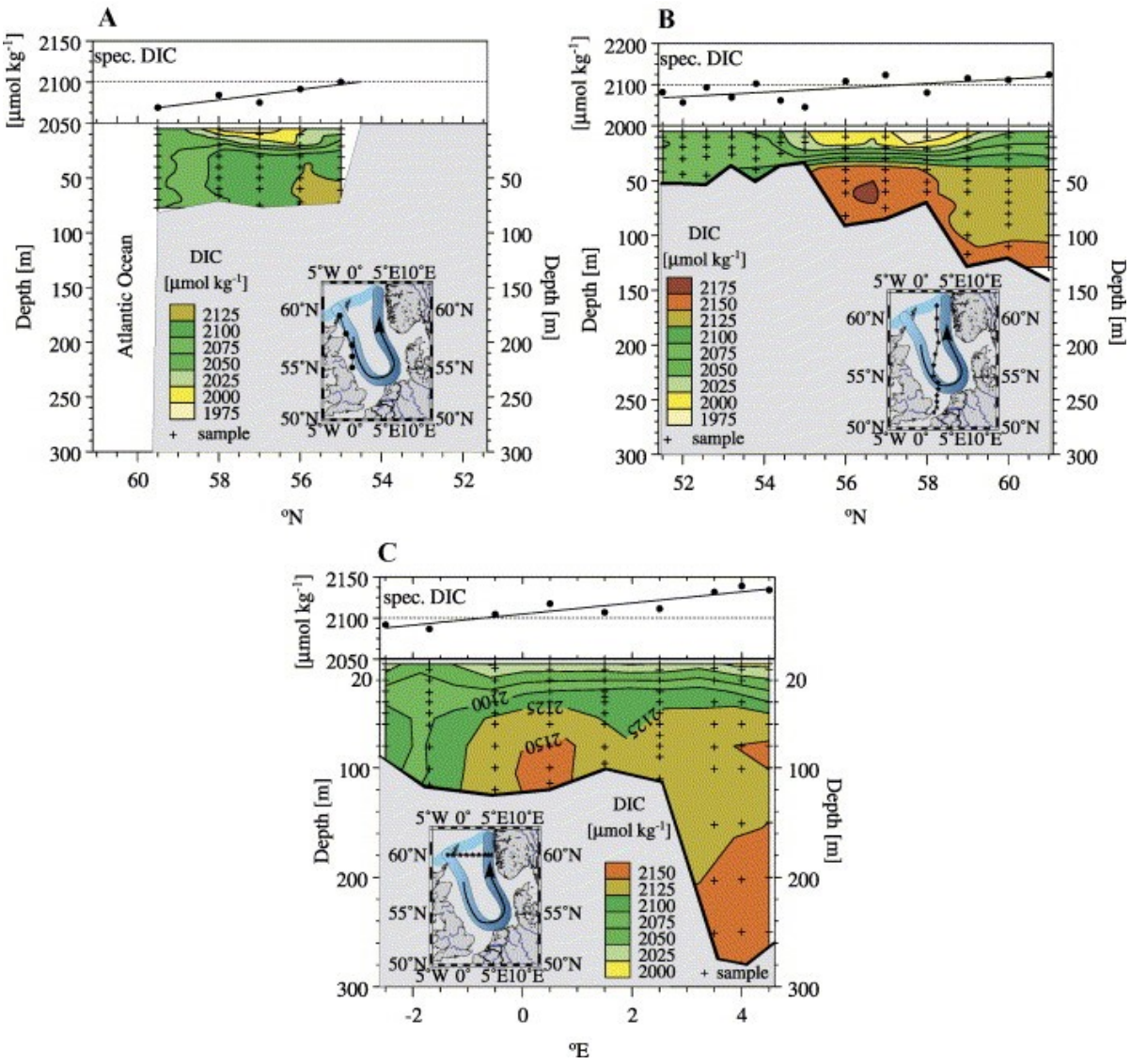

Figure 1.4: Vertical sections of total inorganic carbon concentrations in the North Sea along 0.5° W, 2.5° E and 60° N. Each top plot shows the specific dissolved inorganic carbon concentration (C_T) and the bottom plots the section where A) covers the Atlantic inflow approximately at 0.5° W, B) covers the eastern outflow at 2.5° E and C) covers at 60° N from west to east the North Sea entrance and exit**.** The blue scheme indicates the water circulation with the blue darkening referring to an increase of C_T, figure adapted from Bozec et al., (2005).

1.6 Thesis aims

The work presented herein is a collaboration between the University of East Anglia (UEA), the Centre for Environment Fisheries and Aquaculture Science (Cefas) and the National Oceanography Centre (NOC) in Southampton, United Kingdom.

The aim of the project was to assess at what stage is the development of new carbonate sensors to be used on gliders and in general on autonomous platforms. These sensors can help to constrain carbon uptake, storage rates and subsequently the ecosystem impacts (Bushinsky et al., 2019). Before the development for autonomous platforms the data was mainly gathered from discrete measurements on repeated hydrographic cruises (Gruber et al., 2019; Sabine et al., 2004; Talley et al., 2016) and seasonal time-series stations at a single location (Bates et al., 2014). These methods have several limitations, spatially because large areas of the globe are under sampled and temporally because there is little information on seasonal or interannual variability (Bushinsky et al., 2019).

Despite recent years efforts to improve the analytical methods, to develop new sensors and to coordinate international monitoring activities, the spatial and temporal resolution of oceanic carbon measurements is not as high as for temperature and salinity (Doney, Tilbrook, et al., 2009). The gaps in ocean biogeochemical observations can be filled by routine measurements using moorings, drifters, profiling floats and gliders. The sensors suitable for these platforms need to be automated, miniaturised, low cost, low power, precise and accurate, robust, work in large temperature ranges and withstand high pressures (> 1000 dbar) (Johnson et al., 2016). Miniaturised pH sensors are at the moment the most advanced and commercialised sensors for this purpose. The precision of these sensors need to be < 0.003 to capture the long term pH trends (climate goal) and < 0.02 to identify relative spatial patterns and short-term variation (weather goal) (Newton et al., 2014). These accuracies can be derived using a benchtop spectrophotometer that can reach an accuracy of ±0.0004 and an accuracy of ±0.002 (Table 1.1). However, in many studies pH is derived from A_T and C_T discrete samples leading to an uncertainty of 0.0062 (Table 1.2) that is not sufficient for the climate goal. The use of discrete samples lack of a good spatial and temporal resolution. The use of autonomous sensors is crucial to have a good spatial and temporal that allows to quantify and assess the consequences of OA. Other sensors that can be used to monitor the ocean carbonate system are CO_2 optodes, the principles of which are described in section 2.3.4.

To capture the spatiotemporal variability new observational strategies are required and the use of gliders fulfil the need of cheap, high resolution (< 10 s) and precise observations. New ocean carbonate sensors that can rapidly respond to inorganic carbon changes and also withstand high pressure (1000 m) show great value for ocean monitoring. New sensors that can fulfil this need are tested and deployed in this thesis. In particular, a CO_2 optode developed by Aanderaa, a spectrophotometric pH sensor developed by the Ocean Technology and Engineering Group (OTE) of NOC and two

glass electrode pH sensors developed by (Fluidion, Créteil, France) and (AMT Analysenmesstechnik GmbH, Rostock, Germany) were tested. Before the deployment the three pH sensors, 2 potentiometric and one spectrophotometric, were tested in the laboratory to assess the performance and identify best practices to use these sensors.

1.7 Thesis outline

The chapters are ordered following the timeline of the project, having first the analysis of data received by the University of Bergen for the Seaglider trial of a CO_2 optode (chapter 2). Followed by chapter 3 that explains all the work done on the implementation and tests of a pH sensor for ocean studies. In chapter 4, these sensors are deployed on a Seaglider in the North Sea.

In Chapter 2, I present the first glider deployment of a CO_2 sensor that needed to be corrected for drift, lag and in situ calibration using discrete samples. The corrected data coupled with O_2 were used to calculate 4 months of net community production and O_2 and CO_2 air-sea flux.

In Chapter 3, I assess the performance of two glass electrodesAMT and Fluidion, and a lab-on-a-chip spectrophotometric pH sensor developed by the Ocean Technology and Engineering Group (OTE) of NOC. The quality of the pH measurements were evaluated by looking at the response time, storage solution and the effect of changes in temperature and salinity. Based on these experiments a methodology was developed to calibrate in situ the glass electrodes using the spectrophotometric sensor as reference.

In Chapter 4, I present the first deployment of a pH glass electrode and spectrophotometric pH sensor on a glider, along with the description of their accuracy and corrections. The glider was deployed for 10 days in the North Sea and the data was used to calculate the O_2 and CO_2 air-sea flux, quantify the respiration rate in the bottom waters and look at the spatial and temporal changes.

In Chapter 5 I summarise my work and suggest avenues for future developments.

Chapter 2

Norwegian Sea net community production estimated from O_2 and prototype CO_2 optode measurements on a Seaglider

Publication

This chapter has been previously published in *Ocean Science Discussions* under the title 'Norwegian Sea net community production estimated from O_2 and prototype CO_2 optode measurements on a Seaglider' with co-authors Ingunn Skjelvan, Dariia Atamanchuk, Anders Tengberg, Matthew P. Humphreys, Socratis Loucaides, Liam Fernand, Jan Kaiser. All scientific work and writing was undertaken by Luca Possenti, with improvements made using comments from co-authors. This chapter is as published.

Possenti, L., Skjelvan, I., Atamanchuk, D., Tengberg, A., Humphreys, M. P., Loucaides, S., Fernand, L., and Kaiser, J.: Norwegian Sea net community production estimated from O_2 and prototype CO_2 optode measurements on a Seaglider, Ocean Sci. Discuss., https://doi.org/10.5194/os-2020-72, in review, 2020.

2.1 Summary

We report on a pilot study using a CO_2 optode deployed on a glider in the Norwegian Sea for 8 months (March to October 2014). The optode measurements required drift- and lag-correction, and in situ calibration using discrete water samples collected in the vicinity. We found the optode signal correlated better with the concentration of CO_2, $c(CO_2)$, than with its partial pressure, $p(CO_2)$. Using the calibrated $c(CO_2)$ and a regional parameterisation of total alkalinity (A_T) as a function of temperature and salinity, we calculated total dissolved inorganic carbon concentrations, C_T, which had a standard deviation of 11 µmol kg^{-1} compared with direct C_T measurements. The glider was also equipped with an oxygen (O_2) optode. The O_2 optode was drift-corrected and calibrated using a $c(O_2)$ climatology for deep samples (R^2 = 0.89; RMSE = 0.009 µmol kg^{-1}). The calibrated data enabled the calculation of C_T - and oxygen-based net community production, $N(C_T)$ and $N(O_2)$. To derive N, C_T and O_2 inventory changes over time were

combined with estimates of air-sea gas exchange, entrainment of deeper waters and diapycnal mixing. Glider-based observations captured two periods of increased Chl *a* inventory in late spring (May) and a second one in summer (June). For the May period, we found $N(C_T)$ = (21±5) mmol m^{-2} d^{-1}, $N(O_2)$ = (94±16) mmol m^{-2} d^{-1} and an (uncalibrated) Chl *a* peak concentration of c_{raw}(Chl *a*) = 3 mg m^{-3}. During the June period, c_{raw}(Chl *a*) increased to a summer maximum of 4 mg m^{-3}, which drove $N(C_T)$ to (85±5) mmol m^{-2} d^{-1} and $N(O_2)$ to (126±25) mmol m^{-2} d^{-1}. The high-resolution dataset allowed the quantification of the changes in *N* before, during and after the periods of increased Chl *a* inventory. After the May period, the remineralisation of the material produced during the period of increased Chl *a* inventory decreased $N(C_T)$ to (-3±5) mmol m^{-2} d^{-1} and $N(O_2)$ to (0±2) mmol m^{-2} d^{-1}. The survey area was a source of O_2 and a sink of CO_2 for most of the summer. The deployment captured two different surface waters: the Norwegian Atlantic Current (NwAC) and the Norwegian Coastal Current (NCC). The NCC was characterised by lower $c(O_2)$ and C_T than the NwAC, as well as lower $N(O_2)$, $N(C_T)$ and c_{raw}(Chl *a*). Our results show the potential of glider data to simultaneously capture time and depth-resolved variability in C_T and O_2.

2.2 Introduction

Climate models project an increase in the atmospheric CO_2 mole fraction driven by anthropogenic emissions from a preindustrial value of 280 µmol mol^{-1} (Neftel et al., 1982) to 538-936 µmol mol^{-1} by 2100 (Pachauri and Reisinger, 2007). The ocean is known to be a major CO_2 sink (Sabine et al., 2004; Le Quéré et al., 2009; Sutton et al., 2014), in fact has taken up approximately 25 % of this anthropogenic CO_2 with a rate of (2.5±0.6) Gt a^{-1} (in C equivalents) (Friedlingstein et al., 2019). This uptake alters the carbonate system of seawater and is causing a decrease in seawater pH, a process known as ocean acidification (OA) (Gattuso and Hansson, 2011). The processes affecting the marine carbonate system include air-sea gas exchange, photosynthesis and respiration, transport and vertical and horizontal mixing, and $CaCO_3$ formation and dissolution. For that reason, it is important to develop precise, accurate and cost-effective tools to observe CO_2 variability and related processes in the ocean. Provided that suitable sensors are available, autonomous ocean glider measurements may help resolve these processes.

To quantify the marine carbonate system, four variables are commonly measured: total dissolved inorganic carbon concentration (C_T), pH, total alkalinity (A_T) and the fugacity of CO_2 ($f(CO_2)$). At thermodynamic equilibrium, knowledge of two of the four variables is

sufficient to calculate the other two. Marine carbonate system variables are primarily measured on research ships, commercial ships of opportunity, moorings, buoys and floats (Hardman-Mountford et al., 2008; Monteiro et al., 2009; Takahashi et al., 2009; Olsen et al., 2016; Bushinsky et al., 2019). Moorings equipped with submersible sensors often provide limited vertical and horizontal, but good long-term temporal resolution (Hemsley, 2015). In contrast, ship-based surveys have higher vertical and spatial resolution than moorings but limited repetition frequency because of the expense of ship operations. Ocean gliders have the potential to replace some ship surveys because they are much cheaper to operate and will increase our coastal and regional observational capacity. However, the slow glider speed of 1-2 km h^{-1} only allows a smaller spatial coverage than ship surveys and the sensors require careful calibration to match the quality of data provided by ship-based sampling.

Carbonate system sensors suitable for autonomous deployments have been developed in the past decades, in particular pH sensors (Martz et al., 2010; Rérolle et al., 2013; Seidel et al., 2008) and $p(CO_2)$ sensors (Atamanchuk, 2013; Bittig et al., 2012; Degrandpre, 1993; Goyet et al., 1992; Körtzinger et al., 1996). One of these sensors is the CO_2 optode (Atamanchuk et al., 2014) which has been successfully deployed to monitor an artificial CO_2 leak on the Scottish west coast (Atamanchuk et al., 2015b), on a cabled underwater observatory (Atamanchuk, et al., 2015a), to measure lake metabolism (Peeters et al., 2016), for fish transportation (Thomas et al., 2017) and on a moored profiler (Chu et al., 2020).

Oxygen and C_T can be used to calculate net community production (N), which is defined as the difference between gross primary production (G) and community respiration (R). At steady-state, N is equal to the rate of organic carbon export and transfer from the surface into the mesopelagic and deep waters (Lockwood et al., 2012). N is derived by vertical integration to a specific depth, that is commonly defined relative to the mixed layer depth (z_{mix}) or the bottom of the euphotic zone (Plant et al., 2016). A system is defined as autotrophic when G is larger than R (i.e. N is positive) and as heterotrophic when R is larger than G (i.e. N is negative) (Ducklow and Doney, 2013). N can be quantified using bottle incubations, isotope methods (^{14}C, ^{15}N, $^{16}O/^{17}O/^{18}O$) (Sharples et al., 2006; Quay, et al., 2012; Seguro et al., 2019) or in situ biogeochemical budgets. Bottle incubations involve measuring oxygen concentration driven by production and respiration in vitro under dark and light conditions. Biogeochemical budgets combine O_2 and C_T inventory changes with estimates of air-sea gas exchange, entrainment, advection and vertical mixing (Neuer et al., 2007; Alkire et al., 2014; Binetti et al., 2020).

The Norwegian Sea is a complex environment due to the interaction between the Atlantic Water (NwAC) entering from the south-west, Arctic Water coming from north and the

Norwegian Coastal Current (NCC) flowing along the Norwegian coast (Nilsen and Falck, 2006). In particular, Atlantic Water enters the Norwegian Sea through the Faroe-Shetland Channel and Iceland-Faroe Ridge (Hansen and Østerhus, 2000) with S between 35.1 and 35.3 and temperatures warmer than 6 ˚C (Swift, 1986). Furthermore, the NCC water mass differs from the NwAC with a surface S < 35 (Saetre and Ljoen, 1972) and a seasonal θ signal (Nilsen and Falck, 2006).

Biological production in the Norwegian Sea varies during the year and can be divided into 5 periods (Rey, 2001): (1) winter with the smallest productivity and phytoplankton biomass; (2) a pre-bloom period; (3) the spring bloom when productivity increases and phytoplankton biomass reaches the annual maximum; (4) a post-bloom period with productivity mostly based on regenerated nutrients; (5) autumn with smaller blooms than in summer. Previous estimates of $N(C_T)$ were based on discrete C_T samples (Falck and Anderson, 2005) or were calculated from oxygen-based measurements and converted to C equivalents assuming Redfield stoichiometry of production/respiration (Falck and Gade, 1999; Kivimäe, 2007; Skjelvan et al., 2001). Glider measurements have been used to estimate N in other ocean regions (Nicholson et al., 2008; Alkire et al., 2014; Haskell et al., 2019; Binetti et al., 2020); however, as far as we know, this is the first study of net community production in the Norwegian Sea using a high-resolution glider dataset (>10^6 data points; 40 s time resolution) and the first anywhere estimating N from a glider-mounted sensor directly measuring the marine carbonate system.

2.3 Material and methods

2.3.1 Glider sampling

Kongsberg Seaglider 564 was deployed in the Norwegian Sea on the 16 March 2014 at 63.00° N, 3.86° E and recovered on the 30 October 2014 at 62.99° N, 3.89° E. The glider was equipped with a prototype Aanderaa 4797 CO_2 optode, an Aanderaa 4330F oxygen optode (Tengberg et al., 2006), a Sea-Bird CTD (GPCTD) and a combined backscatter/chlorophyll *a* fluorescence sensor (Wetlabs Eco Puck BB2FLVMT). The mean time needed by the sensors to reach a stable value for an in situ measurement (t) varied with depth (Table 2.1). On average in the top 100 m the CTD performed an in situ measurement every 24 s, the O_2 optode every 49 s, the CO_2 optode every 106 s and the fluorescence sensor every 62 s. The time to perform an in situ measurement increased in depths between 100 to 500 m to 31 s for the CTD, 153 s for the O_2 optode and 233 s for the CO_2 optode. This measurement time reached its maximum at depths between 500 to 1000 m where it was 42 s for the CTD, 378 s for the O_2 optode and 381 s for the

CO_2 optode. These sampling intervals where enough to resolve the vertical changes because the glider vertical speed was 0.05±0.07 m s^{-1}. For example, in the surface 100 m the CO_2 optode sampled every 5 m and in the last 500 m every 19 m.

Table 2.1. Average time needed by the Sea-Bird CTD (GPCTD), Aanderaa 4330F oxygen optode, Aanderaa 4797 CO_2 optode and a combined backscatter/chlorophyll *a* fluorescence sensor (Wetlabs Eco Puck BB2FLVMT) to reach stable readings during in-situ measurement in the top 100 m, from 100 to 500 and from 500 to 1000 m.

Depth / m	*t*(CTD) / s	*t*(O_2) / s	*t*(CO_2) / s	*t*(Chl *a*) / s
0 – 100 m	24	49	106	62
100 – 500 m	31	153	233	-
500 – 1000 m	42	378	381	-

The deployment followed the Svinøy transect, from the open sea towards the Norwegian coast. The glider covered a 536 km long transect 8 times (4 times in each direction) for a total of 703 dives (Figure 2.1).

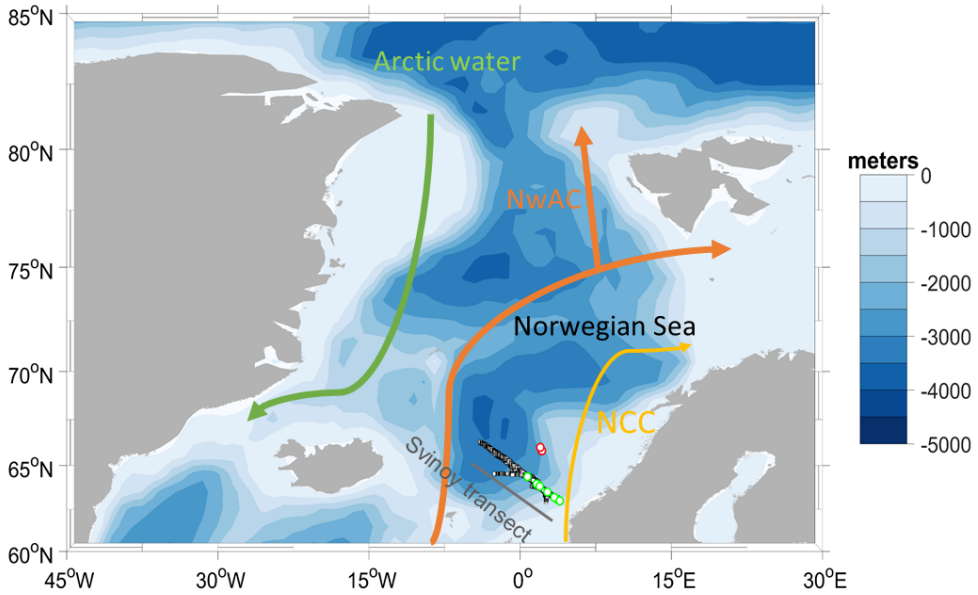

Figure 2.1: Map of the glider deployment and the main water masses. The black dots are the glider dives, the green and the red dots are the water samples collected along the glider section and at OWSM, respectively. The three main currents (Skjelvan et al., 2008) are the Norwegian Coastal Current (NCC, yellow), the Norwegian Atlantic Current (NwAC, orange) and Arctic Water (green).

2.3.2 Discrete sampling

During the glider deployment, 70 discrete water samples from various depths (5, 10, 20, 30, 50, 100, 300, 500 and 1000 m) were collected on 4 different cruises on the R/V Haakon Mosby along the southern half of the glider transect on the 18 March, the 5 May, 6 and 14 June, and the 30 of October 2014. Samples for C_T and A_T were collected from 10 L Niskin bottles following the standard operational procedure (SOP) 1 of Dickson et al. (2007). The C_T and A_T samples were preserved with a saturated $HgCl_2$ solution (final $HgCl_2$ concentration: 15 mg dm^{-3}). Nutrient samples from the same Niskin bottles were preserved with chloroform. C_T and A_T were analysed on-shore according to SOP 2 and 3b (Dickson et al., 2007) using a VINDTA 3D (Marianda) with a CM5011 coulometer (UIC instruments) and a VINDTA 3S (Marianda), respectively. Nutrients were analysed on-shore using an Alpkem Auto Analyzer (Alpkem Analytical, OI, Inc.). In addition, 43 water samples were collected at Ocean Weather Station M (OWSM) on 5 different cruises on the 22 March on R/V Haakon Mosby, the 9 May on R/V G.O. Sars, the 14 June on R/V Haakon Mosby, the 2 August and the 13 November on R/V Johan Hjort from 10, 30, 50, 100, 200, 500, 800 and 1000 m depth. The OWSM samples were preserved and analysed for A_T and C_T similar to the Svinøy samples. No phosphate and silicate samples were collected from OSWM. Temperature (θ) and salinity (S) profiles were measured at each station using a Sea-Bird 911 plus CTD. pH and $f(CO_2)$ were calculated using the MATLAB toolbox CO2SYS (Van Heuven et al., 2011), with the following constants: K_1 and K_2 carbonic acid dissociation constants of Lueker et al. (2000), $K(HSO_4^-/SO_4^{2-})$ hydrogensulfate dissociation constant of Dickson (1990) and borate to chlorinity ratio of Lee et al. (2010). In the OWSM calculations, we used nutrients collected from the Svinøy section at a time as close as possible to the OWSM sampling. In the case of the glider, using the discrete samples collected during the glider deployment at the Svinoy section and OWSM we derived a parameterisation to derive phosphate and silicate concentrations as a function of the discrete sample depth and time. This parameterisation had an uncertainty of 1.3 and 0.13 µmol kg^{-1}, for silicate and phosphate concentrations, respectively.

2.3.3 Oxygen optode calibration

The last oxygen optode calibration before the deployment was performed in 2012 as a two-point calibration at 9.91 °C in air-saturated water and at 20.37 °C in anoxic Na_2SO_3 solution. Oxygen optodes are known to be affected by drift (Bittig et al., 2015), which is worse for the fast-response foils used in the 4330F optode for glider deployments. It has been suggested to calibrate and drift correct the optode using discrete samples or in-air

measurements (Nicholson and Feen, 2017). Unfortunately, no discrete samples were collected at the glider deployment or recovery.

To overcome this problem, we used archived data to correct for oxygen optode drift. These archived concentration data (designated $c_C(O_2)$) were collected at OWSM between 2001 and 2007 (downloaded from ICES database) and from the deployment region (selected between the maximum and minimum latitude and longitude of the deployment) between 2000 and 2018 (extracted from GLODAPv2; Olsen et al., 2016). To apply the correction, we used the oxygen samples corresponding to a potential density σ_0 > 1028 kg m^{-3} (corresponding to depths between 427 and 1000 m), because waters of these potential densities were always well below the mixed layer and therefore subject to limited seasonal and interannual variability. The salinity S of these samples varied from 34.88 to 34.96, with a mean of 34.90±0.01; θ varied from 0.45 to –0.76 °C, with a mean of (–0.15±0.36) °C.

Figure 2.2 shows that the glider oxygen concentration ($c_G(O_2)$) where σ_0 > 1028 kg m^{-3} was characterised by two different water masses separated at a latitude of about 64° N. We used just the samples collected north of 64° N to derive the glider optode correction because this reflects the largest area covered by the glider. It was not possible to use the southern region and was not included in the calibration because it contained samples from only 5 days. For each day of the year with archived samples, we calculated the median concentration of the glider and the archived samples. Figure 2.3 shows a plot of the ratio between $c_C(O_2)/c_G(O_2)$ against the day of the year and a linear fit, which is used to calibrate $c_G(O_2)$ and correct for drift.

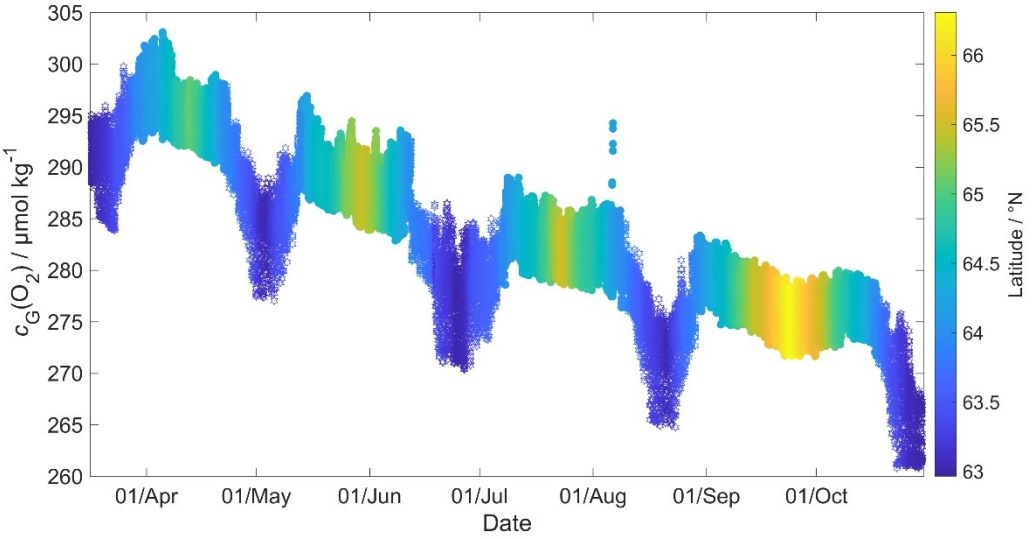

Figure 2.2: Glider oxygen concentration over time (day/month), $c_G(O_2)$, under σ_0 = (1028±0.02) kg m^{-3} coloured by latitude with the filled dots for latitude > 64 and the empty stars for latitude < 64.

No lag correction was applied because the O_2 optode had a fast response foil and showed no detectable lag (<10 s), based on a comparison between descent and ascent profiles.

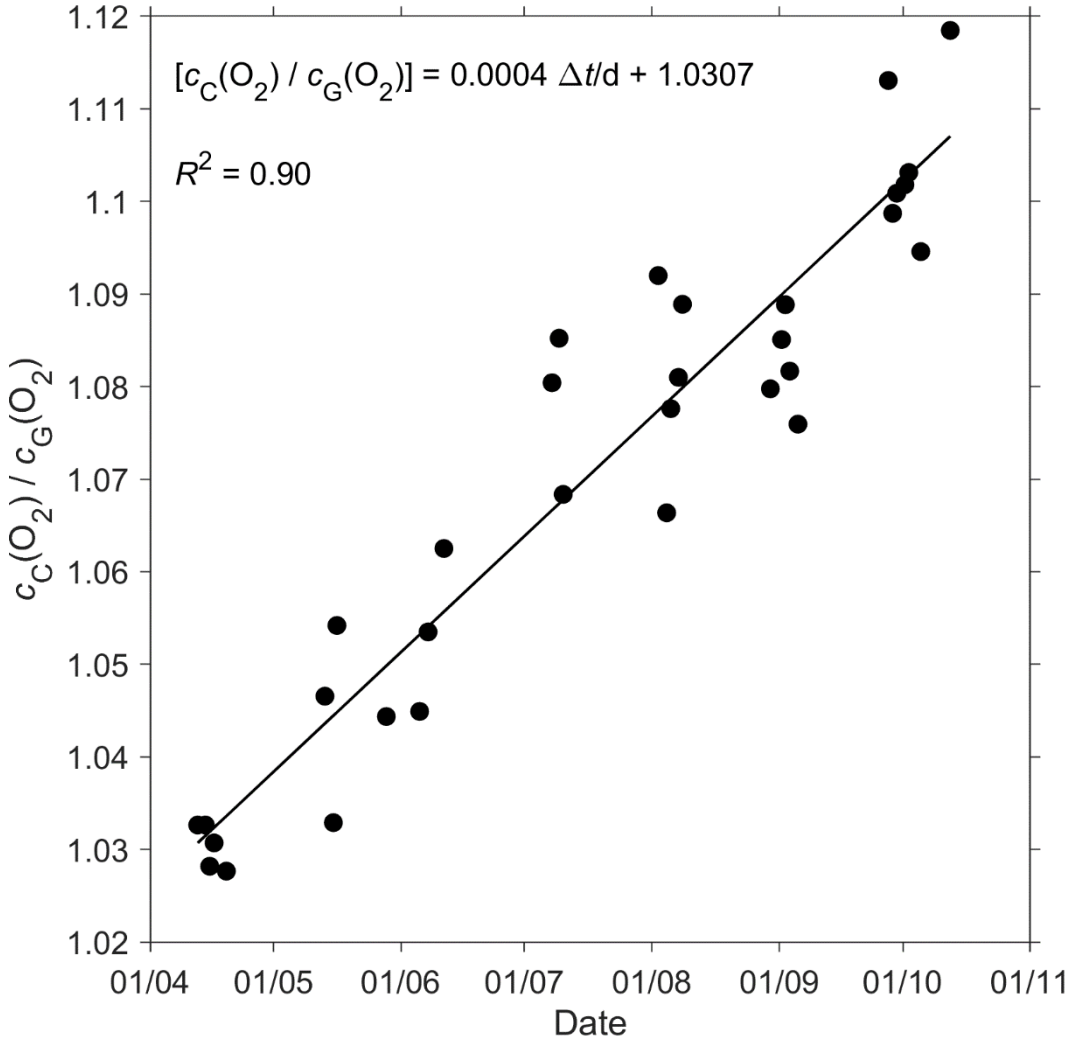

Figure 2.3: The linear fit of the ratio between the daily median of the discrete oxygen samples ($c_C(O_2)$) and glider oxygen data ($c_G(O_2)$) for σ_0 > 1028 kg m^{-3} was used to derive the $c_G(O_2)$ drift and initial offset at deployment. We chose the median to avoid the influence of any outliers and differences in $c_C(O_2)$ given by sampling error. The time interval Δt was calculated with respect to the deployment day of the 16th of March.

2.3.4 CO_2 optode measurement principle

The CO_2 optode consists of an optical and a temperature sensor incorporated into a pressure housing. The optical sensor has a sensing foil comprising two fluorescence indicators (luminophores), of which one is sensitive to pH changes and the other is not and thus used as a reference. The excitation and emission spectra of the two fluorescence indicators overlap, but the reference indicator has a longer fluorescence lifetime than the pH indicator. These two fluorescence lifetimes are combined using an approach known as Dual Lifetime Referencing (DLR) (Klimant et al., 2001; von

Bültzingslöwen et al., 2002). From the phase shift (φ), the partial pressure of CO_2, $p(CO_2)$, is parameterised as an eight-degree polynomial (Atamanchuk et al., 2014):

$$\log [p(CO_2)/\mu atm] = C_0 + C_1 \varphi + \ldots + C_8 \varphi^8 \qquad (2.1)$$

where C_0 to C_8 are temperature-dependent coefficients.

The partial pressure of CO_2 is linked to the CO_2 concentration, $c(CO_2)$, and the fugacity of CO2, $f(CO_2)$, via the following relationship:

$$c(CO_2) = p(CO_2) / [1 - p(H_2O) / p] \, F(CO_2) = K_0(CO_2) \, f(CO_2) \qquad (2.2)$$

where $F(CO_2)$ is the solubility function (Weiss and Price, 1980), $p(H_2O)$ is the water vapour pressure, p is the total gas tension (assumed to be near 1 atm) and $K_0(CO_2)$ is the solubility coefficient. F and K_0 vary according to temperature and salinity.

2.3.5 CO_2 optode lag and drift correction

The CO_2 optode was fully functional between dives 31 (the 21 March 2014) and 400 (the 24 July 2014). After dive 400, the CO_2 optode stopped sampling in the top 150 m. Figure 2.4 shows the outcome of each calibration step described in this section (steps 1 and 2) and section 2.3.6 (step 3): 0) uncalibrated optode output (blue dots), 1) drift correction (red dots), 2) lag correction (green dots) and 3) calibration using discrete water samples (black dots).

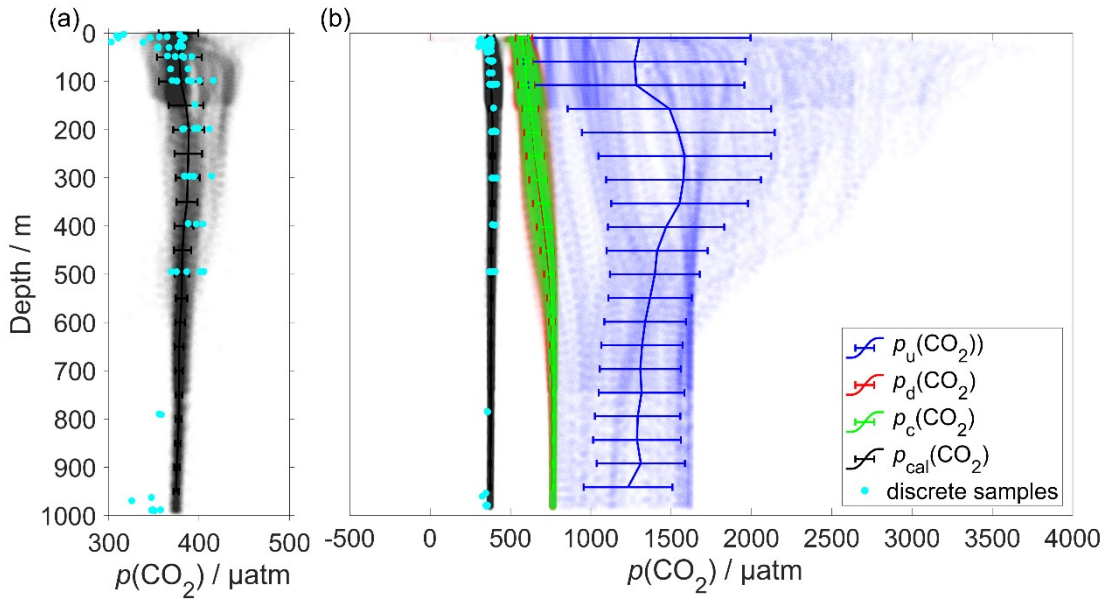

Figure 2.4: vertical profiles of a) in black the calibrated $p(CO_2)$ ($p_{cal}(CO_2)$) and in azure the discrete samples numerically derived from A_T and C_T b) $p(CO_2)$ versus depth where the vertical continuous lines are the moving mean every 50 m and the error bars represent the standard deviation. Blue colour shows $p_u(CO_2)$ without any correction; red shows $p_d(CO_2)$ corrected for drift, green represents $p_c(CO_2)$ corrected for drift and lag; black shows $p_{cal}(CO_2)$ calibrated against water samples (azure dots) collected during the deployment (section 2.6). $p_{cal}(CO_2)$ had a mean standard deviation of 22 µatm and a mean bias of 2 µatm compared with all the discrete samples.

To correct for the drift occurring during the glider mission, we selected the CO_2 optode measurements in water with $\sigma_0 > 1028$ kg m^{-3} (just as for O_2; section 2.3). We calculated the median of the raw optode phase shift data ("CalPhase" φ_{cal}) for each glider dive. Then, we calculated a drift coefficient (m_i) as the ratio between the median φ_{cal} for a given dive divided by the median φ_{cal} of dive 31. Drift-corrected $\varphi_{cal,d}$ values were calculated by dividing the raw φ_{cal} by the specific m_i for each dive.

The CO_2 optode was also affected by lag (Atamanchuk et al., 2014) caused by the slow response of the optode to ambient $c(CO_2)$ changes in time and depth. The lag created a discrepancy between the depth profiles obtained during glider ascents and descents. To correct for this lag we applied the method of Miloshevich et al. (2004), which was previously used by Fiedler et al. (2013) and Atamanchuk et al. (2015b) to correct the lag of the Contros HydroC CO_2 sensor (Fiedler et al., 2013; Saderne et al., 2013). This CO_2 sensor has a different measurement principle (infrared absorption) than the CO_2 optode, but both rely on the diffusion of CO_2 through a gas-permeable membrane.

To apply the lag correction, the sampling interval (Δt) needs to be sufficiently small compared to the sensor response time (τ) and the ambient variability (Miloshevich, 2004). Before the lag correction, $\varphi_{cal,d}$ was rLOWESS-smoothed to remove any outliers and "kinks" in the profile. The smoothing function applies a local regression every 9 points using a weighted robust linear least-squares fit. Subsequently, τ was determined such that the following lag-correction equation (Miloshevich, 2004) minimised the $\varphi_{cal,d}$ difference between each glider ascent and the following descent:

$$p_c(CO_2, t_1) = \frac{p_d(CO_2,t_1) - p_d(CO_2,t_0)\ e^{-\Delta t/\tau}}{1 - e^{-\Delta t/\tau}} \qquad (2.3)$$

where $p_d(CO_2,t_0)$ is the drift-corrected value measured by the optode at time t_0, $p_m(CO_2,t_1)$ is the measured value at time t_1, Δt is the time between t_0 and t_1, τ is the response time, and $p_c(CO_2,t_1)$ is the lag-corrected value at t_1. We calculated a τ value for each glider dive and used the median of τ (1384 s, 25th quartile: 1101 s; 75th quartile: 1799 s) (Figure 2.5), which was larger than Δt (258 s) and therefore met the requirement to apply the Miloshevich (2004) method. This lag correction decreased the average difference between the glider ascent and descent from (71±30) µatm to (21±26) µatm.

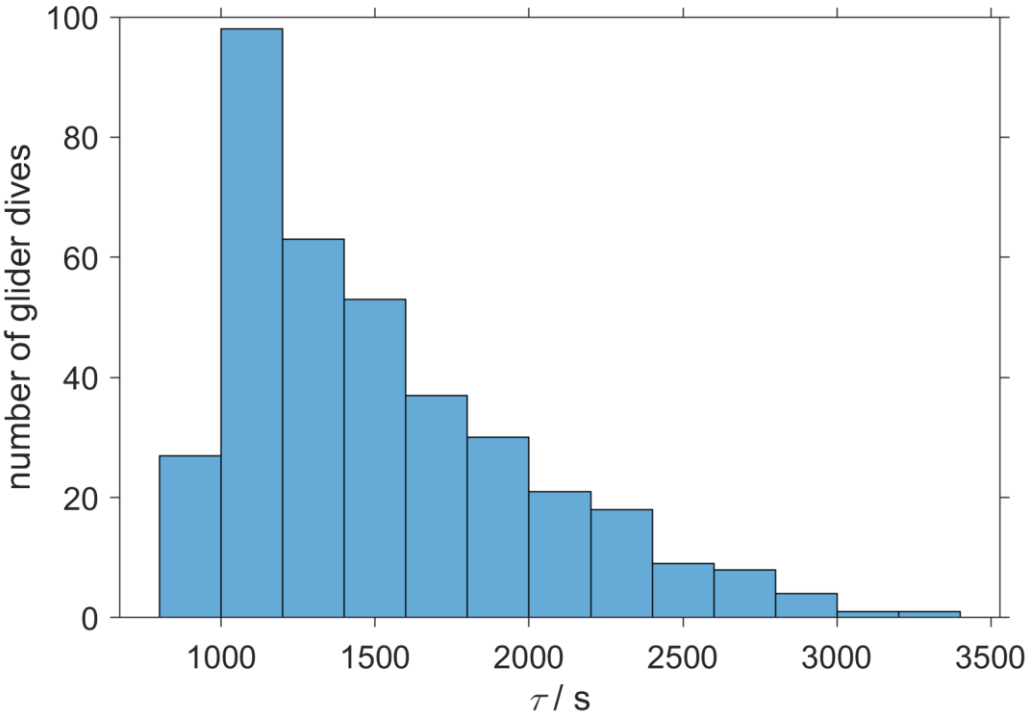

Figure 2.5: The histogram shows the distribution of the τ calculated from glider dive 31 to 400 to correct the CO_2 optode drift using the algorithm of Miloshevich (2004).

2.3.6 CO_2 optode calibration

The CO_2 optode output was calibrated using the discrete samples collected throughout the mission. Using the discrete sample time and potential density σ_0, we selected the closest CO_2 optode output. A linear regression between optode output and $c(CO_2)$ from the discrete samples ($c_{WS}(CO_2)$ was used to calibrate the optode output $p_c(CO_2)$ in terms of $c(CO_2)$. $c(CO_2)$ had a better correlation than $p(CO_2)$ (R^2 = 0.77 vs. R^2 = 0.02). Plotting the regression residuals ($c_r(CO_2)$, calculated as the difference between $c_{WS}(CO_2)$ and the value predicted by the regression) revealed a quadratic relation between the regression residuals and water temperature (θ). We have therefore included θ and θ^2 in the optode calibration (Figure 2.6a). This second calibration increased the correlation coefficient R^2 from 0.77 to 0.90 and decreased the standard deviation of the regression residuals from 1.3 to 0.8 µmol kg^{-1}. Even with the explicit inclusion of temperature in the calibration, the CO_2 optode response remained more closely related to $c(CO_2)$ than $p(CO_2)$ (Figure 2.6b).

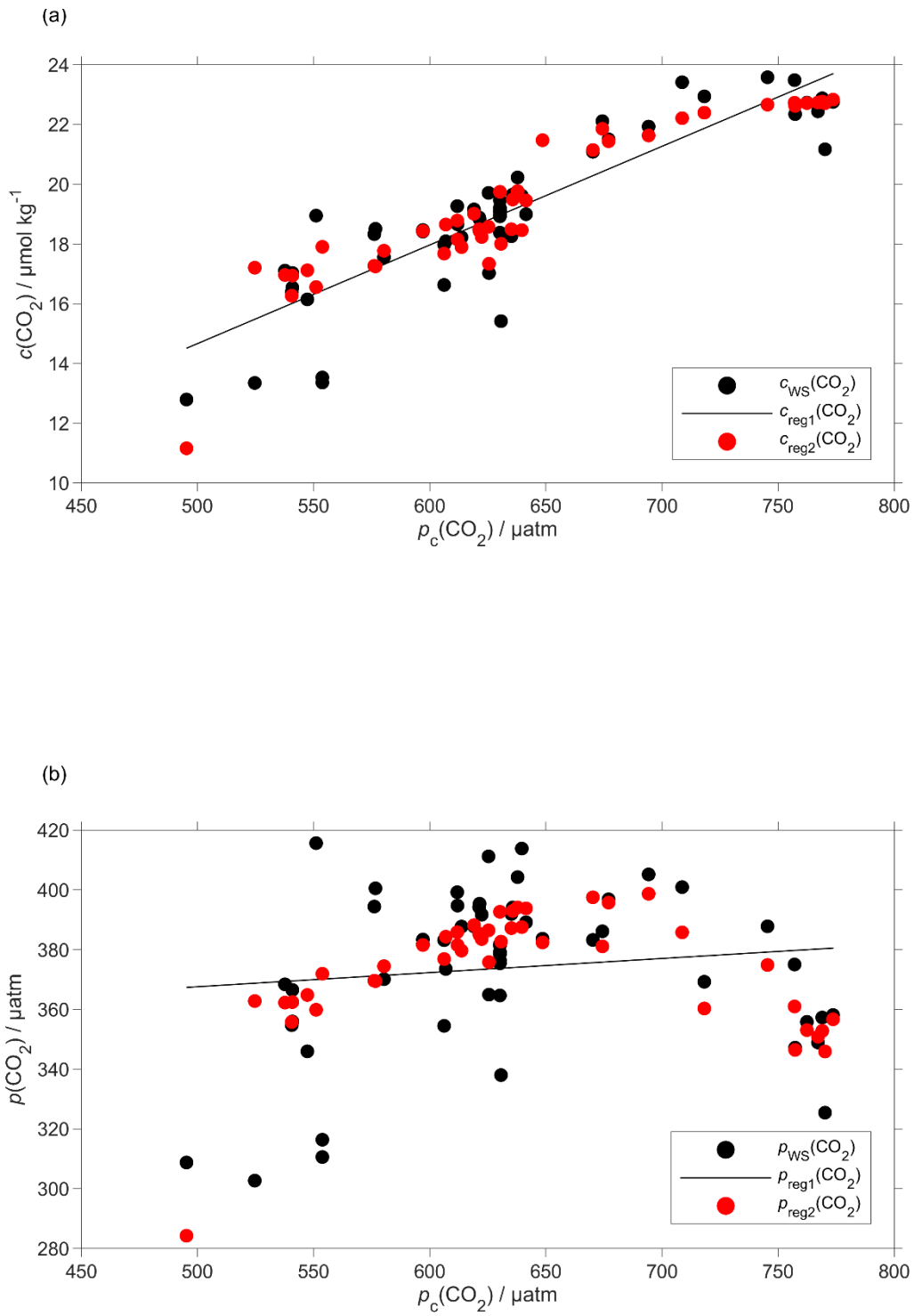

Figure 2.6: Regression (black lines, reg1) of the CO_2 optode output $p_c(CO_2)$ against a) co-located concentration $c_{WS}(CO_2)$ that has an uncertainty of 0.28 µmol kg^{-1} b) and partial pressure $p_{WS}(CO_2)$ of CO_2 in discrete water samples (black dots). Also shown are the values predicted by including θ and θ^2 in the regression used for optode calibration (red dots, reg2). The regression equations are:

a) reg1: $c_{WS}(CO_2)/(\mu mol\ kg^{-1}) = (0.033\pm0.003)p_c(CO_2)/\mu atm - 1.8\pm1.6$ ($R^2 = 0.77$)

a) reg2: $c_{WS}(CO_2)/(\mu mol\ kg^{-1}) = (0.12\pm0.14)\theta/°C - (0.071\pm0.011)(\theta/°C)^2 + (0.0094\pm0.0048)p_c(CO_2)/\mu atm + 16\pm4$ ($R^2 = 0.90$).

b) reg1: $p_{WS}(CO_2)/\mu atm = (0.05\pm0.05)p_c(CO_2)/\mu atm + 344\pm33$ ($R^2 = 0.02$)

b) reg2: $p_{WS}(CO_2)$/µatm] = (21±3)θ/°C – (1.9±0.2)(θ/°C)^2 + (0.2±0.1)$p_c(CO_2)$/µatm + 209±76 (R^2 = 0.60).

2.3.7 Regional algorithm to estimate A_T

To calculate C_T, we used two variables: glider $c(CO_2)$ derived as described in section 2.6 and A_T derived using a regional algorithm that uses the top 1000 m S and θ. The algorithm followed the approach of Lee et al. (2006) and was derived using 663 water samples collected at OWSM from 2004 to 2014 and GLODAPv2 (Olsen et al., 2016) data from 2000 in the deployment region. Discrete samples with S < 33 were removed because these values were lower than the minimum S measured by the glider. The derived A_T parameterisation is:

$$A_{T,reg} / (\mu mol\ kg^{-1}) = 2317.03 + 33.12\ (S–35) + 7.94\ (S–35)^2 + 0.96\ (\theta/°C–20) + 0.01\ (\theta/°C–20)^2 \quad (2.4)$$

The parameterisation has an uncertainty of 8.2 µmol kg^{-1} calculated as the standard deviation of the residual difference between actual and parameterised A_T.

To test this parameterisation, we compared the predicted $A_{T,reg}$ values with discrete measurements ($A_{T,WS}$) collected close in terms of time, potential density (σ_0) and distance to the glider transect (n = 60). These discrete samples and the glider had the mean temperature and salinity differences of (0.17±0.68) °C and (0.03±0.013), respectively. The mean difference between $A_{T,WS}$ and $A_{T,reg}$ was (2.1±6.5) µmol kg^{-1}.

This A_T parameterisation was used in CO2SYS (Van Heuven et al., 2011) to calculate C_T from $A_{T,reg}$ and the calibrated $c(CO_2)$, $c_{G,cal}(CO_2)$. The calculated $C_{T,cal}$ values were compared with $C_{T,WS}$ of the same set of discrete samples used to calibrate $c_{G,cal}(CO_2)$, the only difference being that instead of the actual total alkalinity of the water sample ($A_{T,WS}$), we used $A_{T,reg}$. The mean difference between $C_{T,cal}$ and $C_{T,reg}$ was (1.5±10) µmol kg^{-1}, with the non-zero bias and the standard deviation due to the uncertainties in the A_{Treg} parameterisation and the $c_{G,cal}(CO_2)$ calibration.

2.3.8 Quality control of other measurement variables

The thermal lag of the glider conductivity sensor was corrected using Gourcuff (2014). Single-point outliers in conductivity were visually identified and removed then replaced by linear interpolation. The glider CTD salinity was affected by presumed particulate matter stuck in the conductivity cell (Medeot et al., 2011) during dives 147, 234, 244,

251, 272, 279, 303, 320 and 397 and sensor malfunction caused a poor match between glider ascent and descent during a dives 214, 215, 235 and 243. These dives were removed from the subsequent analysis.

Glider-reported chlorophyll concentrations, c_{raw}(Chl *a*), were affected by photochemical quenching during the daytime dives. To correct for quenching, we used the method of Hemsley et al. (2015) based on the night time relationship between fluorescence and optical backscatter. This relationship was established in the top 60 meters and the night-time values were selected between sunset and sunrise. We calculated a linear fit between c_{raw}(Chl *a*) measured at night, c_N(Chl *a*), and the backscatter signal measured at night (b_N). The slope and the intercept were then used to correct daytime c_D(Chl *a*). The glider-reported chlorophyll concentration has not been calibrated against in situ samples and is not expected to be accurate, even after correction for quenching. However, it should give an indication of the depth of the deep chlorophyll concentration maximum (z_{DCM}) and the direction of chlorophyll concentration change (up/down). 8 day-means of c_{raw}(Chl *a*) were compared with satellite 8 day-composite chlorophyll concentration (Figure 2.7) from Ocean Colour CCI (https://esa-oceancolour-cci.org/) and gave a mean difference of (0.12±0.08) mg m^{-3} (Figure 2.7).

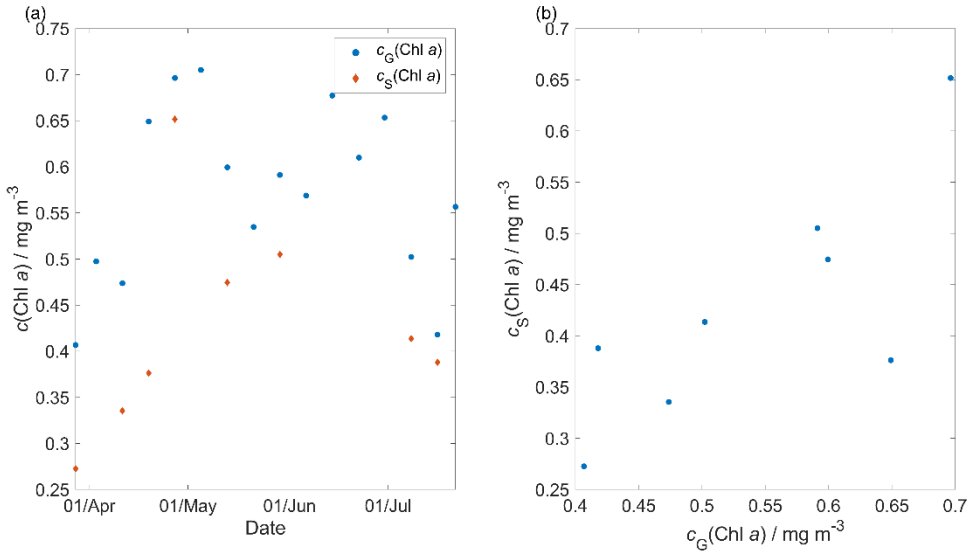

Figure 2.7: Comparison between the 8 days glider *c*(Chl *a*) (c_G(Chl *a*)) mean and the 8 days satellite *c*(Chl *a*) (c_S(Chl *a*)) download from Ocean Colour CCI (https://esa-oceancolour-cci.org/) where in a) c_G(Chl *a*) in red diamond and c_S(Chl *a*) in blue dots variability in time and in b) the direct comparison between c_G(Chl *a*) and c_S(Chl *a*).

2.3.9 Calculation of oxygen-based net community production, $N(O_2)$

Calculating net community production N from glider data is challenging because the glider continuously moves through different water masses. For that reason we subdivided the transect by binning the data into 0.1° latitude intervals to derive O_2 concentration changes every two transects. The changes were calculated between transects in the same direction of glider travel (e.g. transects 1 and 3, both in N-S direction) to have approximately the same time difference (40-58 days) at every latitude. If instead we had used two consecutive transects, this would lead to a highly variable time difference of near-0 to about 50 days along the transect.

We calculated $N(O_2)$ (in mmol m^{-2} d^{-1}) from the oxygen inventory changes ($\Delta I(O_2)/\Delta t$) corrected for air-sea exchange $\Phi(O_2)$, normalised to z_{mix} when z_{mix} was deeper than the integration depth of z_{lim}, entrainment $E(O_2)$ and diapycnal eddy diffusion $F_v(O_2)$:

$$N(O_2) = \frac{\Delta I(O_2)}{\Delta t} + \Phi(O_2)\frac{\min(z_{lim}, z_{mix})}{z_{mix}} - F_E(O_2) - F_v(O_2)) \qquad (2.5)$$

The inventory changes were calculated as the difference between transects of the integrated $c(O_2)$ in the top 45 m. A constant integration depth of 45 m was chosen to capture the deepest extent of the deep chlorophyll maximum (z_{DCM}) found during the deployment, which likely represents the lower bound for the euphotic zone.

The inventory changes were calculated using the following equation:

$$\frac{\Delta I(O_2)}{\Delta t} = \frac{\int_0^{45\,m} C_{n+1} dz - \int_0^{45\,m} C_n dz}{t_{n+1} - t_n} \qquad (2.6)$$

where n is the transect number, t is the day of the year and C is $c(O_2)$.

The air-sea flux of oxygen, $\Phi(O_2)$ was calculated for each glider dive using the median $c(O_2)$, θ and S in the top 10 m. We followed the method of Woolf and Thorpe (1991) that includes the effect of bubble equilibrium supersaturation in the calculations:

$$\Phi(O_2) = k_w(O_2)\{(c(O_2) - [1 + \Delta_{bub}(O_2)]c_{sat}(O_2)\} \qquad (2.7)$$

where $k_w(O_2)$ is the gas transfer coefficient, $\Delta_{bub}(O_2)$ is the increase of equilibrium saturation due to bubble injection and $c_{sat}(O_2)$ is the oxygen saturation. $c_{sat}(O_2)$ was calculated from S and θ using the solubility coefficients of Benson and Krause (1984), as fitted by Garcia and Gordon (1992). $\Delta_{bub}(O_2)$ was calculated from the following equation:

$$\Delta_{bub}(O_2) = 0.01\left(\frac{U}{U_0}\right)^2 \qquad (2.8)$$

where U is 10 m-wind speed with 1 hours resolution (ECMWF ERA5, https://www.ecmwf.int/en/forecasts/datasets/reanalysis-datasets/era5) and U_0 represents the wind speed when the oxygen concentration is 1 % supersaturated and has a value of 9 m s^{-1} (Woolf and Thorpe, 1991). U has a spatial resolution of 0.25° latitude and 0.25° longitude and was interpolated to the glider position at the beginning of the dive.

The transfer velocity $k_w(O_2)$ was calculated based on Wanninkhof (2014):

$$\frac{k_w(O_2)}{\text{cm h}^{-1}} = 0.251 \left(\frac{Sc(O_2)}{660}\right)^{-0.5} \left(\frac{U}{\text{m s}^{-1}}\right)^2 \qquad (2.9)$$

The Schmidt number, $Sc(O_2)$, was calculated using the parameterisation of Wanninkhof (2014). To account for wind speed variability, $k_w(O_2)$ applied to calculate $N(O_2)$ was a weighted mean. This value was calculated using the varying daily-mean wind speed U in the time interval between t_n and t_{n+1} (Δt) (50 days) using a 5 point-median z_{mix} (Reuer et al., 2007). The time interval is the same as used to calculate $\frac{\Delta I(O_2)}{\Delta t}$.

The entrainment flux, $F_E(O_2)$, was calculated as the oxygen flux when the mixed layer depth deepens in time and is greater than z_{lim} at time t_2:

$$F_E(O_2) = \frac{I(O_2,t_1,z_{mix}(t_2))\frac{z_{lim}}{z_{mix(t_2)}} - I(O_2,t_1,z_{lim})}{t_2 - t_1} \qquad (2.10)$$

where $t_2 - t_1$ represents the change in time, z_{mix} is the mixed layer depth, $I(O_2,t_1,z_{mix}(t_2))$ is the expected inventory that would result from a mixed layer deepening to $z_{mix}(t_2)$ between t_2 and t_1, and $I(O_2,t_1,z_{lim})$ is the original inventory at t_1.

The effect of diapycnal eddy diffusion (F_v) was calculated at z_{mix} when it was deeper than z_{lim} and at z_{lim} when z_{mix} was shallower than z_{lim}, using the following equation:

$$F_v(O_2) = K_z \frac{\partial C(O_2)}{\partial z} \qquad (2.11)$$

for a vertical eddy diffusivity (K_z) of 10^{-5} m^2 s^{-1} (Naveira Garabato et al., 2004). The effect of $F_v(O_2)$ on $N(O_2)$ was negligible with a median of (-0.1±0.5) mmol m^{-2} d^{-1}.

Then, we calculated $N(O_2)$ in oxygen units with $\frac{\Delta I(O_2)}{\Delta t}$ corrected for $\Phi(O_2)$, $F_v(O_2)$ and $F_E(O_2)$ using equation 2.5.

2.3.10 Calculation of inorganic carbon-based net community production, $N(C_T)$

$N(C_T)$ was calculated from the C_T inventory changes $\frac{\Delta I(C_T)}{\Delta t}$, air-sea flux of CO_2, $\Phi(CO_2)$, and entrainment $F_E(C_T)$ and diapycnal diffusion $F_v(C_T)$:

$$N(C_T) = -\frac{\Delta I(C_T)}{\Delta t} - \Phi(CO_2)\frac{\min(z_{lim}, z_{mix})}{z_{mix}} + F_E(C_T) + F_v(C_T) \quad (2.12)$$

Firstly, $\Phi(CO_2)$ was calculated using the 10 m wind speed with 1 hours' resolution downloaded from ECMWF ERA5. As for oxygen, we selected the closest wind speed data point at the beginning of each glider dive. We used the monthly mean atmospheric CO_2 dry mole fraction ($x(CO_2)$) downloaded from the Greenhouse Gases Reference Network Site from (https://www.esrl.noaa.gov/gmd/ccgg/ggrn.php) the closest site to the deployment at Mace Head, County Galway, Ireland (Dlugokencky et al., 2015). Using $x(CO_2)$ we calculated the air-saturation concentration $c_{atm}(CO_2)$:

$$c_{atm}(CO_2) = x(CO_2)\, p_{baro}\, F(CO_2) \quad (2.13)$$

where p_{baro} is the mean sea level pressure and $F(CO_2)$ is the CO_2 solubility function calculated from surface θ and S (Weiss and Price, 1980).

The seawater $c(CO_2)$ at the surface was calculated using the median in the top 10 meters between the glider ascent and descent of the following dive $c(CO_2)$. From this, $\Phi(CO_2)$ was calculated:

$$\Phi(CO_2) = k(CO_2)\,[c(CO_2) - c_{atm}(CO_2)]. \quad (2.14)$$

$k(CO_2)$ was calculated using the parameterisation of Wanninkhof (2014):

$$\frac{k(CO_2)}{\text{cm h}^{-1}} = 0.251\left(\frac{Sc(CO_2)}{660}\right)^{-0.5}\left(\frac{U}{\text{m s}^{-1}}\right)^2 \quad (2.15)$$

$Sc(CO_2)$ is the dimensionless Schmidt number at the seawater temperature (Wanninkhof, 2014). To account for wind speed variability, $k_w(CO_2)$ applied to calculate $N(C_T)$ was a weighted mean based on the varying daily-mean wind speed U in the time interval between t_n and t_{n+1} (Δt) used to calculate $\frac{\Delta I(C_T)}{\Delta t}$ and for 40 50 days to calculate $\Phi(CO_2)$ (Reuer et al., 2007).

The inventory changes were calculated in the top 45 m with the following equation:

$$\frac{\Delta I(C_T)}{\Delta t} = \frac{\int_0^{45\text{ m}} C_{n+1}\,dz - \int_0^{45\text{ m}} C_n\,dz}{t_{n+1} - t_n} \quad (2.16)$$

The entrainment flux, $F_E(C_T)$ was calculated as the oxygen flux when the mixed layer depth deepens in time and is greater than z_{lim} at time t_2:

$$F_E(C_T) = \frac{I(C,t_1,z_{mix}(t_2))\frac{z_{lim}}{z_{mix}(t_2)} - I(C,t_1,z_{lim})}{t_2 - t_1} \qquad (2.17)$$

As for oxygen, the effect of diapycnal eddy diffusion (F_v) was calculated at z_{mix} when it was deeper than z_{lim} and at z_{lim} when z_{mix} was shallower than z_{lim}, using the following equation:

$$F_v(C_T) = K_z \frac{\partial c(C_T)}{\partial z} \qquad (2.18)$$

for a K_z of 10^{-5} m^2 s^{-1} (Naveira Garabato et al., 2004). The effect of $F_v(C_T)$ was negligible with a median of (0.1±0.3) mmol m^{-2} d^{-1}.

The contribution of horizontal advection to $N(C_T)$ was considered minimal over the timescales we calculated inventory changes because previous studies have shown that changes in C_T during summer are mainly controlled by biology and air-sea interactions (Gislefoss et al., 1998). For that reason, previous studies that estimated N in the Norwegian Sea have also neglected advective fluxes (Falck and Anderson, 2005; Falck and Gade, 1999; Kivimäe, 2007; Skjelvan et al., 2001).

The uncertainties in $N(C_T)$ and $N(O_2)$ were evaluated with a Monte-Carlo approach. The uncertainties of the input variables are shown in Table 2.2; we repeated the analysis 1000 times. The total uncertainty in N was calculated as the standard deviation of the 1000 Monte-Carlo simulations.

Table 2.2. Uncertainty associated with $N(C_T)$ and $N(O_2)$ input variables calculated by a Monte Carlo approach.

Variable	Error	Reference/Method
C_T	11 µmol kg^{-1}	Standard deviation vs the water samples.
S	0.01	Standard deviation of glider salinities for σ_0 > 1028 kg m^{-3} and latitude > 64° N
θ	0.3 °C	Standard deviation of glider temperature for σ_0 > 1028 kg m^{-3} and latitude > 64° N
$c_{atm}(CO_2)$	1.5 µmol kg^{-1}	Standard deviation of $c_{atm}(CO_2)$
$c(CO_2)$	1.3 µmol kg^{-1}	Error is the standard deviation vs water samples.
$k(CO_2)$	20 %	(Wanninkhof, 2014)
z_{mix}	9 m	Standard deviation compared with z_{mix} based on thresholds ΔT = 0.1 °C (Sprintall and Roemmich, 1999), 0.2 °C (Thompson, 1976) and 0.8 °C (Kara et al., 2000).
z_{mix} latitude	0.32 m	Standard deviation compared with z_{mix} based on thresholds ΔT = 0.1 °C (Sprintall and Roemmich, 1999), 0.2 °C (Thompson, 1976) and 0.8 °C (Kara et al., 2000).
$c_G(O_2)$	2.4 µmol kg^{-1}	Standard deviation of glider oxygen concentrations for σ_0 > 1028 kg m^{-3} and latitude > 64° N

2.4 Results

The uncorrected temperature θ, salinity S, $c(O_2)$, $p(CO_2)$ and c_{raw}(Chl *a*) presented in Figure 2.8 were analysed to dive 400 dive (24 July 2014). In the following dives, the CO_2 optode stopped sampling in the first 150 m (Figure 2.8d). The raw $c(O_2)$ data were calibrated and drift corrected and $c(CO_2)$ was drift-, and lag-corrected and recalibrated, then used to quantify the temporal and spatial changes in N and Φ together with the quenching corrected c_{raw}(Chl *a*) to evaluate the net community production changes.

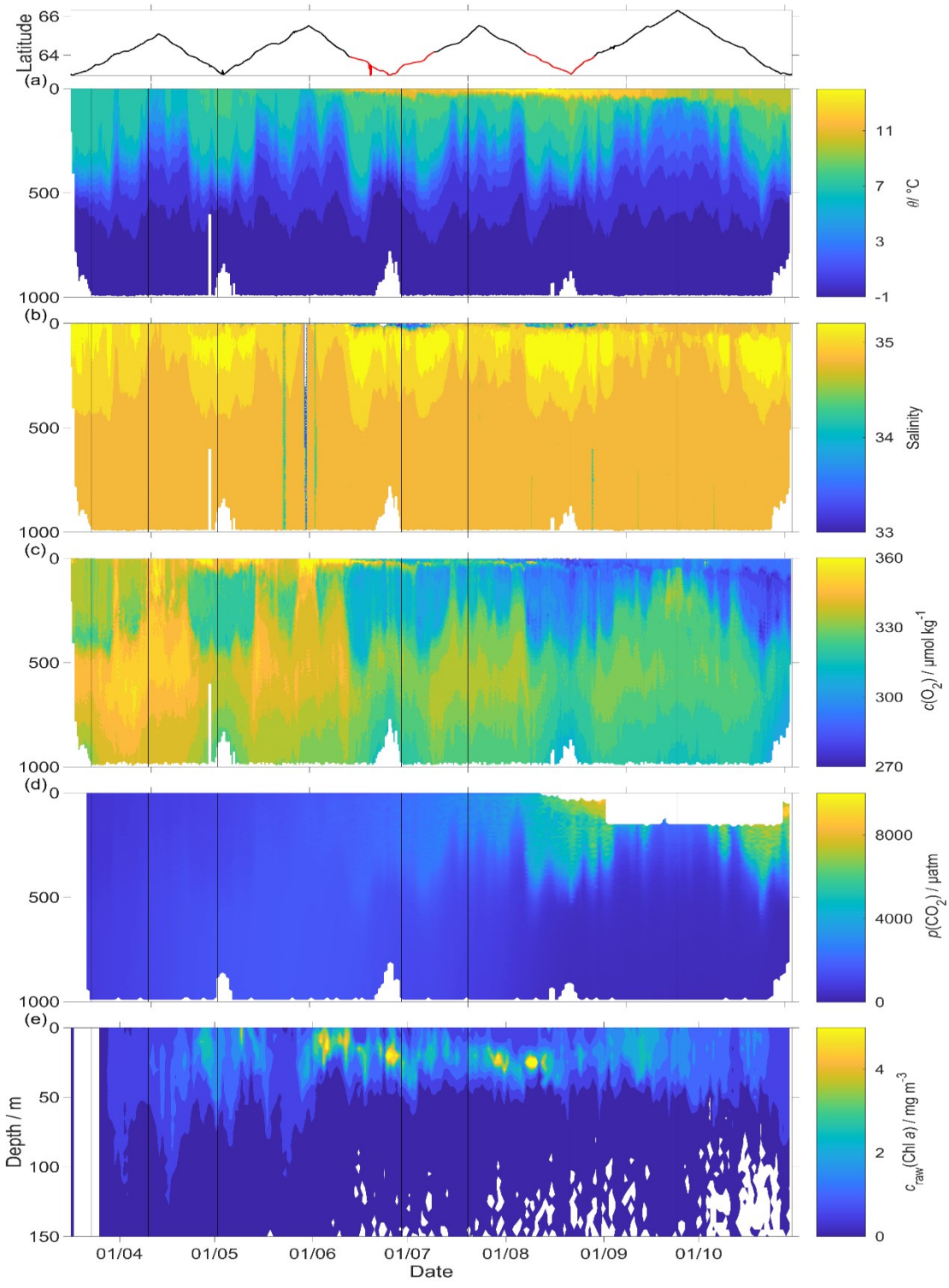

Figure 2.8: Raw glider data for all 703 dives with latitude of the glider trajectory at the top (black: NwAC; red: NCC, separated by a *S* of 35). a) temperature θ, b) salinity *S*, c) uncorrected oxygen concentration $c(O_2)$, d) uncorrected CO_2 optode output $p_u(CO_2)$ and e) chlorophyll *a* concentration c_{raw}(Chl *a*). The white space means that the sensors did not measure any data.

2.4.1 O_2 optode calibration

The uncorrected $c(O_2)$ continually decreased (Figure 2.8c). The ratio $c_C(O_2)/c_G(O_2)$ and against the day of the year used for the drift correction had a good correlation with time (R^2 = 0.90), showing a continuous increase of 0.0004 d^{-1} (Figure 2.3), equivalent to a decrease in the measured glider O_2 concentration of 0.11 µmol kg^{-1} d^{-1}. It was possible to apply the correction because $c_C(O_2)$ had low temporal variability (Figure 2.9). The discrete oxygen samples from OWSM and GLODAPv2 had a mean of (304.6±3.1) µmol kg^{-1}, varying from 294 to 315 µmol kg^{-1}. The drift correction reduced the variability of $c_G(O_2)$ in the selected potential density range from a standard deviation of 7.3 µmol kg^{-1} to a standard deviation of 2.4 µmol kg^{-1} (Figure 2.10).

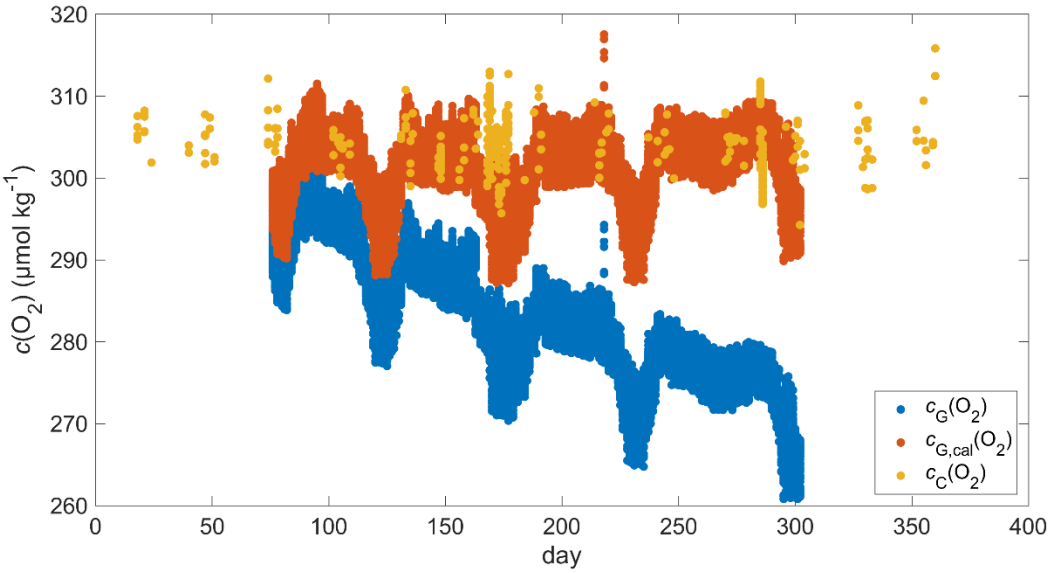

Figure 2.9: discrete samples $c_C(O_2)$ (yellow), raw glider oxygen $c_G(O_2)$ (blue) and drift corrected glider oxygen $c_{G,cal}(O_2)$ (red) for a potential density > 1028 kg m^{-3}.

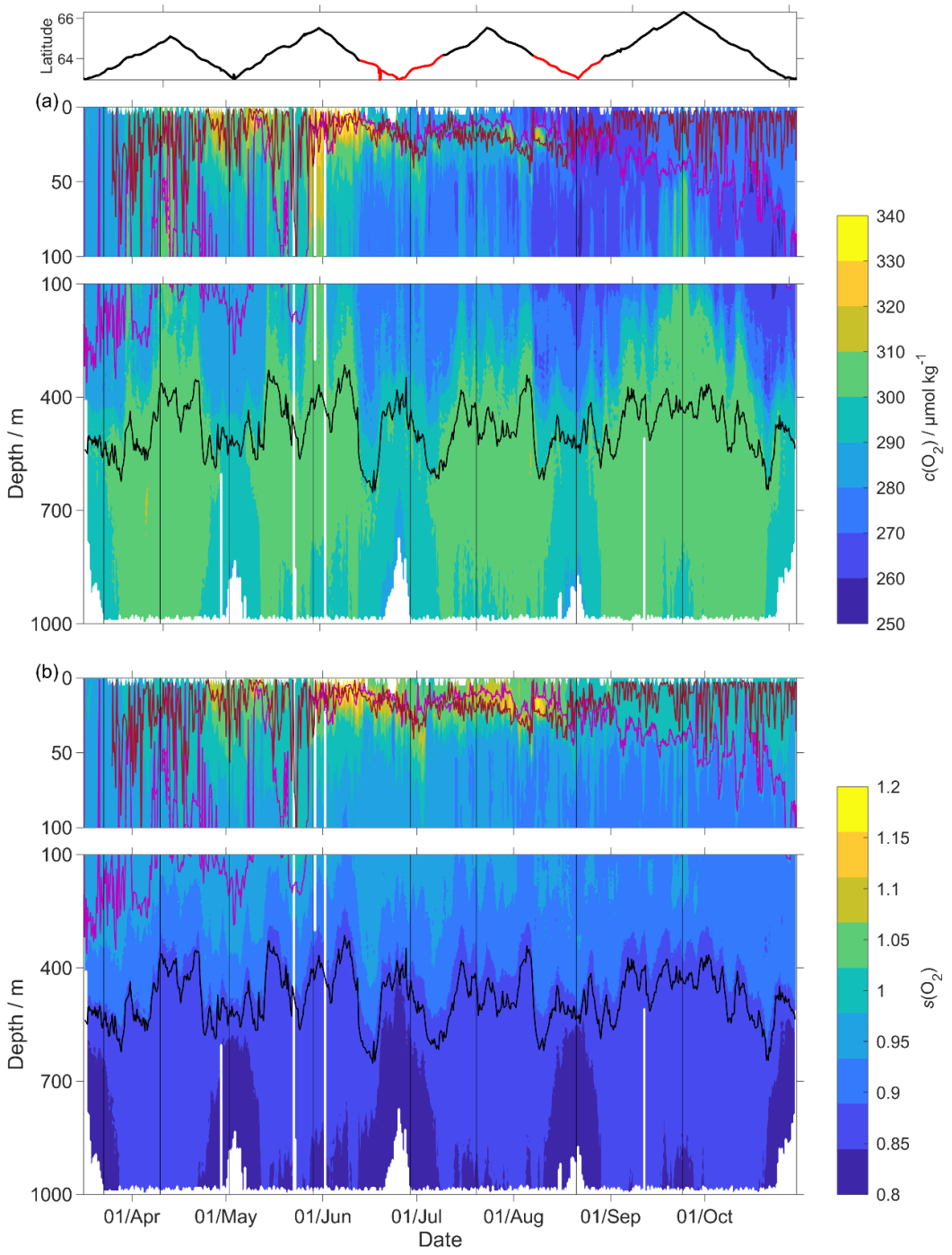
Latitude
66
64
(a)
0
50
100
100
400
700
1000
Depth / m
340
330
320
310
300
290
280
270
260
250
c(O2) / µmol kg-1
(b)
0
50
100
100
400
700
1000
Depth / m
1.2
1.15
1.1
1.05
1
0.95
0.9
0.85
0.8
s(O2)
01/Apr
01/May
01/Jun
01/Jul
01/Aug
01/Sep
01/Oct
Date

Figure 2.10: Distributions of **(**a) dissolved oxygen concentration, $c(O_2)$ (b) and oxygen saturation factor, $s(O_2)$, defined as $c(O_2)/c_{sat}(O_2)$. z_{DCM} (red line) and z_{mix} (pink line) were calculated using a threshold criterion of $\Delta\theta$ = 0.5 °C relative to the median θ of the top 5 m of the glider profile (Obata et al., 1996; United States. National Environmental Satellite and Information Service, Monterey and Levitus, 1997; Foltz et al., 2003). σ_0 = 1028 kg m^{-3} (black line) and at the top the latitude trajectory of the glider in black the Norwegian Atlantic Current (NwAC) and in red the Norwegian Coastal Current (NCC).

2.4.2 CO_2 optode calibration

Following drift, lag and scale corrections, glider fugacity $f_G(CO_2)$ derived from Eq. 2.2 had a mean difference of (2±22) µatm to the discrete samples (n = 55; not shown) and C_T had a standard deviation of 11 µmol kg^{-1} and a mean difference of 3 µmol kg^{-1} (Figure 2.11). $p(CO_2)$ and $f(CO_2)$ are almost the same numbers, specifically $f(CO_2)$ takes into account the non-ideal nature of the gas phase. The optode was able to capture the temporal and spatial variability showing that NCC had a lower concentration of C_T than NwAC. Because of the surface variability between the glider location and OWSM, restricting the discrete samples $f(CO_2)$ to the top 10 m only gave a mean difference of (19±31) µatm (n = 6). We also compared glider $f_G(CO_2)$ with SOCAT $f(CO_2)$ (Bakker et al., 2016) data in the region during the deployment (Figure 2.12). During the whole deployment, there was general agreement between $f_G(CO_2)$ and $f_{SOCAT}(CO_2)$. $f_G(CO_2)$ varied between 204 and 391 µatm while $f_{SOCAT}(CO_2)$ varied between 202 and 428 µatm (Figure 2.12).

Our results are in agreement with Jeansson et al. (2011) who found the surface NCC was the region with the lowest C_T values (2083 µmol kg^{-1}) in the Norwegian Sea. This was confirmed during our deployment because C_T was (2081±39) µmol kg^{-1} in the NCC region and (2146±27) µmol kg^{-1} in the NwAC region (Figure 2.11) and $c(O_2)$ was >300 µmol kg^{-1} in the NwAC and < 280 µmol kg^{-1} in the NCC.

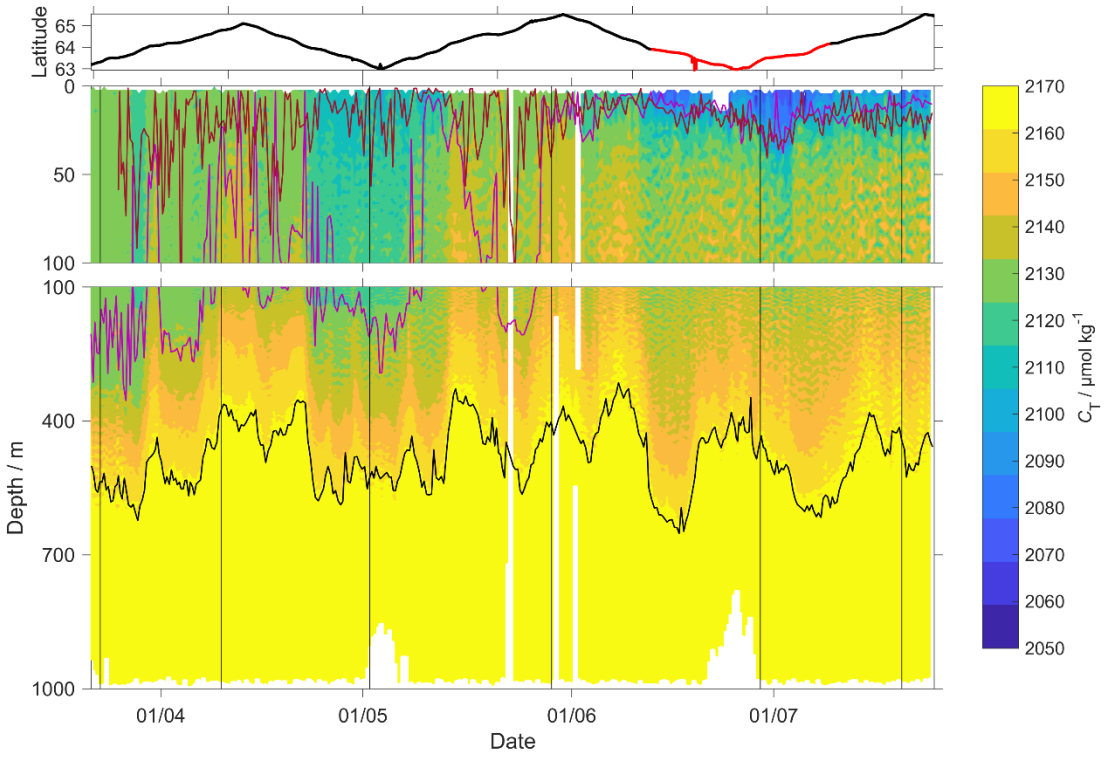

Figure 2.11: C_T contour plot with z_{DCM} (red line) and the z_{mix} (pink line) calculated using a threshold criterion of $\Delta\theta$ = 0.5 °C to median θ of the top 5 m of the glider profile (Obata et al., 1996; United States. National Environmental Satellite and Information Service, Monterey and Levitus, 1997; Foltz et al., 2003), in black σ_0 = 1028 kg m^{-3} and at the top the latitude trajectory of the glider in black NwAC and in red NCC.

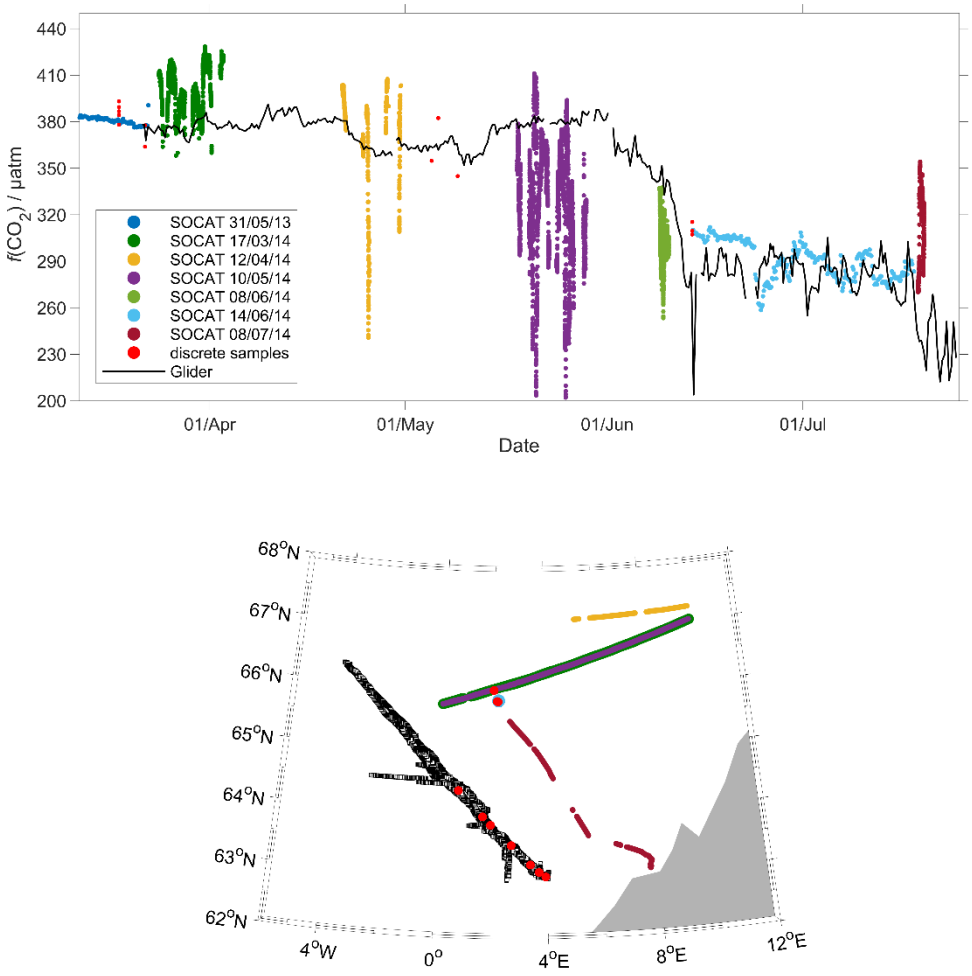

Figure 2.12: The plot represents the surface $f(CO_2)$ from 2014 SOCAT measured during the glider deployment and the glider. The black squares are the median of the glider $f(CO_2)$ in the top 10 meters calculated using the ascent of the single dive and the descent of the next dive. The red dots are the water samples collected during the deployment and the remaining dots are from the SOCAT cruises in the area during the deployment. On the bottom, there is the map of the glider and SOCAT data positions.

2.4.3 Air-sea exchange

The surface water was supersaturated with oxygen all summer (Figure 2.13). From May this supersaturation drove a continuous O_2 flux from the sea to the atmosphere. However, the flux varied throughout the deployment having a median of 25 mmol m^{-2} d^{-1} (5^{th} centile: -31 mmol m^{-2} d^{-1}; 95^{th} centile: 88 mmol m^{-2} d^{-1}). Before the spring period of increased Chl *a* inventory, the supersaturation varied between 0 to 10 µmol kg^{-1}. $\Phi(O_2)$

had a median of -1.4 mmol m^{-2} d^{-1} (5^{th} centile: -49 mmol m^{-2} d^{-1}; 95^{th} centile: 23 mmol m^{-2} d^{-1}). Then, during the spring period of increased Chl *a* inventory, the surface concentration increased by over 35 µmol kg^{-1}, causing a peak in $\Phi(O_2)$ of 140 mmol m^{-2} d^{-1}. A second period of increased Chl *a* inventory was encountered in June and had a larger $\Phi(O_2)$ up to 118 mmol m^{-2} d^{-1}, driven by supersaturation of 68 µmol kg^{-1}. These larger fluxes during the second period of increased Chl *a* inventory were associated with an increase of c_{raw}(Chl a) from 2.5 mg m^{-3} to the summer maximum of 4.0 mg m^{-3}. However, before the spring period of increased Chl *a* inventory, $\Phi(O_2)$ showed a few days of influx into the seawater caused by a decrease of θ from 7.6 °C to 5.9 °C that increased $c_{sat}(O_2)$. The influx at the beginning of the deployment is partly due to the $\Delta_{bub}(O_2)$ correction that increased $[1+\Delta_{bub}(O_2)]c_{sat}(O_2)$ to values larger than $c(O_2)$ for $U >$ 10 m s^{-1}. In August the surface supersaturation decreased to 2.3 µmol kg^{-1} and $\Phi(O_2)$ decreased to a monthly minimum of –7.6 mmol m^{-2} d^{-1}. In the second half of September the surface water became undersaturated by –2.6 µmol kg^{-1}, causing O_2 uptake with a median flux of -13 mmol m^{-2} d^{-1} (5^{th} centile: -39 mmol m^{-2} d^{-1}; 95^{th} centile: 10 mmol m^{-2} d^{-1}).

The CO_2 flux from March to July was always from the air to the sea (Figure 2.13), with a median of -5.2 mmol m^{-2} d^{-1} (5^{th} centile: -14 mmol m^{-2} d^{-1}; 95^{th} centile: -1.5 mmol m^{-2} d^{-1}). An opposing flux direction is expected for $\Phi(O_2)$ and $\Phi(CO_2)$ during the productive season when net community production is the main driver of concentration changes. After the summer period of increased Chl *a* inventory, the flux had a median of -11 mmol m^{-2} d^{-1} (5^{th} centile: –16 mmol m^{-2} d^{-1}; 95^{th} centile: -6.8 mmol m^{-2} d^{-1}). Positive fluxes (from water to air) are in disagreement with previous studies that classified the Norwegian Sea as a CO_2 sink (Takahashi et al., 2002; Skjelvan et al., 2005). Calculating $\Phi(CO_2)$ from the discrete samples from the 18 March to the 14 June (n = 13) the flux varied from 0.1 to -13 mmol m^{-2} d^{-1} with just one positive $\Phi(CO_2)$ in March.

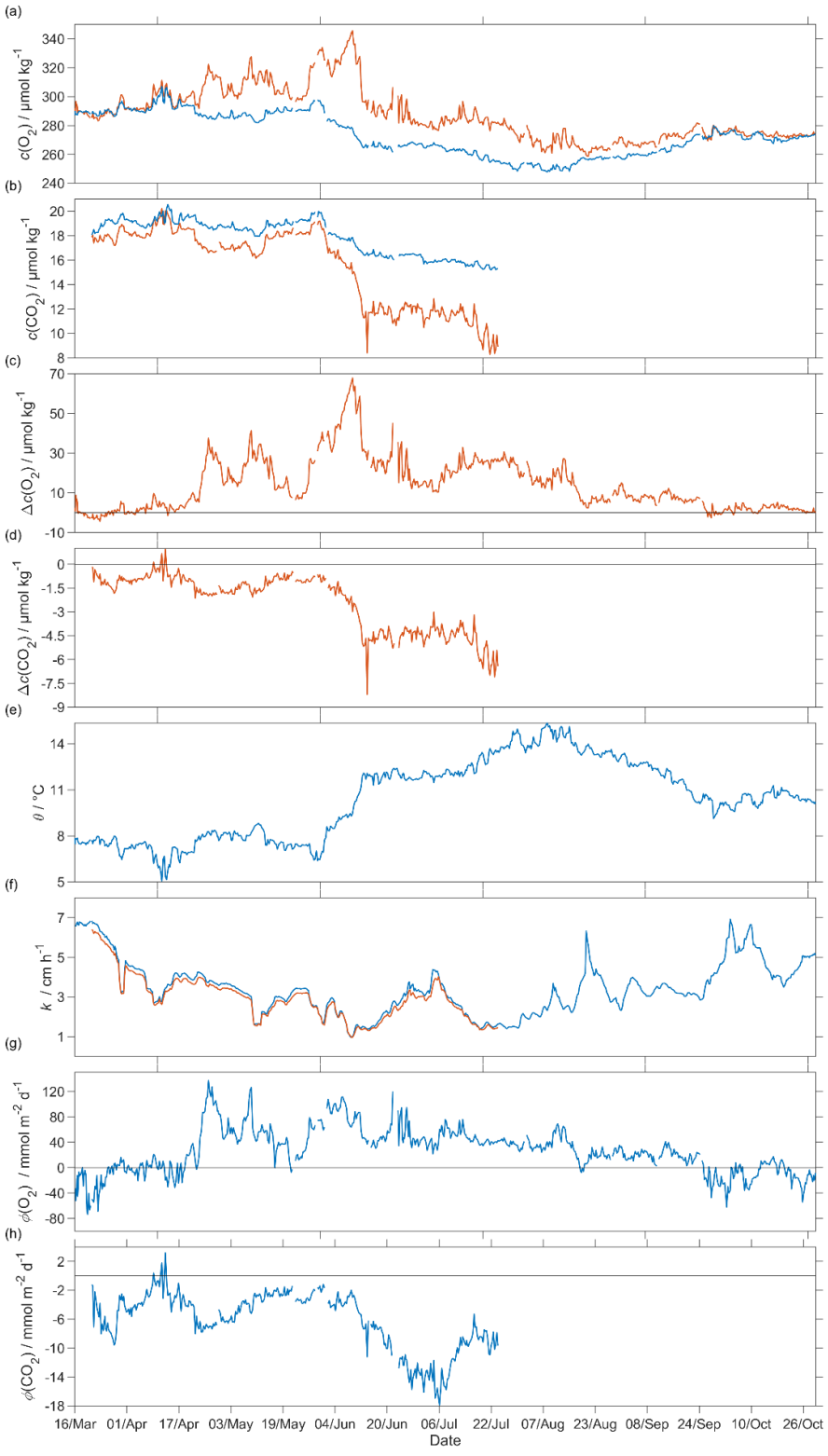

Figure 2.13: Air-sea flux of O_2 and CO_2 during spring and summer for CO_2 and during spring, summer and autumn for O_2, a) $c_{sat}(O_2)$ in blue and $c(O_2)$ in red, b) $c_{sat}(CO_2)$ in blue and $c(CO_2)$ in red, c) $\Delta c(O_2) = c(O_2) - c_{sat}(O_2)$, d) $\Delta c(CO_2) = c(CO_2) - c_{sat}(CO_2)$, e) sea surface temperature, f) $k_w(O_2)$ in blue and $k_w(CO_2)$ in red normalised back to 50 days (Reuer et al., 2007), g) oxygen air-sea flux $\Phi(O_2)$ and h) CO_2 air-sea flux $\Phi(CO_2)$. The flux from sea to air is positive while that from air to sea is negative.

2.4.4 Oxygen-based net community production, $N(O_2)$

To capture the entire euphotic zone, we calculated $N(O_2)$ and N(DIC) using an integration depth of z_{lim} = 45 m because the mean deep chlorophyll maximum (DCM) depth was z_{DCM} = (20±18 m) (Figure 2.10). For comparison, the mixed layer depth was deeper, varied more strongly and had a mean value of z_{mix} = (68±78) m, using a threshold criterion of $\Delta\theta$ = 0.5 °C to the median θ value in the top 5 m of the glider profile (Obata et al., 1996; United States. National Environmental Satellite and Information Service, Monterey and Levitus, 1997; Foltz et al., 2003).

The two N values were calculated as the difference in inventory changes between two transects when the glider moved in the same direction.

During the deployment, we sampled two periods of increased Chl *a* inventory, the first one in May and a second one in June. The chlorophyll *a* inventory ($I_{\mathrm{raw},z_{\mathrm{lim}}}(\mathrm{Chl}\ a)$) was calculated integrating c_{raw}(Chl *a*) to z_{lim}. To remove outliers we used a five-point moving mean of $I_{\mathrm{raw},z_{\mathrm{lim}}}(\mathrm{Chl}\ a)$.

The $N(O_2)$ changes were dominated by $\Phi(O_2)$ that had an absolute median of 34 mmol m^{-2} d^{-1} (5th centile: 4.3 mmol m^{-2} d^{-1}; 95th centile: 86 mmol m^{-2} d^{-1}), followed by $I(O_2)$ that had a median of 15 mmol m^{-2} d^{-1} (5th centile: 2.3 mmol m^{-2} d^{-1}; 95th centile: 29 mmol m^{-2} d^{-1}), $F_v(O_2)$ that had an absolute median of 0.3 mmol m^{-2} d^{-1} (5th centile: 0 mmol m^{-2} d^{-1}; 95th centile: 1.0 mmol m^{-2} d^{-1}) and $F_E(O_2)$ that had a median of 0 mmol m^{-2} d^{-1} (5th centile: -1.2 mmol m^{-2} d^{-1}; 95th centile: 0 mmol m^{-2} d^{-1}).

At the beginning of May, $I_{\mathrm{raw},z_{\mathrm{lim}}}(\mathrm{Chl}\ a)$ increased to 97 mg m^{-2} and $N(O_2)$ = (95±16) mmol m^{-2} d^{-1}. After this period, $I_{\mathrm{raw},z_{\mathrm{lim}}}(\mathrm{Chl}\ a)$ decreased to 49 mg m^{-2} and $N(O_2)$ = (-4.6±1.6) mmol m^{-2} d^{-1}. During the summer $I_{\mathrm{raw},z_{\mathrm{lim}}}(\mathrm{Chl}\ a)$ increased to 110 mg m^{-2}, which caused a sharp increase of $N(O_2)$ to (126±25) mmol m^{-2} d^{-1}. $I_{\mathrm{raw},z_{\mathrm{lim}}}(\mathrm{Chl}\ a)$ remained higher than 50 mg m^{-2} until the end of June when $N(O_2)$ was (31±9) mmol m^{-2} d^{-1}. The passage of the glider from NwAC to NCC accompanied by a drop of surface $c(O_2)$ from 330 to 280 µmol kg^{-1} (Figure 2.10) that resulted in lower $\Phi(O_2)$ and $N(O_2)$ values (Figure 13). At the same time $I_{\mathrm{raw},z_{\mathrm{lim}}}(\mathrm{Chl}\ a)$ decreased to 35 mg m^{-2} showing that the decrease of $N(O_2)$ depended on the passage to NCC and a decrease of biological production. After the beginning of August, $I_{\mathrm{raw},z_{\mathrm{lim}}}(\mathrm{Chl}\ a)$ decreased to 49 mg m^{-2} and $N(O_2)$ turned negative with a minimum of (–23±25) mmol m^{-2} d^{-1}. In October during the last glider transect $I_{\mathrm{raw},z_{\mathrm{lim}}}(\mathrm{Chl}\ a)$ continued decreasing to 27 mg m^{-2} leading to the minimum $N(O_2)$ of (-52±11) mmol m^{-2} d^{-1}.

Integrating $N(O_2)$ from March to October gives a flux of 4.9 mol m^{-2} a^{-1} (Table 2.3; discussed in section 2.5.2).

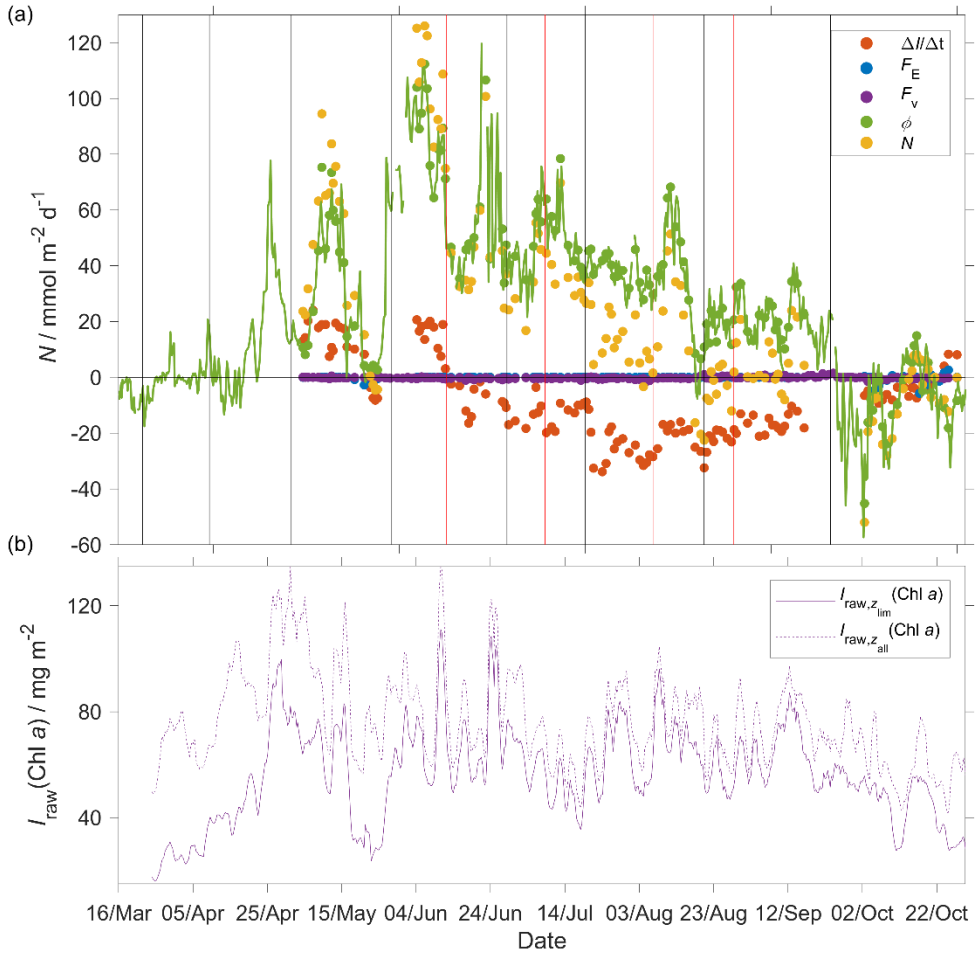

Figure 2.14: a) Components of the $N(O_2)$ calculation: $\Delta I(O_2)/\Delta t$ (red), $E(O_2)$ (blue), $F_v(O_2)$ (violet), $\Phi(O_2)$ (green) with $k_w(O_2)$ weighted over 50 days, $N(O_2)$ (yellow). b) Chl *a* inventory in the top 45 m, $I_{\mathrm{raw},z_{\mathrm{lim}}}(\mathrm{Chl}\ a)$ (violet). Chl *a* inventory for the whole water column, $I_{\mathrm{raw},z_{\mathrm{all}}}(\mathrm{Chl}\ a)$ (violet dotted line). The black vertical lines represent each glider transect. Between the two vertical red lines, the glider was in the NCC region.

2.4.5 Inorganic carbon-based net community production, $N(C_T)$

In the case of $N(C_T)$ the main drivers were the inventory changes with an absolute median of 29 mmol m^{-2} d^{-1} (5^{th} centile: 1.3 mmol m^{-2} d^{-1}; 95^{th} centile: 57 mmol m^{-2} d^{-1}), followed by $\Phi(CO_2)$ that had an absolute median of 7.0 mmol m^{-2} d^{-1} (5^{th} centile: 0.8 mmol m^{-2} d^{-1}; 95^{th} centile: 15 mmol m^{-2} d^{-1}), $F_v(C_T)$ that had an absolute median of 0.2 mmol m^{-2} d^{-1} (5^{th} centile: 0 mmol m^{-2} d^{-1}; 95^{th} centile: 1.3 mmol m^{-2} d^{-1}) and $F_E(C_T)$ had a median of 0 mmol m^{-2} d^{-1} (5^{th} centile: 0 mmol m^{-2} d^{-1}; 95^{th} centile: 3.4 mmol m^{-2} d^{-1}).

During the period of increased Chl *a* inventory $N(C_T)$ was (21±4.5) mmol m^{-2} d^{-1}. Later $I_{\mathrm{raw},z_{\mathrm{lim}}}(\mathrm{Chl}\ a)$ decreased to 30 mg m^{-2} driving $N(C_T)$ to negative values with a minimum of (-2.7±5.0) mmol m^{-2} d^{-1}. In the next transect, the glider measured the maximum $I_{\mathrm{raw},z_{\mathrm{lim}}}(\mathrm{Chl}\ a)$ of 111 mg m^{-2} that increased $N(C_T)$ to (85±4.5) mmol m^{-2} d^{-1}. This maximum was reached during a transect when the glider moved in NCC that had a $c(C_T)$ of 2080 µmol kg^{-1} at the surface compared with the 2150 µmol kg^{-1} in NwAC and drove a continuous positive $N(C_T)$ that had a minimum of (36±7.4) mmol m^{-2} d^{-1} (Figure 2.15).

Integrating $N(C_T)$ from March to July gives a flux of 3.3 mol m^{-2} a^{-1} (Table 2.3; discussed in section 2.5.2).

Table 2.3. Net community production (*N*) estimates in the Norwegian Sea (with integration depth z_{lim}). Falck and Anderson (2005) used year-round data from 1960 to 2000 between 62 and 70° N and from 1991 to 1994 at OWSM. Skjelvan et al. (2001) used year-round data from 1957 to 1970 and from 1991 to 1998 between 67.5° N 9° E and 71.5° N 1° E and along 74.5° N from 7 to 15° E. Kivimäe (2007) used year-round data from 1955 to 2005 and Falck and Gade (1999) used year-round data from 1955 to 1988 in all of the Norwegian Sea. While the previous studies report annual *N* estimates, the present study derives $N(O_2)$ between March and October and $N(C_T)$ between March and July.

Study	$N(C_T)$ / mol m^{-2} a^{-1}	$N(O_2)$ / mol m^{-2} a^{-1}	$N(O_2)$ / $N(C_T)$	z_{lim} / m	*Variables used to derive N*
(Falck and Anderson, 2005), annual	3.4	—		100	$c(NO_3^-)$, $c(PO_4^{3-})$, $c(C_T)$
(Skjelvan et al., 2001), annual	—	2.6		300	$c(O_2)$, $c(PO_4^{3-})$
(Kivimäe, 2007), annual	—	11 (4.7 to 18.3)		z_{mix} until 100 m	$c(O_2)$
(Falck and Gade, 1999), annual	—	3.9		30	$c(O_2)$
This study, March to July	3.1	4.1	1.3	30	$c(O_2)$, $c(C_T)$
This study, March to July	3.3	4.2	1.3	45	$c(O_2)$, $c(C_T)$
This study, March to July	3.3	3.7	1.1	100	$c(O_2)$, $c(C_T)$
This study, March to October		5.0			
This study, March to October		4.9			
This study, March to October		3.6			

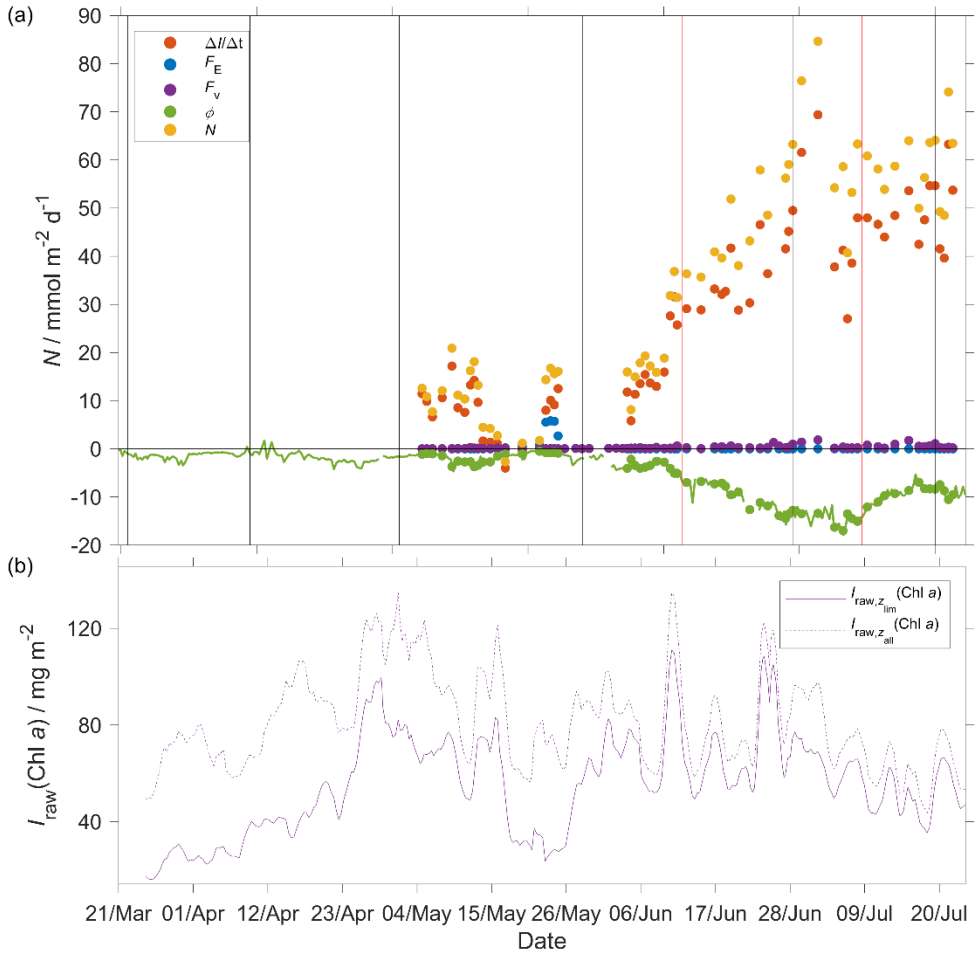

Figure 2.15: a) Components of the $N(C_T)$ calculation: $\Delta I(C_T)/\Delta t$ (red), $F_E(C_T)$ (blue), $F_v(C_T)$ (violet), $\Phi(CO_2)$ (green) with $k_w(CO_2)$ weighted over 50 days, $N(C_T)$ (yellow). b) Chl *a* inventory in the top 45 m, $I_{\mathrm{raw},z_{\mathrm{lim}}}(\mathrm{Chl}\ a)$ (violet). Chl *a* inventory for the whole water column, $I_{\mathrm{raw},z_{\mathrm{all}}}(\mathrm{Chl}\ a)$ (violet dotted line). The black vertical lines represent each glider transect. Between the two vertical red lines, the glider was in the NCC region.

2.5 Discussion

2.5.1 Sensor performance

This study presents data from the first glider deployment with a CO_2 optode. The initial uncalibrated $p(CO_2)$, $p_U(CO_2)$, measured by the CO_2 optode had a median of 604 µatm (5^{th} centile: 566 µatm; 95^{th} centile: 768 µatm) when the $p(CO_2)$ of discrete samples varied from 302 to 421 µatm. This discrepancy was caused by sensor drift before and during deployment of the optode.

We applied corrections for drift (using deep-water samples as a reference point), sensor lag and calibrated the CO_2 optode against co-located discrete samples throughout the water column.

Atamanchuk (2014) reported that the sensor was affected by a lag that varied from 45 to 264 s depending on temperature. These values were determined in an actively stirred beaker. However, in this study the sensor was mounted on a glider and was not actively pumped, which increased the response time to 1384 s, (25^{th} quartile: 1101 s; 75^{th} quartile: 1799 s). Also, the optode was affected by a continuous drift from 637 to 5500 µatm that is larger than the drift found by Atamanchuk et al. (2015a) that increased by 75 µatm after 7 months.

In this study, the drift- and lag-corrected sensor output showed a better correlation with the CO_2 concentration $c(CO_2)$ than with $p(CO_2)$. The latter two quantities are related to each other by the solubility that varies with θ and S (Weiss, 1974) (Eq. 2.2). The better correlation with $c(CO_2)$ was probably due to an inadequate temperature-parameterisation of the sensor calibration function. Including temperature and temperature squared in the calibration gave a better fit for both $c(CO_2)$ than with $p(CO_2)$, but overall still a lower calibration residual for the former. The sensor output depends on the changes in pH that are directly related to the changes of $c(CO_2)$ in the membrane and – indirectly – $p(CO_2)$, via Henry's Law. The calibration is supposed to correct for the temperature-dependence of the sensor output (Atamanchuk et al., 2014). So the fact, that the sensor output correlated better with $c(CO_2)$ than $p(CO_2)$ is perhaps due to a fortuitous cancellation of an inadequate temperature-parameterisation and the Henry's Law relationship between $c(CO_2)$ than $p(CO_2)$.

The calibrated optode output captured the C_T changes in space and time with a standard deviation of 10 µmol kg^{-1} compared with the discrete samples. During the deployment, C_T decreased from 2130 µmol kg^{-1} to 2000 µmol kg^{-1} and increased with depth to 2170 µmol kg^{-1}. This shows the potential of the sensor for future studies that aim to analyse the carbon cycle using a high-resolution dataset.

The optode-derived CO_2 fugacity $f_G(CO_2)$ had a mean bias of (8±22) µatm compared with the discrete samples. These values are comparable with a previous study when the CO_2 optode was tested for 65 days on a wave-powered Profiling crAWLER (PRAWLER) from 3 to 80 m (Chu et al., 2020), which had an uncertainty between 35 and 72 µatm. The PRAWLER optode was affected by a continuous drift of 5.5 µatm d^{-1} corrected using a regional empirical algorithm that uses $c(O_2)$, θ, S and σ_o to estimate A_T and C_T.

2.5.2 Norwegian Sea net community production

Increases in $N(O_2)$ and $N(C_T)$ were associated with increases in depth-integrated c_{raw}(Chl a), designated as periods of increased Chl *a* inventory, at the beginning of May and in

June. During the first period of increased Chl *a* inventory at the beginning of May surface c_{raw}(Chl *a*) reached 3 mg m^{-3}. The second period of increased Chl *a* inventory in June lasted longer and c_{raw}(Chl *a*) increased to 4 mg m^{-3}. Between the two periods of increased Chl *a* inventory, $N(O_2)$ and $N(C_T)$ had negative values indicating that remineralisation of the high Chl *a* inventory material was a dominant process during this period. Even though the fluorometer was uncalibrated, the spring period of increased Chl *a* inventory c_{raw}(Chl *a*) values are in agreement with the study of Rey (2001) who found c_{raw}(Chl *a*) = 3 mg m^{-3} at the beginning of May. The largest period of increased Chl *a* inventory was when the top 50 m θ increased from 7 °C to 11 °C and z_{mix} shoaled from 200 m to 20 m. During this period, $c(O_2)$ reached the summer maximum of 340 µmol kg^{-1} and C_T decreased to the summer minimum at 1990 µmol kg^{-1}. In both cases, the main components of the *N* changes were the inventory and air-sea flux, while the smallest driver was the entrainment. Also, the glider sampled two different water masses characterised by different C_T and $c(O_2)$. This led to smaller values of *N* in NCC compared to NwAC.

During the two blooms the two *N* showed an increase because of photosynthesis that increased O_2 in the water consuming C_T. After the two blooms at the beginning of May and July the organic material produced during the blooms was remineralised turning the two *N* to negative values.

Table 2.3 shows estimates of net community production (*N*) in the Norwegian Sea. All other studies used ships to gather observations. The estimated *N* in the four other studies varied from 2.6 to 11.1 mol m^{-2} a^{-1} for $N(O_2)$ and was 3.4 for $N(C_T)$. In our glider study, we obtained between March and July $N(C_T)$ of 3.3 mol m^{-2} a^{-1} and a $N(O_2)$ of 4.2 mol m^{-2} a^{-1}, in agreement with these studies. The ratio of $N(O_2)$ and $N(C_T)$ for an integration depth of 45 m gave a photosynthetic quotient (PQ) of 1.3, in agreement with the Redfield ratio of 1.45±0.15 (Redfield, 1963; Anderson, 1995; Anderson and Sarmiento, 1994; Laws, 1991). The $N(O_2)$ estimate is influenced primarily by the air-sea exchange flux $\Phi(O_2)$ (median: 34 mmol m^{-2} d^{-1}), followed by the inventory change (15 mmol m^{-2} d^{-1}). In contrast, $N(C_T)$ is dominated by the inventory change (–29 mmol m^{-2} d^{-1}), followed by $\Phi(CO_2)$ (–7.0 mmol m^{-2} d^{-1}). This reflects the slower gas-exchange time constant of CO_2 compared with O_2, due to C_T buffering. To compare our results with previous studies we also used z_{lim} = 30 m (Falck and Gade, 1999) and 100 m (Falck and Anderson, 2005; Kivimäe, 2007). The calculated $N(C_T$; 30 m) was 3.1 mol m^{-2} a^{-1}, $N(C_T$; 100 m) was 3.4 mol m^{-2} a^{-1}, $N(O_2$; 30 m) was 4.1 mol m^{-2} a^{-1} and $N(O_2$; 100 m) was 3.7 mol m^{-2} a^{-1}. The $N(C_T$; 100 m) value is in agreement with the value of 3.4 mol m^{-2} a^{-1} given by Falck and Anderson (2005). However, the latter estimate was for the entire year, whereas our estimate only covers the months from March to July. $N(O_2)$ was similar for z_{lim} = 30 m and 45 m, but lower for z_{lim} = 100 m because of O_2

consumption during organic matter remineralisation below the euphotic zone. The PQ value at 30 m was 1.3 and at 100 m decreased to 1.1. Extending $N(O_2)$ to October increased $N(O_2$; 30 m) and $N(O_2$; 45 m) to 5.0 and 4.9 mol m^{-2} a^{-1}, respectively. Instead, $N(O_2$; 100 m) decreased to 3.6 mol m^{-2} a^{-1}, confirming the consumption of O_2 below the euphotic zone. The calculated $N(O_2)$ until October was in agreement with the previous studies that varied between 2.6 and 11 mol m^{-2} a^{-1}.

Some of the previous N(DIC) estimates derived C_T from other variables such as $c(O_2)$, $c(PO_4^{3-})$, $c(NO_3^-)$, assuming Redfield ratios P:N:C:O_2 1:16:106:-138 (Redfield, 1963). During photosynthesis $c(PO_4^{3-})$ and $c(NO_3^-)$ are taken up by phytoplankton to form organic matter and are released again after remineralisation of the organic matter giving an indication of NCP changes. Our $N(C_T)$ estimate was 3.3 mol m^{-2} a^{-1} and is similar to 3.4 mol m^{-2} a^{-1} estimated by Falck and Anderson (2005) who used C_T samples directly. The carbon/nutrient ratios vary between water masses and during photosynthesis (Thomas et al., 1999; Copin-Montégut, 2000; Osterroht and Thomas, 2000; Körtzinger et al., 2001).

The difference of $N(O_2)$ between the studies can be caused by the yearly variability of N in the Norwegian Sea. In fact, Kivimäe (2007) saw an annual variability of $N(O_2)$ from 1955 to 2005 of 4.7 mol m^{-2} a^{-1} to 18.3 mol m^{-2} a^{-1} and of $N(C_T)$ of 3.6 mol m^{-2} a^{-1} to 14.0 mol m^{-2} a^{-1}. The interannual variability makes it hard to estimate how much we underestimate the net community production. To understand what is causing these interannual changes and accurately quantify the annual Ns, it is important to use available high-resolution datasets that cover the entire year. Also, this study showed that the Norwegian Sea spring and summer N is strongly affected by time and location. For that reason, N estimated from low-resolution datasets make the results strongly dependant on the time and place of sampling. To quantify this interannual variability in N, more high-resolution studies are needed.

2.6 Conclusions

This study was, to the best of our knowledge, the first glider deployment of a CO_2 optode. During the deployment, the optode performance was affected by drift, lag, lack of sampling in the top 150 m after dive 400 (the 24 July 2014), and poor default calibration. We found that the optode response was better correlated with $c(CO_2)$ than $p(CO_2)$. Nevertheless, the optode was able to capture the spatial and temporal changes in the Norwegian Sea after recalibration with discrete samples collected along the glider section and nearby at OWSM during the deployment.

C_T estimated from glider data had a standard deviation of 11 µmol kg-1 and a mean bias of 3 µmol kg^{-1} compared with the discrete samples, while the CO_2 fugacity $f(CO_2)$ had a mean bias of (2±22) µatm. The dataset was used to calculate net community production $N(O_2)$ and $N(C_T)$ from inventory changes, air-sea flux, and entrainment. The two N values had maxima during the summer period of increased Chl *a* inventory of $N(C_T)$ = (85±5) mmol m^{-2} d^{-1} and $N(O_2)$ = (126±25) mmol m^{-2} d^{-1}. At the beginning of April, we sampled a smaller spring period of increased Chl *a* inventory with a $N(C_T)$ = (21±5) mmol m^{-2} d^{-1} and $N(O_2)$ = (94±16) mmol m^{-2} d^{-1}. After the period of increased Chl *a* inventory, $N(C_T)$ decreased due to remineralisation to (-3±5) mmol m^{-2} d^{-1}, and $N(O_2)$ to (0±2) mmol m^{-2} d^{-1}. In particular, the $N(O_2)$ changes were driven by the surface oxygen supersaturation making the seawater a source of oxygen. In contrast, the ocean was a sink of inorganic carbon during the summer, with a continuous CO_2 flux from the atmosphere into the water.

This deployment shows the potential of using small, low energy consuming CO_2 optodes on autonomous observing platforms like gliders to quantify the interactions between biogeochemical processes and the marine carbonate system at high spatiotemporal resolution.

Chapter 3

An evaluation of potentiometric and spectrophotometric pH sensors

3.1 Summary

The performance of two glass electrodes developed by AMT and Fluidion and the lab-on-chip (LoC) spectrophotometric sensor developed by the National Oceanography Centre (NOC) in Southampton, United Kingdom were assessed in a series of experiments. These experiments were performed using buffers made in synthetic seawater (Tris, AMP) and seawater.

The main source of error for the two glass electrodes was the reconditioning when placed directly in seawater from the 3 M KCl storage solution. The sensors were stored in 3 M KCl because this was suggested by the manufacturer. The magnitude of the reconditioning error was assessed during a 4 days experiment placing the two glass electrodes directly in seawater. During the 4 days, the two sensors were unable to measure the expected pH changes and had a continuous negative drift that decreased over time. Over the first day, the AMT sensor had a drift of 0.018 h^{-1} and the Fluidion of 0.013 h^{-1} that decreased on the last day to 0.0007 h^{-1} for AMT and 0.0003 h^{-1} for Fluidion. The results show that the sensor performance would improve storing the glass electrodes in seawater for several weeks before deploying in seawater. The effect of temperature and salinity was smaller than the drift for the two glass electrodes. However, when the temperature was changed the two glass electrodes were unable to capture the full pH change and the offset from the true pH increased with temperature. The effect of salinity was considered negligible but might be important in estuarine environments where salinity changes are larger than 10.

The NOC sensor's performance was not affected by temperature and salinity. It had an accuracy between 0.002 and 0.006 in Tris and 0.005 in seawater. After assessing the pH-indicator dye dependence on temperature, pressure and ionic strength the spectrophotometric method is potentially calibration-free and is not affected by drift. However, before the deployment it is important to calibrate the internal temperature sensors to have an accurate measurement. For that reason, it was used as reference to in situ calibrate the two glass electrodes. The calibration of the two glass electrodes

improved the AMT accuracy with respect to the NOC sensor from 0.069 to 0.002 and from 0.052 to 0.003 for Fluidion. This combination of LoC sensor and glass electrodes could be used for long and short deployments on gliders, floats, moorings and other autonomous systems. The two sensors together give high temporal resolution (1 s) of the glass electrode and the accuracy (< 0.002) of the LoC sensor for long deployments (1 year).

3.2 Introduction

Historically seawater pH was measured using glass electrodes and the measured pH was used to constrain the carbonate system and quantify the trends in ocean acidification (OA) (McLaughlin et al., 2015). These instruments were deployed for decades in coastal regulatory monitoring and research programs, providing some of the most abundant data to describe and quantify OA (McLaughlin et al., 2015). Measurements of pH with glass electrodes are affected by various and systematic effects (Buck et al., 2001). For example, the sensor may not show a Nernstian response because it varies with time having a memory of the previous solution sampled. The response of glass electrodes vary with temperature and it needs to be measured along with pH. Also, the liquid junction potential varies depending on its composition and the geometry of the liquid junction device. Stirring can also affect the sensor measurements and the liquid junction can be clogged limiting the response time and accuracy of the glass electrode. The magnitude of these errors are in general unknown and they need be assessed in further studies (Buck et al., 2001). The comparison between pH measured by different glass electrodes is often challenging. Each sensor has an individual response time to pH changes given by an individual device-dependent liquid junction potential (Buck and Lindner, 1994). This different response time between sensors is caused by different composition of the solution forming the liquid junction and the geometry of the liquid junction device (Naumann et al., 2002). The size of this error cannot be quantified because the liquid junction potential cannot be measured individually, this makes any correction for this effect challenging. Also, the accuracy and the response time of the glass electrodes depend on how often the sensor is used, the age of the probe and carry-over effects from the last solutions measured (Buck et al., 2001). When the glass electrode is transferred between two different solutions the liquid junction requires time to recondition. In the first days the glass electrode's reading remain biased by the composition of the last solution it has been exposed to. The reconditioning time depends on the composition differences between the new and the old solutions and the composition of the liquid

junction. During this reconditioning period, the sensor's pores can be temporarily clogged increasing the electrical resistance of the junction and the pH readings may drift and become noisy (Buck et al., 2001). Fouling can make the sensor unusable blocking the junction or breaking the electrical connection between the electrode and the sample. Clogging can come from two sources: suspended solids in the sample or the solids resulting from a chemical reaction involving the electrolyte filling solution (Kadis and Leito, 2010). A possible solution is to make the junction pores small enough that particles cannot get into the pores but then the material accumulates on the surfaces. These effects can cause an irreversible damage on the glass electrode that needs to be replaced.

Temperature changes can affect the glass electrodes performance, mainly caused by the temperature dependencies of the potential of the glass and reference electrodes (Naumann et al., 2002). Specifically a glass electrode needs to have a series of temperature characteristics: the sensor should respond at different temperatures to pH changes following a Nernst slope factor ($k = (RT/F)\ln 10$, see Eq 1.4), the standard potential should vary linearly with temperature, the electromotive force (EMF) needs to be independent of temperature at pH 7, EMF should be 0 when pH is 7, the cell should have a low thermal capacity, the system should have a monotonic response to temperature changes and should not exhibit thermal hysteresis (Midgley, 1990). The main source of non-linearity in pH measurements at different temperatures is given by the response of liquid junction.

Despite the long usage, a lot is unknown about the performance and maintenance of glass electrodes. New experiments need to be performed to better identify and quantify the temperature effect on the glass electrodes performance (Buck et al., 2001). These experiments need to be designed to identify a univocal method to correct the temperature effect and design a sensor to minimise this source of error (Naumann et al., 2002). Also, other experiments are needed to find the best storage solution to minimise the reconditioning time at the beginning of a new deployment.

In this chapter, I assess the performance and best practices to run in situ pH sensors as automated systems. A series of experiments were performed using two commercially available potentiometric sensors developed by Fluidion and AMT Analysenmesstechnik GmbH and the lab-on-a-chip (LoC) spectrophotometric sensor developed by the National Oceanography Centre (NOC) in Southampton, United Kingdom (Rérolle et al., 2013). The sensor performance was assessed for response time, storage solution effects, temperature and salinity in seawater and equimolar Tris (2-amino-2-hydroxymethyl-propane-1,3-diol) and AMP (2-aminopyridine) buffers made in synthetic seawater with a

known pH (Dickson et al., 2007). Based on the experiments, a methodology was developed to in situ-calibrate the glass electrodes using the NOC sensor as a reference.

3.3 Materials and methods

3.3.1 Sensor description

AMT sensor

According to the manufacturer manual the AMT sensor is a glass electrode developed for in situ pH determination in natural waters like oceans, estuaries and rivers. The sensor is composed of a pressure-balanced glass electrode and a reference electrode (Ag/AgCl) in a plastic rod. The presence of a ceramic diaphragm containing a high number of pores allows a quick equilibration with the external solution. To make the sensor H_2S resistant, the electrolyte is a KCl gel without silver ions. The sensor body is protected by a titanium housing rated to 1200 m.

The raw output has an analogue range of 0 to 5 V DC and can measure pH from 0 to 14. The sensor has a small body with a diameter of 3.7 cm and a length of 24 cm. It has a low power requirement of 13 mA (at 10 V) and the potential to run autonomously using an alkaline or lithium size C battery. AMT suggests an accuracy of 0.05 and a resolution of 0.003 with a response time ($t_{63\ \%}$) of 1 s. To correct the pH for temperature (θ), the sensor is equipped with a Pt100 temperature probe from Thermal Developments International (TDI).

To calibrate the sensor, the raw readings (u) are linearly fitted with the solution pH (AMT Analysenmesstechnik GmbH, 2014):

$$u = a_1\,(\mathrm{pH} - 7) + a_0 \qquad (3.1)$$

where a_1 is the slope and a_0 is the intercept of the calibration fitting.

The manufacturer suggests shifting the calibrated pH to 20 °C using an approximation of the Nernst equation. First, a temperature correction factor is calculated:

$$f(\theta) = A_0 + A_1\theta + A_2\theta^2 \qquad (3.2)$$

where θ is in degrees Celsius and A_0 is 1.0732, A_1 is -3.9093×10^{-3} and A_2 is 1.2333×10^{-5}. These corrections factors are applied to calculate the calibration slope at 20 °C:

$$a_1(20\ ^\circ\mathrm{C}) = a_1(\theta)\, f(\theta). \qquad (3.3)$$

The temperature-corrected pH is calculated using a modified version of the Nernst equation:

$$\mathrm{pH_{AMT}} = \frac{f(\theta)(u - a_0)}{a_{1(20\,^{\circ}\mathrm{C})}} + 7. \qquad (3.4)$$

However, this algorithm is just an approximation of the Nernst equation and for that reason, to define the sample (X) pH we used the actual Nernst equation:

$$\mathrm{pH(X)} = \mathrm{pH(S)} + \frac{E_S - E_X}{RT\ln 10/F} \qquad (3.5)$$

where S is a standard buffer of known pH, *E* is the EMF, *R* is the gas constant, *T* is the temperature in kelvin and *F* is the Faraday constant. At a standard measurement temperature of 298.15 K, the magnitude of *RT* ln10/*F* is 59.16 mV. Using the Nernst equation the sensor temperature correction is the following:

$$\mathrm{pH_{Tc}} = (\mathrm{pH(X)} - 7)\frac{273.15 + \theta_{\mathrm{cal}}/^{\circ}\mathrm{C}}{273.15 + \theta/^{\circ}\mathrm{C}} + 7 \qquad (3.6)$$

where θ_{cal} is 20 °C and θ is the temperature of the sample. The term $f(\theta)$ corresponds to an approximation of the fraction in Eq. (3.5).

Fluidion sensor

The deep-water Fluidion pH sensor is a glass electrode that uses the same probe as the AMT sensor, but different electronics. The sensor to derive pH applies the same equations of the AMT sensor (Eq. 3.1, 3.2, 3.3, 3.4 and 3.5). The sensor was specifically designed for ocean studies using CTD rosettes and autonomous platforms such as floats, gliders and profilers. It is composed of a small and light Delrin (acetal polymer) body with a length of 33 cm and a diameter of 3.1 cm. It weighs 450 g in air and 145 g in water and has a fast (1 Hz) sampling rate, making it suitable for resolving short-scale processes on autonomous vehicles such as gliders. The sensor has a power consumption of 25 mA (at 10 V) during measurement and its oil-filled body is rated to 2000 meters.

Spectrophotometric lab-on-chip sensor

The spectrophotometric sensor was developed by the Ocean Technology and Engineering Group (OTE) of the National Oceanography Centre (NOC) in Southampton, United Kingdom. The pH sensor is based on lab-on-a-chip technology employing a spectrophotometric method using purified meta-cresol purple (*m*CP) as an indicator dye. The sensor includes a long serpentine mixer channel, a built-in optical detector that includes a two-wavelength LED/photosystem and a temperature sensor. These two wavelengths are at 435 and 596 nm close to the absorption maxima of the two charged

*m*CP forms (HI^- and I^{2-}). Absorption measurements at both wavelengths are used to calculate the sample pH taking into account the indicator pH perturbation. The advantage of the microfluidic design is the miniaturised size, the low power consumption (3 W while measuring) and small sample (550 µL) and indicator (2.2 µL) use per measurement. The sample and the indicator are pumped into the sensor by a syringe pump and controlled using solenoid valves. To avoid carryover between measurements, the new sample is flushed through the whole system three times before a measurement is made. The sensor makes a measurement every 10 minutes allowing 6 measurements per hour.

The raw measurement is converted to pH using the following equation:

$$\mathrm{pH_T(NOC)} = -\log_{10}\left(K_2^{\mathrm{T}}\mathrm{e}_2\right) + \log_{10}\left(\frac{R - e_1}{1 - R\frac{e_3}{e_2}}\right) \qquad (3.7)$$

where K_2^{T} is the dissociation constant of HI^- on the total hydrogen scale (Clayton and Bane, 1993),

$$K_2^{\mathrm{T}} = \frac{[\mathrm{I}^{2-}][\mathrm{H}^+]_{\mathrm{T}}[\mathrm{HI}^-]^{-1}}{1\ \mathrm{mol\ kg^{-1}}} \qquad (3.8)$$

where the concentrations are expressed in mol kg^{-1} of solution. *R* in Eq. (3.7) is given by the absorbances at the two wavelengths 435 and 596 nm (λ_1 and λ_2):

$$R = \frac{\mathrm{A}(\lambda_2)}{\mathrm{A}(\lambda_1)} \qquad (3.9)$$

In Eq. (3.7) e_1, e_2 and e_3 are the ratios of molar absorptivities of the HI^- and I^{2-} indicator forms:

$$e_1 = \frac{\varepsilon_{\mathrm{HI}}(\lambda_2)}{\varepsilon_{\mathrm{HI}}(\lambda_1)},\ e_2 = \frac{\varepsilon_{\mathrm{I}}(\lambda_2)}{\varepsilon_{\mathrm{HI}}(\lambda_1)},\ e_3 = \frac{\varepsilon_{\mathrm{I}}(\lambda_1)}{\varepsilon_{\mathrm{HI}}(\lambda_1)} \qquad (3.10)$$

where $\varepsilon_1(\lambda)$ is the molar absorptivity of I^{2-} at wavelength λ and $\varepsilon_{\mathrm{HI}}(\lambda)$ is the molar absorptivity of HI^- at wavelength λ. Knowing the temperature and the salinity of the sample these parameters can be calculated following Liu et al. (2011a):

$$-\log_{10}\left(K_2^{\mathrm{T}}\mathrm{e}_2\right) = a + \left(\frac{b}{T/\mathrm{K}}\right) + c\,\log_{\mathrm{e}} T/\mathrm{K} - \mathrm{d}T/K. \qquad (3.11)$$

Where using the practical salinity (*S*):

$$a = -246.64209 + 0.315971S + 2.8855 \times 10^{-4}S^2 \qquad (3.12)$$

$$b = 7229.23864 - 7.098137S - 0.057034S^2 \qquad (3.13)$$

$$c = 44.493382 - 0.052711S \qquad (3.14)$$

$$d = 0.0781344 \qquad (3.15)$$

The molar absorbance ratios are given by:

$$e_1 = -0.007762 + 4.5174 \times 10^{-5}\theta \; ; \; {}^{e_3}/_{e_2} = -0.020813 + 2.60262 \times 10^{-4}\theta + 1.0436 \times 10^{-4}(S - 35). \qquad (3.16)$$

The sensor needs to be deployed with an independent measurement of the seawater temperature because the sensor measures the pH at its internal temperature. To correct the pH to the environmental in situ temperature a factor of – 0.01582 °C^{-1} is applied (Millero, 2007):

$$pH_c(NOC) = pH(NOC) - 0.01582\ ºC^{-1}\ \Delta\theta \qquad (3.17)$$

where $\Delta\theta$ is the difference between the environmental temperature and the NOC internal temperature (θ(NOC)) and pH(NOC) is the pH measured at θ(NOC).

3.3.2 Temperature probe calibration

The Fluidion, NOC and AMT readings are strongly influenced by temperature (Dickson et al., 2007). For that reason, it is crucial to calibrate the temperature sensor. Before the experiments I calibrated the Pt100 in the AMT and Fluidion sensors. The Pt100 sensing element is a platinum resistor with a nominal 100 Ω resistance at 0 ˚C and has a response time of 0.2 s. The internal NOC sensor thermistors were calibrated by OTE engineers in Southampton.

The calibration was carried out at 11 different temperatures from 0.50 ˚C to 35.00 ˚C in an open water bath filled with deionised water (MilliQ) where the Fluidion and AMT sensors were fully immersed. The temperature values were: 0.5, 4.0, 7.5, 11.0, 14.5, 18.0, 21.5, 25.0, 28.5, 32.0 and 35.0 ˚C. The temperature was changed every 20 minutes and a mercury thermometer was used as a reference. I used the mean temperature measured in the final 5 minutes of the 20 minute-interval when the water bath temperature had been constant for at least 10 min.

The mercury thermometer had a scale of 0.1 ˚C and could cover a temperature range from 0.5 ˚C to 40.5 ˚C. It was possible to determine changes in temperature with a resolution of 0.025 ˚C by looking at the liquid column position between scale lines. The mercury thermometer was not fully immersed into the jacketed beaker because it was longer than the beaker height. For that reason, the mercury thermometer temperature (θ_{Hg}) needed to be corrected for the part of the thermometer stem in air. This stem correction was added to the mercury thermometer temperature (θ_{Hg}):

$$C_s = Kn(\theta_1 - \theta_2) \qquad (3.18)$$

where K is the differential expansion coefficient of the thermometer glass and has a value of 0.00016 °C^{-1} (Wise and Soulen Jr, 1986) n is the length of the liquid column emergent from the bath (expressed in ºC on the thermometer scale), θ_1 is the temperature measured by the mercury thermometer and θ_2 is the temperature outside the bath. The Fludion sensor thermistor placed outside the beaker measured θ_2. C_s varied from -0.15 °C at 0.7 °C to 0.04 °C at 35 °C.

The Pt100 was calibrated using a linear regression between θ_{Hg} and the Pt100 raw temperature (U_T) given by a 16-bit raw data counts (Fig. 3.1). This calibration was used to process the Pt100 raw values for all the following experiments.

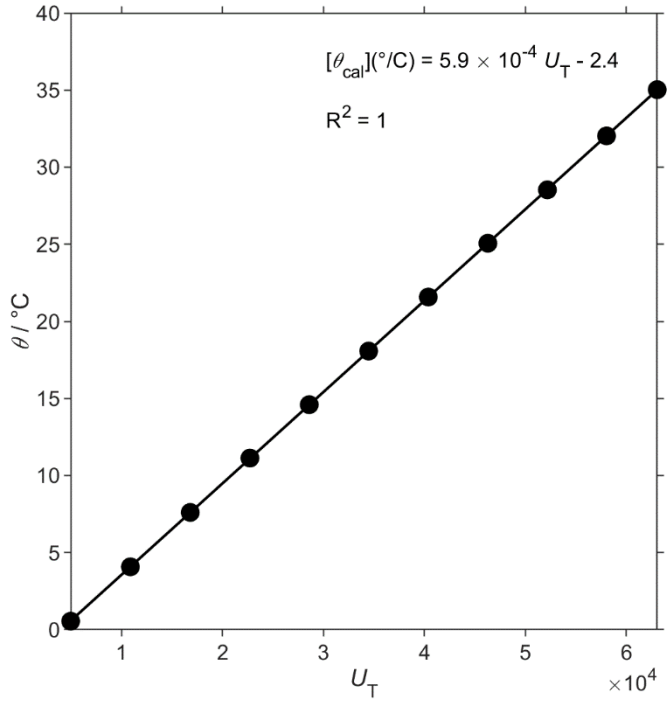

Figure 3.1: Pt100 raw temperature (U_T) calibration using a mercury thermometer (θ_{Hg}) as reference and controlling the temperature with a water bath. The Pt100 temperature needed to be corrected using equation 3.18 because the probe was not fully immersed in the solution (stem correction).

3.3.3 Tris buffer preparation and quality control

To test the performance of the three sensors, Tris/HCl (Tris) and 2-aminopyridine/HCl (AMP) buffers prepared in synthetic seawater were used. The two buffers are characterised on the total scale which includes hydrogensulfate ions (Hansson, 1973).

The Tris and AMP buffers recipes are prepared in synthetic seawater that replaces real seawater bromide, carbonate, bicarbonate and fluoride with chloride and strontium with calcium (Dickson et al., 2007). Tris and AMP buffers have a comparable salinity and ionic strength to seawater of 35 and 0.7 M, respectively. Commercial reference Tris buffers are provided by the laboratory of Professor A. Dickson from the Scripps Institution of Oceanography in San Diego CA, USA.

Following the recipe and the methods of Dickson et al. (2007) I prepared the Tris and AMP buffers. The two buffers were prepared gravimetrically using: $CaCl_2$ (499609 Aldrich), $MgCl_2$ (M8266 Aldrich), HCl (H9892 Sigma), Tris (Trizma base T4661 Sigma), 2-aminopyridine (104541000 Acros organics), KCl (P5405 Sigma), NaCl (S/31 60/60 Fisher Scientific) and Na_2SO_4 (Fisher Scientific).

Following Dickson et al. (2007) the buffer pH(Tris) can be calculated from *T* in kelvin and practical salinity *S*:

$$\mathrm{pH(Tris)} = (11911.08 - 18.2499S - 0.039336S^2)\frac{1}{T/\mathrm{K}} - 366.27059 + 0.53993607S + 0.00016329S^2 + (64.52243 - 0.084041S)\ln\left(T/\mathrm{K}\right) - 0.11149858\left(T/\mathrm{K}\right). \quad (3.19)$$

pH(AMP) (Dickson et al., 2007) is defined as:

$$\mathrm{pH(AMP)} = (111.35 + 5.44875S)\frac{1}{T/\mathrm{K}} + 41.6775 - 0.015683S - 6.20815\ln\left(T/\mathrm{K}\right) - \log_{10}(1 - 0.00106S). \quad (3.20)$$

pH_C(NOC) was used to compare the Tris buffers made at the University of East Anglia and the T30-073 Tris Batch made by Andrew Dickson group. The two buffers were compared using 4 different experiments performed on 14 and 16 November 2018 using the homemade Tris and 27 and 28 November 2018 using Dickson's Tris (Table 3.1). These experiments were performed with the same design used to quantify the temperature effect (section 3.3.4) and the temperature was varied from 25 to 31 °C in 3 °C steps.

Table 3.1: List of experiments performed to assess the performance of the three sensors in seawater, homemade and Dickson's Tris. The experiments were performed increasing and decreasing temperature by $\Delta\theta$ between θ_{max} and θ_{min}. The seawater pH was only affected by temperature changes because it was not in contact with the atmosphere. The Tris buffer was prepared following the recipe of Dickson et al. (2007).

Date	Solution	θ_{min} (°C)	θ_{max} (°C)	$\Delta\theta$ (°C)
14/11/18	Homemade Tris	25	31	3, then –3
16/11/18	Homemade Tris	25	31	3, then –3
19/11/18	Homemade Tris	10	20	5, then –5
21/11/18	Homemade Tris	10	20	5, then –5
27/11/18	Dickson's Tris	28	31	3, then –3
28/11/18	Dickson's Tris	25	31	3, then –3
16/01/19	Homemade Tris	25	31	3, then –3
17/01/19	Homemade Tris	25	31	3, then –3
21/01/19	Homemade Tris	5	15	5, then –5
22/01/19	Homemade Tris	5	15	5, then –5
25/01/19	Seawater	25	31	3, then –3
13/05/19	Seawater	25	31	3, then –3
15/05/19	Seawater	25	31	3, then –3
16/05/19	Seawater	6	12	3, then –3

3.3.4 Temperature effect

The temperature effect on the pH readings of the three sensors was quantified using Tris and seawater collected in February 2009 at Rothera Antarctic Research station. The effect of air-water exchange on the seawater pH was considered negligible because the jacketed beaker was closed with a lid and the sample measured by the NOC sensor was in a closed plastic bag.

The two glass electrodes were placed into a jacketed beaker connected to a water bath filled with deionised water into which the NOC sensor was immersed (Figure 3.2). The water bath temperature was controlled to within 0.1 °C to keep the three sensors at the same temperature. The beaker was gently and continuously stirred to equilibrate the pH and the temperature in the beaker was measured by the Pt100 probe of the AMT sensor.

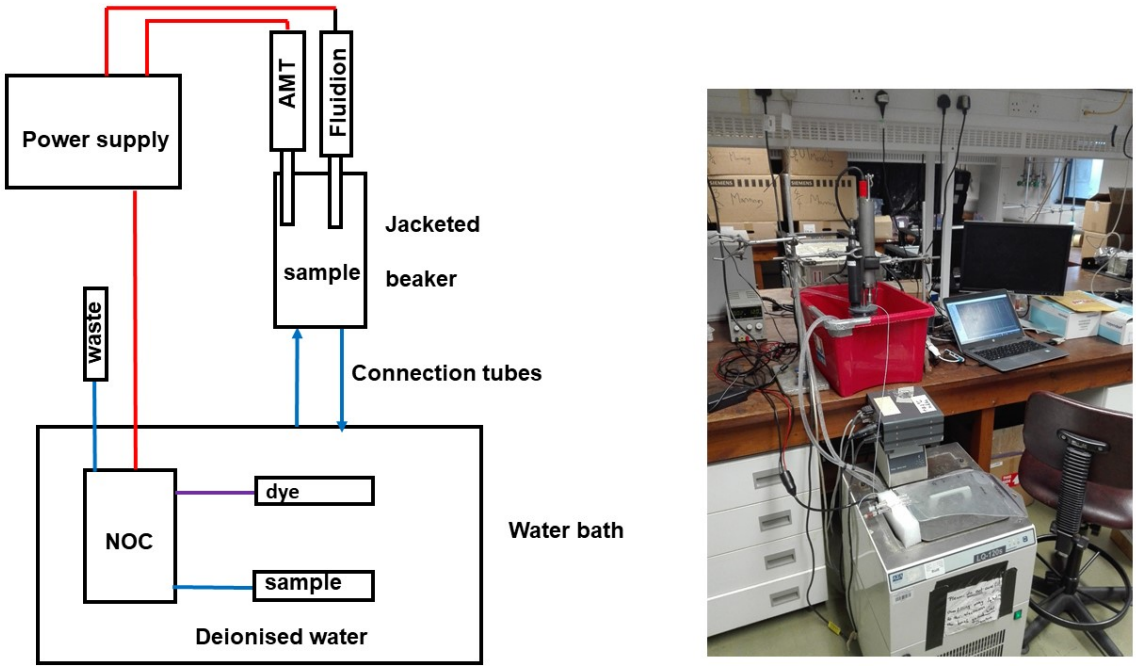

Figure 3.2: Schematic of the experiment to quantify the accuracy and temperature effect on the AMT and Fluidion glass electrodes and the NOC spectrophotometric pH sensor. The red lines represent the electric connections, the blue lines the water connections and the violet line the *m*CP indicator dye supply.

The jacketed beaker and the NOC sensor sampling bag contained the same sample (Tris or seawater). A series of 14 experiments were performed (Table 3.1) decreasing and increasing temperatures from 5 to 31 °C, changing every hour by 3 or 5 °C. Before the experiments, the two glass electrodes were stored in a 3 M KCl storage solution. Using the AMT θ_{Pt100}, pH(NOC) was corrected from the sensor internal temperature to sample temperature.

For the Tris experiments, the temperature effect was quantified as the deviation from the expected pH(Tris) value at each temperature (Eq. 3.19). In the case of seawater, pH(NOC) was used as a reference to quantify the glass electrodes offset from the solution pH.

I used the pH measured in the last 10 minutes of each temperature level when it was no longer affected by temperature changes and I calculated the mean offset as:

$$\Delta pH = pH(sensor) - pH(Tris) \qquad (3.21)$$

where pH(sensor) is the pH measured by the NOC, Fluidion and AMT sensor.

3.3.5 Response time

The response time (τ) needed to measure the complete pH change was calculated by immersing the two glass electrodes in a jacketed beaker filled with AMP buffer. Every 10 minutes the sample pH was decreased adding a drop of 1 M HCl with a plastic pipette (Figure 3.3). Also, to assess the temperature effect on τ the beaker temperature was varied every 30 minutes by 5 °C from 0.5 to 30 °C.

τ was calculated using the glass electrode pH measured every second with the following equation:

$$K_R = \frac{-\ln\frac{pH_1 - pH_\infty}{pH_n - pH_\infty}}{t_1 - t_n} \qquad (3.22)$$

where pH_1 is the initial pH, pH_n is the pH after five seconds, pH_∞ is the pH mean between 200 and 300 s after HCl addition, t_1 and t_n are the initial and the time after five seconds. The final τ was calculated as the median of the inverse of K_R measured in the first 10 s after the acid drop. The outliers were eliminated looking at the difference between the previous τ.

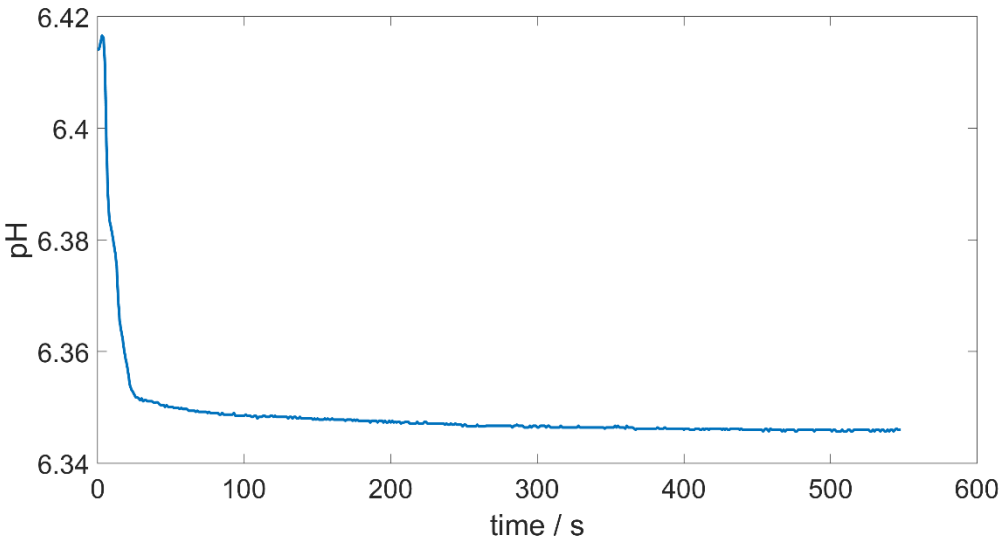

Figure 3.3: Example of the pH measured by the AMT sensor with a logarithmic shape after the acid drop addition.

3.3.6 Sensor performance in seawater

The three sensors were tested in seawater during three consecutive experiments over four days (one day break between the first and second experiments). For the first two experiments, the temperature varied from 25 to 31 °C; for the third experiment, it varied from 5 to 11 °C. To assess the benefit of storing the sensors in seawater, the two glass electrodes were kept in seawater throughout the four days.

3.3.7 Calibration method

I investigated whether pH(NOC) could be used as a reference to calibrate and correct the drift of the two glass electrodes.

Firstly, to eliminate outliers, I calculated a 600 s-long moving median and standard deviation for the glass electrode pH and removed values outside 3 standard deviations from the median. After that, I calculated a 10 s-long moving mean of the glass electrode pH. The pH(NOC) outliers were identified and removed when the sampled pH was smaller than 7 because affected by the presence of bubbles in the system and outside 3 standard deviations from the moving median calculated every 10 samples (2 hours). Afterwards, pH(NOC) and the glass electrode pH were matched in time. I calculated the difference between the glass electrode pH values and pH(NOC). To calibrate the glass electrodes in between these 10 minutes, the pH difference was linearly interpolated between the two NOC samples. Then, the offset was added to the glass electrode pH values.

The calibration method was tested using data collected in Southampton Dock by AMT and NOC sensors and during a series of laboratory experiments. The AMT sensor was deployed in Southampton Dock on 17 February 2017. A CTD (Sea-Bird microcat SBE37) was added to the deployment on 20 February. The NOC sensor was added on 21 February. During the deployment, I collected 6 discrete samples to measure pH in the laboratory using a benchtop spectrophotometer with *m*CP as indicator dye (Dickson et al., 2007). To calculate the uncertainty of the discrete samples, I took three replicates per sample.

3.4 Results

3.4.1 Equimolar Tris buffer quality control

The difference between the pH measured by the NOC sensor and that expected for Tris buffer (ΔpH, Eq. 3.21) was –0.009±0.002 for the Dickson Tris buffer and –0.010±0.02 for homemade Tris (Figure 3.4). The small difference between the two buffers is within the 0.006 uncertainty in the preparation of the Tris buffer (Paulsen and Dickson, 2020). The difference to the Dickson buffer was considered acceptable, and to save on the more expensive Dickson buffer, the homemade buffer was used in subsequent experiments.

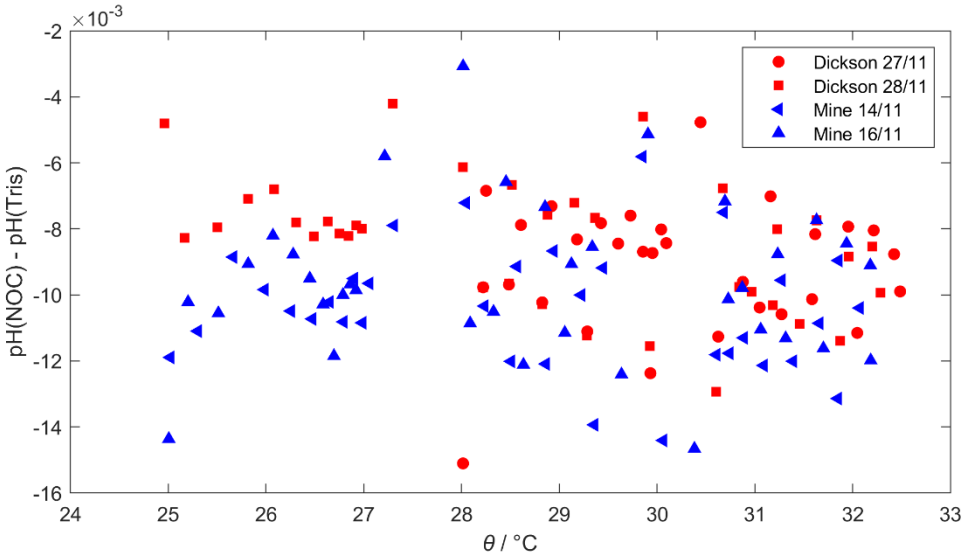

Figure 3.4: Difference pH(NOC) and pH(Tris) made by Dickson (red) and homemade (blue). The solution pH was always lower than pH(Tris) in all the experiments. The red circle represents the 27 November, the red cube the 28 November, the left pointed triangles the 14 November and the normal triangle the 16 November.

3.4.2 Temperature effect on pH measurements

When transferred from 3 M KCl to Tris buffer, all three sensors needed at least one hour to stabilise.

For the first experiment, temperature was varied from 5 to 15 °C in 5 °C steps (Figure 3.5a). pH_{Tc}(AMT) had a standard deviation of 0.009 in the first hour, which decreased to 0.003 afterwards. The standard deviation of pH_{Tc}(Fluidion) at the different temperature values varied between 0.002 and 0.004. pH(NOC) had a standard deviation of 0.005.

For the second experiment, temperature was varied from 10 to 20 °C in 5 °C steps (Figure 3.5b). pH_{Tc}(AMT) had a standard deviation of 0.017 in the first two hours that varied between 0.003 and 0.001 for the rest of the experiment. In the first hour, pH_{Tc}(Fluidion) decreased from 8.704 to 8.500 and had a standard deviation of 0.049. This decreased to 0.003 in the third hour. pH(NOC) had a standard deviation of 0.003.

For the last experiment, temperature was varied from 25 to 31 °C in 3 °C steps (Figure 3.5c). pH_{Tc}(AMT) did not show an initial adaption period and had a standard deviation between 0.004 and 0.003. The first hour pH_{Tc}(Fluidion) decreased from 8.706 to 8.320 and had a standard of 0.017 that varied between 0.004 and 0.001 for the rest of the experiment. pH(NOC) had again a standard deviation of 0.003.

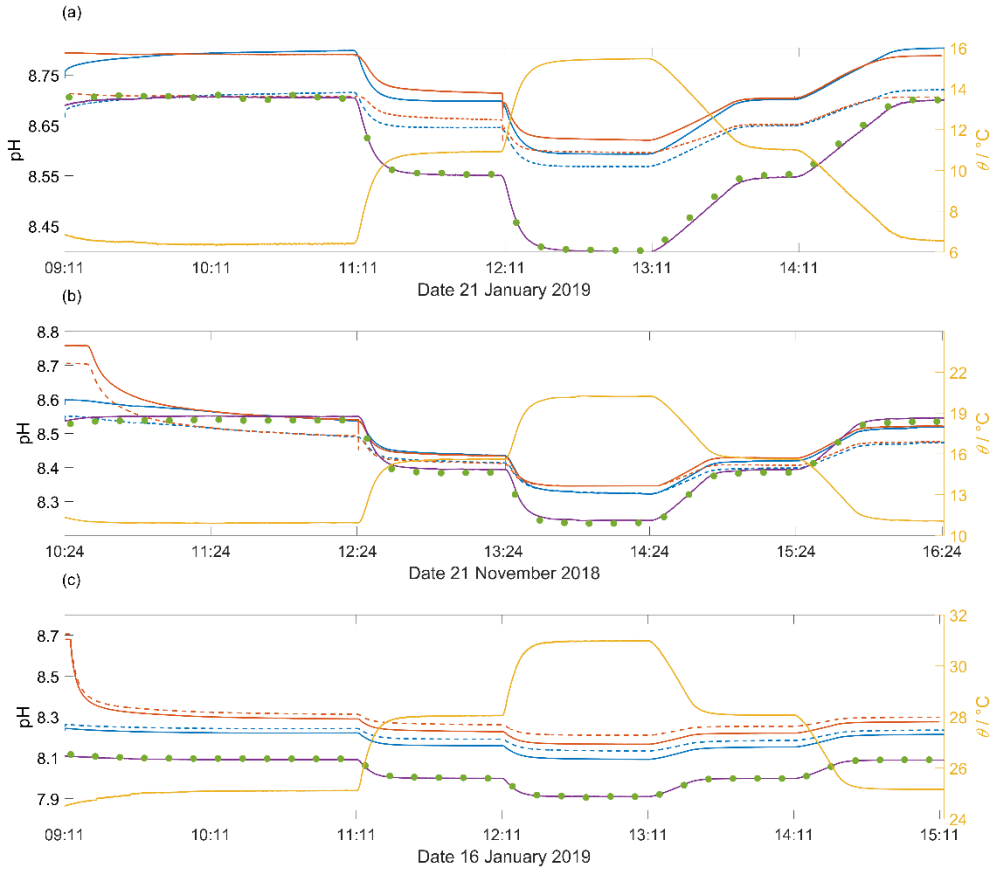

Figure 3.5: Three 6-hour experiments performed to quantify the temperature effect on three sensors a) from 5 to 15 °C; 21 January 2019, b) from 10 to 20 °C; 21 November 2018 and c) from 25 to 31 °C; 16 January 2019. pH(AMT) (blue dotted), pH_{Tc}(AMT) (blue continuous), pH(Fluidion) (red dotted), pH_{Tc}(Fluidion) (red continuous) had a large offset from pH(Tris) (violet) but pH(NOC) (green) was able to capture the pH changes driven by temperature (yellow).

These results show that the most stable and accurate among the three sensors was the NOC sensor. However, after an equilibration time of at least 1 hour, the glass electrodes showed similar or better precision than the NOC sensor.

Next, I evaluated the offset between the expected pH(Tris) and measured pH (ΔpH, Eq. 3.21) and how this is affected by temperature in the range from 5 to 31 ºC (Figure 3.6).

Among the three sensors, the NOC had the smallest offset (minimum and maximum offsets of -0.008 and 0.004). Calculating the median ΔpH value for all experiments at a

given temperature, ΔpH had its minimum at 15 °C with -0.008±0.007 and its maximum at 25 °C with 0.004±0.001.

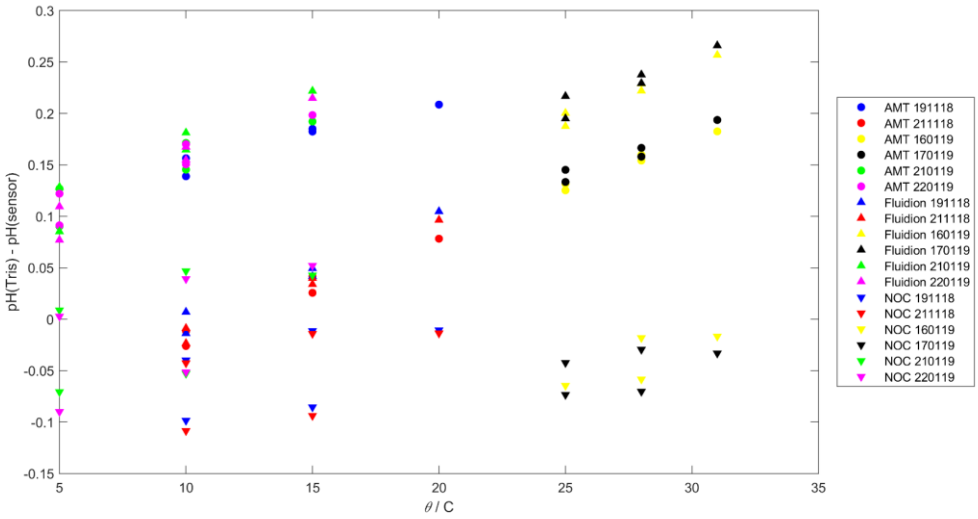

Figure 3.6: Average offset (ΔpH, Eq. 3.21) of pH(AMT) (circles), pH(Fluidion) (upward triangles) pH(NOC) (downward triangle) from pH(Tris) per temperature level using data from experiments on 19 (blue) & 21 (red) November 2018, 16 (yellow) & 17 January (black) 2019 and 21 (green) & 22 (pink) January 2019.

The two glass electrodes showed mostly positive ΔpH values, which did however vary between experiments at the same temperature. For example, at 15 °C, ΔpH(AMT) varied from 0.026 on 21 November 2018 to 0.199 on 22 January 2019 and ΔpH(Fluidion) varied from 0.034 on 21 November 2018 to 0.222 on 21 January 2019. For a given temperature, ΔpH(AMT) was 0.184±0.081 at 15 ºC, which decreased to 0.132±0.008 at 25 °C. At 31 °C, ΔpH(AMT) increased again to 0.189±0.008. ΔpH(Fluidion) decreased from 0.082±0.007 at 5 ºC to 0.046±0.092 at 15 °C, but then increased to 0.261±0.007 at 31 °C (Figure 3.6). The two glass electrodes had their maximum offsets at 31 °C and their offset varied in the opposite direction from 5 to 15 °C. The different glass electrodes offsets in different experiments was caused by the drift during storage and the experiments. However, the general trend was the same suggesting an increase of ΔpH with temperature. These series of experiments show that the response of the glass electrodes was not sufficiently accurate to capture the full pH changes and that the offset was variable between experiments.

The two glass electrodes had a larger offset than the NOC sensor because they were not calibrated before the experiments. However, the two glass electrodes were able to

capture the pH changes and the deviation from the expected pH was reduced at higher temperatures with the lowest standard deviation between 25 and 31 °C.

3.4.3 Sensor performance in seawater

The adaptation of the two glass electrodes to bromide causes shifts in the AgCl reference potential that drove continuous negative drift during and between experiments on subsequent days (Johnson et al., 2016). During the first experiment (Figure 3.7a), pH_{Tc}(AMT) decreased from 8.126 to 8.105 and pH_{Tc}(Fluidion) from 7.936 and 7.923 for the same initial and final temperature of 25 ºC.

The initial pH_{Tc}(AMT) was 8.127. It decreased to 7.449 and 7.399 at the beginning of the second (Figure 3.7b) and third experiment (Figure 3.7c). The initial drift in the third experiment appeared to be lower because the initial temperature was 6 °C instead of 25 °C, causing an increase of seawater pH by 0.301. During the third experiment, the drift decreased to 0.0007 h^{-1} (0.017 d^{-1}) caused by a decrease of pH_{Tc}(AMT) to 7.392. Most importantly, even when temperature was constant pH_{Tc}(AMT) was not stable, especially during the second and third experiments.

The Fluidion sensor was also affected by drift, at the beginning of the first experiment pH_{Tc}(Fluidion) was 7.936 at 25 ºC which decreased to 7.361 at the beginning of the second experiment, also at 25 ºC. In the third experiment, the difference between the initial and the final pH decreased to 0.002 with a drift of 0.0003 h^{-1} (0.008 d^{-1}). pH_{Tc}(Fluidion) was characterised by better stability than pH_{Tc}(AMT). For example, in the third experiment the standard deviation of pH_{Tc}(AMT) was 0.023 and of pH_{Tc}(Fluidion) was 0.007. The results of the third experiment show the benefit of storing the glass electrodes in seawater before deployment but the adaption time to the new solution is longer than four days.

Considering a linear temperature effect during all the experiments the two glass electrodes measured a smaller pH change than expected, –0.01582 $°C^{-1}$ (Millero, 2007). A linear or quadratic function could be used to describe the effect of temperature on pH. When the temperature change is smaller than 10 °C this effect can be considered linear. For example, in the first experiment when the temperature increased from 25 to 28 °C pH_{Tc}(AMT) decreased by -0.024 (0.008 $°C^{-1}$) and pH_{Tc}(Fluidion) by -0.011 (0.004 $°C^{-1}$). The response to pH changes caused by temperature did not improve in the following experiments. In fact, during the last experiment when the temperature was increased from 6 to 9 °C, pH_{Tc}(AMT) changed in the opposite direction increasing by 0.017 (0.006 $°C^{-1}$) and pH_{Tc}(Fluidion) decreased by -0.019 (0.006 $°C^{-1}$).

The NOC sensor was not affected by drift during the experiments and was able to capture the expected pH changes. For example, during the first experiment when temperature increased from 25 to 28 °C the pH decreased by 0.0460 (0.015 °C^{-1}) from 7.654 to 7.608.

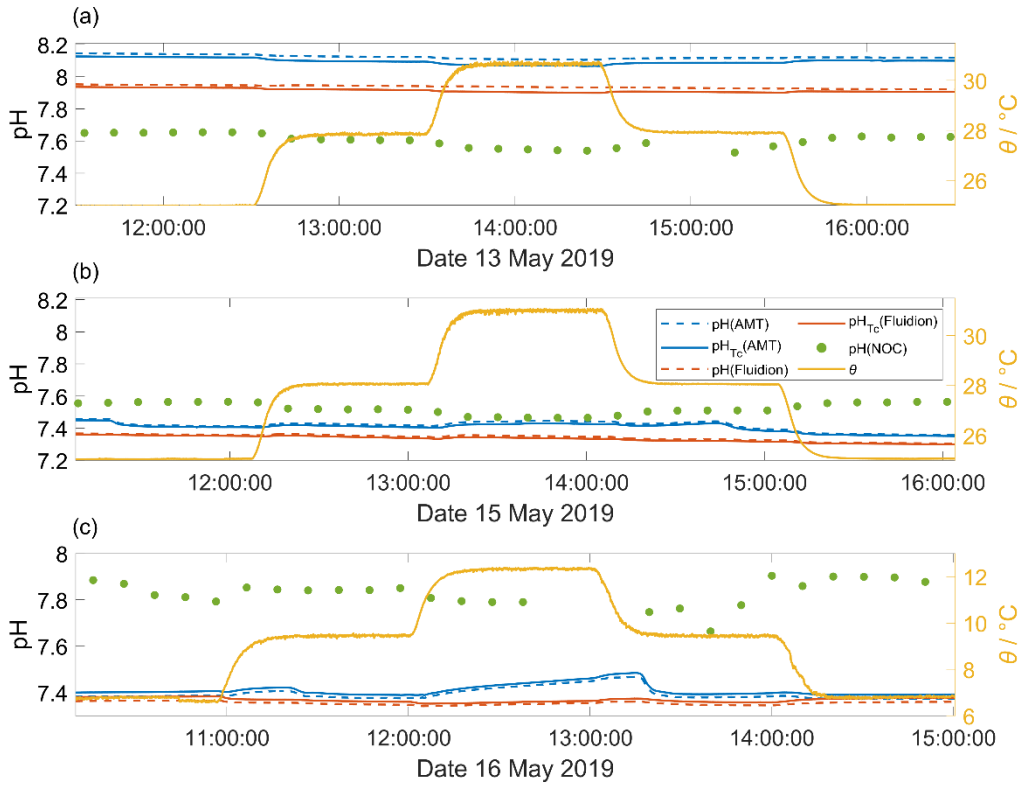

Figure 3.7: 6 hour-experiments performed in seawater collected in February 2009 at Rothera Antarctic Research station varying the temperature every hour. The figures follow the order of the experiments a) performed on the 13 May 2019 from 25 to 31 °C, b) performed on the 15 May 2019 from 25 to 31 °C and c) performed on the 16 May 2019 from 5 to 11 °C. pH(AMT) (blue dotted), pH(AMT)$_{Tc}$ (blue continuous), pH(Fluidion) (red dotted), pH(Fluidion)$_{Tc}$ (red continuous) were not able to capture the pH changes. Instead, pH(NOC) (green) captured the pH changes driven by temperature (yellow). During the third experiment, the presence of bubbles in the sampling tubes did not allow the NOC sensor to measure any samples for 1 hour around 13:00.

3.4.4 Glass electrodes response times

The methodology used to calculate the response time τ of the two glass electrodes required a pH curve with a logarithmic shape (Figure 3.3) after the 1 M HCl drop addition. Depending on the drop position, pH(AMP) changed with two different shape of curves. When the drop was placed next to the glass electrode pH(AMP) had a short and large

pH decrease, followed by a slow pH decrease. Instead, when the drop was placed away from the glass electrodes the pH curve followed a perfect logarithmic scale. I attribute this to incomplete mixing when the drop was placed next to the electrode.

The response time calculated considering all the curves was (13±14) s for AMT and (11±10) s for Fluidion. After removing the curves influenced by the pH spike reduced τ and its variability to (7±4) and (7±3) s for AMT and Fluidion, respectively.

The response time τ of the two sensors varied between 4 and 13 s for the AMT sensor and from 5 to 10 s for the Fluidion sensor (Figure 3.8). It was not affected by temperature because the smallest τ was measured at 25 °C for AMT and 0.5 °C for Fluidion, instead the largest τ was measured at 20 °C for AMT and 10 °C for Fluidion.

The response time calculated during the experiment is larger than the response time suggested by the two manufacturers (1 s) to measure the 63 % pH change. The longer response time might be caused by the time needed by the AMP buffer to be fully mixed after the acid drop. My response time estimates should therefore be considered as upper limits. Even so, these short response times make the two glass electrodes suitable to resolve small scale processes in variable environments such as the pH change in the thermocline during a glider dive.

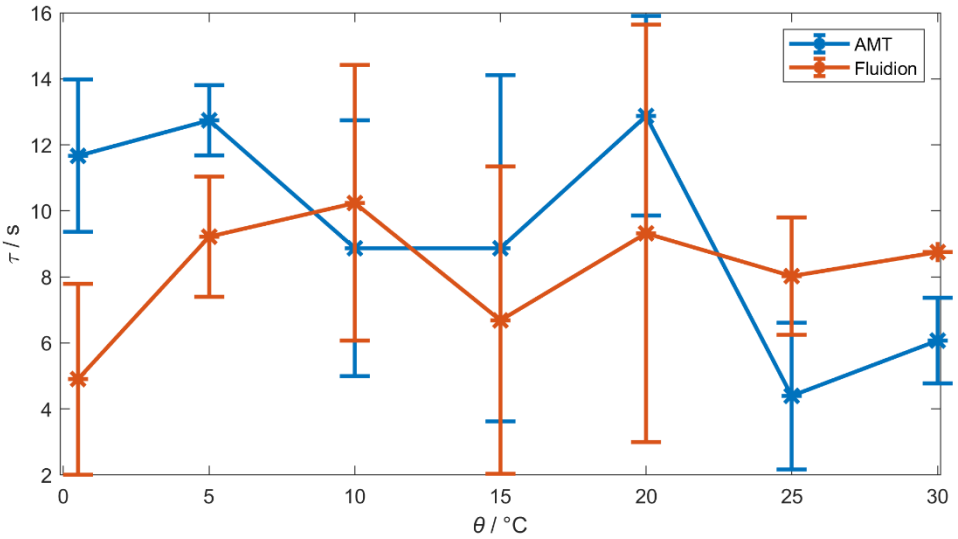

Figure 3.8: Glass electrodes response times (τ) as a function of temperature. τ was calculated using Eq. 3.22 from the time-varying pH signal after adding a drop of 1 M HCl.

3.4.5 Use of the spectrophotometric pH sensor as a reference to calibrate glass electrodes

I tested whether the NOC sensor could serve as a reference to recalibrate the two glass electrodes in Tris and in seawater. The two glass electrodes in Tris had a mean pH offset (ΔpH, Eq. 3.21) of 0.152±0.021 for AMT and 0.222±0.023 for Fluidion. The NOC sensor agreed with pH(Tris) and had ΔpH = 0.002±0.003.

After the recalibration following the procedure of section 3.3.7 the two glass electrodes had ΔpH = 0.002±0.003 (AMT) and 0.002±0.003 (Fluidion) (Figure 3.9).

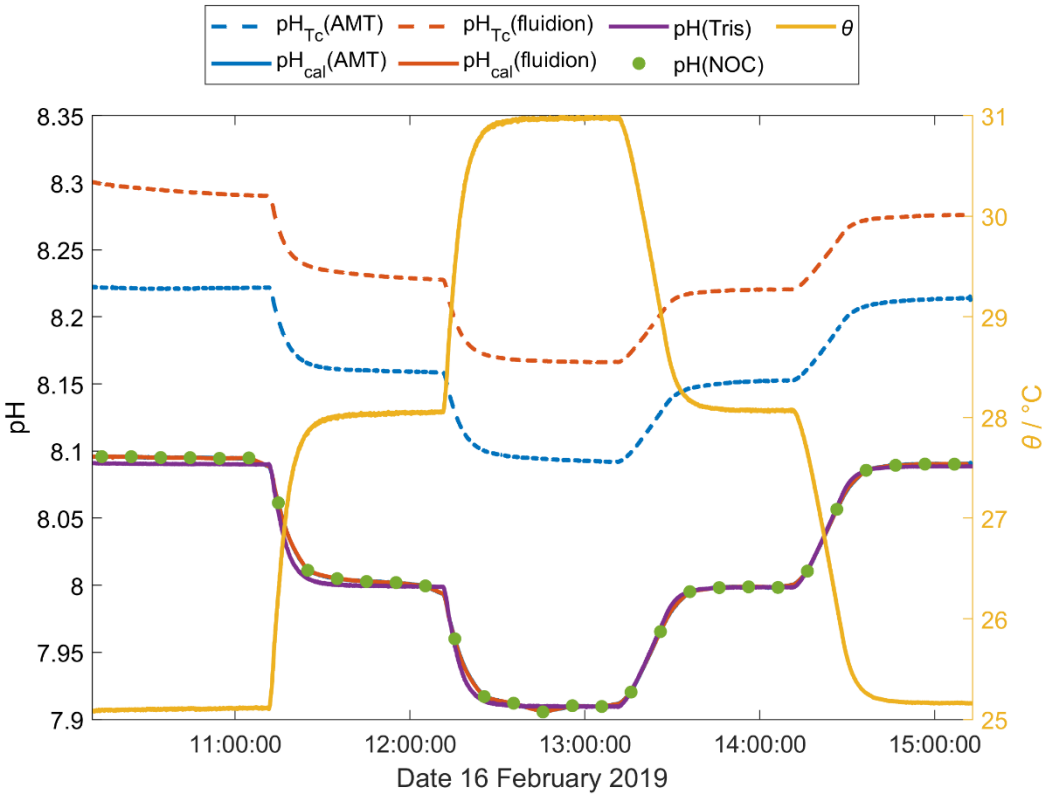

Figure 3.9: pH$_{Tc}$(AMT) (blue dotted) and pH$_{Tc}$(fludion) (red dotted) recalibration using pH(NOC) (green) as a reference. The calibrated pH(AMT) (continuous blue) and pH(Fluidion) (continuous red) agrees with pH(NOC) and pH(Tris) (violet) and responded to pH changes driven by temperature changes (yellow) in Tris the 16 February 2019.

3.4.6 Test in Southampton Dock

During the deployment in the Southampton Dock pH_{Tc}(AMT) had positive spikes up to 8.843 (Fig. 3.10), caused by the connection of the sensor to a computer to download the data. During the night of 22/23 February 2017, θ(CTD) and pH_{Tc}(AMT) showed strong variability: pH_{Tc}(AMT) varied between 8.073 and 8.113 and θ(CTD) between 7.72 to 8.56 °C (Figure 3.10a) and S(CTD) between 31.30 and 31.76 (Figure 3.10b). This variability was likely due to a storm causing an increase of wind speed from 8.8 to 14.6 m s^{-1} (ECMWF ERA InterimDaily, https://apps.ecmwf.int/datasets/data/interim-full-daily/levtype=sfc/). After the storm S(CTD) decreased to 31.30 and θ(CTD) to 7.38 °C, accompanied by a pH decrease from 7.990 to 7.968.

Before calibration, the difference between pH(NOC) and pH_{Tc}(AMT) was 0.110±0.014. The difference between discrete samples pH(WS) and pH_{Tc}(AMT) was 0.129±0.026. The NOC sensor sampled 478 times. After calibration to pH(NOC) every 10 min, the pH(AMT) bias dropped to 0.002±0.005 compared with pH(WS). The residual bias compared with pH(NOC) was <0.001.

The NOC sensor compared with pH(WS) had a mean bias of 0.003±0.005. Part of this error was caused by the uncertainty in measuring pH(WS) with the spectrophotometer. Three replicates per sample had a standard deviation between 0.0006 and 0.001.

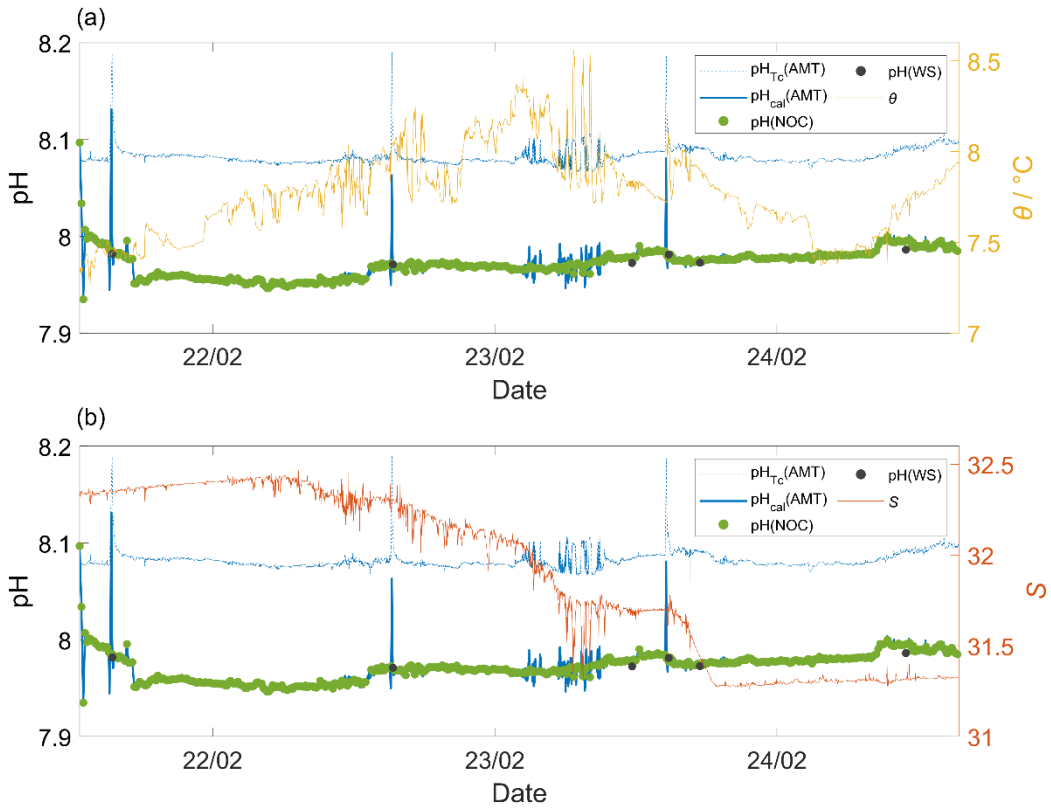

Figure 3.10: Deployment of the AMT and NOC sensor in the dock in Southampton where pH(NOC) (green) was used as reference to recalibrate pH(AMT) (dotted blue). The calibrated pH(AMT) agrees with pH(NOC), pH measured with a benchtop spectrophotometer (black) and temperature changes (yellow).

In the literature, the effect of salinity on glass electrodes is considered negligible in systems where the salinity changes are smaller than 10. McLaughlin et al. (2017) found that a salinity variation between 32 and 35 does not affect glass electrode accuracy. The effect of salinity is important in estuarine systems where the salinity effect can lead to an offset up to 0.028 (Easley and Bane, 2012). During the deployment in the Southampton dock pH_{Tc}(AMT) responded to pH changes caused by salinity (Figure 3.11a) and temperature (Figure 3.11b). On the second day, a salinity decrease from 31.70 to 31.26 coupled with a temperature increase from 7.74 to 8.11 °C (Figure 3.11b) caused an increase in the difference between pH_{Tc}(AMT) and pH(NOC) from 0.1 to 0.12. After this decrease, salinity remained constant at 31.3 and the offset decreased again to 0.1.

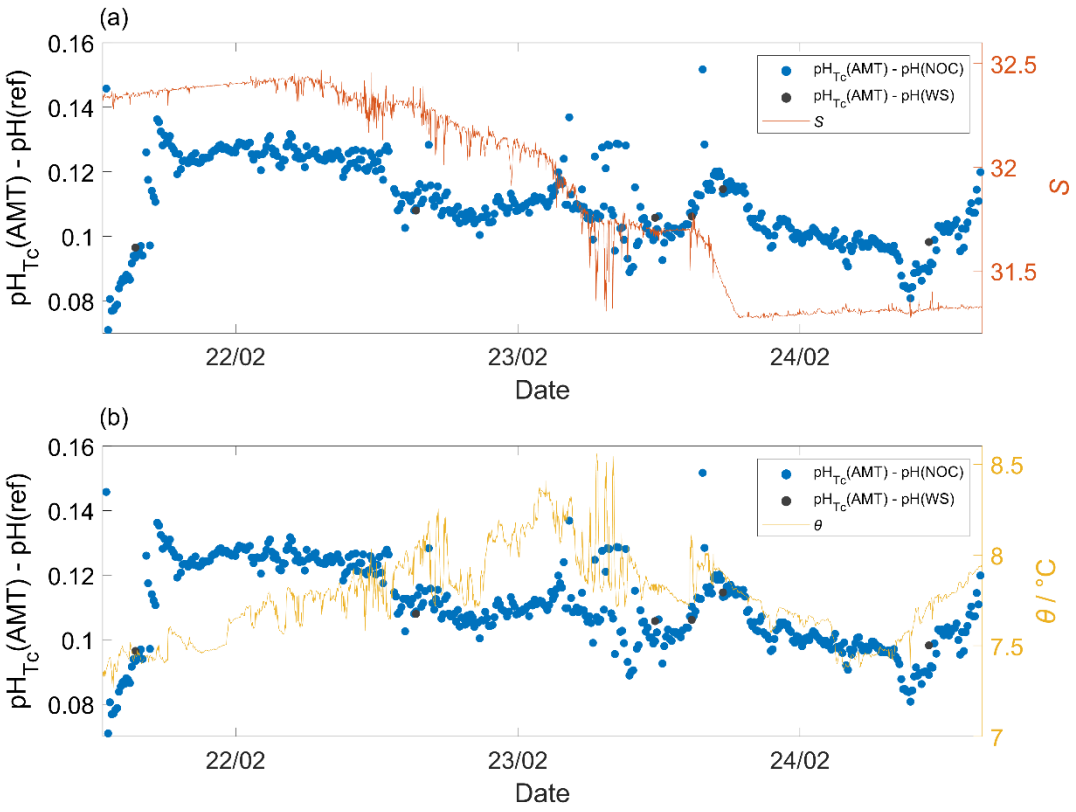

Figure 3.11: the effect of salinity *S* a) and temperature *θ* b) on the AMT sensor performance calculated using the difference between pH_{Tc}(AMT) and pH(ref) that is pH(NOC) (blue dots) and with the discrete samples (pH(WS)) (black dots).

However, pH_{Tc}(AMT) offset was not directly correlated to salinity (Figure 3.12) because it varied from 0.071 for *S* = 32.34 to 0.152 for *S* = 31.65. When the salinity was constant the pH offset varied by more than 0.07, for example when *S* was 32.34 the pH offset varied by 0.075. The deployment suggests that salinity is not directly responsible for the glass electrode offset and its effect can be considered negligible in ocean environments. The main causes of the glass electrode offset were probably the inefficient calibration performed by the manufacturer and the adaption time when placed in seawater. A series of experiments in the laboratory using Tris buffers with a salinity of 33, 35 and 37 were performed to assess the effect of salinity on the AMT and Fluidion glass electrodes. These experiments were inconclusive (Figure A.1) suggesting that drift and other sources were the main causes of error during the dock deployment.

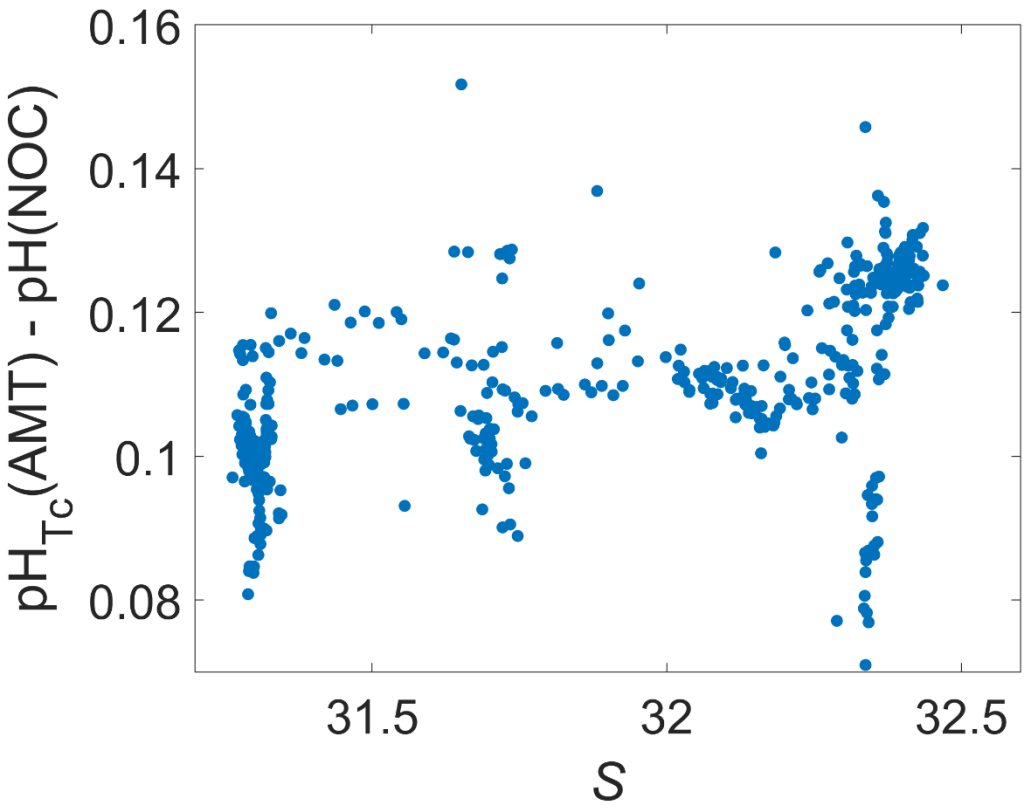

Figure 3.12: Direct correlation between the seawater salinity (*S*) and the difference between pH_{Tc}(AMT) and pH(NOC).

In the case of spectrophotometric pH sensors salinity and temperature need to be measured to calculate the $K_2^T e_2$ term used in Eq (3.6) to calculate the final pH from the absorbances (Liu et al., 2011). However, during the deployment it was not possible to quantify the effect of *S* on the NOC sensor performance because I collected just 6 discrete samples.

3.5 Discussion

3.5.1 Performance of different pH sensors

The two glass electrodes have a stated accuracy of 0.04 and a resolution (short-term precision) of 0.003 for the AMT and 0.001 for the Fluidion sensor. The two glass electrodes had an offset from pH(Tris) larger than 0.1 in most of the experiments because they were not calibrated before the experiments. However, the resolution determined in the temperature-controlled experiments (Section 3.4.2) was found to agree with the manufacturers' quoted performance.

Deployments in Southampton Dock and trials with Rothera seawater showed the glass electrodes to be drifting, with varying offsets to the true pH. Drift was reduced after conditioning in seawater for 4 days, but not eliminated. These results are consistent with McLaughlin et al. (2017) who collected data from several glass electrodes deployed in the Southern California Bight continental shelf that found a difference between glass electrodes pH and discrete samples pH ranging from -0.509 to 0.479 and a mean difference of -0.055.

This study confirms that glass electrodes without a regular calibration cannot be used to measure seawater pH changes smaller than 0.01 (e.g. (Le Bris et al., 2005)). For that reason, glass electrodes are starting to be replaced with more accurate and stable ISFET sensors. The Honeywell Durafet III was tested in a test tank showing a stability of 0.005 per month and 0.0005 h^{-1} (Martz et al., 2010a). A second version rated to 2000 m was developed by Johnson et al. (2016) who reported an accuracy and precision of 0.01 and 0.005 over a multiyear deployment. This sensor was also deployed on a Slocum glider with an accuracy of 0.011 and a precision of 0.005 (Saba et al., 2019).

Several miniaturised spectrophotometric sensors have been developed in recent years (Bellerby et al., 2002; Friis et al., 2004; Seidel et al., 2008). One of these sensors is the lab-on-chip spectrophotometric pH sensor developed by NOC in Southampton (Rérolle et al., 2013). The sensor deployed in an underway system had a precision and accuracy of 0.001 and 0.004 respectively against pH(Tris). Moreover, compared with pH derived from C_T and A_T, the offset varied between 0.005 and 0.013 (Rérolle et al., 2013).

In my study, the NOC sensor had comparable performance with (Rérolle et al., 2013) having a standard deviation of the difference between pH(NOC) and pH(Tris) that varied between 0.002 and 0.006 in the Tris experiments and a mean bias of 0.003±0.005 compared with the discrete samples when deployed in the Southampton dock. Other spectrophotometric sensors have been deployed on different systems with comparable accuracy and precision. Seidel et al., (2008) deployed the SAMI-pH off the pier at Scripps Institution of Oceanography in a temperature range from 6 to 18 °C and a salinity from 33 to 34 and found a precision of 0.004. Nakano et al., (2006) deployed another sensor on a rosette down to 1000 m where the temperature varied from 3 to 16 °C with a precision of 0.002. Friis et al., (2004) deployed another spectrophotometric system on a ship keeping the temperature constant at 22 °C with precision between 0.001 and 0.003. Another sensor was deployed on a FerryBox where the temperature varied from 14 to 22 °C and the salinity from 29 to 34 with a precision of 0.008 (Aßmann et al., 2011).

3.5.2 Storage effect on different pH sensors

The solution where the glass electrodes are stored can affect the performance of the sensors. Commonly these sensors are stored in 3-4 M KCl solutions, which may contribute to sampling bias when deployed in seawater (McLaughlin et al., 2017). This bias is caused by the reaction of the AgCl reference electrode with bromide to form $AgCl_{1-x}Br_x$ that may shift the reference potential by 2 to 5 mV (Takeshita et al., 2014). Storing the sensors in seawater before the deployment reduces this error and improves sensor stability (Johnson et al., 2016; McLaughlin et al., 2017). The two glass electrodes were tested for 4 days in seawater reducing the hourly drift rate in the 6 hours experiment from 0.018 h^{-1} for pH_{Tc}(AMT) and 0.013 h^{-1} for pH_{Tc}(Fluidion) on the first day to 0.0007 h^{-1} for pH_{Tc}(AMT) and 0.0003 h^{-1} for pH_{Tc}(Fluidion) on the fourth day. This experiment suggests that the sensors need to be stored in seawater for longer, up to several weeks. Johnson et al. (2017) stored the Deep-Sea DuraFET in seawater (Johnson et al., 2016) for several weeks before the deployment. This storage coupled with calibration in seawater reduced the sensor drift from –0.083 a^{-1} to 0.003 a^{-1} (Johnson et al., 2017). Also, storing the two glass electrodes in Tris buffer led to the irreversible damage of the glass electrodes. The two glass electrodes started to be very unstable and had a large drift in short time. For that reason, I suggest storing glass electrodes in seawater for ocean deployments and between laboratory experiments.

3.5.3 Temperature effect on different pH sensors

The performance of the two glass electrodes was assessed between 5 and 31 °C. pH_{Tc}(AMT) had the smallest offset compared to pH(Tris) at 25 °C and the maximum at 31 °C and pH_{Tc}(Fluidion) had the minimum at 15 °C and the maximum at 31 °C. This result is in disagreement with previous studies that found a decrease in glass electrodes accuracy with temperature. McLaughlin et al. (2017) quantified the temperature hysteresis on glass electrodes to be 0.0025 $°C^{-1}$. This effect is important also for ISFET sensors, for the Deep-Sea DuraFET it was quantified as -0.018 $°C^{-1}$(Johnson et al, 2016) and -0.021 $°C^{-1}$ for the Shitashima et al. (2002) sensor when deployed on a glider (Hemming et al., 2017).

In a 4 day-experiment in seawater, the two glass electrodes were in most cases able to capture the direction of the pH changes but not the expected magnitude. The measured pH changes varied between 0.005 and 0.003 $°C^{-1}$ when the expected pH change is –

0.01582 °C^{-1} (Millero, 2007). The average pH change measured during the first experiment was 0.014 for 3 °C for pH_{Tc}(AMT) and 0.008 for 3 °C for pH_{Tc}(Fluidion). In the last experiment, the average pH_{Tc}(Fluidion) increased to 0.01 per 3 °C but pH_{Tc}(AMT) stopped responding to the pH changes and for example measured a pH increase when temperature increased.

Seidel et al., (2008) tested two spectrophotometric pH sensors in seawater without finding any systematic trend driven by temperature in the pH difference between the two sensors. This result is in agreement with my laboratory experiments, where the NOC sensor performance was not directly affected by temperature because it had a maximum offset from -0.008±0.007 pH(Tris) at 25 °C and the minimum 0.004±0.001 at 15 °C.

3.5.4 In situ calibration of the glass electrodes

Shortcomings in the calibration of the pH sensors can lead to large errors during the deployment (McLaughlin et al., 2017). Currently, most of the manufacturer's protocols involve calibration using National Bureau of Standards (NBS) buffers (McLaughlin et al., 2017), which have a low ionic strength (0.1 mol kg^{-1}) relative to seawater (0.7 mol kg^{-1}). This ionic strength difference affects the glass electrodes liquid junction potential because the latter is sensitive to the composition and concentration of the solution leading to a potential error between 0.01 and 0.001 (Wedborg et al., 1999).

In recent years new buffers with the same ionic strength of seawater such as AMP and Tris started to become available (Dickson et al., 2007). Scientists have started calibrating the sensors in these solutions before deployment (Hemming et al., 2017; Johnson et al., 2017). However, the use of these buffers can lead to errors in the calibration because they are a simplified seawater system where bromide, fluoride and strontium are not present (Dickson et al., 2007). The use of these buffers does not take into account the bromide effect on the Ag reference electrode (Takeshita et al., 2014) and the preparation of Tris has a potential error of 0.006 (Paulsen and Dickson, 2020). The precision required for seawater pH measurements needs to be better than 0.002 to allow the detection of the average annual decrease in surface ocean pH (Bane et al., 2010a; González-Dávila et al., 2010) that cannot be met using Tris in the calibration. For these reasons, Tris and AMP buffers are increasingly replaced by seawater pH calibrations using benchtop spectrophotometers (Easley and Bane, 2012).

During the deployment the sensor can be affected by a non-monotonous and non-constant drift (Hemming et al., 2017; Saba et al., 2019), making the correction after the recovery challenging. This drift can be 0.02 d^{-1} for glass electrodes (Seiter and

DeGrandpre, 2001) and 0.003 d^{-1} for the Deep-Sea DuraFET when deployed on a Slocum glider (Saba et al., 2019). The sensor drift can be quantified by comparing the pH measured with an estimation of pH calculated using other variables in a multiple linear regression (MLR). This methodology was applied to correct the ISFET sensors drift on SOCCOM floats estimating pH from temperature, salinity, pressure and oxygen or nitrate with an uncertainty between 0.010 and 0.008 (Williams et al., 2016). In many deployments, this methodology is not applicable because it requires the knowledge of regional pH changes in space and time and the pH sensor needs to be coupled with a CTD and other biogeochemical sensors.

Another method is to regularly correct the drift using discrete samples analysed by a benchtop spectrophotometer (Easley and Byrne, 2012; McLaughlin et al., 2017). The regular collection of discrete samples increases the cost of the deployment and is not always possible especially in extreme and remote regions such as Antarctica or the Arctic. An alternative is to couple the ISFET or glass electrode with a miniaturised spectrophotometer that is calibration-free (Rérolle et al., 2012) and has a small size allowing deployments next to high-resolution sensors. This is possible because in recent years these sensors have significantly decreased the power requirements, for example SAMI-pH decreased its power requirement from 6-7 to 1 W (Seidel et al., 2008) and use a low amount of dye (2.2 µL for the NOC sensor) allowing deployments of several months.

In this study, the use of a miniaturised spectrophotometric pH sensor was tested to frequently calibrate two uncalibrated glass electrodes. The direct deployment of uncalibrated glass electrodes can significantly decrease the labour time and costs. The NOC sensor was used as reference improving the glass electrodes stability and accuracy from 0.069 up to 0.002 for AMT and from 0.052 to 0.003 for Fluidion. The combination of a spectrophotometric sensor and a glass electrode can be ideal for in situ long deployments because the glass electrode provides high frequency-sampling (< 1 Hz) and the spectrophotometric sensor a lower frequency, high precision and accurate reference. The two sensors can be used for long and short deployments on gliders, Argo floats, moorings and other autonomous sampling systems.

3.6 Conclusions

Experiments were performed to identify best practices and potential sources of error for different pH sensors. These experiments were performed in the laboratory using seawater, Tris and AMP buffers and in the dock in front of NOC in Southampton. The

sensors tested were two glass electrodes developed by AMT and Fluidion and a miniaturised spectrophotometric pH sensor developed by NOC in Southampton (Rérolle et al., 2013).

The main source of error was the direct deployment of the two glass electrodes from the 3 M KCl storage solution in seawater that shifted the behaviour of the sensors to non-Nernstian. This happened because the seawater bromide reacts with Ag reference electrode to form $AgCl_{1-x}Br_x$ shifting the potential by 2 to 5 mV (Johnson et al., 2016). In a 4-day experiment, the two glass electrodes were not able to capture the seawater pH changes caused by temperature because it varied between 0.005 and -0.003 $°C^{-1}$ when the expected pH change is –0.01582 $°C^{-1}$ (Millero, 2007). The measured pH had a continuous negative drift during the 4 days of experiments with a decrease of the drift in time, in fact the last day it was 0.0003 h^{-1} for pH_{Tc}(Fluidion) and 0.0007 h^{-1} for pH_{Tc}(AMT). The two sensors' performance would improve storing the glass electrodes in seawater for several weeks before sampling.

The effect of temperature in equimolar Tris buffer was assessed between 5 and 31 °C. The two glass electrodes had a large offset because they were not calibrated before the experiments but were able in most cases to capture the size and direction of the pH changes. During the dock deployment, when salinity decreased from 31.70 to 31.26 the pH_{Tc}(AMT) offset from pH(NOC) increased from 0.100 to 0.120. Afterwards, when the salinity was constant the offset decreased again to 0.100 and was not the main cause of the offset. In the same deployment, the NOC sensor was not affected by temperature and salinity but it requires coupling with a CTD to convert the absorbances in pH (Eq (3.7)) and to transform the calculated pH to the seawater temperature.

The NOC sensor accuracy in Tris varied between 0.002 and 0.006 and in seawater was 0.005. The sensor is calibration-free and this accuracy and stability can be used as reference to regularly calibrate the sensors with higher sampling rate such as ISFET and glass electrodes that are prone to drift up to 0.003 d^{-1} (Saba et al., 2019) and 0.02 d^{-1} (Seiter and DeGrandpre, 2001). The calibration of the glass electrodes with this method improved the AMT and Fluidion accuracy to 0.002 and 0.003 in Tris and 0.005 in seawater. This combination can be used for long and short deployments on gliders, floats, moorings and other autonomous systems because the NOC sensor has a low power requirement (3 W) and uses a low amount of *m*CP (2.2 µL). The short response time of <(7±4) s for AMT and <(7±3) s for Fluidion sensors permits resolving short term processes such as the pH change when a glider passes through the thermocline.

Chapter 4

Air-sea exchange and bottom water remineralisation inferred from pH and O_2 sensors on a Seaglider in the North Sea

The Winkler analysis and the CTD oxygen optode calibration were performed by Francesco Pallottino a Plymouth Marine Laboratory (PML) PhD student. All the rest of the scientific work and writing was undertaken by Luca Possenti, with improvements made using comments from supervisors.

4.1 Summary

For the first time, a spectrophotometric lab-on-chip (LoC) pH sensor developed by the UK National Oceanography Centre and a Fluidion potentiometric pH sensor were used on a glider, which was deployed in the North Sea for 10 days in August 2019, covering a 45 km transect from 56.77° N 0.28° E to 57.06° N 0.23° W. The glider was also equipped with an Aanderaa 4831F oxygen optode. During the deployment and recovery cruise with RV Cefas Endeavour (CEND12/19) an additional 96 discrete seawater samples for dissolved inorganic carbon concentration (C_T) and total alkalinity (A_T) determination were collected, as well as 307 Winkler titration samples (3 or 4 duplicates for 91 samples) for determination of dissolved O_2 concentration, $c(O_2)$.

The spectrophotometric pH was corrected for a glider-sensor communication lag and had a mean offset of +0.006±0.008 with respect to the discrete samples. The potentiometric sensor was operated successfully for 2 days and was able to capture the depth-dependent pH changes. The sensor drift was <0.01 over these 2 days, but then the sensor failed due to a software problem. Using glider pH and a new regional parameterisation of A_T as a function of temperature and salinity, I calculated CO_2 concentration, $c(CO_2)$, and C_T.

Glider surface CO_2 and O_2 concentrations were used to calculate air-sea fluxes, $\Phi(O_2)$ and $\Phi(CO_2)$. $\Phi(O_2)$ was always out of the ocean with a median of +25 mmol m^{-2} d^{-1} (5^{th}

centile: 4.4 mmol m^{-2} d^{-1}; 95th centile: 94 mmol m^{-2} d^{-1}). In contrast, $\Phi(CO_2)$ was into the ocean with a median of -0.1 mmol m^{-2} d^{-1} (5th centile: -1.2 mmol m^{-2} d^{-1}; 95th centile: 1.7 mmol m^{-2} d^{-1}).

Three distinct regimes were identified along the transect: regime 1 was characterised by a subsurface oxygen maximum (SOM) at 30 m; regime 2 showed no distinct SOM and regime 3 had a SOM at 15 m. The oxygen increase at the SOM was associated with a deep chlorophyll maximum (DCM) in regime 1, which was detected by the ship's fluorometer mounted on the CTD rosette at the glider deployment site. No other *c*(Chl *a*) profiles were available because the ship's fluorometer failed.

To quantify remineralisation in the three regimes, I calculated Apparent Oxygen Utilisation (AOU) and Apparent Carbon Production (ACP) where regime 1 water was identified as Central North Sea Water (CNSW), regime 2 as a mix of CNSW and North Atlantic Water (NAW) and regime 3 water as NAW. CNSW had an ACP and AOU of 19 and 37 µmol kg^{-1} respectively that decreased to 13 and 33 µmol kg^{-1} respectively in NAW.

Our results show the potential of glider pH and O_2 data to capture time and depth-resolved biogeochemical processes that can vary rapidly over short time and length scales such as air-sea exchange, remineralisation and spatial changes.

4.2 Introduction

Coastal and marginal seas play a key role in the global carbon cycle by linking terrestrial, oceanic and atmospheric reservoirs (Mackenzie et al., 2004; Walsh, 1991). They occupy only 7 % of the global ocean surface area but yield 10-30 % of the global marine primary production (Gattuso et al., 1998). Coastal regions have higher temporal and spatial variability than the open ocean. Ships and gliders are able to resolve processes over different time and space scales. Expensive ship surveys are usually used to survey these regions because they are too shallow or have currents moving too fast for the usage of floats (Bushinsky et al., 2019). In contrast, gliders are cheaper to run than ships, can operate efficiently in water depths as shallow as 50 m and can overcome currents up to about 0.4 m s^{-1}. Thus, gliders can help uncover small-scale variations in space and time of processes such as vertical mixing, air-sea gas exchange, horizontal advection, net community production (NCP) or the size and variability of the North Sea continental shelf pump. Battery power limitations and potential sensor drift suggest that at present the use of gliders in these regions is limited to short-term studies. For shallow dives less than their design operation depth (1000 m) the mission length is limited because gliders use more power to communicate with the base station, detect the ocean bottom using the

altimeter and change the glider direction from descent to ascent. The battery usage can be reduced by decreasing the number of measurements of power-hungry sensors such as spectrophotometric pH sensors.

The North Sea has been studied extensively using observational and modelling tools. Studies focusing on inorganic carbon in the North Sea started in the late 1980s (Hoppema, 1991; Kempe and Pegler, 1991; Pegler and Kempe, 1988). Many of the recent studies focused on the southern North Sea and its coastal systems (Borges, 2003; Schiettecatte et al., 2007; Gypens et al., 2009). The North Sea carbonate system has been studied using voluntary observing ships (VOS) (Thomas et al., 2007), dedicated research cruises (Bozec et al., 2005, 2006; Meyer et al., 2018; Salt et al., 2013; Thomas et al., 2005), VOS and research cruises together (Omar et al., 2010) and models (Artioli et al., 2012; Blackford and Gilbert, 2007; Gypens et al., 2009; Kühn et al., 2010; Prowe et al., 2009). These datasets allowed quantifying changes of surface $p(CO_2)$ in the entire North Sea (Omar et al., 2010; Thomas et al., 2005, 2007), find a correlation of pH and CO_2 with North Atlantic Oscillation (NAO) (Salt et al., 2013), quantify the CO_2 air-sea flux (Meyer et al., 2018), quantify the pH variability and ocean acidification (Blackford and Gilbert, 2007), calculate NCP (Bozec et al., 2006) and quantify the CO_2 continental shelf pump (Bozec et al., 2005; Thomas et al., 2004). These studies mostly used sparse samples in time and space, focusing on changes happening in large spatial areas that in most cases included the entire North Sea.

However, it is also necessary to quantify small scale changes using sensors with a higher temporal resolution (< 10 s). These datasets can help to quantify the North Sea carbon cycle looking at interannual variability, the continental shelf pump and the spatial variability between the southern and the northern North Sea. For these goals, the datasets can be collected by autonomous vehicles (AUV), such as gliders. Queste et al. (2016) deployed a glider in the central North Sea for 3 days equipped with an O_2 optode and a chlorophyll fluorometer. Despite the short deployment, the glider data revealed occasional small scale events and larger oxygen consumption in the bottom mixed layer (BML) than previous studies. The glider used just 5 % of battery capacity and has the capability for longer deployments in shallow seas up to 2 months.

In this study, a spectrophotometric pH sensor has been deployed on a glider for the first time. The sensor was developed by the Ocean Technology and Engineering Group (OTE) of the National Oceanography Centre (NOC) in Southampton, United Kingdom (Rérolle et al., 2012). Ocean pH was measured for the first time using a benchtop spectrophotometer by Bane and Breland (1989). This method was limited to shipboard measurements because it required the use of spectrophotometric blanks and an indicator dye that are challenging to implement in a miniaturised autonomous sensor. As a result,

the first sensors using spectrophotometric pH methods were characterised by high complexity, bulky size, and high power requirement (Martz et al., 2010). However, recent developments reduced the sensors size, complexity and power requirements. The NOC sensor is an example of these recent developments because it has a small size (130 x 140 mm for 920 g in air), low power consumption (3 W, while measuring) and uses a small amount of sample (550 µL) and indicator (2.2 µL). Spectrophotometric pH sensors have advantages over ISFET and glass electrode sensors because they are calibration-free and not affected by drift (Rérolle et al., 2012).

In this study, I gathered the first glider pH data in the North Sea. The sensor performance was validated against a series of discrete samples for A_T and C_T collected during the glider deployment. The data were used to calculate O_2 and CO_2 air-sea fluxes, to quantify respiration in the BML and to compare spatial and temporal variability along the transect with additional discrete samples from the whole of the North Sea.

4.3 Material and methods

4.3.1 Glider sampling

Kongsberg Seaglider 510 was deployed in the North Sea on 19 August 2019 at 56.77° N 0.28° E and was recovered on 29 August 2019 at 57.06° N 0.23° W. The glider covered the 45 km transect for a total of 341 dives (Figure 4.1).

The glider was equipped with a NOC lab-on-chip (LoC) spectrophotometric pH sensor (Rerolle, 2013), a Fluidion potentiometric pH sensor stored for several weeks in seawater before the deployment, an Aanderaa Data Instrument AS, Bergen, Norway 4831F oxygen optode (Tengberg et al., 2006) and a Sea-Bird CT sensor (conductivity and temperature) factory calibrated (Figure 4.2). The O_2 optode was mounted with the sensing foil facing downwards to the glider body to avoid sunlight interference (Binetti et al., 2020). The mean time interval for an in-situ measurement was on average 8.6 s for CTD and O_2 optode and 679 s (11 min) for the spectrophotometric sensor. This was the shortest time interval the glider and sensor software permitted.

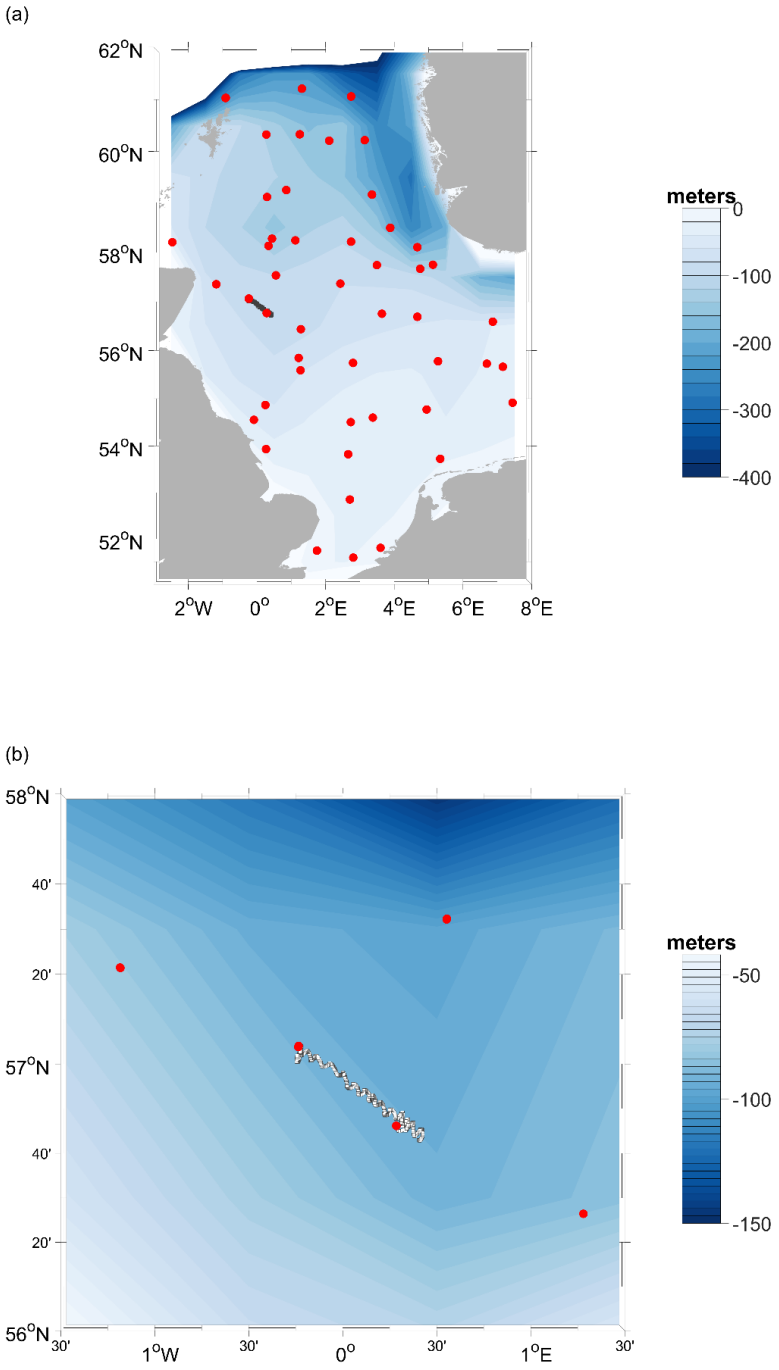

Figure 4.1: a) map of the survey area in the North Sea, b) map of the glider deployment area to show the deployment bathymetry with in a) and b) the glider deployment (black dots) from 19 to 29 August 2019 and the 96 discrete samples (red dots) collected on the RV CEFAS Endeavour CEND12/19 (Lowestoft, UK, 7 August to 5 September 2019).

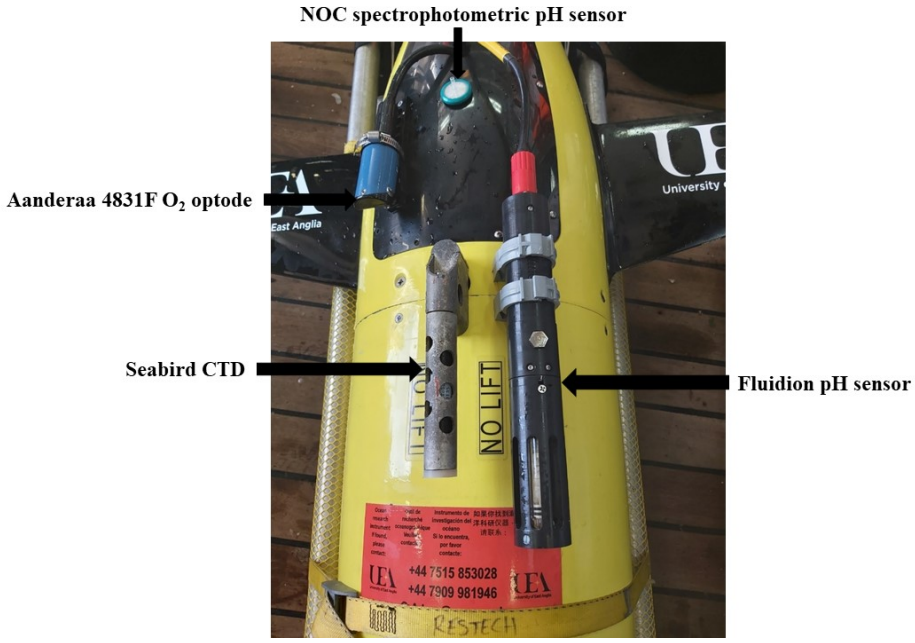

Figure 4.2: Kongsberg Seaglider 510 before the deployment showing the Aanderaa 4831F oxygen optode (Tengberg et al., 2006), a Sea-Bird CT (conductivity and temperature), Fluidion potentiometric pH sensor and the filter used to inject the sample into the NOC lab-on-chip (LoC) spectrophotometric pH sensor (Rerolle et al., 2013).

Every 10 dives and for every dive between dives 51 to 60 the glider was commanded to do longer dives (loiter dives). These dives were designed to increase the vertical resolution and collect more samples by decreasing the glider ascent speed. During loiter dives, the glider had an average vertical speed of 0.04 m s^{-1} that increased in non-loiter dives to 0.09 m s^{-1}. This decrease of vertical speed was important to allow the NOC sensor to collect more measurements. During loiter dives, the NOC sensor performed up to 9 measurements and during normal dives just 2 or 3. The decrease of the vertical speed doubled the duration of the dive from around 30 mins travelling for 0.5 km to more than 1 h travelling for 0.8 km.

The glider altimeter enabled the detection of the bottom depth and agreed with the bottom depth recorded in the General Bathymetric Chart of the Oceans (GEBCO) (Weatherall et al., 2015) except for the first 3 dives when the glider performed shallower dives (Figure 4.3).

Mixed layer depth (z_{mix}) was calculated using a threshold criterion of $\Delta\theta$ = 0.5 °C to the median θ of the top 5 m of the glider profile (Obata et al., 1996; United States. National Environmental Satellite and Information Service, Monterey and Levitus, 1997; Foltz et al., 2003).

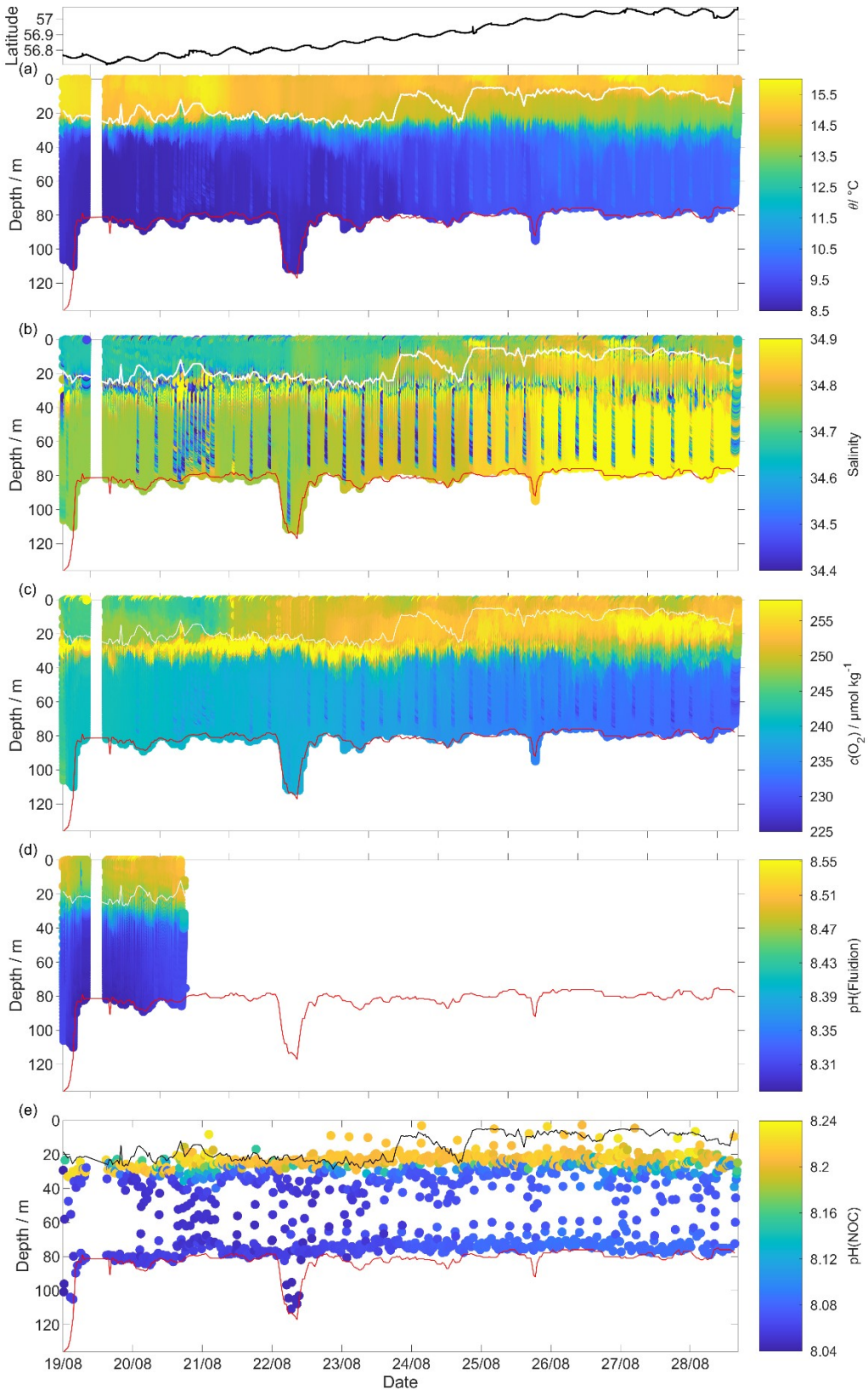

Figure 4.3: Scatter plot of the uncalibrated glider data for all 341 dives (top panel: latitude of the glider location). a) temperature θ, b) salinity S, c) oxygen concentration $c(O_2)$, d) pH(Fluidion) and e) pH(NOC). The white line in a), b), c), d) and the black line in e) is the mixed layer depth (z_{mix}) and the red line is the bathymetry from GEBCO.

4.3.2 Discrete sampling

During the RV Cefas Endeavour cruise CEND12/19 (Lowestoft–Lowestoft, 7 August to 5 September 2019) 96 discrete samples were collected to measure A_T, C_T, phosphate and silicate concentrations. A Sea-Bird CTD SBE-911plus V2 CTD was attached to a SBE 32 rosette of 12 10 L-Niskin bottles. During rough weather, sampling was performed using a single Niskin bottle attached to a wire. The rosette was also equipped with a JFE-Advantech RINKO-III Model ARO-CAV oxygen optode, a Seapoint SCF fluorometer, a Seapoint STM turbidity meter, Satlantic OCR-504 PAR radiometer and a Teledyne-Benthos PSA-916 altimeter. The A_T and C_T discrete samples were collected following Standard Operating Procedure (SOP) 1 of Dickson et al. (2007), using 500 ml serum bottles with chlorobutyl rubber stoppers. The C_T, A_T, phosphate and silicate samples were preserved with saturated $HgCl_2$ solution (final $HgCl_2$ concentration: 15 mg dm^{-3}). When the water column was fully mixed one discrete sample was collected; when it was stratified, one sample each was collected from the surface (SML) and bottom (BML) mixed layer. SML defines the depths above the mixed layer depth (z_{mix}) and BML under the z_{mix}, The C_T and A_T samples were analysed on-shore according to SOPs 2 and 3b (Dickson et al., 2007) using two Versatile INstrument for the Determination of Total inorganic carbon and titration Alkalinity (VINDTA). The results were calibrated using A_T and C_T of certified reference material (CRM) batch 182 obtained from A. G. Dickson at Scripps Institution of Oceanography, San Diego, USA (Dickson et al., 2003). The uncertainty in the measurement of C_T and A_T was calculated as the standard deviation of the CRM C_T and A_T. Comparing the measurements of the reference material, C_T had a mean standard deviation of 1.8 and 10.8 µmol kg^{-1} for the two VINDTAs, and 3.3 and 3.2 µmol kg^{-1} for A_T. The high mean standard deviation of one of the two VINDTA was driven by a C_T value of 2072.8 µmol kg^{-1} that was excluded from the analysis because it disagreed with the remaining CRM samples that had a mean of (2036±2.0) µmol kg^{-1}. pH and $p(CO_2)$ were calculated using the MATLAB toolbox CO2SYS (Van Heuven et al., 2011) with the following constants: K_1 and K_2 carbonic acid dissociation constants of Lueker et al. (2000), hydrogensulfate dissociation constant of Dickson (1990) and borate to chlorinity ratio of Lee et al. (2010).

Nutrient concentrations were measured using a Skalar San++ continuous flow analyser with standard colorimetric reference.68 oxygen Winkler samples were analysed onboard by Francesco Pallottino a Plymouth Marine Laboratory (PML) PhD student, using an automatic Winkler titration to a photometric endpoint (Culberson, 1991; Holley and Hydes, 1995). For each sample, 3 or 4 replicates were analysed (a total of 210 titrations) to quantify a median standard deviation of 0.5 µmol kg^{-1} with a range of standard deviations for each sample between 0.1 to 3.0 µmol kg^{-1}.

4.3.3 Spectrophotometric pH sensor corrections

The NOC pH sensor presented in section 3.3.1 was integrated on a glider and the sensor started sampling when powered at the beginning of each dive.

During the deployment, the NOC sensor was affected by lag (time delay Δt). This lag is visible in Figure 4.3e because for most of the deployment the sensor did not collect any sample in the top 20 m even though it was expected to start sampling immediately after powering it on at the surface. Δt was calculated for each dive as the difference between the timestamps of the first NOC sample and the first glider CTD sample, minus 30 s. The subtraction of 30 s accounts for the flushing period of the whole system before the start of sample measurements. Multiple flushes avoid any carry-over between measurements. The calculated delay Δt varied from 144 to 192 s (Figure 4.4).

After the lag correction, the absorbance ratio (R) was converted to pH using the algorithm from Soli et al. (2013) that takes into account the effects of temperature, salinity and pressure on *m*CP (Eq. 3.7 in Section 3.3.1). The temperature-corrected pH_c was derived from the difference between NOC internal temperature and seawater temperature using a coefficient of –0.01582 $°C^{-1}$ (Millero, 2007) – see Eq. 3.17 in Section 3.3.1.

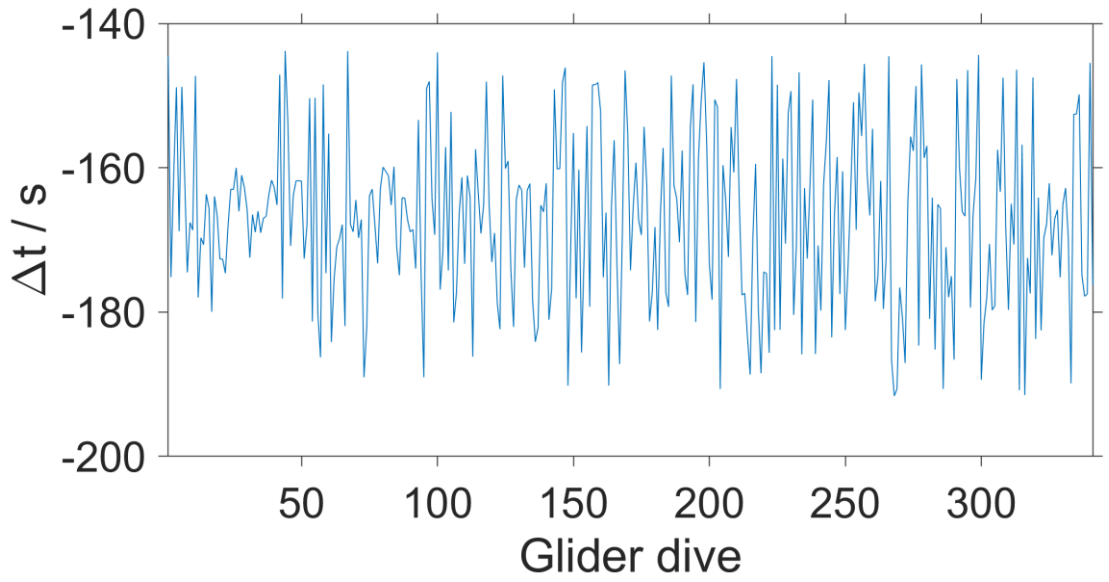

Figure 4.4: The NOC sensor lag calculated for each dive as the difference between the timestamps of the first NOC sample and the first glider CTD sample, minus 30 s to account for the time taken to flush the system.

4.3.4 Potentiometric pH sensor corrections

The potentiometric sensor displayed a mismatch between the pH measured during the glider ascents and descents. This was caused by a thermal lag effect as a comparison between the temperature of the Fluidion probe and the glider CT temperature shows.

To correct for the lag, we first calibrated the Fluidion sensor temperature θ(Fluidion) using the temperature measured by the glider CT sensor, θ(CT), when they were both at equilibrium with the ambient water (i.e. at the beginning of the descent in the SML and the beginning of the ascent in the BML). θ(Fluidion) was calibrated by linear regression of θ(CT) against θ(Fluidion) measured during glider ascent at depths below 50 m and during glider descent in the top 20 m:

$$\theta_{cal}(\text{Fluidion}) = 1.15\ \theta(\text{Fluidion}) - 1.70 \quad (4.1)$$

The temperature effect on pH(Fluidion) was then corrected using pH_c(NOC) as reference using the pH difference against θ_{cal}(Fluidion):

$$pH_{cal}(\text{Fluidion}) = pH(\text{Fluidion}) - 0.02\ \theta_{cal}(\text{Fluidion})/^{o}C + 0.01 \quad (4.2)$$

4.3.5 Regional algorithm to estimate A_T

To calculate C_T and $c(CO_2)$, two variables were used: pH_C(NOC) derived as described in section 4.3.3 and A_T derived using a regional algorithm that uses temperature (θ) and salinity (S). The A_T algorithm follows the approach of Lee et al. (2006) and was derived using 8 discrete samples collected at two stations next to the glider transect (n = 4) and the glider deployment and recovery sites (n = 4). The stations next to the glider transect were at 57.36° N 1.18° W and 57.54° N 0.55° E. The derived A_T parameterisation is as follows:

$$A_{T,reg} / (\mu mol\ kg^{-1}) = 2330.71 + 41.72\ (S–35) + 1.11\ (S–35)^2 + 8.65\ (\theta/°C–20) + 0.66\ (\theta/°C–20)^2 \quad (4.3)$$

The parameterisation has a R^2 of 0.96, p = 0.009 and an uncertainty of 1.8 µmol kg^{-1} calculated as the standard deviation of the residual difference between actual and parameterised A_T (Figure 4.5).

The A_T parameterisation was used in CO2SYS (Van Heuven et al., 2011) to calculate C_T and $c(CO_2)$ from the glider pH measurements. The calculated $C_{T,calc}$ values were compared with $C_{T,WS}$ at the glider recovery and deployment sites. The mean difference was (4.4±4.0) µmol kg^{-1}. In the case of $c_{calc}(CO_2)$, the mean difference was (0.5±0.2)

µmol kg^{-1}. The non-zero biases and the standard deviation are due to uncertainties in the $A_{T,reg}$ parameterisation and pH_C(NOC) (cf. Section 4.4.1).

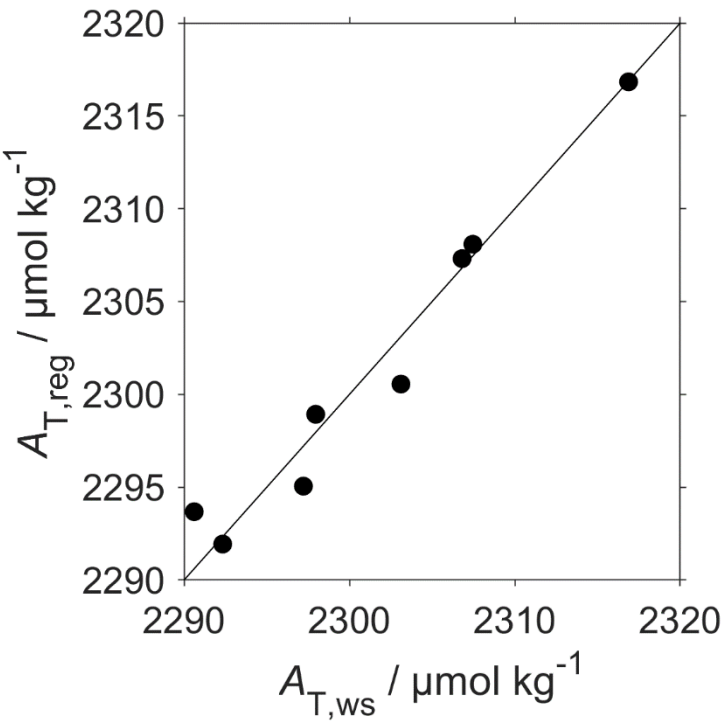

Figure 4.5: The plot shows the relationship between $A_{T,reg}$ and $A_{T,WS}$, calculated for the discrete samples.

4.3.6 Oxygen optode drift correction

Mounting the O_2 optode facing downwards reduced the presence of high $c(O_2)$ spikes (often >500 µmol kg^{-1}) in the first metres of the water column that were encountered on previous missions due to light interference (Binetti et al. 2020). I removed additional $c(O_2)$ values in the top 0.3 m during the glider ascent for night and day time (Figure 4.6). The effect of sunlight on the optode foil is expected only during daylight. For that reason, the remaining high $c(O_2)$ values were possibly caused by the contact of the foil with air or the injection of dissolved bubbles in the surface waters.

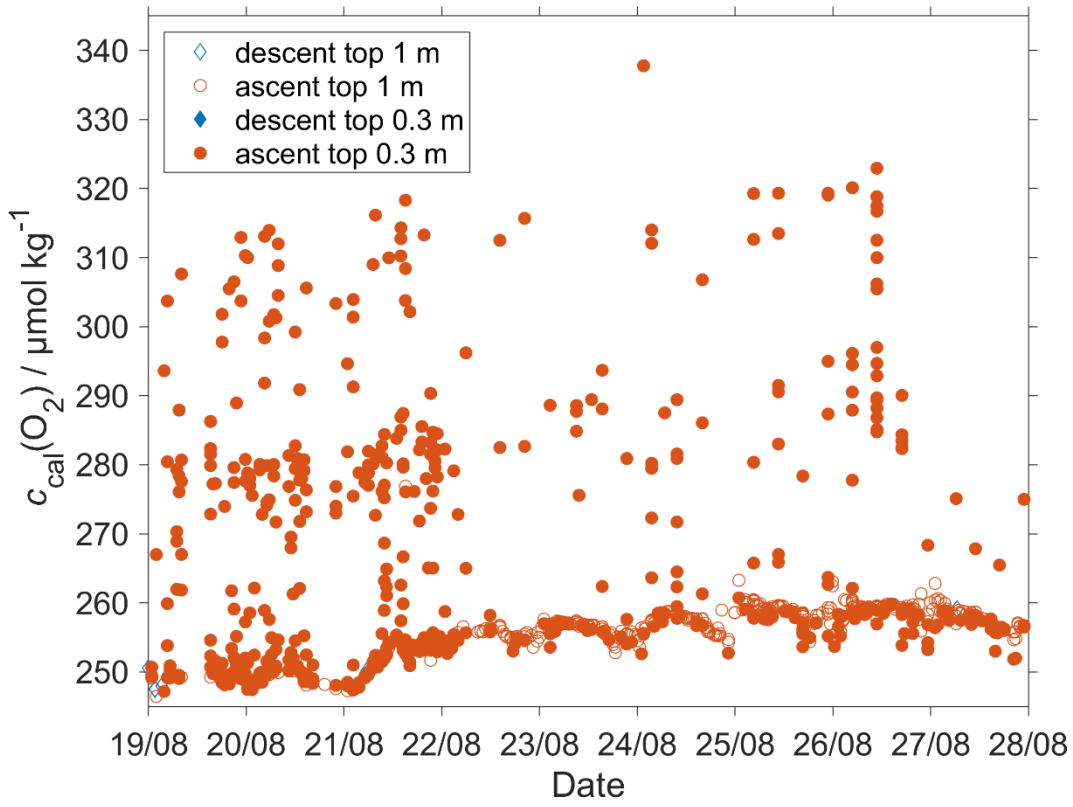

Figure 4.6: Surface 1 m glider $c(O_2)$ after the drift and offset corrections (Eq 4.4) showing the absence of spikes before 0.3 m (empty) and the spikes in the top 0.3 m (filled) during the glider ascent (red dots) and no spikes during the glider descent (blue diamonds). Because the glider ascent speed is slower than the descent, the plot shows more samples collected during the ascent than during the descent.

Oxygen optodes are known to be affected by drift (Bittig et al., 2015), which is worse for the fast-response foils used in the 4831F optode. The optode $c(O_2)$ was recalibrated and drift corrected using discrete samples ($c_{ws}(O_2)$) (Nicholson and Feen, 2017) collected at glider deployment (4 and 97 m) and recovery (20 and 73 m). Individual replicates for a given depth disagreeing by more than 3 µmol kg^{-1} from the other 2 replicates for the same depth were removed and the average was then calculated (section 4.4.2). The optode $c(O_2)$ ($c_G(O_2)$) offset was corrected using a gain approach, between $c_{ws}(O_2)$ and $c_G(O_2)$:

$$[c_{ws}(O_2)/c_G(O_2)] = 0.0014\ \Delta t/\mathrm{d} - 1.0013. \qquad (4.4)$$

The optode output was corrected for lag using the method of Hahn (2013).

Using the calibrated and drift-corrected $c_G(O_2)$, I calculated oxygen saturation ($s(O_2)$) as the ratio between $c_G(O_2)$ and the saturation concentration ($c_{sat}(O_2)$) (Garcia and Gordon,

1992) at the atmospheric pressure of 1013.25 hPa. Then, I calculated Apparent Oxygen Utilisation (AOU) as the difference between $c_{sat}(O_2)$ and $c_G(O_2)$.

The optode attached to the rosette was calibrated based on a linear regression between $c_{ws}(O_2)$ and the oxygen measured by rosette optode ($c_{ctd}(O_2)$):

$$c_{ctd,\,c}(O_2) = (1.045\ c_{ctd}(O_2) + 13.7\ \mu mol\ kg^{-1}). \qquad (4.5)$$

4.3.7 Quality control of CTD measurements

The thermal lag of the glider conductivity sensor was corrected using the method of Gourcuff (2014). The glider CT cell was affected by unstable temperature readings during the glider ascent in loiter dives. The temperature variability during the ascent in loiter dives caused large salinity and $c(O_2)$ spikes especially close and under the thermocline (Figure 4.7). For that reason, all temperatures, salinities and $c(O_2)$ measured during loiter dive ascents were removed.

Glider salinity (S_g) was calibrated using as reference the rosette salinity (S_r) measured at the glider recovery. The difference between S_g and S_r in the BML at the deployment and recovery sites was -0.019 and -0.012, respectively. The glider CT cell is not expected to drift and the temperature difference between the glider and the rosette was smaller at recovery (0.040 °C at the deployment and 0.010 °C at the recovery). For that reason, the glider salinity was adjusted using the offset to S_r measured at glider recovery.

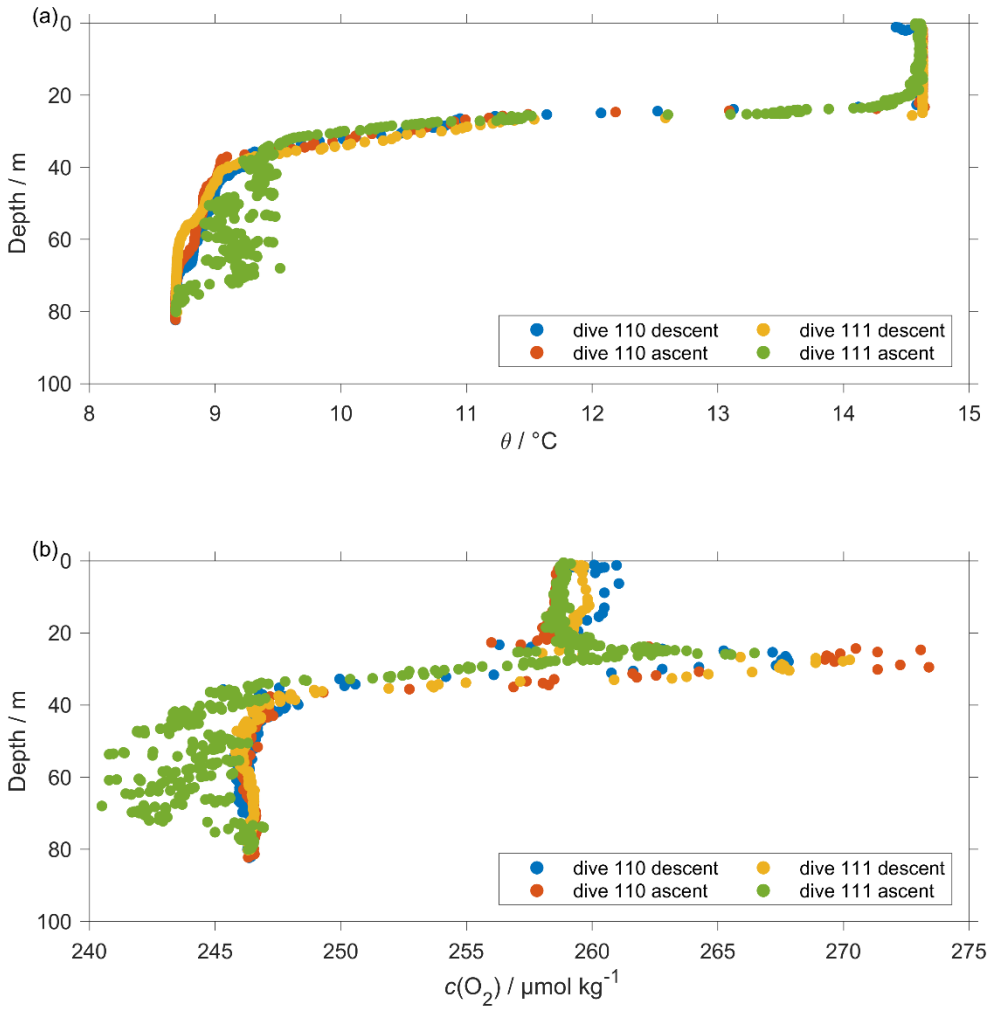

Figure 4.7: Comparison between a normal dive and a loiter dive. a) The first dive (110) was a normal dive and the data were stable. b) The next dive (111) was a loiter dive and caused noisy readings for ascent temperature θ, c(O_2) and conductivity (not shown).

4.3.8 Air-sea exchange calculation

The air-sea flux of oxygen ($\Phi(O_2)$) was calculated for each glider dive using the median of $c(O_2)$, θ and S in the top 10 m. I used the parameterisation of Woolf and Thorpe (1991) to include the bubble equilibrium supersaturation :

$$\Phi(O_2) = k_w(O_2)\,\{(c(O_2) - [1 + \Delta_{bub}(O_2)]c_{sat}(O_2)\} \qquad (4.6)$$

where $k_w(O_2)$ is the gas transfer coefficient, $\Delta_{bub}(O_2)$ is the increase of equilibrium saturation due to bubble injection and $c_{sat}(O_2)$ is the oxygen saturation. $c_{sat}(O_2)$ was calculated from S and θ using the solubility coefficients of Benson and Krause (1984),

as fitted by Garcia and Gordon (1992). $\Delta_{bub}(O_2)$ was calculated from the following equation:

$$\Delta_{\mathrm{bub}}(\mathrm{O_2}) = 0.01 \left(\frac{U}{U_0}\right)^2 \qquad (4.7)$$

where U is 10 m-wind speed with 1-hour resolution (ECMWF ERA5, https://www.ecmwf.int/en/forecasts/datasets/reanalysis-datasets/era5) and U_0 represents the wind speed when the oxygen concentration is 1 % supersaturated and has a value of 9 m s^{-1} (Woolf and Thorpe, 1991). U has a spatial resolution of 0.25° latitude and 0.25° longitude and it was interpolated to the glider position at the beginning of each dive.

The transfer velocity $k_w(O_2)$ was calculated based on Wanninkhof (2014):

$$\frac{k_{\mathrm{w}}(\mathrm{O_2})}{\mathrm{cm\ h^{-1}}} = 0.251 \left(\frac{Sc(\mathrm{O_2})}{660}\right)^{-0.5} \left(\frac{U}{\mathrm{m\ s^{-1}}}\right)^2 \qquad (4.8)$$

The Schmidt number, $Sc(O_2)$, was calculated using the parameterisation of Wanninkhof (2014).

The CO_2 air-sea flux ($\Phi(CO_2)$) was calculated using the 10 m wind speed with 1-hour resolution downloaded from ECMWF ERA5. As for oxygen, the closest wind speed at the beginning of each glider dive was used. The mean atmospheric CO_2 dry mole fraction ($x(CO_2)$) was 400.95 µmol mol^{-1} downloaded from the Greenhouse Gases Reference Network Site (https://www.esrl.noaa.gov/gmd/ccgg/ggrn.php) from the closest site to the deployment at Mace Head, County Galway, Ireland (Dlugokencky et al., 2015). Using $x(CO_2)$ the air-saturation concentration $c_{atm}(CO_2)$ was calculated:

$$c_{atm}(CO_2) = x(CO_2)\ p_{baro}\ F(CO_2) \qquad (4.9)$$

where p_{baro} is the mean sea level pressure obtained by ECMWF ERA5 and $F(CO_2)$ is the CO_2 solubility function calculated from surface θ and S (Weiss and Price, 1980).

The seawater $c(CO_2)$ at the surface was calculated using the median in the top 10 meters between the glider ascent and descent of the following dive $c(CO_2)$. $\Phi(CO_2)$ was then calculated as:

$$\Phi(CO_2) = k(CO_2)\ [c(CO_2) - c_{atm}(CO_2)]. \qquad (4.10)$$

$k(CO_2)$ was calculated using the parameterisation of Wanninkhof (2014):

$$\frac{k(\mathrm{CO_2})}{\mathrm{cm\ h^{-1}}} = 0.251 \left(\frac{Sc(\mathrm{CO_2})}{660}\right)^{-0.5} \left(\frac{U}{\mathrm{m\ s^{-1}}}\right)^2 \qquad (4.11)$$

$Sc(CO_2)$ is the dimensionless Schmidt number at the seawater temperature (Wanninkhof, 2014).

The uncertainties in $\Phi(O_2)$ and $\Phi(CO_2)$ were evaluated with a Monte-Carlo approach. The uncertainties of the input variables are shown in Table 4.1; the analysis was repeated 1000 times. The total uncertainty in Φ was calculated as the standard deviation of the 1000 Monte-Carlo simulations.

Table 4.1. The uncertainty associated with $\Phi(CO_2)$ and $\Phi(O_2)$ input variables calculated by a Monte-Carlo approach

Variable	Error	Reference/Method
S	0.007	Standard deviation of glider salinities in the first 100 dives below 80 m
θ	0.07 °C	Standard deviation of glider temperature in the first 100 dives below 80 m
$c_{atm}(CO_2)$	1.4 µmol kg^{-1}	Standard deviation of $c_{atm}(CO_2)$
$c(CO_2)$	0.5 µmol kg^{-1}	Mean difference from the glider and discrete samples $c(CO_2)$
$k(CO_2)$	20 %	(Wanninkhof, 2014)
$c_G(O_2)$	0.6 µmol kg^{-1}	Mean difference from the glider and the discrete samples $c(O_2)$ collected at the glider deployment and recovery

4.3.9 Apparent Carbon Production

To quantify respiration rates in deep waters, I calculated the Apparent Carbon Production (ACP). In the calculations, I assumed that the water mass was for the last time in contact with the atmosphere in January 2019 in the North Atlantic (59.7° N, 5.5° W). This assumption was made because the water residence time in the North Sea is less than 1 year and the northern North Sea is dominated by the Atlantic inflow (Salt et al., 2013). The North Sea starts to stratify in March/April (Sharples et al., 2006), therefore the water in BML has not been in contact with the atmosphere at least from March. The January 2019 atmospheric mole fraction $x(CO_2)$ was 414.3 µmol mol^{-1} from Mace Head, County Galway, Ireland (Dlugokencky et al., 2015). Using the 2 m dewpoint temperature (T_{dp} in °C) and mean sea level pressure (P_{baro}) downloaded from ECMWF, I calculated the atmospheric $p(CO_2)$ ($p_{atm}(CO_2)$) (Alduchov and Eskridge, 1996; Lawrence, 2005).

$A_{T,reg}$ and $p_{atm}(CO_2)$ were used as inputs in CO2SYS (Van Heuven et al., 2011) to calculate the C_T saturation ($C_{T,sat}$). ACP was calculated as the difference between glider C_T ($C_{T,G}$) and $C_{T,sat}$.

4.4 Results

4.4.1 Spectrophotometric pH sensor lag correction

Theoretically, in a well-stratified sea pH should be correlated with θ having the maximum pH and θ in SML and the minimum in BML. Also, as SML and BML are fully mixed pH and θ are expected to remain constant in the two layers. The only evident change should be visible at the thermocline that divides SML from BML. At the thermocline, a significant decrease in pH and θ is expected.

Before the lag correction, the NOC sensor did not collect any sample in the top 20 m (Figure 4.3e). This sampling delay caused the presence at the thermocline of high pH values measured in SML and low pH values measured in BML (Figure 4.8a). This is showed by the variability up to 0.15 at the same θ. This mix between high and low pH values was visible for pH(NOC) measured at the sensor internal θ and pH_N(NOC) corrected for the seawater temperature. After the lag correction, the pH at the sensor temperature (pH_T(NOC)) showed a correlation with θ, having a mean pH under 10 °C of (7.926±0.017) that increased to (8.068±0.021) for θ > 14 °C (Figure 4.8b). The correlation between pH and θ was also visible for the pH corrected to seawater θ, pH_C(NOC), that had a mean pH of (8.007±0.013) under 10 °C and increased to (8.056±0.018) for θ > 14 °C. These results show the success of the lag correction that divided the pH values measured in BML and SML and reconstructed the expected pH profile.

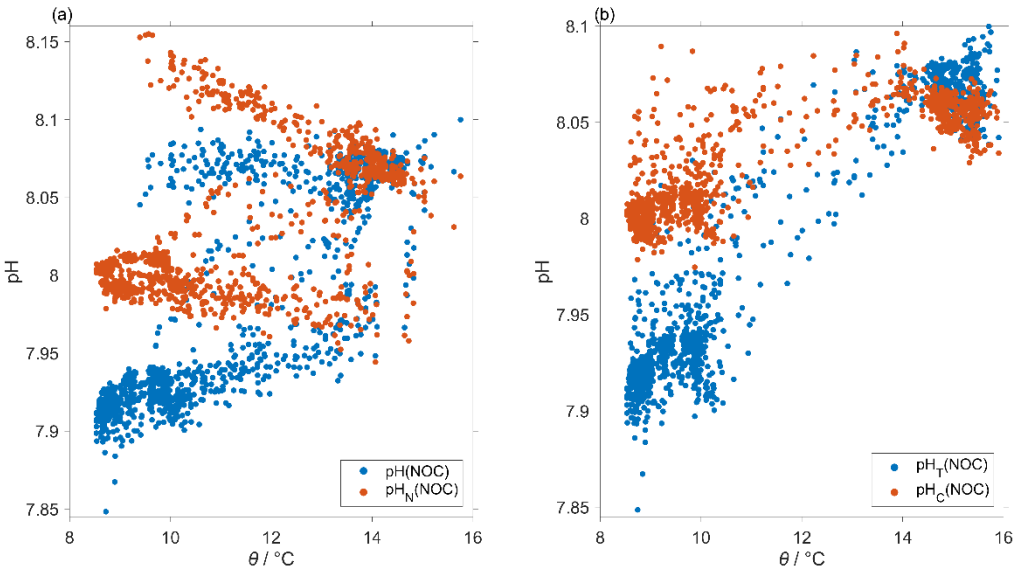

Figure 4.8: Temperature (θ in °C) against the NOC pH, a) pH(NOC) is the raw pH measured by the glider (blue) and pH_N(NOC) temperature corrected using Eq. 3.17 (red) and b) the NOC pH lag corrected following the procedure explained in section 4.3.3 where pH_T(NOC) (blue) is at the NOC internal temperature and pH_C(NOC) is corrected at the seawater temperature.

Figure 4.9 shows the final result after all the corrections have been applied to pH(NOC): first the pH was lag corrected (pH_T(NOC)) and later corrected to the seawater temperature (pH_C(NOC)). The lag and temperature corrected pH had a mean offset of 0.006±0.008 when compared to the pH of the discrete samples collected at deployment and recovery ($pH_{WS,G}$) (n = 4). Also, pH_C(NOC) agreed with the discrete samples collected next to the glider transect ($pH_{WS,cNS}$) selected between 55 to 58° N and between 2° E to 1.5° W (Figure 4.9). One $pH_{WS,cNS}$ discrete sample collected at the surface was in disagreement with pH_C(NOC) having a pH value of 8.01 when the lowest pH_C(NOC) was 8.029. This low $pH_{WS,cNS}$ value was driven by a higher temperature of 16.2 °C at the sample location compared to the highest surface temperature measured by the glider (15.9 °C). This temperature difference shows that the discrete sample and the glider sampled two different water masses. Also, $pH_{WS,G}$ collected at the glider deployment in BML was 8.022 and the highest pH_C(NOC) measured in BML was 8.015. The reason for that might be that the NOC sensor during the first dives was conditioning to seawater and was not able to perform accurate measurements. Another explanation can be that the glider and rosette measured different waters because the two platforms had a temperature difference of 0.04 °C.

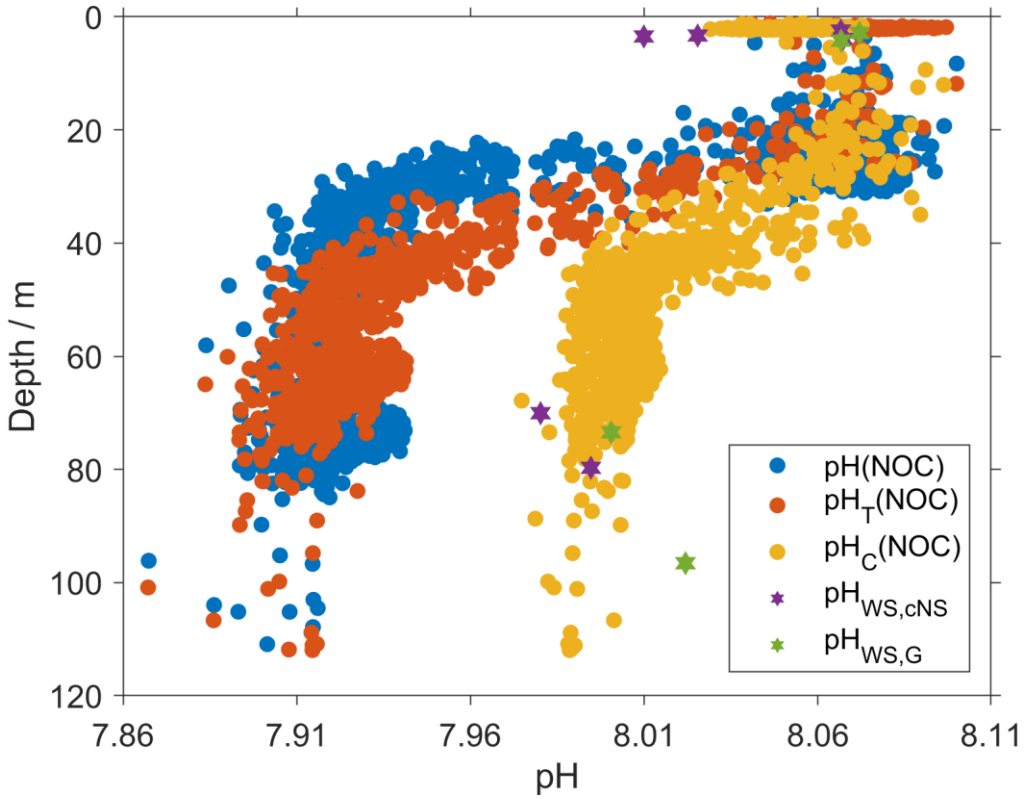

Figure 4.9: Each step of the NOC pH corrections, blue - the uncorrected pH (pH(NOC)), red - the lag corrected pH (pH_T(NOC)), yellow - the lag corrected pH transformed to the seawater temperature (pH_C(NOC)). Discrete samples, presented as green stars, collected at the glider deployment and recovery ($pH_{WS,G}$) and in violet near the deployment area ($pH_{WS,cNS}$) selected from 55 to 58°N and 2° E to 1.5° W.

4.4.2 O_2 optode calibration

The initial optode offset was 6.6 µmol kg^{-1} calculated as the difference at 97 m between $c_{ws}(O_2)$ and $c_G(O_2)$ (Figure 4.10a). The optode drift was -0.2 µmol kg^{-1} d^{-1} calculated as the difference between $c_{ws}(O_2)$ and $c_G(O_2)$ in BML at the glider deployment and recovery (Figure 4.10b).

The drift-corrected $c_G(O_2)$ compared to all the $c_{ws}(O_2)$ at the glider deployment and recovery had a standard deviation of 1.8 µmol kg^{-1} and a mean difference of 1.3 µmol kg^{-1}. After the calibration and drift correction, $c_G(O_2)$ profiles agree with the oxygen optode attached to the rosette $c_{ctd}(O_2)$ profiles calibrated using all the 307 oxygen discrete samples.

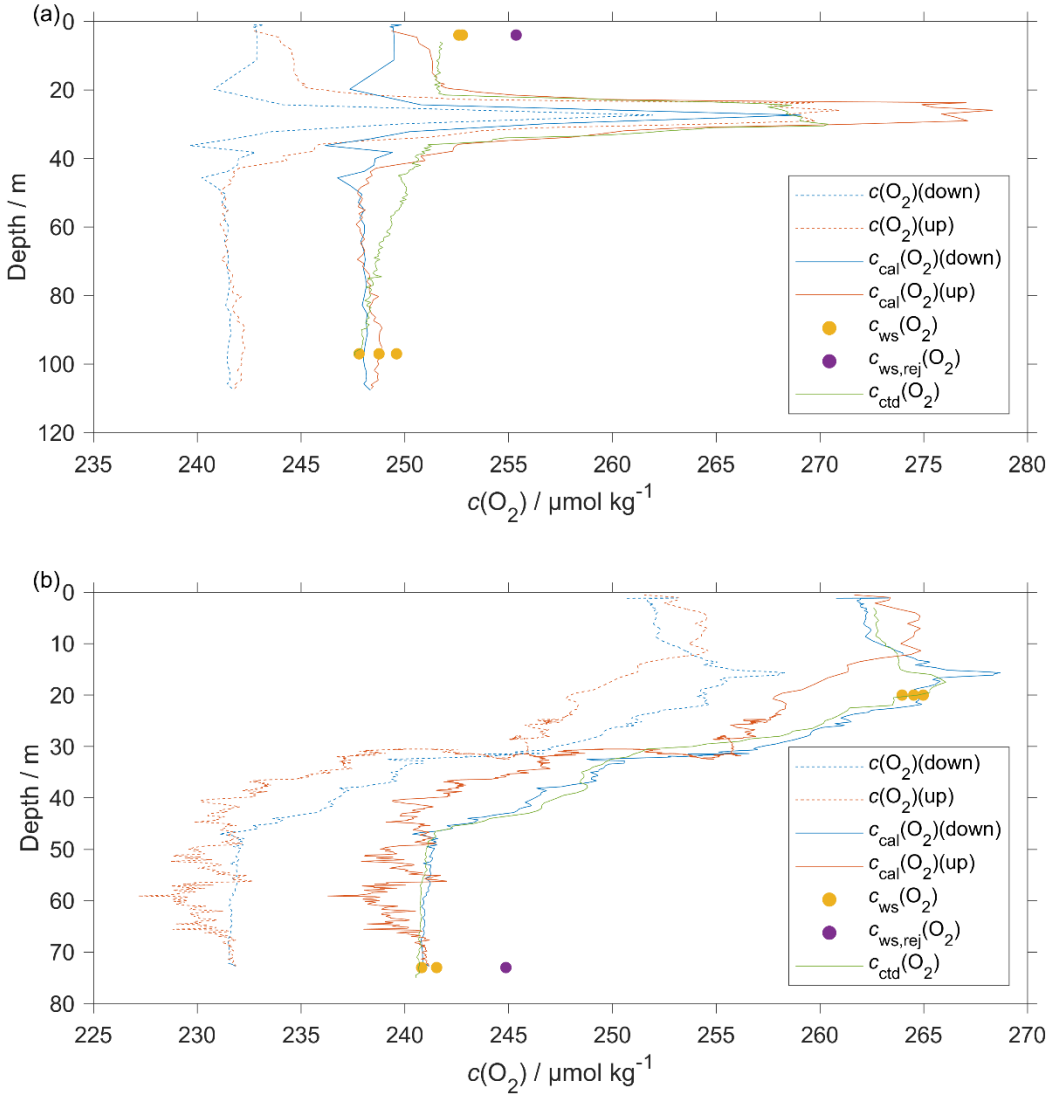

Figure 4.10: The glider oxygen optode output was drift corrected and calibrated using a gain method that had as reference the discrete samples collected in BML. The dotted lines represent the uncorrected $c_G(O_2)$, the continuous lines the corrected $c_G(O_2)$ during descent (down) and ascent (up). The dots are the discrete samples; rejected samples ($c_{ws,rej}(O_2)$) were identified as outliers by comparison with the CTD optode rosette ($c_{ctd}(O_2)$) collected a) at the glider deployment and b) at the glider recovery.

4.4.3 Three different regimes along the glider transect

The glider was deployed in the seasonally stratified northern North Sea (Figure 4.11 and 4.12) where SML and BML were divided by a strong thermocline that formed a mixed layer depth (z_{mix}) between 5 and 29 m. The water column was stratified from around 54 °N to the northern part of the North Sea with the exception of the shallow Dogger Bank

at 56 °N (Figure 4.13). In the SML, *S* gradually increased from 34.7 to 34.8 (Figure 4.3b) and on 22 August θ decreased from 15.8 to 14.7 °C (Figure 4.3a) and remained constant until 26 August with a median of 14.9 °C (5th centile: 14.6 °C; 95th centile: 15.4 °C) when it started to increase reaching its maximum of 15.5 °C on 28 August. At the same time $c(O_2)$ in SML increased from 250 to 264 µmol kg^{-1} (Figure 4.14c), however the surface pH did not show the same spatial trend and remained constant during all the deployment with a median of 8.058 (5th centile: 8.040; 95th centile: 8.065) (Figure 4.15).

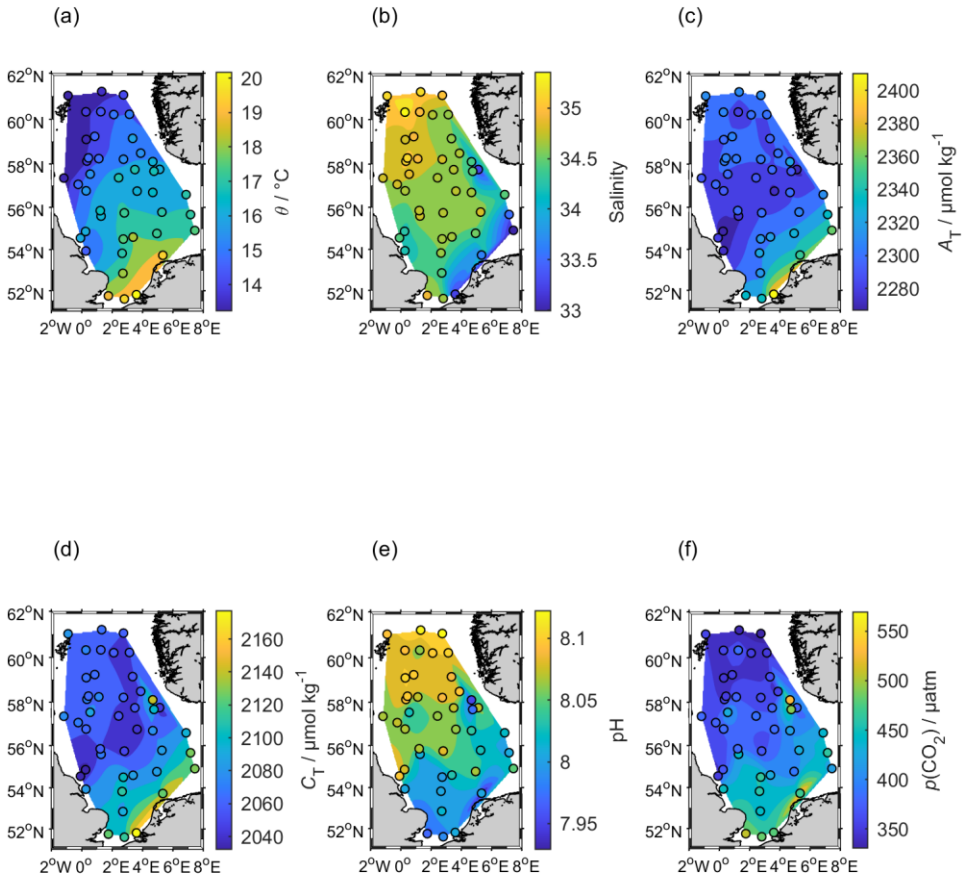

Figure 4.11: Surface discrete samples collected during CEND12/19 cruise for a) temperature θ, b) salinity *S*, c) total alkalinity A_T, d) dissolved inorganic carbon C_T, e) pH and f) partial pressure of CO_2 $p(CO_2)$.

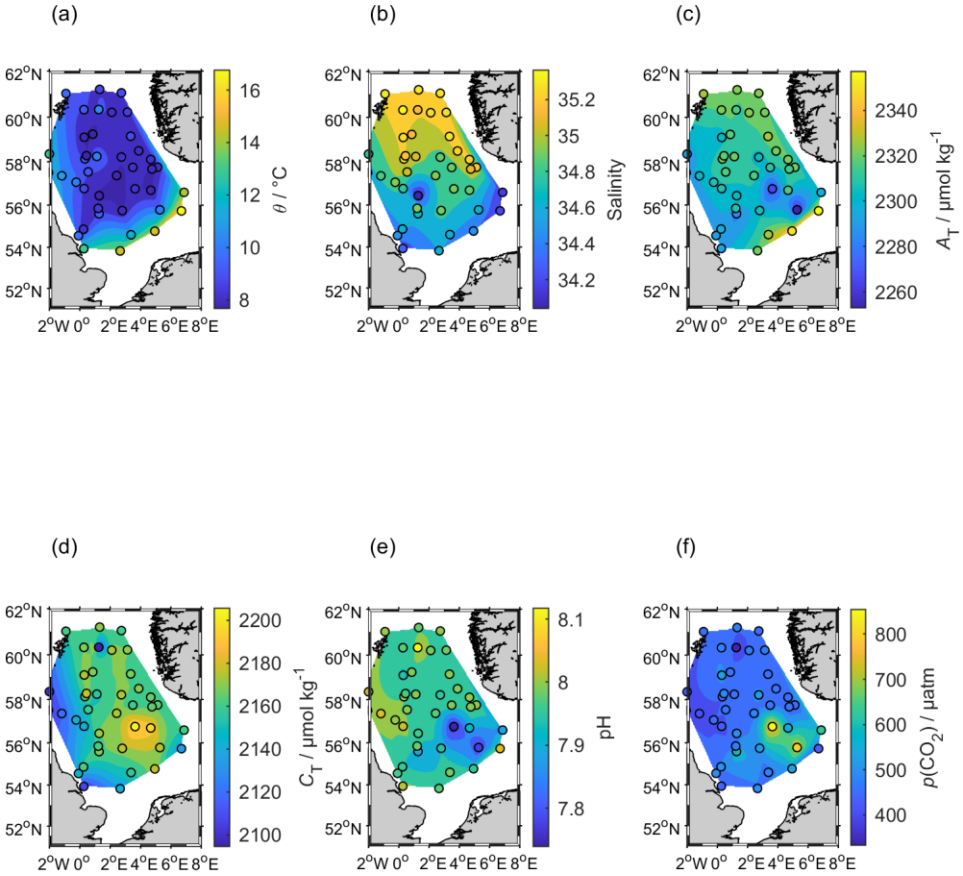

Figure 4.12: Deep discrete samples collected during CEND12/19 cruise for a) temperature θ, b) salinity S, c) total alkalinity A_T, d) dissolved inorganic carbon C_T, e) pH and f) partial pressure of CO_2 $p(CO_2)$.

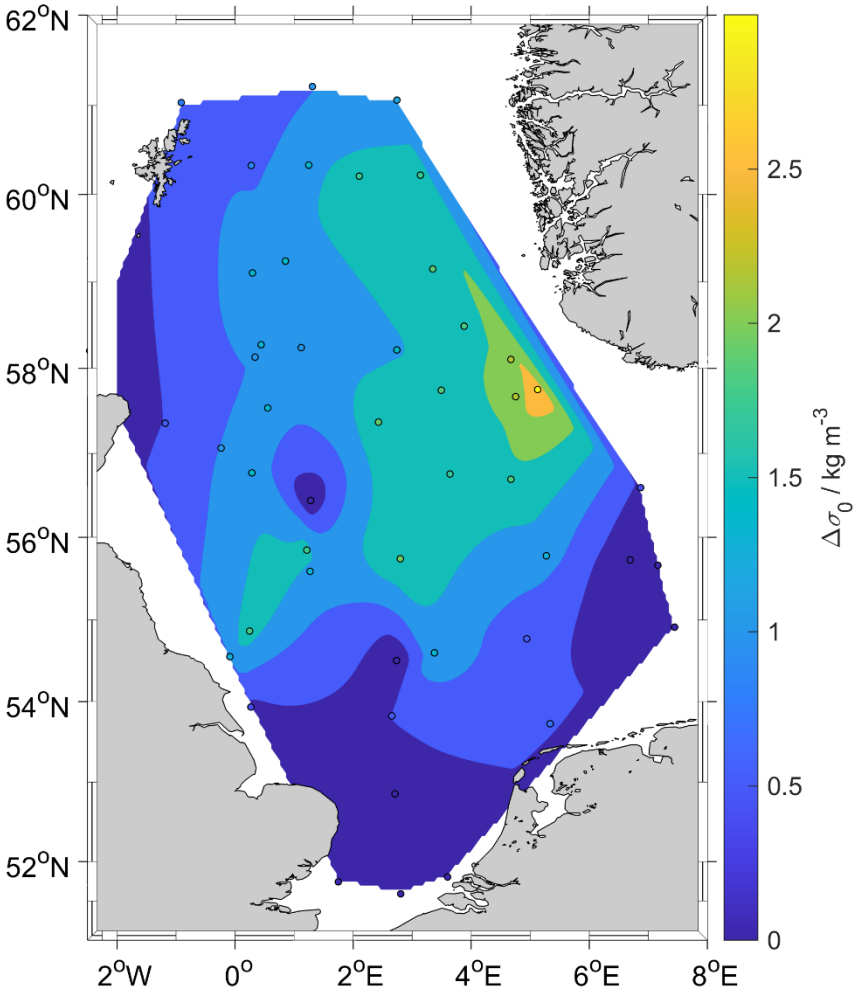

Figure 4.13: Difference between the deep water density (σ_0) and the surface σ_0, to show where the stratification started during the cruise.

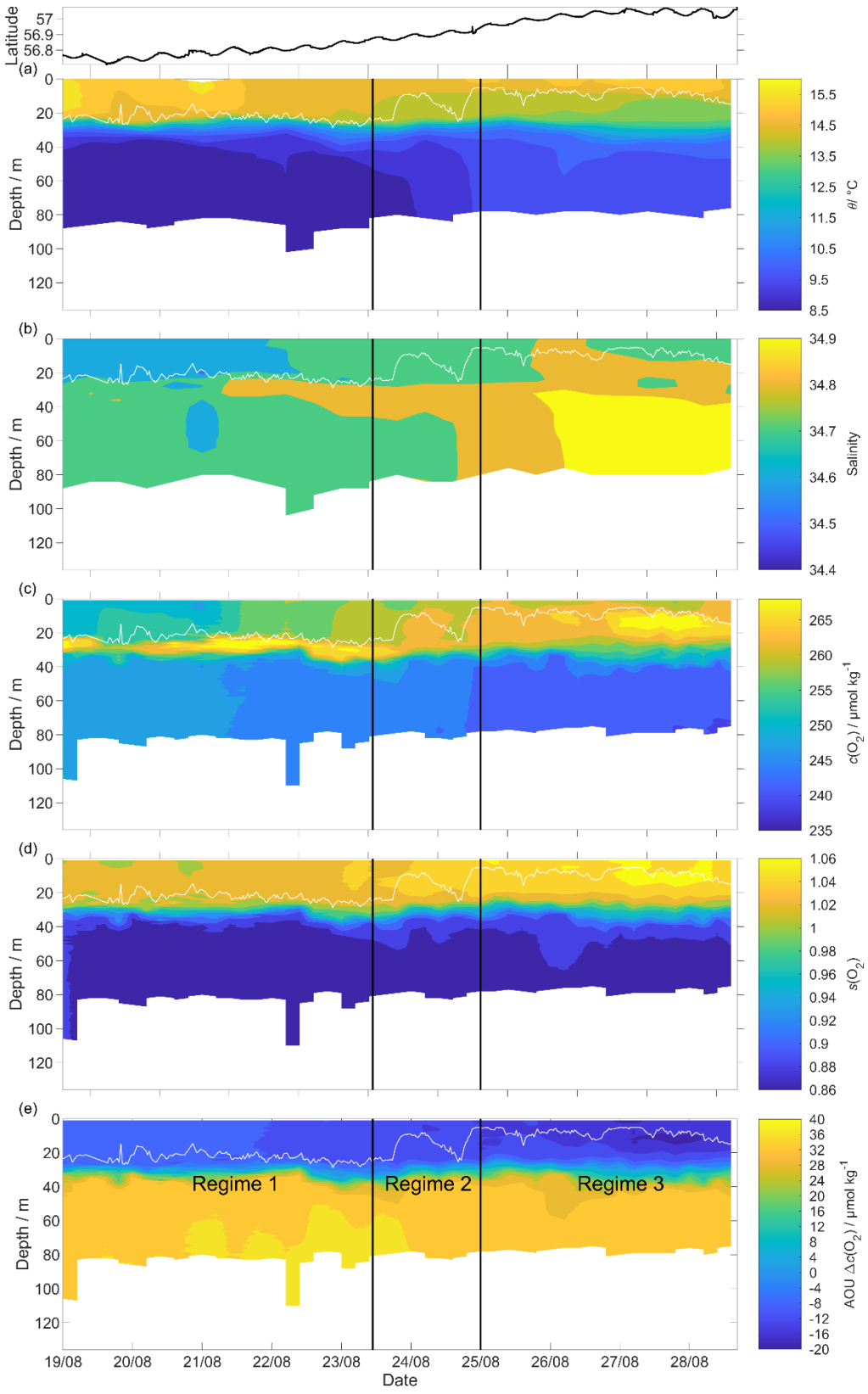

Figure 4.14: Contour plots of the glider deployment versus depth time showing that the glider data can be divided into 3 different regimes looking at a) temperature θ, b) salinity S c) $c(O_2)$, d) the saturation ratio ($s(O_2)$) that is defined as $c(O_2)/c_{sat}(O_2)$ and e) the

apparent oxygen utilisation (AOU). The two vertical black lines show the end of each regime and the white line is the mixed layer depth (z_{mix}).

Based on the $c(O_2)$ transect the deployment can be divided into three distinct biogeochemical regimes (Figure 4.14). Regime 1 (56.72 - 56.86 °N) was characterised by a subsurface oxygen maximum (SOM) below z_{mix} located from 20 to 30 m. The maximum $c(O_2)$ was 269 µmol kg^{-1} and surface $c(O_2)$ increased over time (or south-to-north) from 247 to 258 µmol kg^{-1}. SML was always oxygen supersaturated because $s(O_2)$ varied from 1.01 to 1.03. Regime 2 (56.87 - 56.93 °N) was characterised by the absence of SOM and z_{mix} shoaled from 24 to 9 m that enhanced biological production in SML by mixing in BML nutrient-rich waters. Also, the surface S increased from 34.6 to 34.8 because the glider encountered Atlantic-influenced waters (Queste et al., 2013) that drove the increase of $c(O_2)$ in SML. In fact, $c(O_2)$ in SML increased to 261 µmol kg^{-1}, driving $s(O_2)$ to 1.05. Regime 3 (56.94 - 57.08 °N) had a second SOM located under z_{mix} between 10 and 20 m. The surface $c(O_2)$ reached the deployment maximum of 263 µmol kg^{-1} in SML with a $s(O_2)$ maximum of 1.06. The largest $c(O_2)$ was measured at SOM with a maximum of 269 µmol kg^{-1} and a $s(O_2)$ of 1.06. The NOC pH sensor was not able to capture the SOM because it collected just 90 of 1232 samples between 10 and 30 m (Figure 4.15). Interestingly, during the first two days of deployment the Fluidion sensor did not detect a pH change at SOM, either (Figure 4.3d). The SOM was not captured by the C_T and $p(CO_2)$ derived from Fluidion pH and A_T derived using a regional algorithm (section 4.3.5). However, during the first two days of deployment the Fluidion sensor did detect a pH increase of about 0.02 at the SOM (Figure 4.16). The high pH at the surface are inconsistent with the oxygen measurements and can be explained by an incomplete calibration performed before the deployment that could not be fixed using pH_c(NOC) as reference.

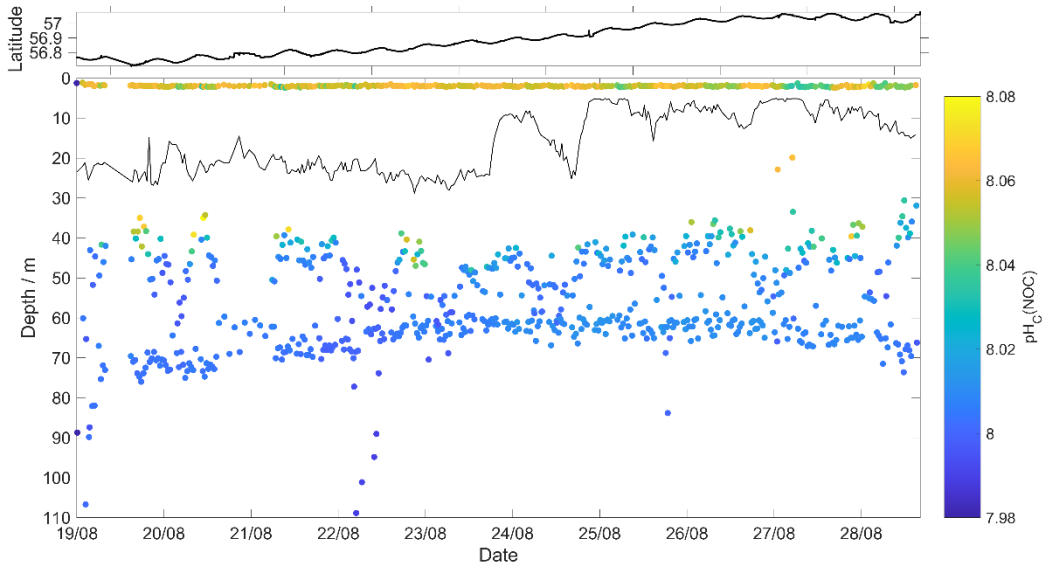

Figure 4.15: The plot shows all the measurements of the NOC pH sensor corrected for lag and to the seawater temperature (pH_C(NOC)) following the procedure in section 4.3.3. The latitude changes during the transect is showed in the top plot and the black line is the mixed layer depth (z_{mix}).

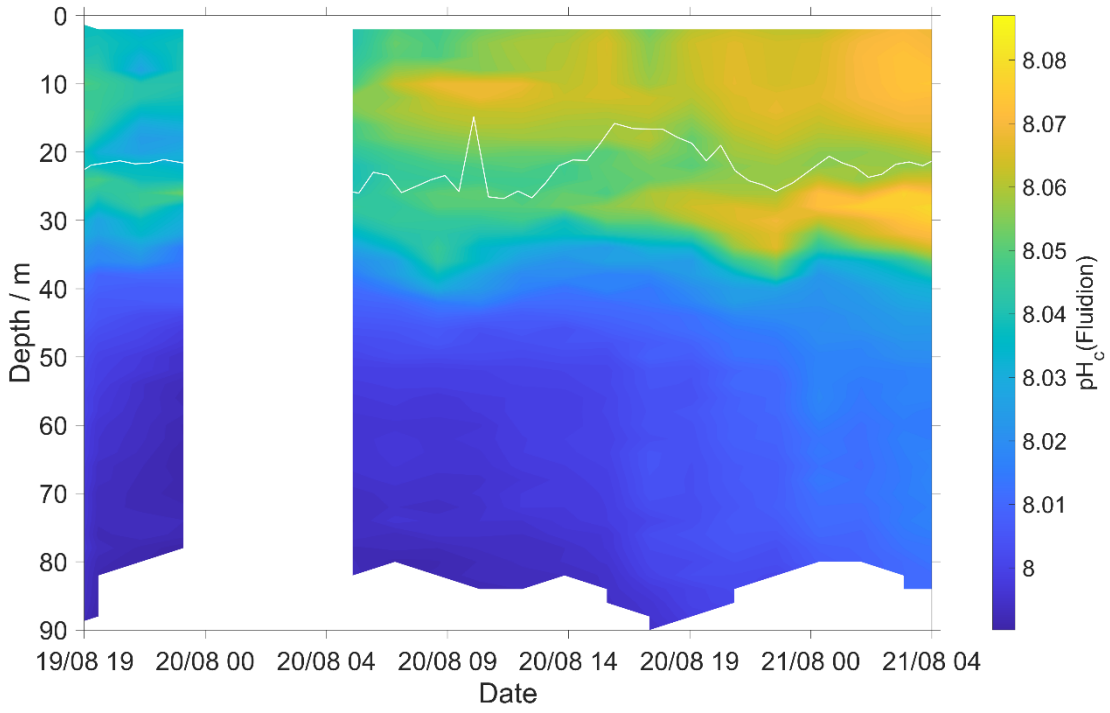

Figure 4.16: Thermal-lag corrected and calibrated Fluidion pH sensor measurements (Eq. 4.2) White line: surface mixed layer depth (z_{mix}).

4.4.4 Air-sea exchange

During the entire transect, despite the quick air-sea exchange the SML was oxygen supersaturated probably driven by high primary production that kept the surface $c(O_2)$ oversaturated (Figure 4.17). This surface supersaturation was (4.7±1.1) µmol kg^{-1} at deployment and continuously increased to (17±0.9) µmol kg^{-1} (Figure 4.17b). $\Phi(O_2)$ was always positive, driving a flux from the sea to the air with a median of 25 mmol m^{-2} d^{-1} (5^{th} centile: 4.2 mmol m^{-2} d^{-1}; 95^{th} centile: 95 mmol m^{-2} d^{-1}). In the first three days, the surface seawater had a median supersaturation of 5.1 µmol kg^{-1} (5^{th} centile: 3.9 µmol kg^{-1}; 95^{th} centile: 6.1 µmol kg^{-1}), this small $\Delta c(O_2)$ resulted in the smallest $\Phi(O_2)$ of (0.9±0.2) mmol m^{-2} d^{-1}. An increase of U from 7.0 m s^{-1} to 13 m s^{-1} increased $k_w(O_2)$ leading to the largest $\Phi(O_2)$ of (120±18) mmol m^{-2} d^{-1}. U remained larger than 8 m s^{-1} until 22 August keeping $\Phi(O_2)$ always larger than (30±6) mmol m^{-2} d^{-1}. On 28 August U increased to 9.6 m s^{-1} driving $\Phi(O_2)$ to (99±20) mmol m^{-2} d^{-1}.

For most of the deployment, the direction of $\Phi(CO_2)$ was from the air to the sea with a median of -0.1 mmol m^{-2} d^{-1} (5^{th} centile: -1.2 mmol m^{-2} d^{-1}; 95^{th} centile: 1.7 mmol m^{-2} d^{-1}) (Figure 4.18). The maximum $\Phi(CO_2)$ was (9.6±4.6) mmol m^{-2} d^{-1} when the glider had the largest $\Delta c(CO_2)$ of (1.1±0.5) µmol kg^{-1} and encountered the largest U of 13 m s^{-1} that increased $k(CO_2)$ from 0.2 to 8.6 m d^{-1} (Eq. 4.9). Until the 27 August U was < 9 m s^{-1} and led to a decrease of $\Phi(CO_2)$ to a median of -0.2 mmol m^{-2} d^{-1} (5^{th} centile: -1.4 mmol m^{-2} d^{-1}; 95^{th} centile: 0.4 mmol m^{-2} d^{-1}). On 28 August U increased to 9 m s^{-1}, $k(CO_2)$ increased from 0.5 to 4.7 m d^{-1}, $c(CO_2)$ from (14±0.4) to (15±0.8) µmol kg^{-1} and $\Delta c(CO_2)$ to (0.9±0.5) µmol kg^{-1}. This resulted in a brief interval of CO_2 emissions with a median of 0.84 mmol m^{-2} d^{-1} (5^{th} centile: -1.2 mmol m^{-2} d^{-1}; 95^{th} centile 2.4 mmol m^{-2} d^{-1}).

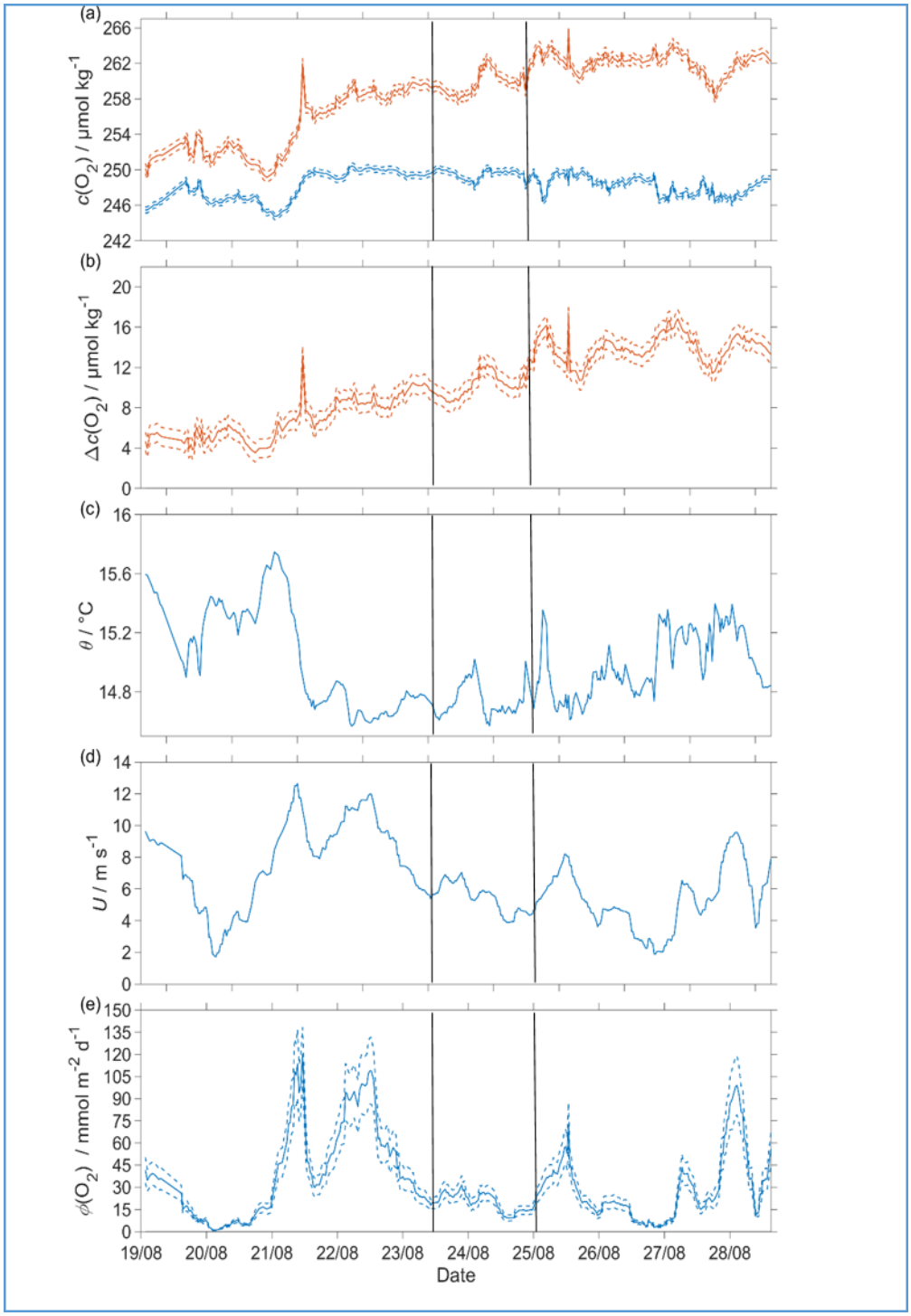

Figure 4.17: Oxygen air-sea flux and the calculation uncertainty where a) shows in blue $c_{sat}(O_2)$ and in red $c(O_2)$ with the dashed lines showing the measurement error, b) $\Delta c(O_2) = c(O_2) - c_{sat}(O_2)$, c) sea surface temperature, d) 10 metre wind speed (U) and e) oxygen air-sea flux $\Phi(O_2)$ with the dashed line showing the calculation error derived using a Monte-Carlo approach (Table 4.1). The flux from sea to air is positive while that from air to sea is negative and black vertical lines divide Region 1 – Region 2 and Region 2 – Region 3.

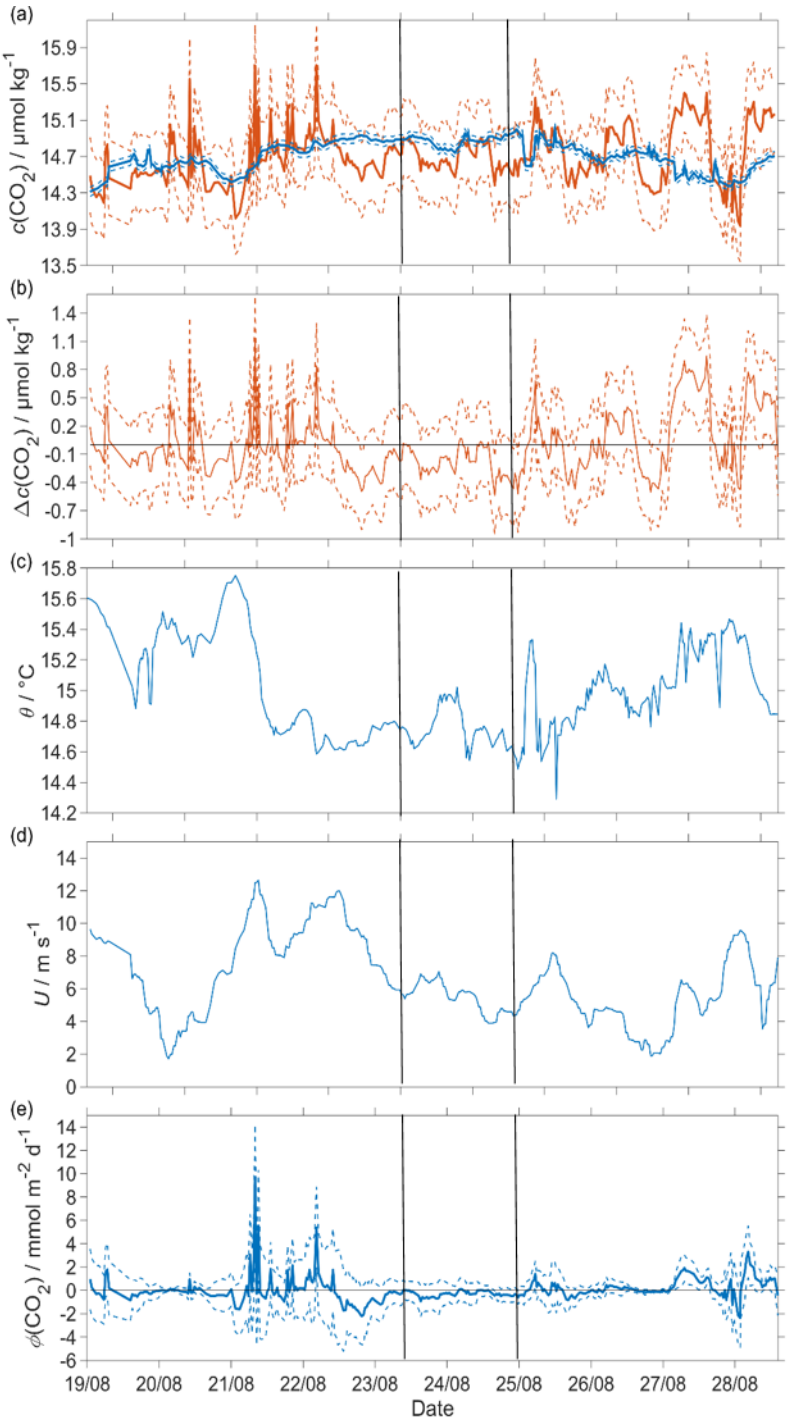

Figure 4.18: CO_2 air-sea flux and the calculation uncertainty where a) shows in blue $c_{sat}(CO_2)$ and in red $c(CO_2)$ with the dashed lines showing the measurement error, b) $\Delta c(CO_2) = c(CO_2) - c_{sat}(CO_2)$, c) sea surface temperature, d) 10 metre wind speed (U) and e) CO_2 air-sea flux $\Phi(CO_2)$ with the dashed line showing the calculation error derived using a Monte-Carlo approach (Table 4.1). The flux from sea to air is positive while that from air to sea is negative and black vertical lines divide Region 1 – Region 2 and Region 2 – Region 3.

4.4.5 Remineralisation in deep waters

During the deployment, the glider encountered three distinct regimes in the BML characterised by different $c(O_2)$ and C_T (Figure 4.19). The water masses in BML were identified using the regime subdivision of section 4.4.3. The southern water mass was identified as CNSW (S was < 34.8), the second regime for S between 34.8 and 34.82 and the northern water mass as NAW (S > 34.82). In regime 1 AOU had a median of 36 µmol kg^{-1} (5th centile: 35.7 µmol kg^{-1}; 95th centile: 36.6 µmol kg^{-1}) and ACP had a median of 16.8 µmol kg^{-1} (5th centile: 15.6 µmol kg^{-1}; 95th centile: 18.9 µmol kg^{-1}). In particular, AOU increased from 36 µmol kg^{-1} to 36.7 µmol kg^{-1} with a rate of (0.2±0) µmol kg^{-1} d^{-1} driven by a decrease of $c(O_2)$ from 248.1 to 245.7 µmol kg^{-1}. ACP decreased from 17.6 to 15.7 µmol kg^{-1} with a rate of -0.1±0.1 µmol kg^{-1} d^{-1} for a decrease of C_T from 2149 to 2145 µmol kg^{-1}. In regime 2 AOU increased to 37.2 µmol kg^{-1} and ACP was 15.9 µmol kg^{-1} comparable with the final ACP of regime 1. In the regime, AOU decreased to 34.8 µmol kg^{-1} with a rate of (-1.5±0.2) µmol kg^{-1} d^{-1} and ACU to 14.9 µmol kg^{-1} with a rate of -1.1±0.2 µmol kg^{-1} d^{-1}. These changes were driven by a decrease of $c(O_2)$ from 245.7 to 243.9 µmol kg^{-1} and C_T from 2148 to 2142 µmol kg^{-1}. In regime 3 AOU remained constant with a median of 34.2 µmol kg^{-1} (5th centile: 33.5 µmol kg^{-1}; 95th centile: 34.6 µmol kg^{-1}). Instead, ACP had a median of 15.7 µmol kg^{-1} (5th centile: 13.8 µmol kg^{-1}; 95th centile: 18.2 µmol kg^{-1}) and increased from 14 to 18.4 µmol kg^{-1} with a rate of 0.9±0.1 µmol kg^{-1} d^{-1} for an increase of C_T from 2141 to 2146 µmol kg^{-1}. The contrast between regimes was stronger in AOU than ACP and the largest change was visible in regime 2 where the glider moved from CNSW to NAW. This may partly be down to the higher measurement uncertainty in the derived inorganic carbon variables compared with the direct oxygen concentration measurements. These calculation errors were one of the reasons for the opposite sign of AOU and ACP rates in regime 1 and 3.

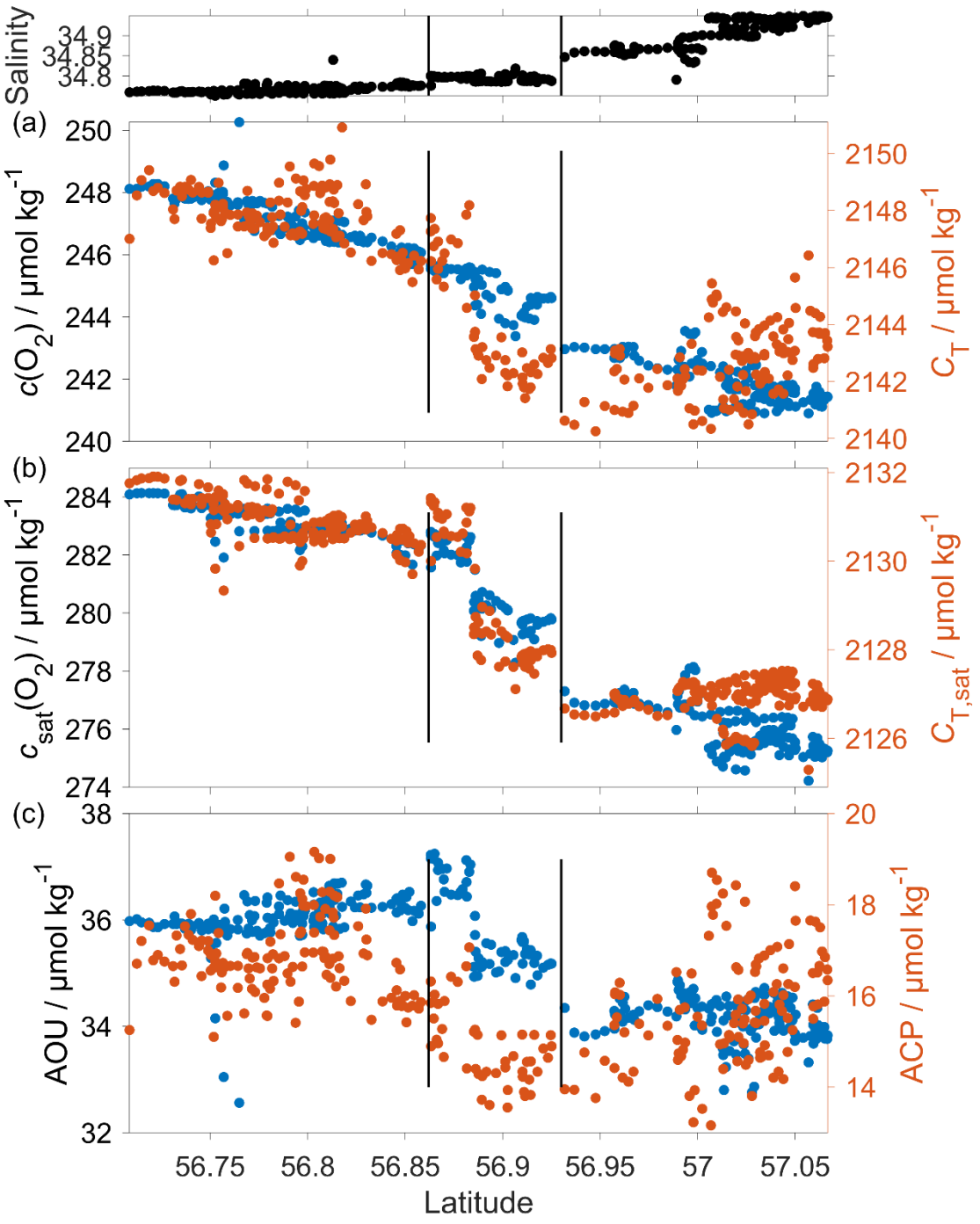

Figure 4.19: The plot shows the different ACP and AOU in BML between the Central North Sea water mass (CNSW) and the North Atlantic water (NAW), a) shows the decrease of C_T (red) and $c(O_2)$ (blue) from CNSW to NAW, b) the decrease of $C_{T,sat}$ (red) and $c_{sat}(O_2)$ (blue) and c) the decrease of ACP (red) and AOU (blue). The top plot shows the increase of salinity in the south to the north transect and the black vertical line shows the passage from regime 1, regime 2 and regime 3.

4.4.6 O_2 and pH diel cycle

I expected that during summer, when mixed layer depths are relatively shallow, the photosynthetic production on the surface causes maxima in pH and $c(O_2)$ in the evening. During the night the main process is respiration leading to daily minima in pH and $c(O_2)$ in the morning. During the deployment, it was not possible to recognise any clear diel cycle in the surface 5 m for pH and $c(O_2)$ (Figure 4.20), indicating that productivity was too low to overcome physical transport effects. To eliminate the effect of temperature on pH and isolate the biological changes, pH_C(NOC) was normalised to 15 °C using a factor of –0.01582 $°C^{-1}$ (Millero, 2007).

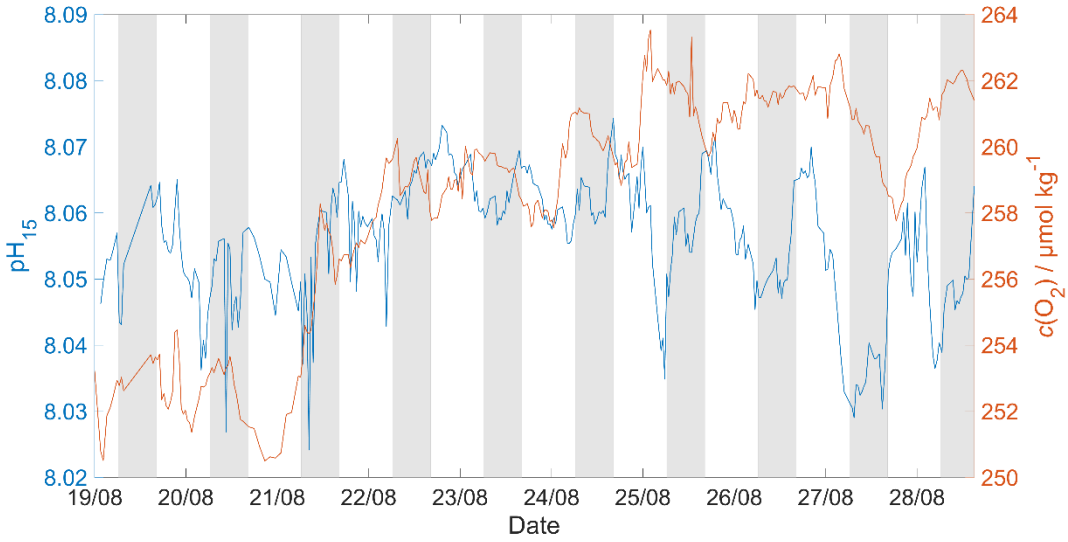

Figure 4.20: Surface 5 meters pH(NOC) normalised to 15 °C (blue) and $c(O_2)$ (red) where the white areas are the periods of the day with sunlight and shaded areas the nights.

4.5 Discussion

4.5.1 pH sensor performance

This is the first study that deployed a spectrophotometric sensor and a glass electrode together on a glider.

The potentiometric sensor (Fluidion) was able to capture the depth pH changes measuring during the first 20 dives every 5 to 20 s. The profiles collected showed a decrease of pH with depth with the maximum at the surface and the minimum at the bottom for a maximum decrease of 0.17. The largest pH change during the profile was measured at the thermocline where the pH changed by 0.12. Before the deployment, the

sensor was not calibrated and for that reason the measured pH (pH(Fluidion)) was 0.4 higher than pH_C(NOC) and pH_{ws}. However, pH(Fludion) could be calibrated in situ using pH_C(NOC) as reference. To avoid reconditioning error on the glass electrode when placed in seawater, the glass electrode was stored for 2 months in seawater before the deployment (McLaughlin et al., 2017). During the deployment, the sensor was not affected by drift because pH(Fluidion) under 60 m was stable with a standard deviation of 0.01 (n = 2308). This value is smaller than the standard deviation at the same depths for pH_C(NOC) that was 0.004 and the general drift for glass electrodes that can reach a maximum of 0.02 d^{-1} (Seiter and DeGrandpre, 2001). Unfortunately, the sensor (Fluidion) failed on the 20 August after 2 days due to a file system management problem (a new file was created for each sample, which the processor was too slow to manage). For that reason, the data collected by the Fluidion sensor were not used in any further analysis due to the limited spatial and temporal coverage. After the deployment, Fluidion solved this problem and now the sensor creates a single file for all the deployment.

After the lag correction (section 4.3.3) the NOC sensor was stable and accurate throughout the deployment. Compared with the discrete samples collected at the glider deployment and recovery the NOC sensor had a mean pH offset of 0.006±0.008. This performance fulfils the Global Ocean Acidification Observing Network (GOA-ON) weather goal (<0.02) but is not sufficient for the climate goal (<0.003) (Newton et al., 2014). Also, these values are in agreement with previous deployments of the sensor. Rérolle (2013a) operated the sensor continuously on a cruise with an accuracy that varied from 0.005 to 0.013. Later the sensor was tested on another cruise in the Arctic on an underway seawater supply (intake at 6 m depth) with an uncertainty of 0.007 (Rérolle et al., 2016).

4.5.2 North Sea subsurface oxygen maximum

In shelf seas, deep chlorophyll maximum (DCMs) can be found when nutrient-rich bottom waters are isolated from the surface by the formation of a seasonal thermocline. DCMs are the most productive layers accounting for 58 % of all water column production (Weston et al., 2005). In the northern North Sea, the formation of DCMs is common (Richardson et al., 1998; Richardson, Visser and Pedersen, 2000; Fernand et al., 2013) and up to 70 % of the daily primary production occurs at the DCM (Richardson et al.. 1998).

During the glider deployment, two SOMs were observed, which shows that the SML was nutrient-limited. Nutrients in the SML are consumed during the spring bloom allowing

phytoplankton production only below z_{mix}, supported by the nutrient-rich BML (Fernand et al., 2013). After the spring bloom, the limiting nutrient for new production is generally nitrate (Riegman et al., 1990; Skogen et al., 2004). Typically, these SOMs are related to the presence of a DCM. The rosette fluorometer confirmed the presence of a DCM because at the glider deployment a c(Chl a) maximum of 2.9 mg m^{-3} measured at the same depth of SOM (30 m). The fluorometer was not calibrated, therefore this value is not expected to be accurate. Unfortunately, the fluorometer failed in the second half of the cruise and c(Chl a) could not be measured at glider recovery.

Queste et al. (2016) in August 2011 deployed at 56.41° N, 2.26° E a glider next to Dogger Bank for 3 days equipped with a 4330F oxygen optode and a chlorophyll fluorometer. The glider measured the presence of a DCM with a c(Chl a) maximum of 2.5 mg m^{-3} associated, with an increase of $c(O_2)$ from 250 µmol dm^{-3} in the SML to 270 µmol dm^{-3} at the DCM. This increase of $c(O_2)$ from SML to SOM is in agreement with my results that showed an increase of 25 µmol kg^{-1} when the SOM was at 30 m. However, when the SOM was at 10 m the increase of $c(O_2)$ from SML to SOM was just 10 µmol kg^{-1}.

In the same deployment, Queste et al. (2016) measured a strong increase in time of AOU in the BML by 2.8±0.3 µmol dm^{-3} d^{-1}. This strong increase led to a maximum AOU of 85 µmol dm^{-3} indicating the presence of an unknown oxygen sink. Queste et al. (2016) hypothesised this high oxygen consumption was linked to localized depocentres and rapid remineralisation of resuspended organic matter.

The change of AOU is larger than AOU and ACP changes measured in my study. My deployment uncovered the presence of three different biogeochemical regimes, characterised by a different $c(O_2)$, S and θ signals and DCM depth. When in the same regime the maximum AOU change was -1.5±0.2 µmol kg^{-1} d^{-1} and was -1.1±0.2 µmol kg^{-1} d^{-1} for ACP. The results of my study suggest that the high oxygen consumption measured by Queste et al. (2016) could be affected by the presence of different regimes and not just by temporal changes. The presence of different regimes would explain the large increase in AOU. For future studies, to quantify the changes of AOU and ACP, the glider should be deployed in the same regime remaining in the same location.

The large spatial variability was confirmed by the satellite 5 day-composite chlorophyll concentration (c_S(Chl a)) from Ocean Colour CCI (https://esa-oceancolour-cci.org/) measured the 5 days before the glider deployment, the first and last 5 days of the deployment. During and before the deployment the satellite chlorophyll increased from south to north and from east to west, following the glider transect (Figure 4.21). Despite the presence of the DCM the lowest c(Chl a) was in regime 1 with 0.4 mg m^{-3} in the first 5 days of deployment and 0.3 mg m^{-3} in the last 5 days. This low concentration can be

explained by the deep DCM (30 m) that could not be captured by the satellite. This result shows the limitation in the use of satellite chlorophyll to capture the biological production in presence of DCMs. In particular, the 30 m deep DCM had the largest increase of $c(O_2)$ from SML and the use of c_S(Chl a) would lead to large uncertainties in the estimation of biological production. The maximum c(Chl a) was measured in regime 3 when DCM was at 15 m with 0.6 mg m^{-3} in the first 5 days of deployment and 0.5 mg m^{-3} in the last 5 days.

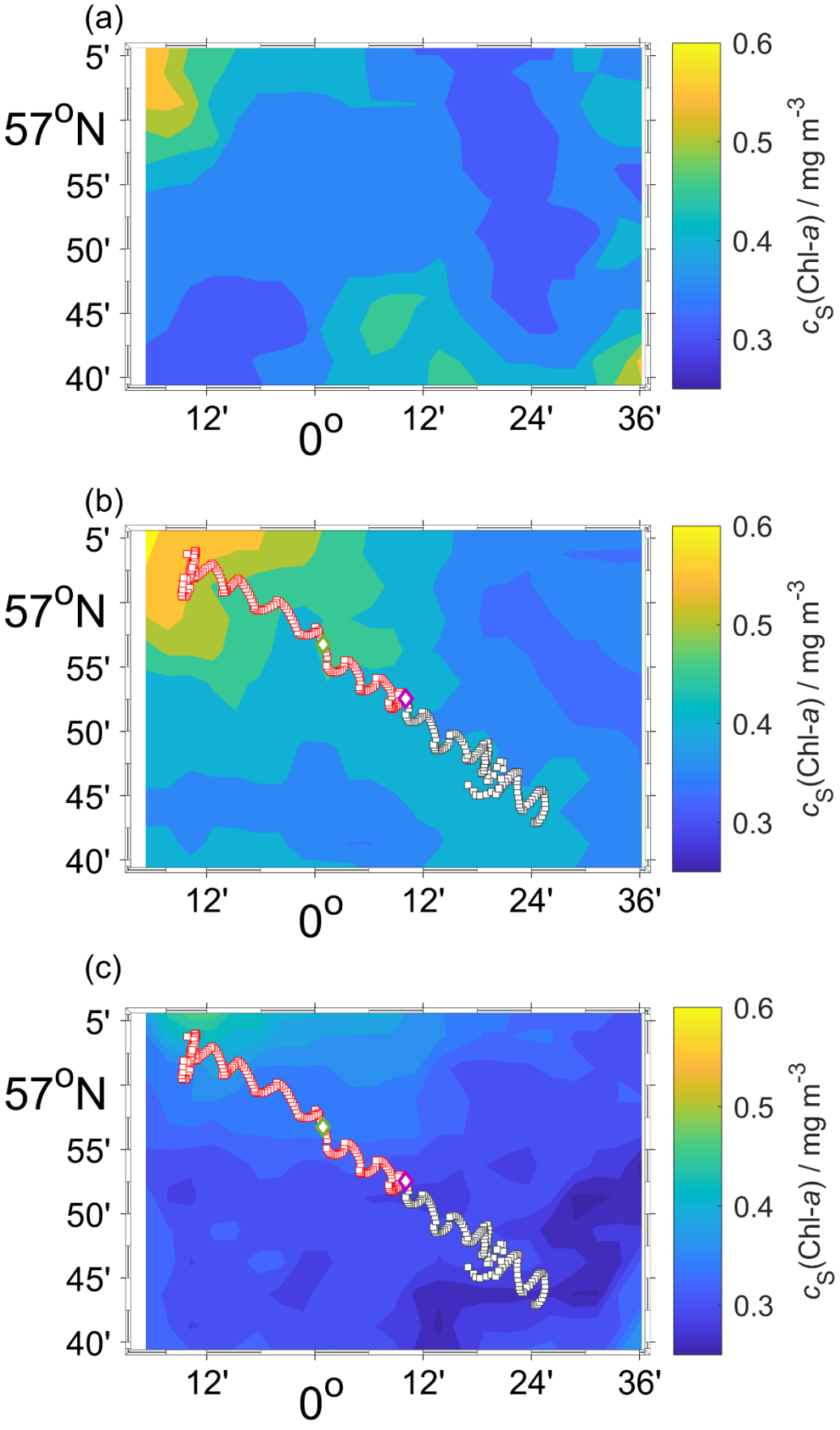
(a)
(b)
(c)
57°N
5'
55'
50'
45'
40'
0°
12'
24'
36'
0.6
0.5
0.4
0.3
c_S(Chl-*a*) / mg m^{-3}

Figure 4.21: 5 days composite mean of the satellite chlorophyll (https://esa-oceancolour-cci.org/). a) shows the days between 14 to 19 of August b) from 19 to 24 of August and c) from the 24 to the 29 August, the black dots represent the glider transect from the 19 to the 24 August and the red dots from the 24 to 29 August. The pink diamond shows the dive when the glider passed from regime 1 to regime 2 and the green diamond from regime 2 to regime 3.

4.5.3 North Sea air-sea exchange

The North Sea air-sea flux varies in space and time; during winter the North Sea appears as an equilibrated system with a positive $\Phi(CO_2)$ in the southern North Sea up to 10 mmol m^{-2} $month^{-1}$ and a negative $\Phi(CO_2)$ in the northern part up to -10 mmol m^{-2} $month^{-1}$. Later, when the spring bloom decreases the surface $p(CO_2)$ all the North Sea acts as a sink for atmospheric CO_2. During the summer the stratified northern North Sea continues acting as a CO_2 sink but in the fully mixed southern part the increase of temperature and remineralisation turns the surface seawater into a CO_2 source. In autumn the end of the primary production in all North Sea turns the system in a CO_2 sink, making on the annual scale the North Sea a net CO_2 sink (Thomas et al., 2004, 2005). In agreement with our discrete samples (Figure 4.22), another study from Bozec et al. (2005) found that in late summer (mid-August-September) the whole North Sea acted as a CO_2 sink in the range of -1.5 to -2.2 mmol m^{-2} d^{-1} with the southern North Sea acting as a CO_2 source between 0.8 and 1.7 mmol m^{-2} d^{-1}. In the northern North Sea, the flux varied from -2.4 to -3.8 mmol m^{-2} d^{-1}. Considering the whole year the northern North Sea is a CO_2 sink (-2.06 mol m^{-2} a^{-1}) and the southern North Sea is a weak net CO_2 source (0.78 mol m^{-2} a^{-1}). The northern North Sea $\Phi(CO_2)$ changes are controlled by the high NCP and in the southern North Sea NCP is generally low and $\Phi(CO_2)$ changes are controlled by temperature (Prowe et al., 2009).

The expected inversion of $\Phi(CO_2)$ direction was located by Thomas et al. (2005) at 54° N. The glider was deployed in the northern North Sea (Figure 22) and the high temporal resolution was able to capture the hourly $\Phi(CO_2)$ changes. During the glider deployment, the surface layer acted as a moderate sink (-0.1 mmol m^{-2} d^{-1}), however the $\Phi(CO_2)$ direction and size changed several times during the deployment mainly driven by U and $c(CO_2)$ changes (Figure 4.18). The high-resolution dataset uncovered a smaller $\Phi(CO_2)$ than Bozec et al. (2005) because it was able to capture the hourly changes of $\Phi(CO_2)$. The data collected gave new insights into the flux drivers showing that $\Phi(CO_2)$ was heterogeneous in space but was not in agreement with the changes in the three biogeochemical regimes that were confined just in the bottom mixed layer, BML.. Even

if O_2 is less soluble in seawater than CO_2, $\Phi(CO_2)$ was up to 10 times smaller than $\Phi(O_2)$ that was an O_2 source throughout the deployment (25 mmol m^{-2} d^{-1}). The smaller $\Phi(CO_2)$ compared to $\Phi(O_2)$ is explained by larger $c_{sat}(O_2)$ compared with $c_{sat}(CO_2)$ driving larger $\Delta c(O_2)$ than $\Delta c(CO_2)$. In fact, the maximum $\Delta c(O_2)$ was about 17 times larger than $\Delta c(CO_2)$. For that reason, the CO_2 equilibration time is about 20 times longer than for O_2 (Zeebe and Wolf-Gladrow, 2001). This slow equilibration time depends on the ocean carbonate chemistry because CO_2 is just a small part (0.5 %) of C_T.

As for $\Phi(CO_2)$ despite the measurement of three different biogeochemical regimes the $\Phi(O_2)$ changes did not vary in space but were mostly driven by U and $\Delta c(O_2)$. Also, $\Phi(O_2)$ was heterogeneous in space but its changes were not in agreement with the three biogeochemical regimes. Because most production takes place in the SOM, most of the corresponding changes in $c(O_2)$ were confined within the BML deeper than z_{mix}, and thus could not affect the surface $c(O_2)$.

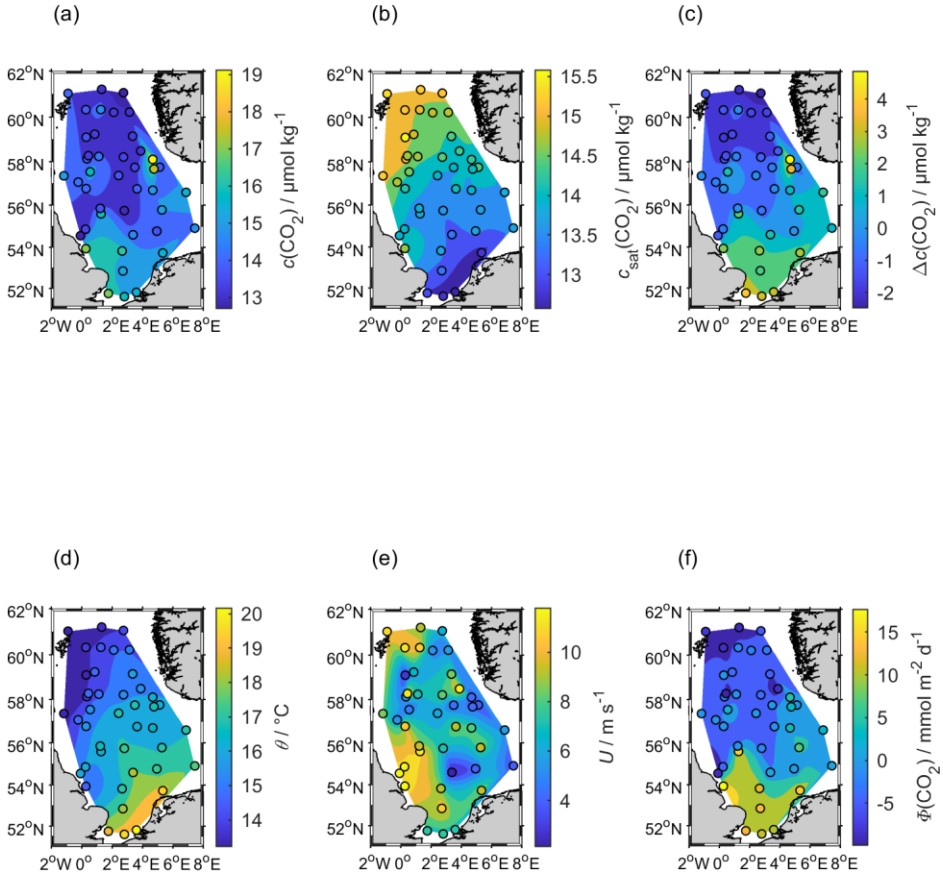

Figure 4.22: CO_2 air-sea flux ($\Phi(CO_2)$) calculated using the surface discrete samples collected on CEND12/19 cruise where a) shows the $c(CO_2)$ derived from C_T and A_T, b) $c_{sat}(CO_2)$, c) the difference between $c(CO_2)$ and $c_{sat}(CO_2)$ ($\Delta c(CO_2)$), d) temperature (θ), e) wind speed (U) and f) $\Phi(CO_2)$.

4.6 Conclusions

This study was one of the first glider deployment of a spectrophotometric and potentiometric pH sensor. This deployment shows the potential of using miniaturised pH sensors on autonomous observing platforms like gliders to quantify the interactions between biogeochemical processes and the marine carbonate system at high spatiotemporal resolution. In particular, the study was located in the northern North Sea where the depth was always shallower than 150 m. This deployment required the use of loiter dives because of the NOC sensor's long sampling time (11 min). Loiter dives tripled

the glider battery usage but allowed the collection up to 9 pH measurements per dive compared to 2 ona normal dive. The number of samples collected by the NOC sensor can be reduced to 1 or 2 per day when coupled to a functional pH glass electrode. In this configuration pH(NOC) will be used to calibrate and drift correct the glass electrode allowing longer deployments. The use of a spectrophotometric sensor can reduce the mission costs because the collection of discrete samples will not be required. The Fluidion sensor has the potential to be used in such deployments but its performance needs to be assessed in future deployments. In this study, the sensor showed a good potential for studies that want to look at short term in situ changes (< 0.02) and long term ocean acidification studies (< 0.003) because in 2 days was stable with non-detectable drift (< 0.001) and was able to capture the pH changes with depth.

This study showed that mounting the O_2 optode facing downward looking at the glider body could eliminate the spikes caused by the sunlight hitting the sensing foil. The residuals spikes were probably caused by the contact of the sensor with air and the injection of dissolved bubbles in the surface waters. In future deployments, these residual spikes can be eliminated mounting the O_2 optode 30 cm under the current position on the glider body.

The calculation of NCP in shelf seas is challenging because of the spatial variability. For example, the data collected during this deployment did not allow the calculation of the NCP because of the large spatial variability. To calculate NCP, the glider must be always in the same water mass and during this deployment in just 10 days the glider moved in 3 different biogeochemical regimes. Also, the pH measured by the NOC sensor was too sparse to enable the measurement of the key processes influencing NCP such as entrainment, vertical mixing, horizontal advection and inventory changes. In chapter 2 it was possible to calculate NCP because the glider was for several months in the same water mass and the O_2 and CO_2 optode measured a complete profile with high temporal resolution (< 110 s in the top 100 m).

Chapter 5

Conclusions and Outlook

5.1 Best practices in the use of pH sensors

In this thesis, two potentiometric pH sensors developed by AMT and Fluidion and a NOC lab-on-chip spectrophotometric pH sensor were tested in the laboratory. A series of experiments were performed to identify the best practices to use these sensors in ocean studies. Here, I discuss the results and implications of these experiments.

Commonly glass electrodes are stored in 3 M KCl and then placed directly in seawater causing a drift due to the reconditioning to seawater. This drift was quantified for the 2 glass electrodes in a 4 days laboratory experiment where the sensors were placed in seawater from 3 M KCl. On the first day, the AMT sensor had a drift of 0.018 h^{-1} and the Fluidion sensor of 0.013 h^{-1} that decreased on the fourth day to 0.007 h^{-1} for AMT and 0.0003 h^{-1} for Fluidion. In previous studies storing the sensor in seawater significantly decreased the reconditioning time allowing accurate measurements from the first day of deployment (Johnson et al., 2017; McLaughlin et al., 2017). The results show that the glass electrodes are affected by drift when placed in seawater and this drift can be minimised by storing the sensor in seawater for several weeks. Also, storing and using the glass electrodes in a Tris buffer made in synthetic seawater (Dickson et al., 2007) causes irreversible damage to the glass electrodes the glass electrodes. The AMT and Fluidion electrodes needed to be replaced after several months of experiments in Tris.

Temperature has an important effect on glass electrodes performance that McLaughlin et al. (2017) quantified as an increase of the offset from the reference pH by 0.0025 $°C^{-1}$. During my laboratory experiments, the AMT and Fluidion sensor did not measure the expected Tris pH and as during McLaughlin et al. (2017) experiments the size of the offset from the expected pH increased with temperature. However, the two glass electrodes were not affected by salinity and more experiments are needed to assess if larger salinities changes (> 10) can have an effect.

For ocean studies pH sensors need to have an accuracy < 0.02 to identify relative spatial patterns and short-term variation (weather goal) and < 0.003 for ocean acidification (OA) studies that assess long term trends (climate goal) (Newton et al., 2014). The

spectrophotometric method is not affected by drift, is precise (<0.001) and does not require any calibration (Rérolle et al., 2012). The calibration is not needed because the method determines the absorption ratio of the acidic and basic forms of the indicator dye. During the experiments in Tris, the NOC sensor mean offset from the Tris pH varied from 0.002 to 0.006 and was 0.005 compared with the pH of the discrete samples (n = 6) when tested in the dock in front of the National Oceanography Centre in Southampton, United Kingdom. The two glass electrodes were not calibrated before the experiments and their offsets from the Tris pH varied from -0.026 to 0.267. The use of a miniaturised spectrophotometric sensor for in situ deployments is generally limited by the sensor complexity requiring several valves and pumps to propel the sample and indicator dye through the system. Other problems are the power consumption, bulky size, frequent measurement of blanks and the use of indicator dye. The NOC sensor overcomes all these problems because it has low power consumption (3 W while measuring), uses a small amount of indicator dye (2.2 µL) and the sample waste is usually stored in a separate bag for environmental protection reasons. However, the *m*CP indicator dye is not harmful to the environment and in future deployments the sampled seawater can be released in the ocean. The storage of the sampled seawater would need a specific bag that can be filled in a couple of weeks and would significantly reduce the length of the deployment. Another limitation is the necessity to deploy the NOC sensor coupled with a CTD to convert the absorbance ratio (R) in pH using temperature, salinity and pressure (Soli et al., 2013) and then to convert the measured pH from the sensor internal temperature to the environmental temperature. For future mooring and float deployments, the NOC sensor can be integrated with a CTD into a single system and perform all the calculations automatically.

Many research groups calibrate glass electrodes in the laboratory using buffers made in synthetic seawater such as Tris and AMP or the National Bureau Standards of (NBS) (McLaughlin et al., 2017). A precise procedure is required for preparing Tris to ensure the error in the final pH of the buffer is within 0.006 of the published pH value(Paulsen and Dickson, 2020). The use of NBS buffers is not optimal for ocean studies because they have lower ionic strength (0.1 mol kg^{-1}) than seawater (0.7 mol kg^{-1}) that can lead to an error in the liquid junction potential (Wedborg et al., 1999). To overcome these calibration problems the sensor should be calibrated in situ using discrete seawater samples or a miniaturised spectrophotometric pH sensor. The use of a miniaturised spectrophotometric sensor does not require the preparation of any buffers, reduces labour costs and allows long unattended deployments. Moreover, in prolonged deployments the methodology can correct for the temperature effect on glass electrodes, drift and possible salinity hysteresis in estuarine environments. Coupling the NOC sensor and the Fluidion glass electrode is perfect for a series of platforms such as moorings,

floats and gliders. In chapter 3 the NOC sensor was used as a reference to calibrate the two glass electrodes reducing the mean offset in Tris to 0.002 and in the Southampton dock from 0.129 to 0.002 compared with the discrete samples. The deployment of the NOC and Fluidion sensors can be prolonged up to 1 year, the NOC power and dye consumption can be reduced by sampling once a day. The collection of one sample per day is acceptable because the NOC pH is used to quantify and correct the glass electrode drift and assess the glass electrode accuracy. However, this is only possible if the glass electrode is stable as in the North Sea deployment and not unstable as during the laboratory experiments. The required stability can be reached storing the glass electrodes in seawater for more than 2 months before the deployment. The advantage of using glass electrodes is the 1 s (AMT Analysenmesstechnik GmbH, 2014) time resolution that allows resolving at high temporal resolution processes such as air-sea flux, vertical and horizontal mixing, remineralisation and respiration and $CaCO_3$ dissolution and formation.

Despite all these limitations the NOC sensor and the glass electrode together have the potential to be used in OA studies. The deployment will require the two sensors together with a CTD and the spectrophotometric pH will be used as reference to daily calibrate the glass electrode. Deploying the two sensors as an automated system can help to fill the gap of large areas of the planet that remain under sampled and can help to reduce the research costs required to run large research vessels. The same configuration can be applied replacing the glass electrodes with other high-resolution sensors such as optodes and ISFET pH sensors.

5.2 New carbonate sensors on a glider

In recent years efforts to study the carbonate system using automated in situ platforms such as gliders are growing. The sensors to be implemented on a glider to measure the oceanic carbonate system need to have a compact size, low-cost and high temporal (< 100 s) and spatial resolution (< 2 m vertically). This thesis focused on the implementation of a CO_2 optode and two pH sensors (potentiometric and spectrophotometric) on a Seaglider. The sensors used are still at an experimental stage and still need improvements to be commercialised. The deployments focused on assessing the sensor's performance and suggest possible future improvements.

The O_2 and CO_2 optodes drift and lack of sampling at the surface were probably caused by the sunlight hitting on the sensing foil. To avoid the effect of sunlight that causes the bleach of the foil indicator dyes, Binetti et al. (2020) suggested to face down the O_2

optode with the foil looking at the glider body. During the North Sea deployment the O_2 optode was placed in this position eliminating the effect of sunlight on the optode readings. The same positioning might help to reduce the measurement noise at the surface and increase the accuracy of the CO_2 optode. For long deployments, the CO_2 optode needs to be accurately calibrated in the range of the expected $c(CO_2)$ in the deployment region. The regional concentrations and the spatial and temporal variability can be compared with online databases such as GLobal Ocean Data Analysis Project (GLODAP) (Olsen et al., 2016) or the Surface Ocean CO_2 Atlas (SOCAT) (Bakker et al., 2016). Also, the sensor needs to be calibrated using $c(CO_2)$ rather than $p(CO_2)$ and the final output should be reported as $c(CO_2)$.

Despite all these problems, the CO_2 optode was able to quantify the inorganic carbon changes in space and time with a temporal resolution of 106 s in the top 100 m which increased to 381 s from 500 to 1000 m. The temporal resolution can be reduced to less than 10 s as for the O_2 optode in the North Sea deployment. With a series of improvements and a better understanding of the sensor sampling principle, the CO_2 optode can be routinely used to measure the carbonate system on gliders. These deployments can last up to 8 months and the sensor can be coupled with other sensors because of the low power consumption of 80 mW at 5 s sampling frequency and 7 mW at 60 s sampling frequency (Atamanchuk et al., 2014) and the small size.

Chapter 4 describes a 10 days glider deployment in the North Sea using the Fluidion glass electrode and the NOC pH sensor. After storing the Fluidion sensor in seawater for 2 months, it was not affected by drift (<0.001) and was able to capture the pH changes with depth. The sensor failed after 2 days because it created a new file every measurement (5 s) and after two days the internal memory was full and was not able to perform any further measurement. After the deployment, Fludion worked to resolve this problem and now during a glider deployment the sensor writes all the results in an unique file. This gives the potential to use the Fluidion sensor for future deployments on autonomous underwater vehicles. New deployments need to be performed to assess the stability and accuracy of the sensor in a prolonged mission. The NOC sensor was affected by a lag (time-shift) between 144 and 192 s. The deployment showed the potential of using lab-on-chip sensors on gliders to capture spatial and temporal changes. However, the 11 minutes sampling rate did not allow measuring the full pH profile but just 2 to 9 samples per 100 m dive. The number of samples increased from 2 to 9 during loiter dives where the glider buoyancy was reduced. The use of loiter dives reduced the glider vertical speed during the ascent but increased by 3 times the battery usage. Loiter dives in a prolonged mission would significantly reduce the mission length. For that reason, to resolve small-scale processes such as vertical mixing and have a

complete profile it is necessary to use a second carbonate sensor with a higher measurement frequency (ideally < 1 min).

It is necessary to measure two different carbonate quantities to calculate the two remaining carbonate variables. Currently for glider deployments, it is only possible to couple a pH sensor with a CO_2 optode because miniaturised, in situ A_T and C_T sensors are still at an initial development stage. The sensors that can be potentially used are the ISFET and potentiometric pH sensors and the CO_2 optode. However, the pairing of pH with $p(CO_2)$ is the worst coupling because leads to an error of ±21 μmol kg^{-1} in the estimation of A_T and ±18 μmol kg^{-1} for C_T (Table 1.2) (Millero, 2007). Routinely, the second quantity coupled with pH or $p(CO_2)$ is A_T derived from a regional parameterisations that uses temperature and salinity. In the coming years, new sensors that measure A_T and C_T need to be developed along with existing $p(CO_2)$ and pH sensors. Measuring two carbonate quantities at the same time can for instance reduce the uncertainties in the calculation of net community production, air-sea gas exchange, respiration and remineralisation and aragonite saturation state. New sensors to in situ measure C_T (Liu et al., 2013; Fassbender et al., 2015; Wang et al., 2015; Chu et al., 2018) and A_T (Spaulding et al., 2014) have been successfully tested but are still bulky, have high energy consumption and use multiple valves and pumps to be deployed on a glider. New lab-on-chip A_T and C_T sensors are currently being developed by the OTE group at NOC in Southampton and have the potential to fill this gap.

This is the third study to deploy a pH sensor on a glider and the first study to deploy a CO_2 optode on a glider. The previous studies deployed two ISFET sensors on a Seaglider and Slocum glider (Hemming et al., 2017; Saba et al., 2019). The ISFET technology is probably the most mature for in situ pH measurements, in fact the Deep-Sea DuraFET is used on 86 Argo floats deployed in the Southern Ocean as part of the SOCCOM project (Williams et al., 2017). The ISFET sensors are expected to become commercially available in the next few years and have the potential to replace the glass electrodes for ocean studies. At the moment, ISFET sensors are commercially available just in the SeapHOx system that integrates an ISFET pH sensor, a CTD and an oxygen sensor. However, the use of the ISFET sensors on gliders is limited by the requirement of a pumped CTD that increases battery usage reducing the deployment length and limits the coupling with other sensors. In Hemming et al. (2017) deployment an ISFET sensor was deployed without a pumped CTD and the sensor stability was poor and drifted in a non-monotonous fashion. In another deployment, Saba et al. (2019) coupled a Deep-Sea ISFET sensor (Johnson et al., 2016; Martz et al., 2010) with a pumped CTD improving the final pH stability and accuracy. Also, in prolonged deployments ISFET sensors require to be regularly calibrated to correct the sensor drift.

The use of these sensors on gliders can be used along with research ships, moorings, buoys and floats to expand the knowledge on the ocean inorganic carbon. The two deployments showed the potential of using carbonate sensors on autonomous observing platforms like gliders to quantify the interactions between biogeochemical processes and the marine carbonate system at high spatiotemporal resolution. In the two deployments, the data was used to calculate air-sea gas exchange, net community production, remineralisation and respiration and the spatial and temporal changes. Ocean gliders have the advantage of being cheaper to operate than research ships and unlike moorings and floats, the pilot can select the horizontal direction of travel. The results show that it is fundamental to accurately and frequently calibrate the sensors before and during the deployment. The calibration can be performed in the laboratory or in situ during the deployment using miniaturised spectrophotometric sensors or discrete samples. When a spectrophotometric sensor cannot be deployed it is necessary to collect discrete samples at the glider deployment and recovery and at least every 2 weeks. These discrete samples can be used to validate the sensor performance, in situ calibrate the sensors and correct any potential drift. Instead, when a miniaturised spectrophotometric sensor is deployed is not necessary to collect any discrete samples reducing the deployment costs.

5.3 Best practices to calculate net community production using gliders

The deployment of inorganic carbon sensors on gliders can be used to quantify the net community production (NCP). In chapter 2 the O_2 and dissolved inorganic carbon (C_T) NCP in the Norwegian Sea, $N(O_2)$ and $N(C_T)$ were calculated. The deployment was affected by the presence of two different water masses the Norwegian Atlantic Current (NwAC) and the Norwegian Coastal Current (NCC), which limited the NCP temporal coverage. In the future to accurately estimate the annual Norwegian Sea $N(O_2)$ and $N(C_T)$ at least one glider needs to be always in the water sampling the Svinøy transect all year. Kivimäe, (2007) showed that $N(C_T)$ and $N(O_2)$ are variable between years. The continuous presence of a glider on the Svinøy transect can help to identify the causes of this variability. In my study, the presence of two different surface water masses led to a period when $N(C_T)$ and $N(O_2)$ were not calculated. For that reason, an ideal deployment needs two gliders in the water at the same time, one next to the Norwegian coast in NCC (5° E 63° N) and the second in the middle of the Norwegian Sea in NwAC (10° W 63° N). Moreover, to calculate the horizontal advection the two gliders should follow a butterfly shape transect to be completed in 4-5 days (20 x 20 km) (Alkire et al., 2014). To

compare the glider measurements and have a second estimate of the horizontal advection the gliders should be deployed next to a buoy carrying the same sensors of the glider and completing the same depth profiles (1000 m) of the glider. Also, to validate the buoy and glider measurements A_T and C_T discrete samples should be collected at least once a week. The ideal scenario would be to deploy one extra glider per water mass completing in 12 days a larger butterfly shape transect (50 x 50 km) to identify larger horizontal gradients and have another reference to estimate the stability of the sensors (Figure 5.1). The calculation of advection using glider data relies on that O_2 and C_T changes vary on time scales longer than 4 days. Shorter butterflies transect can help to calculate the short-time changes of the advective flux. However, this is not necessary when advection is calculated using the buoy data along with the glider. To capture this short time changes the buoy needs to be deployed in the middle of one of the two ties of the butterfly transect. To reduce the deployment costs a spectrophotometric sensor can be deployed on the buoy. The spectrophotometric sensor can be used as reference to assess the sensors performance and quantify the horizontal advection. Using this configuration means that the collection of discrete samples is not necessary.

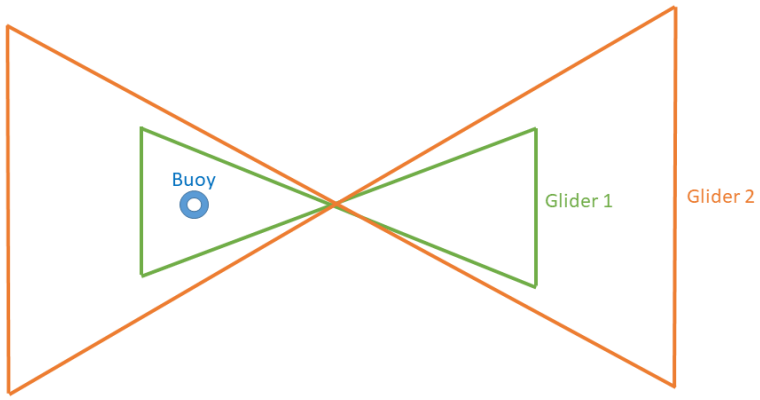

Figure 5.1: Ideal glider mission to calculate the net community production (NCP). The deployment requires two gliders performing a butterfly shape transect 20 x 20 km in 5 days (green), 50 x 50 km in 12 days (orange) and a buoy (blue).

Similar deployments can be used in other areas of the globe to fill the gaps in the estimates of $N(C_T)$ and $N(O_2)$. In particular, other sensors can be used to derive C_T such as pH glass electrodes, ISFET and spectrophotometric pH sensors. The coupling of the

CO_2 optode along with a pH sensor can be used for a second estimate of A_T that can be compared with A_T calculated using a temperature and salinity regional parameterisation. The deployment of a spectrophotometric sensor allows the calculation of NCP in remote areas of the globe such as the Southern Ocean and the Arctic where it is not possible to weekly collect discrete samples. A possible combination would be a glass electrode (Fluidion) and the spectrophotometric sensor (NOC) but the deployment length would be significantly shorter than the 8 months achieved with the CO_2 and O_2 optode.

Around the globe to identify the size and causes of the interannual variability in NCP, it is important to have continuous datasets collecting data in the same location for several years. Following the examples of SOCCOM (Johnson et al., 2017; Williams et al., 2017), globally this can be achieved by collaborations between institutions to build a global network of gliders deployed in different areas of the planet to measure $N(C_T)$ and $N(O_2)$. In particular, this has high potential in under-sampled areas of the globe such as the Southern Ocean and the Arctic. Also, it can be used in well-studied areas such as the North and Mediterranean Sea to reduce the monitoring costs and compare the NCP estimates with previous studies that used other sampling strategies.

5.4 Capture ocean inorganic carbon and oxygen changes using gliders

The two glider deployments in the North and Norwegian Sea allowed capturing several oceanographic characteristics of the two regions. In the Norwegian Sea, the calculated net community production (NCP) all the spring and summer periods was mostly positive showing the presence of an autotrophic system. However, after the spring and summer bloom the NCP turned negative showing a heterotrophic system. In agreement with the literature, from March to July the surface water was a source of O_2 and a sink of CO_2 (Takahas*hi* et al., 2002; Skjelvan et al., I2005, Skjelvan et al., 2001). In August, the surface water became undersaturated by –2.6 µmol kg^{-1}, causing an O_2 uptake with a median flux of -13 mmol m^{-2} d^{-1}. Also, the glider was able to capture the different concentrations of C_T, $c(O_2)$ and chlorophyll (c_{raw}(Chl *a*)) between the different water masses in the region. The Norwegian Coastal Current (NCC) was characterised by a lower concentration of C_T and $c(O_2)$ than the Norwegian Atlantic Current (NwAC). The C_T concentration in NCC was (2081±39) µmol kg^{-1} and in NwAC was (2146±27) µmol kg^{-1} and $c(O_2)$ was >300 µmol kg^{-1} in the NwAC and <280 µmol kg^{-1} in the NCC. These different concentrations lead to lower NCP values in NCC. The calculated NCP was mostly driven by inventory changes, air-sea gas exchange with a smaller contribution

of entrainment and diapycnal mixing. The values of the derived NCPs were in agreement with previous studies that used low-resolution datasets (mostly discrete samples). The results showed that the use of high-resolution data did not change the integrated production over time and the regional net community production had not a strong interannual variability. Also, the derived photosynthesis quotients (PQ) were in agreement with the original Redfield ratio of 1.45±0.15 (Redfield, 1963; Anderson, 1995; Anderson and Sarmiento, 1994; Laws, 1991). The agreement with the Redfield ratio showed that the NCP variability was controlled by biological production. In particular, PQ was 1.3 using an integration depth of 30 and 45 m and decreased to 1.1 with an integration depth of 100 m. The lower PQ at 100 m was driven by lower oxygen NCP because of O_2 consumption during organic matter remineralisation below the euphotic zone.

The 10 days glider deployment in the North Sea allowed quantifying the air-sea gas exchange, deep water remineralisation and pH and O_2 spatial and temporal changes. The surface water was a source of oxygen during all the deployment with a median of +25 mmol m^{-2} d^{-1}. In contrast, the CO_2 air-sea gas exchange was almost zero with a median of -0.1 mmol m^{-2} d^{-1}. This result is unexpected because previous studies showed that in late summer (August-September) the northern North Sea is a CO_2 sink (Bozec et al. 2005; Thomas et al., 2004, 2005). This difference might be caused by interannual variability or a smaller CO_2 air-sea gas exchange compared with the previous studies performed more than 15 years ago. Continuous monitoring over time is needed to quantify the interannual and temporal variability. Despite the short transect (45 km), the glider captured 3 different biogeochemical regimes. The first regime was characterised by a subsurface oxygen maximum (SOM) at 30 m; the second regime had no distinct SOM and the third regime had a SOM at 15 m. The shallowing of the SOM and mixed layer depth caused an increase of surface $c(O_2)$ from 250 to 264 µmol kg^{-1}. However, this increase was not visible in the measured pH that a median of 8.058 (5^{th} centile: 8.040; 95^{th} centile: 8.065). The Fludion pH sensor in the first two days of deployment captured a pH maximum at 30 m associated with the SOM. The oxygen increase at the SOM was associated with a deep chlorophyll maximum (DCM). The presence of DCM is typical of the northern North Sea (Richardson et al., 1998; Richardson, Visser and Pedersen, 2000; Fernand et al., 2013) and can be found when nutrient-rich bottom waters are isolated from the surface by the formation of a seasonal thermocline. In deep water (>50 m) the glider identified two different water masses the Central North Sea Water (CNSW) and the North Atlantic Water (NAW). The two water masses had a positive Apparent Oxygen Utilisation (AOU) and Apparent Carbon Utilisation (ACP) showing that the system was heterotrophic. CNSW had an ACP and AOU of 19 and 37 µmol kg^{-1} respectively that decreased to 13 and 33 µmol kg^{-1} respectively in NAW. Queste

et al. (2016) deployed in the same region a glider measuring an increase of AOU in the BML by 2.8±0.3 µmol dm^{-3} d^{-1}. Queste et al. (2016) hypothesised a high oxygen consumption linked to localized depocentres and rapid remineralisation of resuspended organic matter. Instead, this study showed that the variability measured by Queste et al. (2016) was probably caused by oxygen consumption and North Sea spatial variability. Also, in my deployment the decrease of AOU and ACP between CNSW and NAW showed that NAW was in contact with the atmosphere more recently than CNSW. Typically CNSW leaves the North Sea to the Atlantic Ocean following the Norwegian Trench with a decrease of $c(O_2)$ and increase of C_T. This process is known as continental shelf pump (Tsunogai et al., 1999) transfers 93 % of the absorbed CO_2 to the North Atlantic Ocean. Future glider deployments on the Norwegian trench and in front of the Scottish coast can help to quantify the exact size of this process.

References

Alduchov, O. A. and Eskridge, R. E.: Improved Magnus form approximation of saturation vapor pressure, J. Appl. Meteorol., 35(4), 601–609, 1996.

Alkire, M. B., Lee, C., D'Asaro, E., Perry, M. J., Briggs, N., Cetinić, I. and Gray, A.: Net community production and export from Seaglider measurements in the North Atlantic after the spring bloom, J. Geophys. Res. Ocean., 119(9), 6121–6139, 2014.

Artioli, Y., Blackford, J. C., Butenschön, M., Holt, J. T., Wakelin, S. L., Thomas, H., Borges, A. V and Allen, J. I.: The carbonate system in the North Sea: Sensitivity and model validation, J. Mar. Syst., 102, 1–13, 2012.

Aßmann, S., Frank, C. and Körtzinger, A.: Spectrophotometric high-precision seawater pH determination for use in underway measuring systems, Ocean Sci., 7(5), 597–607, 2011.

Atamanchuk, D.: Development and use of an optical pCO2 sensor in marine studies, PhD Thesis, University of Gothenburg, 2013.

Atamanchuk, D., Tengberg, A., Thomas, P. J., Hovdenes, J., Apostolidis, A., Huber, C. and Hall, P. O. J.: Performance of a lifetime-based optode for measuring partial pressure of carbon dioxide in natural waters, Limnol. Oceanogr. Methods, 12(2), 63–73, doi:10.4319/lom.2014.12.63, 2014.

Atamanchuk, D., Kononets, M., Thomas, P. J., Hovdenes, J., Tengberg, A. and Hall, P. O. J.: Continuous long-term observations of the carbonate system dynamics in the water column of a temperate fjord, J. Mar. Syst., 148, 272–284, doi:10.1016/j.jmarsys.2015.03.002, 2015a.

Atamanchuk, D., Tengberg, A., Aleynik, D., Fietzek, P., Shitashima, K., Lichtschlag, A., Hall, P. O. J. and Stahl, H.: Detection of CO2 leakage from a simulated sub-seabed storage site using three different types of pCO2 sensors, Int. J. Greenh. Gas Control, 38, 121–134, doi:10.1016/j.ijggc.2014.10.021, 2015b.

Bakker, D. C. E., Pfeil, B., Landa, C. S., Metzl, N., Brien, K. M. O., Olsen, A., Smith, K., Cosca, C., Harasawa, S. and Jones, S. D.: A multi-decade record of high-quality fCO2 data in version 3 of the Surface Ocean CO2 Atlas (SOCAT), Earth Syst. Sci. Data, 383–413, doi:10.5194/essd-8-383-2016, 2016.

Bates, N. R., Astor, Y. M., Church, M. J., Currie, K., Dore, J. E., González-Dávila, M., Lorenzoni, L., Muller-Karger, F., Olafsson, J. and Santana-Casiano, J. M.: A Time-Series View of Changing Surface Ocean Chemistry Due to Ocean Uptake of

Anthropogenic CO_2 and Ocean Acidification, Oceanography, 27(1), 126–141, 2014.

Bellerby, R. G. J., Olsen, A., Johannessen, T. and Croot, P.: A high precision spectrophotometric method for on-line shipboard seawater pH measurements: The automated marine pH sensor (AMpS), Talanta, 56(1), 61–69, doi:10.1016/S0039-9140(01)00541-0, 2002.

Benson, B. B. and Krause Jr, D.: The concentration and isotopic fractionation of oxygen dissolved in freshwater and seawater in equilibrium with the atmosphere 1, Limnol. Oceanogr., 29(3), 620–632, 1984.

Binetti, U., Kaiser, J., Damerell, G. M., Rumyantseva, A., Martin, A. P., Henson, S. and Heywood, K. J.: Net community oxygen production derived from Seaglider deployments at the Porcupine Abyssal Plain site (PAP; northeast Atlantic) in 2012–13, Prog. Oceanogr., 183, 102293, 2020.

Bittig, H. C.: Tackling Oxygen Optode Drift : Near-Surface and In-Air Oxygen Optode Measurements on a Float Provide an Accurate in Situ Reference, , (November), 1536–1543, doi:10.1175/JTECH-D-14-00162.1, 2015.

Bittig, H. C., Fiedler, B., Steinhoff, T. and Körtzinger, A.: A novel electrochemical calibration setup for oxygen sensors and its use for the stability assessment of Aanderaa optodes, Limnol. Oceanogr.: Methods, 1, 921–933, doi:10.4319/lom.2012.10.921, 2012.

Bittig, H. C., Körtzinger, A., Neill, C., van Ooijen, E., Plant, J. N., Hahn, J., Johnson, K. S., Yang, B. and Emerson, S. R.: Oxygen Optode Sensors: Principle, Characterization, Calibration, and Application in the Ocean, Front. Mar. Sci., 4(January), 1–25, doi:10.3389/fmars.2017.00429, 2018.

Blackford, J. C. and Gilbert, F. J.: pH variability and CO2 induced acidification in the North Sea, J. Mar. Syst., 64(1–4), 229–241, 2007.

Borges, A. V.: Distribution of surface carbon dioxide and air-sea exchange in the English Channel and adjacent areas, J. Geophys. Res., 108(C5), 3140, doi:10.1029/2000JC000571, 2003.

Bozec, Y., Thomas, H., Elkalay, K. and De Baar, H. J. W.: The continental shelf pump for CO 2 in the North Sea - Evidence from summer observation, Mar. Chem., 93(2–4), 131–147, doi:10.1016/j.marchem.2004.07.006, 2005.

Bozec, Y., Thomas, H., Schiettecatte, L.-S., Borges, A. V, Elkalay, K. and de Baar, H. J. W.: Assessment of the processes controlling the seasonal variations of dissolved inorganic carbon in the North Sea, Limnol. Oceanogr., 51(6), 2746–2762,

doi:10.4319/lo.2006.51.6.2746, 2006.

Bresnahan, P. J., Wirth, T., Martz, T. R., Andersson, A. J., Cyronak, T., D'Angelo, S., Pennise, J., Melville, W. K., Lenain, L. and Statom, N.: A sensor package for mapping pH and oxygen from mobile platforms, Methods Oceanogr., 17, 1–13, doi:10.1016/j.mio.2016.04.004, 2016.

Briggs, E. M., Sandoval, S., Erten, A., Takeshita, Y., Kummel, A. C. and Martz, T. R.: Solid State Sensor for Simultaneous Measurement of Total Alkalinity and pH of Seawater, ACS Sensors, 2(9), 1302–1309, doi:10.1021/acssensors.7b00305, 2017.

Le Bris, N., Zbinden, M. and Gaill, F.: Processes controlling the physico-chemical micro-environments associated with Pompeii worms, Deep Sea Res. Part I Oceanogr. Res. Pap., 52(6), 1071–1083, 2005.

Brown, J., Hill, A. E., Fernand, L. and Horsburgh, K. J.: Observations of a seasonal jet-like circulation at the central North Sea cold pool margin, Estuar. Coast. Shelf Sci., 48(3), 343–355, 1999.

Buck, R. P. and Lindner, E.: Recommendations for nomenclature of ionselective electrodes (IUPAC Recommendations 1994), Pure Appl. Chem., 66(12), 2527–2536, 1994.

Buck, R. P., Rondinini, S., Covington, A. K., Baucke, F. G. K., Brett, C. M. A., Camoes, M. F., Milton, M. J. T., Mussini, T., Naumann, R. and Pratt, K. W.: The measurement of pH–definition, standards and procedures. Report of the Working Party on pH. IUPAC Provisional Recommendation, 2001.

von Bültzingslöwen, C., McEvoy, A. K., McDonagh, C., MacCraith, B. D., Klimant, I., Krause, C. and Wolfbeis, O. S.: Sol–gel based optical carbon dioxide sensor employing dual luminophore referencing for application in food packaging technology, Analyst, 127(11), 1478–1483, 2002.

Bushinsky, S. M., Takeshita, Y. and Williams, N. L.: Observing Changes in Ocean Carbonate Chemistry: Our Autonomous Future, Curr. Clim. Chang. reports, 5(3), 207–220, 2019.

Byrne, R. H. and Breland, J. A.: High precision multiwavelength pH determinations in seawater using cresol red, Deep Sea Res. Part A, Oceanogr. Res. Pap., 36(5), 803–810, doi:10.1016/0198-0149(89)90152-0, 1989.

Byrne, R. H., Robert-Baldo, G., Thompson, S. W. and Chen, C. T. A.: Seawater pH measurements: an at-sea comparison of spectrophotometric and potentiometric methods, Deep Sea Res. Part A, Oceanogr. Res. Pap., 35(8), 1405–1410,

doi:10.1016/0198-0149(88)90091-X, 1988.

Byrne, R. H., Mecking, S., Feely, R. A. and Liu, X.: Direct observations of basin-wide acidification of the North Pacific Ocean, Geophys. Res. Lett., 37(2), doi:10.1029/2009GL040999, 2010.

Carter, B. R., Radich, J. A., Doyle, H. L. and Dickson, A. G.: An automated system for spectrophotometric seawater pH measurements, Limnol. Oceanogr. Methods, 11(1), 16–27, 2013.

Chou, J.-C. and Weng, C.-Y.: Sensitivity and hysteresis effect in Al2O3 gate pH-ISFET, Mater. Chem. Phys., 71(2), 120–124, 2001.

Chu, S. N., Wang, Z. A., Gonneea, M. E., Kroeger, K. D. and Ganju, N. K.: Deciphering the dynamics of inorganic carbon export from intertidal salt marshes using high-frequency measurements, Mar. Chem., 206, 7–18, 2018.

Chu, S. N., Sutton, A. J., Alin, S. R., Lawrence-Slavas, N., Atamanchuk, D., Mickett, J. B., Newton, J. A., Meinig, C., Stalin, S. and Tengberg, A.: Field evaluation of a low-powered, profiling pCO2 system in coastal Washington, Limnol. Oceanogr. Methods, 2020.

Clarke, J. S., Achterberg, E. P., Rérolle, V. M. C., Abi Kaed Bey, S., Floquet, C. F. A. and Mowlem, M. C.: Characterisation and deployment of an immobilised pH sensor spot towards surface ocean pH measurements, Anal. Chim. Acta, 897, 69–80, doi:10.1016/j.aca.2015.09.026, 2015.

Clayton, T. D. and Byrne, R. H.: Spectrophotometric seawater pH measurements : total hydrogen results, Deep. Res., 40(10), 2115–2129, doi:10.1016/0967-0637(93)90048-8, 1993.

Copin-Montégut, C.: Consumption and production on scales of a few days of inorganic carbon, nitrate and oxygen by the planktonic community: results of continuous measurements at the Dyfamed Station in the northwestern Mediterranean Sea (May 1995), Deep Sea Res. Part I Oceanogr. Res. Pap., 47(3), 447–477, 2000.

Culberson, C. H.: WHP Operations and Methods, Dissolved Oxygen. WHP Office Report WHPO 91-1, WOCE Report., 1991.

Degrandpre, M. D.: Measurement of Seawater pC02 Using a Renewable-Reagent Fiber Optic Sensor with Colorimetric Detection, Anal. Chem., 1172(8), 331–337, doi:10.1021/ac00052a005, 1993.

DeGrandpre, M. D., Hammar, T. R., Smith, S. P. and Sayles, F. L.: In situ

measurements of seawater pCO2, Limnol. Oceanogr., 40(5), 969–975, 1995.

DelValls, T. A. and Dickson, A. G.: The pH of buffers based on 2-amino-2-hydroxymethyl-1,3-propanediol ('tris') in synthetic sea water, Deep. Res. Part I Oceanogr. Res. Pap., 45(9), 1541–1554, doi:10.1016/S0967-0637(98)00019-3, 1998.

Dickson, A. G.: pH scales and proton-transfer reactions in saline media such as sea water, Geochim. Cosmochim. Acta, 48(11), 2299–2308, 1984.

Dickson, A. G.: Thermodynamics of the dissociation of boric acid in synthetic seawater from 273.15 to 318.15 K, Deep Sea Res. Part A. Oceanogr. Res. Pap., 37(5), 755–766, 1990.

Dickson, A. G.: The measurement of sea water pH, Mar. Chem., 44(2–4), 131–142, doi:10.1016/0304-4203(93)90198-W, 1993.

Dickson, A. G.: The carbon dioxide system in seawater: equilibrium chemistry and measurements, Guid. to best Pract. Ocean Acidif. Res. data Report., 1, 17–40, 2010.

Dickson, A. G. and Riley, J. P.: The estimation of acid dissociation constants in seawater media from potentionmetric titrations with strong base. I. The ionic product of water—Kw, Mar. Chem., 7(2), 89–99, 1979.

Dickson, A. G., Afghan, J. D. and Anderson, G. C.: Reference materials for oceanic CO2 analysis : a method for the certification of total alkalinity, Mar. Chem., 80, 185–197, 2003.

Dickson, A. G., Sabine, C. L. and Christian, J. R.: Guide to best practices for ocean CO2 measurements., North Pacific Marine Science Organization., 2007.

Dlugokencky, E. J., Lang, P. M., Masarie, K. A., Crotwell, A. M. and Crotwell, M. J.: Atmospheric carbon dioxide dry air mole fractions from the NOAA ESRL Carbon Cycle Cooperative Global Air Sampling Network, 1968–2014, NOAA ESRL Glob. Monit. Div. Boulder, CO, USA, 2015.

Doney, S. C. and Schimel, D. S.: Carbon and climate system coupling on timescales from the Precambrian to the Anthropocene, Annu. Rev. Environ. Resour., 32, 31–66, 2007.

Doney, S. C., Fabry, V. J., Feely, R. A. and Kleypas, J. A.: Ocean Acidification: The Other CO 2Problem, Ann. Rev. Mar. Sci., 1(1), 169–192, doi:10.1146/annurev.marine.010908.163834, 2009a.

Doney, S. C., Tilbrook, B., Roy, S., Metzl, N., Le Quéré, C., Hood, M., Feely, R. A. and Bakker, D.: Surface-ocean CO2 variability and vulnerability, Deep Sea Res. Part II Top.

Stud. Oceanogr., 56(8–10), 504–511, 2009b.

Duarte, C. M., Regaudie-de-Gioux, A., Arrieta, J. M., Delgado-Huertas, A. and Agustí, S.: The oligotrophic ocean is heterotrophic, Ann. Rev. Mar. Sci., 5, 551–569, 2013.

Ducklow, H. W. and Doney, S. C.: What Is the Metabolic State of the Oligotrophic Ocean ? A Debate, Annu. Rev. of Mar. Sci., doi:10.1146/annurev-marine-121211-172331, 2013.

Easley, R. A. and Byrne, R. H.: Spectrophotometric calibration of pH electrodes in seawater using purified m-cresol purple, Environ. Sci. Technol., 46(9), 5018–5024, doi:10.1021/es300491s, 2012.

Eriksen, C. C., Osse, T. J., Light, T., Wen, R. D., Lehmann, T. W., Sabin, P. L., Ballard, J. W., Seaglider, a M. C. and a: Long Range Autonomous Underwater Vehicle for Oceanographic Research, IEEE J. Ocean. Eng., 26(4), 424–436, doi:10.1109/48.972073, 2001.

Fabry, V. J., Seibel, B. A., Feely, R. A. and Orr, J. C.: Impacts of ocean acidification on marine fauna and ecosystem processes, ICES J. Mar. Sci., 65(3), 414–432, 2008.

Falck, E. and Anderson, L. G.: The dynamics of the carbon cycle in the surface water of the Norwegian Sea, Mar. Chem., 94, 43–53, doi:10.1016/j.marchem.2004.08.009, 2005.

Falck, E. and Gade, G.: Net community production and oxygen fluxes in the Nordic Seas based on O2 budget calculations, Global biogeochem cy, 13(4), 1117–1126, 1999.

Fassbender, A. J., Sabine, C. L., Lawrence-slavas, N., Carlo, E. H. De, Meinig, C. and Jones, S. M.: Robust Sensor for Extended Autonomous Measurements of Surface Ocean Dissolved Inorganic Carbon, Environ. Sci. Technol, doi:10.1021/es5047183, 2015.

Feely, R. A., Sabine, C. L., Schlitzer, R., Bullister, J. L., Mecking, S. and Greeley, D.: Oxygen utilization and organic carbon remineralization in the upper water column of the Pacific Ocean, J. Oceanogr., 60(3), 45–52, doi:10.1023/B:JOCE.0000038317.01279.aa, 2004.

Feely, R. A., Sabine, C. L., Hernandez-Ayon, J. M., Ianson, D. and Hales, B.: Evidence for upwelling of corrosive" acidified" water onto the continental shelf, Science (80-.)., 320(5882), 1490–1492, 2008.

Fernand, L., Weston, K., Morris, T., Greenwood, N., Brown, J. and Jickells, T.: The

contribution of the deep chlorophyll maximum to primary production in a seasonally stratified shelf sea, the North Sea, Biogeochemistry, 113(1–3), 153–166, 2013.

Fiedler, B., Fietzek, P., Vieira, N., Silva, P., Bittig, H. C. and Körtzinger, A.: In situ CO2 and O2 measurements on a profiling float, J. Atmos. Ocean. Technol., 30(1), 112–126, doi:10.1175/JTECH-D-12-00043.1, 2013.

Foltz, G. R., Grodsky, S. A., Carton, J. A. and McPhaden, M. J.: Seasonal mixed layer heat budget of the tropical Atlantic Ocean, J. Geophys. Res. Ocean., 108(C5), 2003.

Friedlingstein, P., Jones, M., O'Sullivan, M., Andrew, R., Hauck, J., Peters, G., Peters, W., Pongratz, J., Sitch, S. and Le Quéré, C.: Global carbon budget 2019, Earth Syst. Sci. Data, 11(4), 1783–1838, 2019.

Friis, K., Körtzinger, A. and Wallace, D. W. R.: Spectrophotometric pH measurement in the ocean: Requirements, design, and testing of an autonomous charge-coupled device detector system, Limnol. Oceanogr. Methods, 2(5), 126–136, doi:10.4319/lom.2004.2.126, 2004.

Garcia, H. E. and Gordon, L. I.: Oxygen solubility in seawater: Better fitting equations, Limnol. Oceanogr., 37(6), 1307–1312, 1992.

Gattuso, J.-P. and Hansson, L.: Ocean acidification, Oxford University Press., 2011.

Gattuso, J.-P., Frankignoulle, M. and Wollast, R.: Carbon and Carbonate Metabolism in Coastal Aquatic Ecosystems, Annu. Rev. Ecol. Syst., 29(1), 405–434, doi:10.1146/annurev.ecolsys.29.1.405, 1998.

Gislefoss, J. S., Nydal, R., Slagstad, D., Sonninen, E. and Holmén, K.: Carbon time series in the Norwegian Sea, Deep Sea Res. Part I Oceanogr. Res. Pap., 45(2–3), 433–460, 1998.

GmbH, A. A.: pH Shallow water sensor - Operating instruction 1,200 meter version -, pp. 1–9, 2014.

Gonski, S. F., Cai, W. J., Ullman, W. J., Joesoef, A., Main, C. R., Pettay, D. T. and Martz, T. R.: Assessment of the suitability of Durafet-based sensors for pH measurement in dynamic estuarine environments, Estuar. Coast. Shelf Sci., 200, 152–168, doi:10.1016/j.ecss.2017.10.020, 2018.

González-Dávila, M., Santana-Casiano, J. M., Rueda, M. J. and Llinás, O.: The water column distribution of carbonate system variables at the ESTOC site from 1995 to 2004, Biogeosciences, 7(10), 3067–3081, doi:10.5194/bg-7-3067-2010, 2010.

Gourcuff, C.: ANFOG Slocum CTD data correction, (March), 2014.

Goyet, C. and Poisson, A.: New determination of carbonic acid dissociation constants in seawater as a function of temperature and salinity, Deep Sea Res. Part A. Oceanogr. Res. Pap., 36(11), 1635–1654, 1989.

Goyet, C., Walt, D. R. and Brewer, P. G.: Development of a fiber optic sensor for measurement of pCO2 in sea water: design criteria and sea trials, Deep Sea Res. Part A. Oceanogr. Res. Pap., 39(6), 1015–1026, 1992.

Gruber, N., Clement, D., Carter, B. R., Feely, R. A., Van Heuven, S., Hoppema, M., Ishii, M., Key, R. M., Kozyr, A. and Lauvset, S. K.: The oceanic sink for anthropogenic CO2 from 1994 to 2007, Science (80-.)., 363(6432), 1193–1199, 2019.

Gypens, N., Borges, A. V. and Lancelot, C.: Effect of eutrophication on air-sea CO2 fluxes in the coastal Southern North Sea: A model study of the past 50 years, Glob. Chang. Biol., 15(4), 1040–1056, doi:10.1111/j.1365-2486.2008.01773.x, 2009.

Hahn, J.: Oxygen variability and eddy-driven meridional oxygen supply in the tropical North East Atlantic oxygen minimum zone, PhD Thesis, University of KIEL, 2013.

Hakonen, A. and Hulth, S.: A high-performance fluorosensor for pH measurements between 6 and 9, Talanta, 80(5), 1964–1969, 2010.

Hansen, B. and Østerhus, S.: North atlantic–nordic seas exchanges, Prog. Oceanogr., 45(2), 109–208, 2000.

Hansson, I.: A new set of pH-scales and standard buffers for sea water, Deep Sea Res. Oceanogr. Abstr., 20(5), 479–491, doi:10.1016/0011-7471(73)90101-0, 1973.

Hardman-Mountford, N. J., Moore, G., Bakker, D. C. E., Watson, A. J., Schuster, U., Barciela, R., Hines, A., Moncoiffé, G., Brown, J., Dye, S., Blackford, J., Somerfield, P. J., Holt, J., Hydes, D. J. and Aiken, J.: An operational monitoring system to provide indicators of CO 2-related variables in the ocean, ICES J. Mar. Sci., 65(8), 1498–1503, doi:10.1093/icesjms/fsn110, 2008.

Haskell, W. Z., Hammond, D. E., Prokopenko, M. G., Teel, E. N., Seegers, B. N., Ragan, M. A., Rollins, N. and Jones, B. H.: Net Community Production in a Productive Coastal Ocean From an Autonomous Buoyancy-Driven Glider, J. Geophys. Res. Ocean., 124(6), 4188–4207, 2019.

Hemming, M. P., Kaiser, J., Heywood, K. J., Bakker, D. C. E., Boutin, J., Shitashima, K., Lee, G., Legge, O. and Onken, R.: Measuring pH variability using an experimental sensor on an underwater glider, Ocean Sci., 13(3), 427–442, doi:10.5194/os-13-427-2017, 2017.

Hemmink, G. J., Oors, J., Weusten, B. L., Bredenoord, A. J., Timmer, R. and Smout, A.: S1938 Ambulatory Esophageal pH-Impedance Reflux Monitoring: A Comparison Between Antimony, ISFET and Glass pH Electrodes, Gastroenterology, 136(5), A-297, 2009.

Hemsley, J. M.: OBSERVATIONS PLATFORMS| Buoys, 2015.

Hemsley, V. S., Smyth, T. J., Martin, A. P., Frajka-williams, E., Thompson, A. F., Damerell, G. and Painter, S. C.: Estimating Oceanic Primary Production Using Vertical Irradiance and Chlorophyll Profiles from Ocean Gliders in the North Atlantic, Environ Sci. Technol., doi:10.1021/acs.est.5b00608, 2015.

Van Heuven, S., Pierrot, D., Rae, J. W. B., Lewis, E. and Wallace, D. W. R.: MATLAB program developed for CO2 system calculations, ORNL/CDIAC-105b. Carbon Dioxide Inf. Anal. Center, Oak Ridge Natl. Lab. US Dep. Energy, Oak Ridge, Tennessee, 530, 2011.

Hill, A. E., Brown, J., Fernand, L., Holt, J., Horsburgh, K. J., Proctor, R., Raine, R. and Turrell, W. R.: Thermohaline circulation of shallow tidal seas, Geophys. Res. Lett., 35(11), 2008.

Hofmann, G. E., Smith, J. E., Johnson, K. S., Send, U., Levin, L. A., Paytan, A., Price, N. N., Peterson, B., Takeshita, Y., Matson, P. G., Crook, E. D., Kroeker, K. J., Gambi, M. C., Rivest, E. B., Frieder, C. A., Yu, P. C. and Martz, T. R.: High-Frequency Dynamics of Ocean pH : A Multi- Ecosystem Comparison, PloS one, 6(12), doi:10.1371/journal.pone.0028983, 2011.

Holley, S. E. and Hydes, D. J.: Procedures for the determination of dissolved oxygen in seawater, University of Southampton, 1995.

Hopkins, T. S.: The GIN Sea—A synthesis of its physical oceanography and literature review 1972–1985, Earth-Science Rev., 30(3–4), 175–318, 1991.

Hoppema, J. M. J.: The seasonal behaviour of carbon dioxide and oxygen in the coastal North Sea along the Netherlands, Netherlands J. Sea Res., 28(3), 167–179, 1991.

ICES: Flushing times of the North Sea, Coop. Res. Rep., 123, 1983.

Jeansson, E., Olsen, A., Eldevik, T., Skjelvan, I., Omar, A. M., Lauvset, S. K., Nilsen, J. E. Ø., Bellerby, R. G. J., Johannessen, T. and Falck, E.: The Nordic Seas carbon budget : Sources , sinks , and uncertainties, Global Biogeochem Cy, 25(2002), 1–16, doi:10.1029/2010GB003961, 2011.

Johnson, K. S., Jannasch, H. W., Coletti, L. J., Elrod, V. A., Martz, T. R., Takeshita, Y., Carlson, R. J. and Connery, J. G.: Deep-Sea DuraFET: A Pressure Tolerant pH Sensor Designed for Global Sensor Networks, Anal. Chem., 88(6), 3249–3256, doi:10.1021/acs.analchem.5b04653, 2016.

Johnson, K. S., Plant, J. N., Coletti, L. J., Jannasch, H. W., Sakamoto, C. M., Riser, S. C., Swift, D. D., Williams, N. L., Boss, E. and Haëntjens, N.: Biogeochemical sensor performance in the SOCCOM profiling float array, J. Geophys. Res. Ocean., 122(8), 6416–6436, 2017.

Kadis, R. and Leito, I.: Evaluation of the residual liquid junction potential contribution to the uncertainty in pH measurement: A case study on low ionic strength natural waters, Anal. Chim. Acta, 664(2), 129–135, 2010.

Kara, A. B., Rochford, P. A. and Hurlburt, H. E.: An optimal definition for ocean mixed layer depth, J. Geophys. Res. Ocean., 105(C7), 16803–16821, 2000.

Kempe, S. and Pegler, K.: Sinks and sources of CO2 in coastal seas: the North Sea, Tellus B, 43(2), 224–235, 1991.

Kivimäe, C.: Carbon and oxygen fluxes in the Barents and Norwegian Seas: production, air-sea exchange and budget calculations, University of Bergen PhD thesis, 2007.

Klimant, I., Huber, C., Liebsch, G., Neurauter, G., Stangelmayer, A. and Wolfbeis, O. S.: Dual lifetime referencing (DLR)—a new scheme for converting fluorescence intensity into a frequency-domain or time-domain information, in New Trends in Fluorescence Spectroscopy, pp. 257–274, Springer., 2001.

Körtzinger, A., Thomas, H., Schneider, B., Gronau, N., Mintrop, L. and Duinker, J. C.: At-sea intercomparison of two newly designed underway pCO2 systems—encouraging results, Mar. Chem., 52(2), 133–145, 1996.

Körtzinger, A., Koeve, W., Kähler, P. and Mintrop, L.: C: N ratios in the mixed layer during the productive season in the northeast Atlantic Ocean, Deep Sea Res. Part I Oceanogr. Res. Pap., 48(3), 661–688, 2001.

Kühn, W., Pätsch, J., Thomas, H., Borges, A. V., Schiettecatte, L. S., Bozec, Y. and Prowe, A. E. F.: Nitrogen and carbon cycling in the North Sea and exchange with the North Atlantic-A model study, Part II: Carbon budget and fluxes, Cont. Shelf Res., 30(16), 1701–1716, doi:10.1016/j.csr.2010.07.001, 2010.

Larsen, M., Borisov, S. M., Grunwald, B., Klimant, I. and Glud, R. N.: A simple and inexpensive high resolution color ratiometric planar optode imaging approach:

application to oxygen and pH sensing, Limnol. Oceanogr. Methods, 9, 348–360, doi:10.4319/lom.2011.9.348, 2011.

Lawrence, M. G.: The relationship between relative humidity and the dewpoint temperature in moist air: A simple conversion and applications, Bull. Am. Meteorol. Soc., 86(2), 225–234, 2005.

Lee, K., Tong, L. T., Millero, F. J., Sabine, C. L., Dickson, A. G., Goyet, C., Park, G. H., Wanninkhof, R., Feely, R. A. and Key, R. M.: Global relationships of total alkalinity with salinity and temperature in surface waters of the world's oceans, Geophys. Res. Lett., 33(19), 1–5, doi:10.1029/2006GL027207, 2006.

Lee, K., Kim, T., Byrne, R. H., Millero, F. J., Feely, R. A. and Liu, Y.: The universal ratio of boron to chlorinity for the North Pacific and North Atlantic oceans, Geochim. Cosmochim. Acta, 74(6), 1801–1811, doi:10.1016/j.gca.2009.12.027, 2010.

Lenhart, H. J., Radach, G., Backhaus, J. O. and Pohlmann, T.: Simulations of the North Sea circulation, its variability, and its implementation as hydrodynamical forcing in ERSEM, Netherlands J. Sea Res., 33(3–4), 271–299, 1995.

Lenhart, H. J., Pätsch, J., Kühn, W., Moll, A. and Pohlmann, T.: Investigation on the trophic state of the North Sea for three years (1994-1996) simulated with the ecosystem model ERSEM? the role of a sharp NAOI decline, Biogeosciences Discuss., 2004.

Liebsch, G., Klimant, I., Krause, C. and Wolfbeis, O. S.: Fluorescent imaging of pH with optical sensors using time domain dual lifetime referencing, Anal. Chem., 73(17), 4354–4363, doi:10.1021/ac0100852, 2001.

Liu, X., Patsavas, M. C. and Byrne, R. H.: Purification and characterization of meta-cresol purple for spectrophotometric seawater pH measurements, Environ. Sci. Technol., 45(11), 4862–4868, 2011.

Liu, X., Byrne, R. H., Adornato, L., Yates, K. K., Kaltenbacher, E., Ding, X. and Yang, B.: In Situ Spectrophotometric Measurement of Dissolved Inorganic Carbon in Seawater, Environ Sci. Technol., 2013.

Lockwood, D., Quay, P. D., Kavanaugh, M. T., Juranek, L. W., Feely RA: High-resolution estimates of net community production and air-sea CO2 flux in the northeast Pacific, Global Biogeochem Cy, 26, 1–16, doi:10.1029/2012GB004380, 2012.

Lueker, T. J., Dickson, A. G. and Keeling, C. D.: Ocean pCO2 calculated from DIC, TA, and the Mehrbach equations for K1 and K2: Validation using laboratory measurements of CO2 in gas and seawater at equilibrium, Abstr. Pap. Am. Chem. Soc., 217, U848–

U848, 2000.

Mackenzie, F. T., Lerman, A. and Andersson, A. J.: Past and present of sediment and carbon biogeochemical cycling models, Biogeosciences, 1(1), 11–32, doi:10.5194/bg-1-11-2004, 2004.

Martin, J. H., Knauer, G. A., Karl, D. M. and Broenkow, W. W.: VERTEX: carbon cycling in the northeast Pacific, Deep Sea Res. Part A. Oceanogr. Res. Pap., 34(2), 267–285, 1987.

Martz, T. R., Carr, J. J., French, C. R. and DeGrandpre, M. D.: A submersible autonomous sensor for spectrophotometric pH measurements of natural waters, Anal. Chem., 75(8), 1844–1850, 2003.

Martz, T. R., Connery, J. G. and Johnson, K. S.: Testing the Honeywell Durafet® for seawater pH applications, Limnol. Oceanogr. Methods, 8(5), 172–184, 2010.

McLaughlin, K., Weisberg, S. B., Dickson, A. G., Hofmann, G. E., Newton, J. A., Aseltine-Neilson, D., Barton, A., Cudd, S., Feely, R. A. and Jefferds, I. W.: Core principles of the California Current Acidification Network: Linking chemistry, physics, and ecological effects, Oceanography, 28(2), 160–169, 2015.

McLaughlin, K., Nezlin, N. P., Weisberg, S. B., Dickson, A. G., Booth, J. A., Cash, C. L., Feit, A., Gully, J. R., Johnson, S. and Latker, A.: An evaluation of potentiometric pH sensors in coastal monitoring applications, Limnol. Oceanogr. Methods, 15(8), 679–689, 2017.

Medeot, N., Nair, R. and Gerin, R.: Laboratory Evaluation and Control of Slocum Glider C – T Sensors, JTECH, 838–846, doi:10.1175/2011JTECHO767.1, 2011.

Meyer, M., Pätsch, J., Geyer, B. and Thomas, H.: Revisiting the Estimate of the North Sea Air-Sea Flux of CO2 in 2001/2002: The Dominant Role of Different Wind Data Products, J. Geophys. Res. Biogeosciences, 123(5), 1511–1525, 2018.

Midgley, D.: Glass pH electrodes with improved temperature characteristics: use of a low-impedance pH sensor as the inner reference electrode, Analyst, 115(10), 1283–1287, 1990.

Millero, F.: The marine inorganic carbon cycle., Chem. Rev., 107(Table 1), 308–341, doi:10.1021/cr0503557, 2007.

Millero, F. J., Zhang, J.-Z., Lee, K. and Campbell, D. M.: Titration alkalinity of seawater, Mar. Chem., 44(2–4), 153–165, 1993.

Miloshevich, L.: Development and Validation of a Time-Lag Correction for Vaisala

Radiosonde Humidity Measurements, JTECH , 1305–1328, 2004.

Monteiro, P. M. S., Schuster, U., Hood, M., Lenton, A., Metzl, N., Olsen, A., Rogers, K., Sabine, C., Takahashi, T. and Tilbrook, B.: A global sea surface carbon observing system: Assessment of changing sea surface CO2 and air-sea CO2 fluxes, Proc. Ocean., 9, 702–714, 2009.

Monterey, G. I. and Levitus, S.: US National Environmental Satellite and Information Service: Seasonal variability of mixed layer depth for the world ocean, US Department of Commerce, National Oceanic and Atmospheric Administration, Silver Spring, MD, 1997. Nakano, Y., Kimoto, H., Watanabe, S., Harada, K. and Watanabe, Y. W.: Simultaneous vertical measurements of in situ pH and CO2 in the sea using spectrophotometric profilers, J. Oceanogr., 62(1), 71–81, doi:10.1007/s10872-006-0033-y, 2006.

Naumann, R., Alexander-Weber, C., Eberhardt, R., Giera, J. and Spitzer, P.: Traceability of pH measurements by glass electrode cells: performance characteristic of pH electrodes by multi-point calibration, Anal. Bioanal. Chem., 374(5), 778–786, 2002.

Naveira Garabato, A. C., Oliver, K. I. C., Watson, A. J. and Messias, M.: Turbulent diapycnal mixing in the Nordic seas, J. Geophys. Res. Ocean., 109(C12), 2004.

Neftel, A., Oeschger, H., Schwander, J., Stauffer, B. and Zumbrunn, R.: Ice core sample measurements give atmospheric CO 2 content during the past 40,000 yr, Nature, 295(5846), 220–223, 1982.

Nemzer, B. V. and Dickson, A. G.: The stability and reproducibility of Tris buffers in synthetic seawater, Mar. Chem., 96(3–4), 237–242, doi:10.1016/j.marchem.2005.01.004, 2005.

Neuer, S., Cianca, A., Helmke, P., Freudenthal, T., Davenport, R., Meggers, H. and Knoll, M.: Biogeochemistry and hydrography in the eastern subtropical North Atlantic gyre . Results from the European time-series station ESTOC, Prog. Oceanogr., 72, 1–29, doi:10.1016/j.pocean.2006.08.001, 2007.

Newton, J. A., Feely, R. A., Jewett, E. B., Williamson, P. and Mathis, J.: Global Ocean Acidification Observing Network: Requirements and Governance Plan, (September), 57 pp. [online] Available from: http://goa-on.org/docs/GOA-ON_Plan_final_Sept_2014.pdf, 2014.

Nicholson, D., Emerson, S. and Eriksen, C. C.: Net community production in the deep euphotic zone of the subtropical North Pacific gyre from glider surveys, Limnol.

Oceanogr., 53(5 PART 2), 2226–2236, doi:10.4319/lo.2008.53.5_part_2.2226, 2008.

Nicholson, D. P. and Feen, M. L.: Air calibration of an oxygen optode on an underwater glider, Limnol. Oceanogr. Methods, 15(5), 495–502, doi:10.1002/lom3.10177, 2017.

Nilsen, J. E. Ø. and Falck, E.: Variations of mixed layer properties in the Norwegian Sea for the period 1948 – 1999, Progr. Oceanogr., 70, 58–90, doi:10.1016/j.pocean.2006.03.014, 2006.

Nondal, G., Bellerby, R. G. J., Olsen, A., Johannessen, T. and Olafsson, J.: Optimal evaluation of the surface ocean CO2 system in the northern North Atlantic using data from voluntary observing ships, Limnol. Oceanogr. Methods, 7(1), 109–118, 2009.

Obata, A., Ishizaka, J. and Endoh, M.: Global verification of critical depth theory for phytoplankton bloom with climatological in situ temperature and satellite ocean color data, J. Geophys. Res. Ocean., 101(C9), 20657–20667, 1996.

Olsen, A., Key, R. M., Van Heuven, S., Lauvset, S. K., Velo, A., Lin, X., Schirnick, C., Kozyr, A., Tanhua, T., Hoppema, M., Jutterström, S., Steinfeldt, R., Jeansson, E., Ishii, M., Pérez, F. F. and Suzuki, T.: The global ocean data analysis project version 2 (GLODAPv2) - An internally consistent data product for the world ocean, Earth Syst. Sci. Data, 8(2), 297–323, doi:10.5194/essd-8-297-2016, 2016.

Omar, A. M., Olsen, A., Johannessen, T., Hoppema, M., Thomas, H. and Borges, A. V: Spatiotemporal variations of fCO(2) in the North Sea, Ocean Sci., *6*(1), pp.77-89, 2010.

Osterroht, C. and Thomas, H.: New production enhanced by nutrient supply from non-Redfield remineralisation of freshly produced organic material, J. Mar. Syst., 25(1), 33–46, 2000.

Otto, L., Zimmerman, J. T. F., Furnes, G. K., Mork, M., Saetre, R. and Becker, G.: Review of the physical oceanography of the North Sea, Netherlands J. Sea Res., 26(2–4), 161–238, doi:10.1016/0077-7579(90)90091-T, 1990.

Pachauri, R. K. and Reisinger, A.: IPCC fourth assessment report, IPCC Fourth Assess. Rep., 1, 976 [online] Available from: http://www.construible.es/construible%5Cbiblioteca%5Cpresentacion_informe_ipcc.pdf%5Cnpapers2://publication/uuid/DD3ABB67-E411-4C0F-A29C-DA693B95B789, 2007.

Paulsen, M. and Dickson, A. G.: Preparation of 2-amino-2-hydroxymethyl-1, 3-propanediol (TRIS) pHT buffers in synthetic seawater, Limnol. Oceanogr. Methods, 2020.

Peeters, F., Atamanchuk, D., Tengberg, A., Encinas-Fernández, J. and Hofmann, H.:

Lake metabolism: Comparison of lake metabolic rates estimated from a diel CO2-and the common diel O2-technique, PLoS One, 11(12), 2016.

Pegler, K. and Kempe, S.: The carbonate system of the North Sea: determination of alkalinity and TCO2 and calculation of PCO2 and SIcal (spring 1986), Mitt geol-paläont Inst Univ Hamb, 65, 35–87, 1988.

Plant, J. N., Johnson, K. S., Sakamoto, C. M., Jannasch, H. W., Coletti, L. J., Riser, S. C. and Swift, D. D.: Net community production at Ocean Station Papa observed with nitrate and oxygen sensors on profiling floats, Global Biogeochem. Cycles, 30(6), 859–879, 2016.

Prowe, A. E. F., Thomas, H., Pätsch, J., Kühn, W., Bozec, Y., Schiettecatte, L. S., Borges, A. V. and de Baar, H. J. W.: Mechanisms controlling the air-sea CO2 flux in the North Sea, Cont. Shelf Res., 29(15), 1801–1808, doi:10.1016/j.csr.2009.06.003, 2009.

Quay, P., Stutsman, J. and Steinhoff, T.: Primary production and carbon export rates across the subpolar N. Atlantic Ocean basin based on triple oxygen isotope and dissolved O2 and Ar gas measurements, Global Biogeochem. Cycles, 26(2), 2012.

Le Quéré, C., Raupach, M. R., Canadell, J. G., Marland et al., G., Le Quéré et al., C., Le Quéré et al., C., Raupach, M. R., Canadell, J. G., Marland, G., Bopp, L., Ciais, P., Conway, T. J., Doney, S. C., Feely, R. A., Foster, P., Friedlingstein, P., Gurney, K., Houghton, R. A., House, J. I., Huntingford, C., Levy, P. E., Lomas, M. R., Majkut, J., Metzl, N., Ometto, J. P., Peters, G. P., Prentice, I. C., Randerson, J. T., Running, S. W., Sarmiento, J. L., Schuster, U., Sitch, S., Takahashi, T., Viovy, N., van der Werf, G. R. and Woodward, F. I.: Trends in the sources and sinks of carbon dioxide, Nat. Geosci., 2(12), 831–836, doi:10.1038/ngeo689, 2009.

Queste, B., Fernand, L., Jickells, T., Heywood, K. and Hind, A.: Drivers of summer oxygen depletion in the central North Sea, Biogeosciences, 13, 1209–1222, 2016.

Queste, B. Y., Heywood, K. J., Kaiser, J., Lee, G. A., Matthews, A., Schmidtko, S., Walker-Brown, C. and Woodward, S. W.: Deployments in extreme conditions: Pushing the boundaries of Seaglider capabilities, in 2012 IEEE/OES Autonomous Underwater Vehicles (AUV), pp. 1–7, IEEE., 2012.

Queste, B. Y., Fernand, L., Jickells, T. D. and Heywood, K. J.: Spatial extent and historical context of North Sea oxygen depletion in August 2010, Biogeochemistry, 113(1–3), 53–68, 2013.

Redfield, A. C.: The influence of organisms on the composition of seawater, Sea, 2, 26–77, 1963.

Rérolle, V.: DEVELOPMENT AND DEPLOYMENT OF AN IN SITU SENSOR FOR SEAWATER pH BASED ON THE SPECTROPHOTOMETRIC METHOD, PhD Thesis, University of Southampton, (March), 167 [online] Available from: http://eprints.soton.ac.uk/359137/1/Rerolle, V_VR_PhD_Thesis_130719.pdf, 2013.

Rérolle, V., Ruiz-Pino, D., Rafizadeh, M., Loucaides, S., Papadimitriou, S., Mowlem, M. and Chen, J.: Measuring pH in the Arctic Ocean: Colorimetric method or SeaFET?, Methods Oceanogr., 17, 32–49, doi:10.1016/j.mio.2016.05.006, 2016.

Rérolle, V. M. C., Floquet, C. F. A., Mowlem, M. C., Connelly, D. P., Achterberg, E. P. and Bellerby, R. R. G. J.: Seawater-pH measurements for ocean-acidification observations, TrAC - Trends Anal. Chem., 40(0), 146–157, doi:10.1016/j.trac.2012.07.016, 2012.

Rérolle, V. M. C., Floquet, C. F. A., Harris, A. J. K., Mowlem, M. C., Bellerby, R. R. G. J. and Achterberg, E. P.: Development of a colorimetric microfluidic pH sensor for autonomous seawater measurements, Anal. Chim. Acta, 786, 124–131, 2013.

Reuer, M. K., Barnett, B. A., Bender, M. L., Falkowski, P. G. and Hendricks, M. B.: New estimates of Southern Ocean biological production rates from O2/Ar ratios and the triple isotope composition of O2, Deep Sea Res. Part I Oceanogr. Res. Pap., 54(6), 951–974, 2007.

Rey, B. F.: 5 . Phytoplankton : the grass of the sea, in: The Norwegian Sea Ecosystem, edited by: Skjodal, H. R., Tapir, Trondheim, Norway, 93–112, 2004.

Richardson, K., Nielsen, T. G., Pedersen, F. B., Heilmann, J. P., Løkkegaard, B. and Kaas, H.: Spatial heterogeneity in the structure of the planktonic food web in the North Sea, Mar. Ecol. Prog. Ser., 168, 197–211, 1998.

Richardson, K., Visser, A. W. and Pedersen, F. B.: Subsurface phytoplankton blooms fuel pelagic production in the North Sea, J. Plankton Res., 22(9), 1663–1671, 2000.

Riegman, R., Colijn, F., Malschaert, J. F. P., Kloosterhuis, H. T. and Cadee, G. C.: Assessment of growth rate limiting nutrients in the North Sea by the use of nutrient-uptake kinetics, Netherlands J. Sea Res., 26(1), 53–60, 1990.

Rodwell, M. J., Rowell, D. P. and Folland, C. K.: Oceanic forcing of the wintertime North Atlantic Oscillation and European climate, Nature, 398(6725), 320–323, 1999.

Rudnick, D. L.: Ocean Research Enabled by Underwater Gliders, Ann. Rev. Mar. Sci., 8(1), 519–541, doi:10.1146/annurev-marine-122414-033913, 2016.

Saba, G., Wright-Fairbanks, E. K., Chen, B., Cai, W.-J., Barnard, A., Jones, C.,

Branham, C. W., Wang, K. and Miles, T.: The development and validation of a profiling glider deep ISFET-based pH sensor for high resolution observations of coastal and ocean acidification, Front. Mar. Sci., 6, 664, 2019.

Sabine, C. L., Feely, R. A., Gruber, N., Key, R. M., Lee, K., Bullister, J. L., Wanninkhof, R., Wong, C. S. S., Wallace, D. W. R., Tilbrook, B., Millero, F. J., Peng, T.-H. T.-H., Kozyr, A., Ono, T., Rios, A. F., A., F. R., Gruber, N., Key, R. M., Lee, K., Bullister, J. L., Wanninkhof, R., Wong, C. S. S., Wallace, D. W. R., Tilbrook, B., Millero, F. J., Peng, T.-H. T.-H., Kozyr, A., Ono, T. and Rios, A. F.: The oceanic sink for anthropogenic CO2, Science (80-.)., 305(5682), 367–371, doi:10.1126/science.1097403, 2004.

Saderne, V., Fietzek, P. and Herman, P. M. J.: Extreme Variations of pCO2 and pH in a Macrophyte Meadow of the Baltic Sea in Summer: Evidence of the Effect of Photosynthesis and Local Upwelling, PLoS One, 8(4), 2–9, doi:10.1371/journal.pone.0062689, 2013.

Saetre, R. and Ljoen, R.: THE NORWEGIAN COASTAL CURRENT, Port and Ocean Engineering under Arctic Conditions, Technical University of Norway, Bergen, Norway, 1–22, 1972.

Sætre, R.: Features of the central Norwegian shelf circulation, Cont. Shelf Res., 19(14), 1809–1831, doi:10.1016/S0278-4343(99)00041-2, 1999.

Salt, L. A., Thomas, H., Prowe, A. E. F., Borges, A. V., Bozec, Y. and De Baar, H. J. W.: Variability of North Sea pH and CO2 in response to North Atlantic Oscillation forcing, J. Geophys. Res. Biogeosciences, 118(4), 1584–1592, doi:10.1002/2013JG002306, 2013.

Schiettecatte, L. S., Thomas, H., Bozec, Y. and Borges, A. V.: High temporal coverage of carbon dioxide measurements in the Southern Bight of the North Sea, Mar. Chem., 106(1-2 SPEC. ISS.), 161–173, doi:10.1016/j.marchem.2007.01.001, 2007.

Schröder, C. R., Weidgans, B. M. and Klimant, I.: pH fluorosensors for use in marine systems, Analyst, 130(6), 907–916, 2005.

Seguro, I., Marca, A. D., Painting, S. J., Shutler, J. D., Suggett, D. J. and Kaiser, J.: High-resolution net and gross biological production during a Celtic Sea spring bloom, Prog. Oceanogr., 177, 101885, 2019.

Seidel, M. P., Degrandpre, M. D. and Dickson, A. G.: A sensor for in situ indicator-based measurements of seawater pH, Mar. Chem., 109, 18–28, doi:10.1016/j.marchem.2007.11.013, 2008.

Seiter, J. C. and DeGrandpre, M. D.: Redundant chemical sensors for calibration-

impossible applications, Talanta, 54(1), 99–106, doi:10.1016/S0039-9140(00)00635-4, 2001.

Sharples, J., Ross, O. N., Scott, B. E., Greenstreet, S. P. R. and Fraser, H.: Inter-annual variability in the timing of stratification and the spring bloom in the North-western North Sea, Cont. Shelf Res., 26(6), 733–751, 2006.

Sherman, J., Davis, R. E., Owens, W. B. and Valdes, J.: The autonomous underwater glider" Spray", IEEE J. Ocean. Eng., 26(4), 437–446, 2001.

Shitashima, K., Kyo, M., Koike, Y. and Henmi, H.: Development of in situ pH sensor using ISFET, in Proceedings of the 2002 Interntional Symposium on Underwater Technology (Cat. No. 02EX556), pp. 106–108, IEEE., 2002.

Skjelvan, I., Falck, E., Anderson, L. G. and Rey, F.: Oxygen fluxes in the Norwegian Atlantic Current, Mar. Chem., 73(3–4), 291–303, doi:10.1016/S0304-4203(00)00112-2, 2001.

Skjelvan, I., Anderson, L. G., Falck, E. and Anders, K.: A Review of the Inorganic Carbon Cycle of the Nordic Seas and Barents Sea, The Nordic Seas: An Integrated Perspective, 14, 157, https://doi.org/10.1029/GM158, 2005.

Skjelvan, I., Falck, E., Rey, F. and Kringstad, S. B.: Inorganic carbon time series at Ocean Weather Station M in the Norwegian Sea, Biogeosciences, 549–560, 2008.

Skogen, M. D., Søiland, H. and Svendsen, E.: Effects of changing nutrient loads to the North Sea, J. Mar. Syst., 46(1–4), 23–38, 2004.

Soli, A. L., Pav, B. J. and Byrne, R. H.: The effect of pressure on meta-Cresol Purple protonation and absorbance characteristics for spectrophotometric pH measurements in seawater, Mar. Chem., 157, 162–169, doi:10.1016/j.marchem.2013.09.003, 2013.

Spaulding, R. S., Degrandpre, M. D., Beck, J. C., Hart, R. D., Peterson, B., Carlo, E. H. De, Drupp, P. S. and Hammar, T. R.: Autonomous in Situ Measurements of Seawater Alkalinity, Environ. Sci. Technol, *48*(16), pp.9573-9581, 2014.

Sprintall, J. and Roemmich, D.: Characterizing the structure of the surface layer in the Pacific Ocean, J. Geophys. Res. Ocean., 104(C10), 23297–23311, 1999.

Stommel, H.: The slocum mission, Oceanography, 2(1), 22–25, 1989.

Sutton, A. J., Sabine, C. L., Meinig, C. and Feely, R. A.: A high-frequency atmospheric and seawater pCO2 data set from 14 open-ocean sites using a moored autonomous system, Earth Syst. Sci. Data, 353–366, doi:10.3334/CDIAC/OTG.TSM, 2014.

Swift, J. H.: The arctic waters, in The Nordic Seas, pp. 129–154, Springer., 1986.

Takahashi, T., Sutherland, S. C., Sweeney, C., Poisson, A., Metzl, N., Tilbrook, B., Bates, N., Wanninkhof, R., Feely, R. A., Sabine, C., Olafsson, J. and Nojiri, Y.: Global sea – air CO2 flux based on climatological surface ocean pCO2 , and seasonal biological and temperature effects, Deep Sea Res. Part II: Topical Stud. in Oceanogr., 49, 1601–1622, 2002.

Takahashi, T., Sutherland, S. C., Wanninkhof, R., Sweeney, C., Feely, R. A., Chipman, D. W., Hales, B., Friederich, G., Chavez, F., Sabine, C., Watson, A., Bakker, D. C. E., Schuster, U., Yoshikawa-Inoue, H., Ishii, M., Midorikawa, T., Nojiri, Y., Körtzinger, A., Steinhoff, T., Hoppema, M., Olafsson, J., Arnarson, T. S., Johannessen, T., Olsen, A., Bellerby, R., Wong, C. S., Delille, B., Bates, N. R. and de Baar, H. J. W.: Climatological mean and decadal change in surface ocean pCO2, and net sea–air CO2 flux over the global oceans, Deep Sea Res. Part II Top. Stud. Oceanogr., 56(8), 554–577, doi:10.1016/j.dsr2.2008.12.009, 2009.

Takeshita, Y., Martz, T. R., Johnson, K. S. and Dickson, A. G.: Characterization of an ion sensitive field effect transistor and chloride ion selective electrodes for pH measurements in seawater, Anal. Chem., 86(22), 11189–11195, 2014.

Talley, L. D., Feely, R. A., Sloyan, B. M., Wanninkhof, R., Baringer, M. O., Bullister, J. L., Carlson, C. A., Doney, S. C., Fine, R. A. and Firing, E.: Changes in ocean heat, carbon content, and ventilation: a review of the first decade of GO-SHIP global repeat hydrography, Ann. Rev. Mar. Sci., 8, 185–215, 2016.

Tengberg, A., Hovdenes, J., Andersson, H. J., Brocandel, O., Diaz, R. and Hebert, D.: Evaluation of a lifetime-based optode to measure oxygen in aquatic systems, Limnol. Oceanogr.: Methods, (1964), 7–17, 2006.

Thomas, H., Ittekkot, V., Osterroht, C. and Schneider, B.: Preferential recycling of nutrients—the ocean's way to increase new production and to pass nutrient limitation?, Limnol. Oceanogr., 44(8), 1999–2004, 1999.

Thomas, H., Bozec, Y., Elkalay, K. and De Baar, H. J. W.: Enhanced open ocean storage of CO2 from shelf sea pumping, Science (80-.)., 304(5673), 1005–1008, 2004.

Thomas, H., Bozec, Y., Elkalay, K., de Baar, H. J. W., Borges, A. V and Schiettecatte, L. S.: Controls of the surface water partial pressure of CO2 in the North Sea, Biogeosciences, 2(4), 323–334, 2005.

Thomas, H., Prowe, A. E. F., van Heuven, S., Bozec, Y., de Baar, H. J. W., Schiettecatte, L. S., Suykens, K., Koné, M., Borges, A. V., Lima, I. D. and Doney, S. C.:

Rapid decline of the CO2 buffering capacity in the North Sea and implications for the North Atlantic Ocean, Global Biogeochem. Cycles, 21(4), 1–13, doi:10.1029/2006GB002825, 2007.

Thomas, P. J., Atamanchuk, D., Hovdenes, J. and Tengberg, A.: The use of novel optode sensor technologies for monitoring dissolved carbon dioxide and ammonia concentrations under live haul conditions, Aquac. Eng., 77, 89–96, 2017.

Thompson, R. O. R. Y.: Climatological numerical models of the surface mixed layer of the ocean, J. Phys. Oceanogr., 6(4), 496–503, 1976.

Tsunogai, S., Watanabe, S. and Sato, T.: Is there a 'continental shelf pump' for the absorption of atmospheric CO2?, Tellus, Ser. B Chem. Phys. Meteorol., 51(3), 701–712, doi:10.1034/j.1600-0889.1999.t01-2-00010.x, 1999.

Turrell, W. R., Henderson, E. W., Slesser, G., Payne, R. and Adams, R. D.: Seasonal changes in the circulation of the northern North Sea, Cont. Shelf Res., 12(2–3), 257–286, doi:10.1016/0278-4343(92)90032-F, 1992.

Walsh, J. J.: Importance of continental margins in the marine biogeochemical cycling of carbon and nitrogen, Nature, 350(6313), 53–55, doi:10.1038/350053a0, 1991.

Wang, Z. A., Liu, X., Byrne, R. H., Wanninkhof, R., Bernstein, R. E., Kaltenbacher, E. A. and Patten, J.: Simultaneous spectrophotometric flow-through measurements of pH, carbon dioxide fugacity, and total inorganic carbon in seawater, Anal. Chim. Acta, 596(1), 23–36, 2007.

Wang, Z. A., Sonnichsen, F. N., Bradley, A. M., Hoering, K. A., Lanagan, T. M., Chu, S. N., Hammar, T. R. and Camilli, R.: In Situ Sensor Technology for Simultaneous Spectrophotometric Measurements of Seawater Total Dissolved Inorganic Carbon and pH, Environ. Sci. Technol., doi:10.1021/es504893n, 2015.

Wanninkhof, R.: Relationship between wind speed and gas exchange over the ocean revisited, Limnol. Oceanogr.: Methods, 351–362, doi:10.4319/lom.2014.12.351, 2014.

Weatherall, P., Marks, K. M., Jakobsson, M., Schmitt, T., Tani, S., Arndt, J. E., Rovere, M., Chayes, D., Ferrini, V. and Wigley, R.: A new digital bathymetric model of the world's oceans, Earth Sp. Sci., 2(8), 331–345, 2015.

Webb, D. C., Simonetti, P. J. and Jones, C. P.: SLOCUM: An underwater glider propelled by environmental energy, IEEE J. Ocean. Eng., 26(4), 447–452, 2001.

Wedborg, M., Turner, D. R., Anderson, L. G. and Dyrssen, D.: Determination of pH, Methods seawater Anal., 109–125, 1999.

Weiss, R. F.: Carbon dioxide in water and seawater: the solubility of a non-ideal gas, Mar. Chem., 2(3), 203–215, doi:10.1016/0304-4203(74)90015-2, 1974.

Weiss, R. F. and Price, B. A.: Nitrous oxide solubility in water and seawater, Mar. Chem., 8(4), 347–359, 1980.

Weston, K., Fernand, L., Mills, D. K., Delahunty, R. and Brown, J.: Primary production in the deep chlorophyll maximum of the central North Sea, J. Plankton Res., 27(9), 909–922, 2005.

Williams, N. L., Juranek, L. W., Johnson, K. S., Feely, R. A., Riser, S. C., Talley, L. D., Russell, J. L., Sarmiento, J. L. and Wanninkhof, R.: Empirical algorithms to estimate water column pH in the Southern Ocean, Geophys. Res. Lett., 43(7), 3415–3422, 2016.

Williams, N. L., Juranek, L. W., Feely, R. A., Johnson, K. S., Sarmiento, J. L., Talley, L. D., Dickson, A. G., Gray, A. R., Wanninkhof, R., Russell, J. L., Riser, S. C. and Takeshita, Y.: Calculating surface ocean pCO2 from biogeochemical Argo floats equipped with pH: An uncertainty analysis, Global Biogeochem. Cycles, 31(3), 591–604, doi:10.1002/2016GB005541, 2017.

Williams, P. J. B., Quay, P. D., Westberry, T. K. and Behrenfeld, M. J.: The Oligotrophic Ocean is autotrophic, Annu. Rev. Mar Sci., doi:10.1146/annurev-marine-121211-172335, 2013.

Wise, J. A. and Soulen Jr, R. J.: Thermometer calibration: a model for state calibration laboratories, STIN, 86, 25756, 1986.

Woolf, D. K. and Thorpe, S. A.: Bubbles and the air-sea exchange of gases in near-saturation conditions, J. Mar. Res., 49(3), 435–466, 1991.

Zeebe, R. and Wolf-Gladrow, D.: CO2 in Seawater-Equilibrium, Kinetics, Isotopes, Elsevier, 100, doi:10.1016/S0422-9894(01)80002-7, 2001.

Zhu, Q., Aller, R. C. and Fan, Y.: High-performance planar pH fluorosensor for two-dimensional pH measurements in marine sediment and water, Environ. Sci. Technol., 39(22), 8906–8911, 2005.

Appendices

A Supplementary Figures

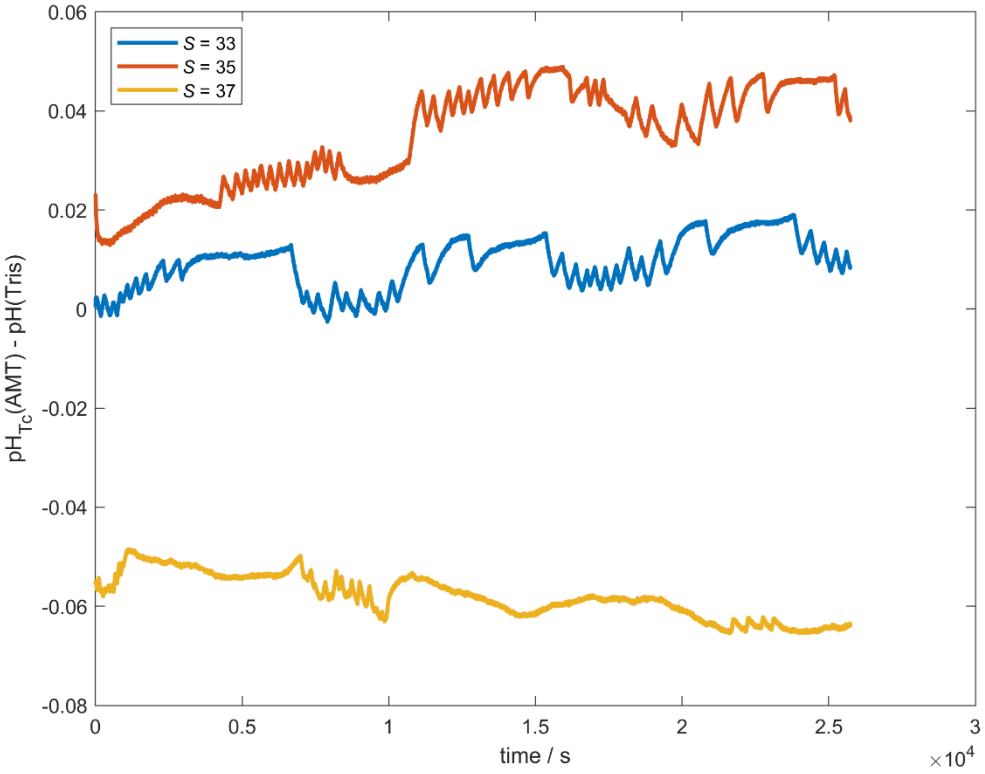

Figure A.1: Three experiments performed in three different Tris buffers solution with a salinity of 33 (blue) 18 May 2017, 35 (red) 22 May 2017 and 37 (yellow) 11 May 2017. The experiments were performed to quantify the effect of salinity on the AMT glass electrode keeping the temperature constant at 20 °C to isolate the salinity effect.